2014

Techniques For Characterization Of Third Order Optical Nonlinearities

Manuel Ferdinandus
University of Central Florida

TECHNIQUES FOR CHARACTERIZATION OF THIRD ORDER OPTICAL NONLINEARITIES

by

MANUEL R. FERDINANDUS
B.S. Seattle University, 1998
M.S. Rochester Institute of Technology, 2005

A dissertation submitted in partial fulfillment of the requirements
for the degree of Doctor of Philosophy
in CREOL the College of Optics and Photonics
at the University of Central Florida
Orlando, Florida

Spring Term
2014

Major Professors: David J. Hagan and Eric W. Van Stryland

ABSTRACT

This dissertation describes the development of novel techniques for characterization of nonlinear properties of materials. The dissertation is divided into two parts, a background and theory section and a technique development section.

In the background and theory section we explain the origins of the nonlinear optical response of materials across many different spatial and temporal scales. The mechanisms that we are most interested in are the electronic nuclear and reorientational responses, which occur on the range of sub-femtosecond to several picoseconds. The electronic mechanism is due to the electrons of a material experiencing a non-parabolic potential well due a strong electric field and occurs on the sub-femtosecond timescale. The nuclear or vibrational effect results from the motion of the nuclei of the atoms and typically occurs on the order of a few hundred femtoseconds. Finally the reorientational nonlinearity is due to the alignment of the molecule to the electric field, which alters the polarizability of the molecule and typically occurs on the scale of a few picoseconds. There are other mechanisms can induce nonlinear optical effects such as thermal effects and electrostriction, but these effects typically occur on much larger timescales than we are interested in, and hence will not be a major focus of this dissertation.

In the nonlinear characterization techniques section, we describe previous research into the field of nonlinear optical characterization techniques, describing the techniques used to characterize the nonlinear properties of materials, their applications and limitations. We will trace the development of two recently developed techniques for nonlinear spectroscopy − the Dual Arm

Z-Scan and the Beam Deflection techniques. The Dual Arm Z-Scan technique is an enhancement of the standard Z-Scan technique that allows for the measurement of small nonlinear signals in the presence of large background signals. This technique allows for the measurement of materials under certain conditions not previously measureable using the standard Z-Scan technique, such materials with low damage thresholds, poor solubility and thin films.

In addition to the Dual Arm Z-Scan, we have developed a new method for characterizing nonlinear refraction, the Beam Deflection technique, which is a variation of the photothermal beam deflection technique previously used to measure very weak absorption signals. This technique offers relative ease of use, the ability to measure the absolute magnitude and sign of both the real and imaginary parts of $\chi^{(3)}$ simultaneously with high sensitivity. We fully develop the theory for materials with instantaneous and non-instantaneous nonlinearities, with nonlinear absorption and group velocity mismatch. We also demonstrate the power of this technique to separate the isotropic and reorientational contributions of liquids by examining the temporal response and polarization dependences.

Lastly, we summarize our conclusions and describe two promising future research directions that would benefit from the Dual Arm Z-Scan and Beam Deflection techniques.

TABLE OF CONTENTS

ABSTRACT ii

TABLE OF CONTENTS iv

LIST OF FIGURES vii

LIST OF TABLES xviii

LIST OF NOMENCLATURE xix

CHAPTER 1: INTRODUCTION 1

1.1. Origins of Optical Response 5

1.1.1. Electronic Response 6

1.1.2. Reorientational Response 26

1.1.3. Excited State Absorption 30

CHAPTER 2: MEASUREMENT TECHNIQUES 33

2.1. Linear Characterization Techniques 33

2.2. Nonlinear Characterization Techniques 34

2.2.1. Excitation Source 35

2.2.2. Tunable Frequency Source 37

2.2.3. Excite-Probe 39

2.2.4. Z-Scan 43

CHAPTER 3: TECHNIQUE DEVELOPMENT 61

3.1. Dual-Arm Z-Scan 62

3.1.1. Experimental Apparatus 64

3.1.2. Theory and Analysis.....66

3.1.3. Application - Organic Solutes in Solvents 75

3.1.4. Application - Thin Films 86

3.2. Beam Deflection 88

3.2.1. Experimental Apparatus 90

3.2.2. Theory and Analysis.....93

3.2.3. Application - Solids Without NLA 143

3.2.4. Application - Liquids Without NLA 145

3.2.5. Application - Solids with NLA and GVM.....151

CHAPTER 4: CONCLUSIONS.....156

4.1. Future Work.....157

4.1.1. Nondegenerate Enhancement in Organic Dyes 157

4.1.2. Nonlinear Measurement of Gases 165

APPENDIX A: DERIVATION OF ANGULAR DEFLECTION 169

APPENDIX B: ESSENTIAL STATE MODEL DERIVATION.....172

APPENDIX C: BEAM DEFLECTION SCHEMATICS 181

APPENDIX D: COPYRIGHT PERMISSIONS 188

LIST OF REFERENCES.....192

LIST OF FIGURES

Figure 1: Energy level diagram of 1PA and 2PA. $|g$ is the ground state, $|e$ is the first excited state and $|e'$ is the second excited state. 2

Figure 2: Energy level diagram for three level SOS model for symmetric molecules. 22

Figure 3: Real (left) and imaginary (right) parts of N terms (dashed) and D terms (dotted) and total (solid) vs. frequency with $\omega e'g = 1.2\omega eg$, $\Gamma eg = \omega eg200$, $\Gamma e'g = \Gamma eg$ and $\mu gex = \mu ee'x$ and ωeg = 1. 23

Figure 4: (left) Real and (right) imaginary parts of $\chi xxxx(3)$ for damping values Γeg = 1/200 (dotted), 1/400 (dashed) and 1/800 (solid), $\Gamma e'g = 10\Gamma eg$, $\omega e'g$ = 1.2ωeg, and μeg = $\mu e'g$. Increasing the damping parameter Γ reduces the peak and broadens the features of $\chi xxxx(3)$. 24

Figure 5: (left) Real and (right) imaginary parts of $\chi xxxx(3)$ for $\omega e'g/\omega eg$ = 0.75 (dotted), 1 (dashed) and 1.25 (solid), Γeg = 1/200ωeg, $\Gamma e'g = 10\Gamma eg$, and μeg = $\mu e'g$. Increasing $\omega e'g/\omega eg$ increases the magnitude of the peak of $\chi xxxx(3)$ as well as shift 25

Figure 6: (left) FOM for damping values Γeg = 1/200 (solid), 1/400 (dashed) and 1/800 (dotted) and $\Gamma e'g = 10\Gamma eg$; (right) FOM for ratio of transition dipole moments $\omega eg/\omega e'g$ = 0.8 (dotted), 1.0 (dashed) and 1.2 (solid). All other parameters are the same as those used in Figure 3. 26

Figure 7: a) diagram of CS_2; b) diagram of transverse and longitudinal polarizability. For a linear molecule of this type the longitudinal polarizability is much higher than the transverse polarizability due to the increased length. 27

Figure 8: Energy level diagram of ESA. 31

Figure 9: 1PA spectrum of AJBC 3702 Dimethylformamine (DMF). The peak molar absorbance is 1.58×10^5 cm^{-1} M^{-1} at a wavelength of λ = 853 nm. 34

Figure 10: Diagram of Clark-MXR CPA 2110, (left) generation stage (right) amplification stage. 36

Figure 11: Diagram of Coherent Elite Duo. 37

Figure 12: Diagram of Light Conversion TOPAS-C. Path length equalization optics have been omitted for clarity. 38

Figure 13: Excite-probe schematic. 40

Figure 14: Nondegenerate excite-probe measurement of ZnO with λe = 1800 nm, λp = 440 nm. 42

Figure 15: Z-Scan schematic. 43

Figure 16: OA signal for GaAs for λ = 1300 nm, E = 1.52 nJ, $w0$ = 24.5 μm (HW1/e^2M), τ = 120 fs (FWHM), n = 3.4, and L = 0.48 mm. The fit value for $\alpha 2$ = 2.4×10^{-10} m/W. 44

Figure 17: CA signal for CS_2 with λ = 1300 nm, E = 23 nJ, $w0$ = 24.5 (HW1/e^2M), τ = 120 fs (FWHM), n = 1.6 and L = 1 mm. The fit value for $n2$ = 4.0×10^{-19} m^2/W. 46

Figure 18: OA, CA and CA/OA Z-Scan signal [54] for $\Delta\phi 0$ = -0.5 and $q0$ = 0.3 53

Figure 19: Fractional error in $n2$ vs. SNR (solid), fitting error (bashed), parameter uncertainty (dotted).....57

Figure 20: DA Z-Scan experimental apparatus. 65

Figure 21: DA Z-Scan data analysis. (a) Low energy scans of solution $TS(Z)|E \approx 0$ and solvent $TV(Z)|E \approx 0$. (b) Subtraction of $TS(Z)|E \approx 0$ and $TV(Z)|E \approx 0$. (c) High energy scans of solution TSZ and solvent TVZ. (d) Subtraction of TSZ and TVZ. (e) Extracted solute signal $TU(Z)$ and fit with $\Delta\phi 0$ = -0.06 and $q0$ = 0.03.....67

Figure 22: Signal due to 1% (dotted), 5% (dashed) and 10% (solid) energy mismatch for typical Z-Scan parameters in Table 3. 72

Figure 23: Signal due to 1% (dotted), 5% (dashed) and 10% (solid) beam waist mismatch for typical Z-Scan parameters in Table 3. 73

Figure 24: Signal due to 1% (dotted), 5% (dashed) and 10% (solid) of $z0$ sample Z-positioning mismatch for typical Z-Scan parameters in Table 3. 74

Figure 25: Structure and linear absorption spectra of SD-O 2405. 76

Figure 26: Sequential CA single-arm Z-Scans of toluene (open red triangles) and SD-O 2405 in toluene (closed black squares) at 695 nm with C = 47 μm, E = 31 nJ ($I0$ = 51 GW/cm^2) and S = 0.33; (b) the subtraction of $TV(Z)$ from $TS(Z)$ from sequential scans (open green squares); (c) Simultaneous CA DA Z-Scans of toluene (open red triangles) and SD-O 2405 in toluene (closed black squares) at 695 nm; (d) the subtraction of $TV(Z)$ from $TS(Z)$ from simultaneous scans after LEB subtraction (open green squares) and corresponding fit using $\Delta\phi 0$ = -0.16, $q0$ = 0.077 (solid blue). 77

Figure 27: Sequential Z-Scans of the solution SD-O-2405 in toluene (closed black squares) and solvent toluene (open red triangles) at 780 nm, E = 50 nJ ($I0$ = 88 GW/cm^2), C = 0.60 mM and (b) subtraction of solution and solvent CA Z-Scan signals (open green squares) along with the OA Z-Scan of the solution (closed black circles) and corresponding 2PA and CA fit (solid red and blue line, respectively) with $\alpha 2, U-Fit$ = 0.013 cm/GW and $n2, U-Fit$ = -0.35 ×10^{-19} m^2/W; (c) DA Z-Scans of solution (closed black squares) and solvent (open red triangles) taken simultaneously; (d) Simultaneous subtraction of solution and solvent yielding solute signal (open green squares) and fit incorporating both 2PA and NLR (solid blue line) with $\Delta\phi 0$ = -0.25, $q0$ = 0.11, using S = 0.33. 79

Figure 28: CA DA Z-scans at λ = 880 nm, E = 13 nJ, C = 0.60 mM, , S = 0.33, and $I0$ = 22 GW/cm^2 for (a) toluene (open black circles) and (b) solution (open black circles) along with independent fits for $n2-\Delta n2$ (solid blue line) and $n2+\Delta n2$ (solid green line) ; (c) $TU(Z)$ (open green squares) of SD-O 2405 and fit (solid blue line) with $\Delta\phi 0$ = -0.023, $q0$ = 0.0020. 82

Figure 29: (a) 2PA cross section (open red circles) and three level SOS fit (solid red) vs. wavelength and incident photon energy and (b) NLR cross section (open blue circles) and three level SOS fit (solid blue) 84

Figure 30: Comparison of nonlinear spectra of single arm and DA Z-Scan techniques. The DA Z-Scan techniques allows for determination of $n2$ farther into the IR. 85

Figure 31: (upper left) Sequential single arm CA Z-Scans of ZnO on quartz substrate (black) and quartz substrate alone (red) and (upper right) subtraction of sequential scans in left figure. Note

that the signal is masked by the uncorrelated noise such that $n2$ cannot be determined. (lower) CA scan of ZnO via DA Z-Scan (green) and fit (black) with $n2 = 10 \times 10^{-15}$ cm^2/W. 87

Figure 32: Co-propagating, cross propagating and mirage effect configurations for photothermal beam deflection. We will modify the co-propagating geometry for ultrafast nonlinearities...89

Figure 33: BD schematic. (a) probe beam (b) delay stage (c) excitation beam (d) sample (e) deflected beam (f) segmented bi-cell detector. 90

Figure 34: (left) Quad cell detector schematic with probe beam centered on quad cell so that $\Delta EE = 0$, (right) probe shifted on quad cell so that $S = \Delta EE > 0$.....91

Figure 35: (left) Weighted excitation slope weighted over probe profile (solid) and linear approximation of slope (dashed) of excitation beam at the point of maximum slope vs. R. (right) Error in linear approximation of slope vs. weighted slope vs. R. 96

Figure 36: Overlap of excitation (red) and probe (blue) beam for maximum deflection for typical BD parameters given in Table 4.....97

Figure 37: Signal vs. delay using simple prism approximation for typical BD parameters given in Table 4 and $n2 = 0.25 \times 10^{-19}$ m^2/W (dashed), $n2 = 1.0 \times 10^{-19}$ m^2/W (dotted), and $n2 = 4.0 \times 10^{-19}$ m^2/W (solid).....102

Figure 38: Maximum sensitivity vs. minimum detectable signal for typical BD parameters given in Table 4. 103

Figure 39: Effect of transmission gradient (solid black) on probe beam (solid blue). The transmission gradient makes it appear as if the probe has been laterally translated (dashed blue).

Both the probe and translated probe beam have been normalized to their peak irradiance to facilitate comparison of their profiles. 104

Figure 40: Probe beam (solid) and transmission profiles in x (dashed) and y (dotted) directions. The x direction gradient is approximately uniform, while the y direction gradient is approximately linear across the probe beam. 106

Figure 41: Transmission signal vs. delay with 1 (dotted), 2 (dashed) and 11 (solid) terms in summation using typical BD parameters given in Table 4. 110

Figure 42: Deflection signal due to NLR (blue), NLA (red) and the total (black) vs. delay with 1 (dotted), 2 (dashed) and 11 (solid) terms in summation using typical BD parameters given in Table 4. Even with only one term in the summation used the accuracy of the approximation is very good, with an error < 1%. 111

Figure 43: Error in peak deflection signal vs. $q0$ using typical BD parameters given in Table 4. 112

Figure 44: Summation order required for an error of less than 1% as a function of absorption parameter. 113

Figure 45: Effect of translation of probe beam on deflection signal. (left) Effect of translation for a small probe spot size on the detector. Most of the probe beam has been shifted to the right side of the detector. (right) Effect of the same translation for a large spot size on the detector. A smaller portion of the probe beam has been shifted to the right side of the detector. As the distance between the sample and the detector is increases, the probe spot size on the detector increases and the effect of the translation on $\Delta Ep/Ep$ is reduced. 114

Figure 46: Deflection signal due to absorption as a function of distance from sample to detector. 115

Figure 47: Peak deflection signal due to NLA vs. $q0$. At high NLA the peak absorption signal is pathological due to distortion of the probe beam. 116

Figure 48: Non-instantaneous response function using typical experimental parameters with rise time of 100 fs (FWHM) and decay time of 1 ps. 117

Figure 49: Deflection signal for non-instantaneous material response using parameters used in Figure 48. 118

Figure 50: Error in $\Delta\phi 0$ vs. error in $q0$ for SNR = 10 and 10% error in parameter knowledge (25% error in $q0$ and 20% error in $z0$). 121

Figure 51: Error in $\Delta\phi 0$ vs. ρ for SNR = 10 and 10% error in parameter knowledge (25% error in $q0$ and 20% error in $z0$). 123

Figure 52: (left) Z-Scan CA/OA signal for $\Delta\phi 0$ = 0.12 and $q0$ = 0 (dotted), $q0$ = 0.28 (dashed) and $q0$ = 0.56 (solid). Increasing the NLA changes the signal from a valley-peak structure to a valley-peak-valley structure; (right) Z-Scan CA/OA signal for $q0$ = 0.28 and $\Delta\phi 0$ = 0.041 (solid) corresponding to ρ = 3, 0.031 (dashed) corresponding to ρ = 4 and 0.016 (dotted) corresponding to ρ = 5. As the NLA is increased the positive and negative valleys become closer together. 124

Figure 53: (left) CA (red), OA (blue) and CA/OA (black) signals for $q0$ = 0.28 and ρ = 19 ($\Delta\phi 0$ = 0.007). $\Delta Tp - v$ = 1.82%. The CA and CA/OA signals are nearly symmetric within the

system noise, making it very difficult to determine the value of $n2$ accurately; (right) zoom of CA/OA in left figure. 125

Figure 54: Z-Scan of AJBC-3702 at 1400 nm, (a) OA data (red circles) and fit (solid red), (b) CA data (blue circles) and fit (solid blue), (c) CA/OA data (black circles) and fit (solid black) with $\alpha 2 = 0.12 \times 10^{-11}$ m/W and $n2 = 0.1 \times 10^{-15}$ m^2/W ($\rho = 13.4$). At this ρ it is difficult to determine an accurate value of $n2$ since the signal is dominated by the NLA. 126

Figure 55: (left) Responsivity vs. beam waist ratio W and (right) responsivity vs. pulse duration ratio T for typical BD parameters given in Table 4. 128

Figure 56: Broadening factor $\tau out/\tau$ vs. length of BK7 glass traversed at $\lambda = 650$ nm. 132

Figure 57: Input pulse (solid) and output pulse (dashed) broadened by SPM in a $L = 5$ mm thick quartz lens with $I0 = 2.0 \times 10^{15}$ W/m^2, $\lambda = 650$ nm and $\tau = 35$ fs (FWHM). The input spectrum is 27 nm (FWHM) while the output spectrum is 34 nm. 133

Figure 58: left) Temporal profile $U(0,t)$ of pulse at focus due to distortion by chromatic aberration for various values of $T = 0$ (solid), $T = 2$ (dashed) and $T = 4$ (dotted); right) ratio of apparent pulse duration to actual pulse duration $\tau measured/\tau$ vs. ratio of chromatic aberration parameter to actual pulse duration T/τ. 135

Figure 59: BD of quartz using left) mirrors and right) lenses as the focusing elements before the sample. Using mirrors produces the expected cross correlation signal of 80 fs (FWHM), while using lenses gives an artificially lengthened cross correlation width of 150 fs (FWHM). ... 136

Figure 60: BD signal for typical experimental parameters and increasing amounts of GVM. No GVM (blue), small amount of GVM (green), large amount of GVM (red). 141

Figure 61: Co-polarized (black) and cross polarized (red) BD scan of quartz with L = 1 mm, λp = 650 nm, wp = 35 µm, τp = 170 fs (FWHM), λe = 780 nm, we = 132 µm, τe = 241 fs (FWHM), Ee = 3.6 µJ and $I0,e$ = 5.1×10^{14} W/m^2. The asymmetry is due to the nuclear response quartz. 143

Figure 62: BD scan of quartz with L = 1 mm, λp = 650 nm, wp = 35 µm, τp = 170 fs (FWHM), λe = 780 nm, we = 132 µm, τe = 241 fs (FWHM), Ee = 23 nJ and $I0,e$ = 3.5×10^{12} W/m^2. 144

Figure 63: Noise extracted using high pass filter of Figure 62.....145

Figure 64: Index change vs. delay for CS_2 with L = 1 mm, λp = 650 nm, wp = 105 µm, τp = 110 fs (FWHM), λe = 780 nm, we = 105 µm, τe = 105 fs (FWHM), and $I0,e$ = 7.4×10^{13} W/m^2. 146

Figure 65: BD scan of CS_2 at co-polarized, cross polarized and magic angle configurations with L = 1 mm, λp = 650 nm, wp = 33 µm, τp = 135 fs (FWHM), λe = 800 nm, we = 175 µm, τe = 47 fs (FWHM), and $I0,e$ = 3.0×10^{14} W/m^2. 147

Figure 66: Isotropic response as function of relative polarization angle θ. The cross polarized response is 1/3 the co-polarized response. 148

Figure 67: Decomposition of co-polarized signal shown in Figure 65 into isotropic and reorientational responses. 149

Figure 68: Comparison of co-polarized, cross polarized and reconstructed co-polarized reorientational response. 150

Figure 69: Comparison of measured and reconstructed cross polarized responses from Figure 65. 150

Figure 70: (left) Transmission vs. delay and (right) deflection vs. delay for ZnO with λe = 800 nm, λp = 400 nm, τe = 50 fs (FWHM), τp = 100 fs (FWHM), we = 178 μm (HW1/e^{2}M), wp = 45 μm (HW1/e^{2}M), Ee = 235 nJ, $I0,e$ = 7.94×10^{13} W/m^2, ne = 1.95, np = 2.21, $\partial ne \partial \lambda$ = -0.114 μm^{-1}, and $\partial np \partial \lambda$ = -5.56 μm^{-1}. The data (open blue circles) was fit (solid black line) with $\alpha 2$ = 7.2×10^{-11} m/W and $n2$ = -3.9×10^{-18} m^2/W. 152

Figure 71: Fine range scan of ZnO for ZnO for λe = 800 nm, λp = 400 nm, τe = 50 fs (FWHM), τp = 100 fs (FWHM), we = 178 μm (HW1/e^{2}M), wp = 45 μm (HW1/e^{2}M), Ee = 235 nJ, $I0,e$ = 7.94×10^{13} W/m^2, ne = 1.95, np = 2.21, $\partial ne \partial \lambda$ = -0.114 μm^{-1}, and $\partial np \partial \lambda$ = -5.56 μm^{-1}. The data (open blue circles) was fit (solid black line) with $\alpha 2$ = 7.2×10^{-11} m/W and $n2$ = -3.9×10^{-18} m^2/W. Note that the fit line matches the data, indicating that the rise time of the response is the cross-correlation of the pulses. 154

Figure 72: (top) electro-optic based Mach-Zehnder interferometer switch and (bottom) nonlinear based Mach-Zehnder interferometer based switch. 158

Figure 73: Anti-bonding (top) and bonding (bottom) of σ bond. 159

Figure 74: Anti-bonding (top) and bonding (bottom) and of π bond. 160

Figure 75: Polymethine dye. n indicates the number of methine groups in the conjugation chain and $R1$ and $R2$ are the terminal end groups. 160

Figure 76: 1PA spectrum of YZ-V-69 in CCl4. The peak molar absorbance is 2.57×10^5 cm^{-1} M^{-1} at 977 nm. 162

Figure 77: NLR and 2PA of YZ-V-69. Data taken from Hu [33]. 163

Figure 78: GM and RGM for YZ-V-69 using three level model parameters from Table 5.....164

Figure 79: GM (dotted red) and RGM (solid blue) for YZ-V-69 using fit parameters from Table 5 with excitation at 2.03 μm and probe from 1.1 to 1.8 μm. 165

Figure 80: BD schematic using Clark-MXR excitation with TOPAS-C probe (Clark-C).....182

Figure 81: BD schematic using Coherent Elite Duo excitation with WLC probe (Coherent-WL). 184

Figure 82: BD schematic using Coherent Elite Duo excitation with TOPAS-800 probe (Coherent-800).....186

LIST OF TABLES

Table 1: Summary of second order NLO processes. 9

Table 2: Summary of third order NLO processes. 10

Table 3: Typical Z-Scan parameters used in calculations. 71

Table 4: Typical BD parameters used for calculations. 93

Table 5: Three level model fit parameters for YZ-V-69. 163

LIST OF NOMENCLATURE

Acronym/Unit	Description
1PA	One Photon Absorption
2PA	Two Photon Absorption
CA	Closed Aperture
CA/OA	Closed Aperture Over Open Aperture
CPM	Cross Phase Modulation
CARS	Coherent Anti-stokes Raman Scattering
DMF	Dimethylformamine
D-2PA	Degenerate Two-Photon Absorption
DFG	Difference Frequency Generation
D-FWM	Degenerate Four-Wave Mixing
ESA	Excited State Absorption
ESE	Excited State Effects
ESR	Excited State Refraction
FOM	Figure Of Merit
FROG	Frequency Resolved Optical Grating
FWM	Four-Wave Mixing
GSA	Ground State Absorption
GVD	Group Velocity Dispersion

GVM	Group Velocity Mismatch
HOKE	Higher Order Kerr Effect
KTP	Potassium Titanyl Phosphate
LEB	Low Energy Background
ND-2PA	Nondegenerate Two-Photon Absorption
NLA	Nonlinear Absorption
NLR	Nonlinear Refraction
OA	Open Aperture
OHD	Optically Heterodyne Detection
OKT	Optical Kerr Technique
OPA	Optical Parametric Amplifier
OPG	Optical Parametric Generator
OR	Optical Rectification
PTD	Propagation Time Difference
RIC	Refractive Index Change
SDG	Semiconductor Doped Glass
SFG	Sum Frequency Generation
SHG	Second Harmonic Generation
SVEA	Slowly Varying Envelope Approximation
SNR	Signal to Noise Ratio
SOS	Sum Over States
TAS	Transient Absorption Spectroscopy

THG	Third Harmonic Generation

CHAPTER 1: INTRODUCTION

Nonlinear optical phenomena have their origins in the response of materials to high intensity electromagnetic waves. In first order or linear optics, we can approximate that the response of the material is proportional to the electromagnetic field strength. From this we can derive a number of different optical phenomena, such as linear absorption and refraction [1]. These phenomena have been extensively studied and are well understood and implemented in numerous technologies from lenses to fiber optics.

By considering higher order terms in the response of materials to the electromagnetic field, we can derive a number of different nonlinear optical phenomena such as Sum Frequency Generation (SHG), Difference Frequency Generation (DFG), Optical Rectification (OR), Nonlinear Absorption (NLA) and Nonlinear Refraction (NLR) [2]. These phenomena are utilized in many technologies, such as frequency conversion [3, 4], optical limiting [5] and optical switching [6]. However, the nonlinear response of many materials of interest is not completely understood, making this an exciting research area. In this work we will be primarily concerned with two electronic nonlinear effects, NLR and NLA

Two-Photon Absorption (2PA) is the near simultaneous absorption of two photons in order to promote an electron from one state to a higher state. This requires that the photons arrive at the same location within the time period as determined by the uncertainty principle [7]. As this time is ultrashort (sub-femtosecond), this requires that the local photon flux be very high, i.e. a high irradiance. Contrast this to the commonly observed phenomena of One Photon Absorption (1PA),

in which a single photon promotes an electron from one state to a higher state and occurs at all irradiances.

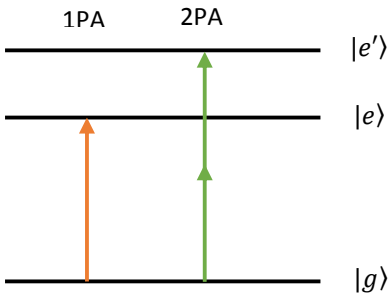

Figure 1: Energy level diagram of 1PA and 2PA. $|g\rangle$ is the ground state, $|e\rangle$ is the first excited state and $|e'\rangle$ is the second excited state.

For 1PA the rate of attenuation is proportional to the irradiance. For 2PA the rate of attenuation is proportional to the square of the irradiance. Typically, these effects occur simultaneously, so that

$$\frac{\partial I}{\partial z} = -\alpha I - \alpha_2 I^2, \tag{1.1}$$

where I is the irradiance, α is the linear absorption coefficient and α_2 is the 2PA coefficient. Note that higher order effects are being neglected in this expression. The first term in Eq. (1.1) corresponds to 1PA and the second term corresponds to 2PA. 2PA was first identified as a possibility by Maria Goppert-Mayer in 1931 [8]. However, because 2PA requires such high irradiances, observing and measuring it was not possible until the invention of high power coherent light sources i.e. the laser in 1960 [9].

The quadratic irradiance dependence on the 2PA has proven useful for numerous applications such as optical limiting [10] and optical switching in ring resonators [11]. Also, in the

case of direct gap semiconductors because 2PA requires two photons to promote one electron from the ground state to the excited state, each individual photon is itself below the band gap energy of the material allowing it to penetrate deep into materials. This particular property of 2PA has thus been utilized for two-photon microscopy [12] and two-photon polymerization manufacturing [13].

NLR is an intensity dependent change in the index of refraction

$$n(I) = n_0 + n_2 I, \tag{1.2}$$

where n_0 is the linear index of refraction and n_2 is the nonlinear index of refraction. NLR has found applications that require altering the polarization of an electromagnetic wave such as mode locking of high power pulsed lasers [14], altering the divergence of a beam like optical limiting [10] or high speed beam steering as in optical switching [6].

Nonlinear optical phenomena derive from many sources, such as electronic nonlinearity [2], thermal nonlinearity [15], vibrational-electronic coupling (Raman) [16], electrostriction [15], molecular reorientation [15] and intermolecular interaction [17]. In this work we will particularly interested in the electronic, reorientational and nuclear effects.

One application of particular interest to us is All Optical Signal Processing (AOSP). Currently, while much information transmission occurs using optical technologies such as optical fibers, information switching and processing remain the realm of electronic technologies. An AOSP technology would be much faster, as it would be based on the optical Kerr effect which is an ultrafast process occurring at the sub-femtosecond level [18].

Much effort has been spent in developing these AOSP technologies, which are currently in the nascent stage. To this end organic dyes have been identified as a promising class of candidate

materials [19]. In this work we will study the optical nonlinear properties one of more promising of these materials in order to evaluate its potential for AOSP technologies.

Typically, techniques for measuring NLA and NLR involve using a high intensity laser beam to induce nonlinear effects within the material. This change in the material properties induced by the beam is then measured. In some techniques, such as the optical Kerr [20], excite-probe [21] and four wave mixing techniques [22], a second beam called the probe is used to measure the effects induced by the excitation beam. Other techniques such as the Z-Scan require only a single beam so that the excitation and probe beams are the same beam [23].

Of the two effects, NLA is usually the easier of the two to measure. Since NLA reduces the transmission of the material, it can easily be determined by measuring the received energy of the probe beam using a photodiode. NLR is typically more difficult to measure, as photodiodes are not sensitive to the phase of the probe beam. In this case, some mechanism must be used to transform the induced phase change into a change in pulse energy, which can be measured by the photodiode.

While using established techniques it is possible to measure most aspects of interest for nonlinear effects, there still remains room for improvement. Each of the established techniques has drawbacks, such as limited sensitivity or stringent alignment requirement. In this work we will be concerned with improving on current techniques and developing new techniques for measuring NLA and NLR that combine high sensitivity and ease of implementation. We will apply these new techniques to the study of materials optimized for AOSP applications.

1.1. Origins of Optical Response

The optical response of materials to electromagnetic fields is due to many different factors. Starting at the smallest scale, and moving outward, we can summarize the primary factors that contribute to the nonlinear response.

At the individual atomic scale, the bound electronic response is the response of the electrons to the electromagnetic field [2]. As we will describe in Section 1.1.1, the electronic response to a non-parabolic potential can lead to a host of nonlinear effects.

At the scale of molecules, the Raman response is the optical response due to vibrational-electronic coupling [24]. Molecular reorientation is the optical response due to the reorientation of the molecule relative to the polarization axis of the electromagnetic field [15]. Finally, inter-molecular interaction is the response due to molecular collisions [17]. This includes molecular libration, which is the response due to the hindered rotation of the molecules when in liquid form, where they rock back and forth constrained by interactions with the nearest neighbor molecules [17], as well as Dipole-Induced Dipole (DID) interactions in which the dipole of one molecule may affect the dipole of a neighboring one [25].

At the macroscopic scale of many molecules, electrostriction is due to a change in the density of the material due to the acoustic wave traveling through it [15]. This acoustic wave is often generated by the absorption of a high repetition rate pulsed laser source. Thermal nonlinearities are due to changes in the density of the material due to localized heating [15] caused by the absorption of laser pulses.

Typically, several of these factors will be operating at the same time, often at different time scales. In this work we will be primarily interested in the femtosecond and picosecond time scales, so we will focus on the electronic, nuclear and reorientational responses.

1.1.1. Electronic Response

The optical properties of materials originate in the response of the electrons to an oscillatory electric field such as

$$E = E_0 \frac{1}{2}\left(e^{-i(k\,z-\omega t)} + e^{+i(k\,z-\omega\,t)}\right), \tag{1.3}$$

where E_0 is the electric field strength, $k = 2\,\pi/\lambda$ is the wavenumber, z is the propagation distance, $\omega = 2\pi\nu$ is the angular frequency, ν is the frequency and t is the time. The time varying electric field exerts a force on the electron cloud and the nucleus, inducing an oscillatory motion of the two.

Because the nucleus is much more massive than the electrons, the motion induced in the nucleus is much smaller than that of the electron cloud such that we can ignore the motion of the nucleus and approximate that only the electron cloud is being distorted. The distortion of the electron cloud induces a dipole moment in the atom.

The dipole moment can be expanded as a power series

$$\mu_i = \mu_i^0 + \epsilon_0\left(\alpha_{ij}E_j + \beta_{ijk}E_jE_k + \gamma_{ijkl}E_jE_jE_l + \cdots\right), \tag{1.4}$$

where μ_i^0 is the permanent dipole moment, a_{ij} represents the first order polarizability, and β_{ijk} and γ_{ijkl} are the second and third order polarizability. This can be rewritten in terms of the macroscopic polarization

$$P_i = P_0^i + \epsilon_0\left(\chi_i^{(1)}E_j + \chi_{ij}^{(2)}E_jE_k + \chi_{ijk}^{(3)}E_jE_kE_l + \cdots\right). \quad (1.5)$$

The first term P_0^i is the permanent polarization moment; the second term $\epsilon_0\chi_i^{(1)}E_j$ is the linear polarization response to the driving field and accounts for the linear properties of the material such as the index of refraction and some absorption phenomena. The higher order terms account for the nonlinear properties of the material, such as the NLR and multiple photon absorption. We will consider each term and their corresponding phenomena.

1.1.1.1. First Order Linear Response

To determine the first order polarization response, we approximate that the restoring force on the electron is proportional to the distance the electron has been displaced by the time varying electric field. This is akin to taking only the second terms in the expansion of Eq. (1.5)

$$\mu = \alpha\, E, \quad (1.6)$$

where α is the polarizability of the material. We can write the bulk polarization P for a given atomic density N as

$$P = N\,\mu = N\,\alpha\,E = \epsilon_0\,\chi^{(1)}E, \quad (1.7)$$

where ϵ_0 is the permittivity of free space and $\chi^{(1)}$ is the first order susceptibility. Now using this polarization in Maxwell's equations we can derive the wave equation as a solution to Maxwell's equations

$$\nabla^2 E = \mu_0\,\epsilon_0\left(1+\chi^{(1)}\right)\frac{\partial^2 E}{\partial t^2} = \mu_0\,\epsilon_0\,\epsilon_r\frac{\partial^2 E}{\partial t^2} = \frac{\eta^2}{c^2}\frac{\partial^2 E}{\partial t^2}, \tag{1.8}$$

where ϵ_r is the relative dielectric constant, and $\eta = n + i\,\kappa$ is the complex index of refraction. The real part of η corresponds to the linear index of refraction $n = c/v$ which is the ratio of the propagation speed v relative to the speed of light c

$$n = \sqrt{\frac{1}{2}\left(|\epsilon_r| + Re(\epsilon_r)\right)}. \tag{1.9}$$

The imaginary part of η corresponds to the absorption coefficient α which determines the rate of attenuation of the electromagnetic wave in a material which obeys Beers law $T = e^{-\alpha\,z}$

$$\alpha = \frac{4\,\pi\,\kappa}{\lambda_0} = \frac{4\,\pi}{\lambda_0}\sqrt{\frac{1}{2}\left(|\epsilon_r| - Re(\epsilon_r)\right)}. \tag{1.10}$$

These two parameters n and α allow us to characterize many of the common phenomena that we observe in our everyday world, such as the absorption of materials and reflection from surfaces. However, there are a great many phenomena that cannot be adequately explained with first order theory, especially when dealing with the high irradiances used in laser beams.

1.1.1.2. Second Order Nonlinear Response

For the second order nonlinear response, the polarization response is

$$P^{(2)}(\omega) = \epsilon_0 \int_{-\infty}^{\infty} \int_{-\infty}^{\infty} \chi^{(2)}(\omega, \omega_a, \omega_b,)\, E(\omega_a)\, E(\omega_b)\, \delta(\omega - \omega_a - \omega_b)\, d\omega_a\, d\omega_b. \quad (1.11)$$

For two different electromagnetic waves at two different frequencies (two eigenmode inputs) $E(\omega_a)$ and $E(\omega_b)$ this yields 16 terms that can be grouped together in classes of similar effects. There is the polarization responses $P^{(2)}(2\omega_a)$ and $P^{(2)}(2\omega_b)$, which are referred to as Second Harmonic Generation (SHG), there is the $P^{(2)}(0)$ static response which is known as Optical Rectification (OR), the Sum Frequency Generation (SFG) responses at $P^{(2)}(\omega_a + \omega_b)$, and the Difference Frequency response at $P^{(2)}(\omega_a - \omega_b)$. SHG and OR can occur when there are one or two beams, while SFG and DFG require two beams of differing frequencies.

SHG can be observed in various nonlinear crystals such as Potassium Titanyl Phosphate (KTP) which is frequently used in laser systems to double the output frequency of a Nd:YAG laser. SFG and DFG are the basis for Optical Parametric Amplifiers (OPA) and Optical Parametric Generators (OPG) [3], which are laboratory instruments used to convert the output of a laser from one wavelength to another.

The following table summarizes the second order nonlinear processes as summarized by Fu [26].

Table 1: Summary of second order NLO processes.

Second Order Process	In	Out	Term
Second Harmonic Generation (SHG)	Single beam at ω	Single beam at 2ω	$\chi^{(2)}(2\omega; \omega, \omega)$

Sum Frequency Generation (SFG)	Two beams at ω_1, ω_2	Single beam at $\omega_3 = \omega_1 + \omega_2$	$\chi^{(2)}(\omega_3; \omega_1, \omega_2)$
Difference Frequency Generation (DFG)	Two beams at ω_1, ω_2	Single beam at $\omega_3 = \omega_1 - \omega_2$	$\chi^{(2)}(\omega_3; \omega_1, -\omega_2)$
Optical Rectification (OR)	Single beam at ω	Static electric field	$\chi^{(2)}(0; \omega, \omega)$

1.1.1.3. Third Order Nonlinear Response

The third order nonlinear response originates from the third order term in the polarization. The third order polarization response is

$$P^{(3)}(\omega) = \epsilon_0 \int_{-\infty}^{\infty} \int_{-\infty}^{\infty} \chi^{(3)}(\omega, \omega_a, \omega_b, \omega_c)\, E(\omega_a) E(\omega_b) E(\omega_c) \times \delta(\omega - \omega_a - \omega_b - \omega_c)\, d\omega_a\, d\omega_b d\omega_c. \tag{1.12}$$

For three electromagnetic waves at three different frequencies (three eigenmode inputs), $E(\omega_a)$, $E(\omega_c)$ and $E(\omega_c)$ this yields 64 terms. As before, these terms can be grouped together into classes of similar effects. Again following Fu [26], Table 2 summarizes the terms and their associated nonlinear optical effects.

Table 2: Summary of third order NLO processes.

Third Order Process	In	Out	Term
Third Harmonic Generation (THG)	Single beam at ω	Single beam at 3ω	$\chi^{(3)}(3\omega; \omega, \omega, \omega)$
Self-Phase Modulation (SPM) or	Single beam at ω	Single beam at ω, phase shifted	$\chi^{(3)}(\omega; \omega, -\omega, \omega)$

Third Order Process	In	Out	Term
Degenerate Nonlinear Refraction (D-NLR)			
Degenerate Two-Photon Absorption (D-2PA)	Single beam at ω	Single beam at ω, attenuated	$\chi^{(3)}(\omega;\omega,-\omega,\omega)$
Degenerate Four-wave Mixing (D-FWM)	Three beams at ω	New beam at ω	$\chi^{(3)}(\omega;\omega,-\omega,\omega)$
Cross Phase Modulation (CPM) or Nondegenerate Nonlinear Refraction (ND-NLR)	Two beams at ω_1, ω_2	Two beams at ω_1, ω_2, phase shifted	$\chi^{(3)}(\omega_1;\omega_1,-\omega_2,\omega_2)$
Nondegenerate Two-Photon Absorption (ND-2PA)	Two beams at ω_1, ω_2	Two beams at ω_1, ω_2, attenuated	$\chi^{(3)}(\omega_1;\omega_1,-\omega_2,\omega_2)$
General Four-wave Mixing (ND-FWM)	Three beams at ω_1, ω_2, ω_3	New beam at ω_4	$\chi^{(3)}(\omega_4;\omega_1,\omega_2,\omega_3)$

THG, NLR, D-2PA and D-FWM are degenerate processes that can occur with a single beam, while the other processes require an additional beam. For this work, the primary effects of interest are D-NLR and D-2PA which are related to the $\chi^{(3)}(\omega;\omega,-\omega,\omega)$ term, as well as ND-NLR and ND-2PA which are related to the $\chi^{(3)}(\omega_1;\omega_1,-\omega_2,\omega_2)$ term.

1.1.1.4. Slowly Varying Amplitude Equations for NLA and NLR

For the case of nondegenerate beams we have for the electric fields

$$E(z,t) = E_a(z,t) + E_b(z,t), \tag{1.13}$$

$$E_a(z,t) = \frac{1}{2}\mathcal{E}_a(z)exp\big(i\,(k_a z + \omega_a t)\big) + c.c., \tag{1.14}$$

$$E_b(z,t) = \frac{1}{2}\mathcal{E}_b(z)exp\big(i\,(k_b z + \omega_b t)\big) + c.c.. \tag{1.15}$$

The wave equation for the propagation is

$$\nabla^2 E(z,t) - \frac{1}{c^2}\frac{\partial^2 E(z,t)}{\partial t^2} = \mu_0 \frac{\partial^2 P^{(3)}(z,t)}{\partial t^2}. \tag{1.16}$$

Substituting the electric field into the wave equation gives

$$\begin{aligned} &\frac{1}{2}\Bigg(\Bigg(\frac{\partial^2 \mathcal{E}_a(z)}{\partial z^2} + 2ik_a\frac{\partial \mathcal{E}_a(z)}{\partial z} \\ &+ \Big(\frac{n_a}{c}\Big)^2\left(\frac{\partial^2 \mathcal{E}_a(z)}{\partial t^2} - 2i\omega_a\frac{\partial \mathcal{E}_a(z)}{\partial t}\right)\Bigg)e^{-i(\omega_a t - k_a x)} + \Bigg(\frac{\partial^2 \mathcal{E}_b(z)}{\partial z^2} \\ &+ 2ik_b\frac{\partial \mathcal{E}_b(z)}{\partial z} + \Big(\frac{n_b}{c}\Big)^2\left(\frac{\partial^2 \mathcal{E}_b(z)}{\partial t^2} - 2i\omega_b\frac{\partial \mathcal{E}_b(z)}{\partial t}\right)e^{-i(\omega_a t - k_a x)}\Bigg) + c.c\Bigg) \\ &= \mu_0\frac{\partial^2 P(z)}{\partial t^2}. \end{aligned} \tag{1.17}$$

Generally, there will be a polarization response at a number of different frequencies as described in Table 2. In our particular case we are interested in the NLA and NLR, which occur at frequencies ω_a and ω_b, so that the polarization response can be written as

$$P^{(3)}(z,t) = \frac{1}{2}\big(\mathcal{P}_j(\omega_a)e^{i(k_a z - \omega_a t)} + \mathcal{P}_j(\omega_b)e^{i(k_b z - \omega_b t)}\big), \tag{1.18}$$

$$\mathcal{P}_j(\omega_a) = \frac{3}{4}\chi^{(3)}(\omega_a;\omega_a)|E_a(z,t)|^2 E_a(z,t)e^{ik_a z} + \tag{1.19}$$

$$\frac{6}{4}\chi^{(3)}(\omega_a;\omega_b)|E_b(z,t)|^2E_a(z,t)e^{ik_az},$$

$$\mathcal{P}_j(\omega_b)=\frac{3}{4}\chi^{(3)}(\omega_b;\omega_b)|E_b(z,t)|^2E_b(z,t)e^{ik_bz}+ \tag{1.20}$$

$$\frac{6}{4}\chi^{(3)}(\omega_b;\omega_a)|E_a(z,t)|^2E_b(z,t)e^{ik_bz},$$

where $\chi^{(3)}(\omega_i;\omega_i)$ is the shorthand notation for $\chi^{(3)}(\omega_i;\omega_i,-\omega_i,\omega_i)$ and $\chi^{(3)}\left(\omega_i;\omega_j\right)$ is the shorthand notation for $\chi^{(3)}\left(\omega_i;\omega_i,-\omega_j,\omega_j\right)$, where the index i can be either a or b, referring to either the degenerate or nondegenerate susceptibility. The first terms of Equations (1.19) and (1.20) containing $\chi^{(3)}(\omega_i;\omega_i)$ represent the self-induced nonlinearity, while those containing $\chi^{(3)}\left(\omega_i;\omega_j\right)$ represent the nonlinearity induced in one beam by the presence of the other.

Initially, consider the polarization response at ω_a. In this case we can rewrite Eq. (1.17) as

$$\left(\frac{\partial^2\mathcal{E}_a(z)}{\partial z^2}+2ik_a\frac{\partial\mathcal{E}_a(z)}{\partial z}\right)=-\omega_a^2\mu_0\mathcal{P}_j(\omega_a)e^{i\Delta kz}, \tag{1.21}$$

where $\Delta k = 0$ in this case as the phase matching is automatic. Because the envelope of the field varies relatively slowly, we can apply the approximation

$$\frac{\partial^2\mathcal{E}_a(z)}{\partial t^2}\ll 2k\frac{\partial\mathcal{E}_a(z)}{\partial z}. \tag{1.22}$$

This is known as the Slowly Varying Envelope Approximation (SVEA). Using Eq. (1.22) we can write Eq. (1.21) as

$$\frac{\partial\mathcal{E}_a(z)}{\partial z}=i\frac{\omega_a}{8nc}\left(\chi^{(3)}(\omega_a;\omega_a)|\mathcal{E}_a(z)|^2\mathcal{E}_a+2\chi^{(3)}(\omega_a;\omega_b)|\mathcal{E}_b(z)|^2\mathcal{E}_a(z)\right). \tag{1.23}$$

We now rewrite the complex electric field envelope in terms of magnitude and phase,

$$\mathcal{E}_a(z) = A_a(z)e^{i\phi_a(z)}. \tag{1.24}$$

Separating Eq. (1.23) into real and imaginary parts and substituting Eq. (1.24) to rewrite it in terms of amplitude and phase yields the following equations

$$\frac{dA_a(z)}{dz} = -\frac{\omega_a}{8nc} Im\left(\chi^{(3)}(\omega_a;\omega_a) + 2\chi^{(3)}(\omega_a;\omega_b)\right) A_a(z)^3, \tag{1.25}$$

$$\frac{d\phi_a(z)}{dz} = \frac{\omega}{8nc} Re\left(\chi^{(3)}(\omega_a;\omega_a) + 2\chi^{(3)}(\omega_a;\omega_b)\right) A_a(z)^2. \tag{1.26}$$

Converting to irradiance using $I(z) = (1/2)\, nc\epsilon_0 A(z)^2$ we rewrite Eq. (1.25) as

$$\begin{aligned}\frac{\partial I_a(z)}{\partial z} &= -\frac{\omega_a}{n^2c^2\epsilon_0} Im\left(\chi^{(3)}(\omega_a;\omega_a) + 2\chi^{(3)}(\omega_a;\omega_b)\right) I_a(z)^2 \\ &= \alpha_2(\omega_a;\omega_a)I(z)^2 + 2\alpha_2(\omega_a;\omega_b)I_a(z)I_b(z).\end{aligned} \tag{1.27}$$

This allows us to define α_2, the 2PA coefficient

$$\alpha_2(\omega_a;\omega_i) = \frac{\omega_a}{2n^2c^2\epsilon_0} Im\left(\chi^{(3)}(\omega_a;\omega_i)\right), \tag{1.28}$$

where the index i can take be either a or b, referring to either the D-2PA or ND-2PA absorption coefficient. Performing a similar procedure for the phase, Eq. (1.26) can be written as

$$\begin{aligned}\frac{\partial \phi_a(z)}{\partial z} &= \frac{\omega_a}{2n^2c^2\epsilon_0}\left(Re\left(\chi^{(3)}(\omega_a;\omega_a)\right) I_a(z) + Re\left(2\chi^{(3)}(\omega_a;\omega_b)\right)\right) I_b(z) \\ &= k_a n_2(\omega_a;\omega_a)I_a(z) + k_a n_2(\omega_a;\omega_b)I_b(z).\end{aligned} \tag{1.29}$$

This allows us to define n_2, the nonlinear index of refraction

$$n_2(\omega_a;\omega_i) = \frac{1}{2n^2c\epsilon_0} Re\left(\chi^{(3)}(\omega_a;\omega_i)\right). \tag{1.30}$$

The same procedure can be performed when considering the polarization response at ω_b, in which case the indices a and b swap throughout the derivation.

1.1.1.5. Electronic Susceptibility Tensor

For third order nonlinearity, the polarization $\mathcal{P}_j(\omega_b)$ depends on the input of three fields, hence $\chi^{(3)}_{ijkl}(\omega_4;\omega_1,\omega_2,\omega_3)$ is a fourth rank tensor. This tensor has 261 independent elements, however, a number of symmetries can be exploited to reduce the amount. First, since the order of the fields does not matter, any of the indices pertaining to the individual fields can be swapped so that $\chi^{(3)}_{\alpha_4\alpha_1\alpha_2\alpha_3}(\omega_4;\omega_1,\omega_2,\omega_3)$ is invariant with permutation of the pairs (α_n,ω_n) for n = 1-3. This is known as intrinsic permutation symmetry and reduces the number of independent elements to 81.

In addition to intrinsic permutation symmetry, we can interchange all pairs of arguments (α_n,ω_n) of $\chi^{(3)}_{\alpha_4\alpha_1\alpha_2\alpha_3}(\omega_4;\omega_1,\omega_2,\omega_3)$ so long as the first argument is the sum of the following arguments (i.e. $\chi^{(3)}_{\alpha_4\alpha_1\alpha_2\alpha_3}(\omega_4=\omega_1+\omega_2+\omega_3;\omega_1,\omega_2,\omega_3)=\chi^{(3)}_{\alpha_1\alpha_2\alpha_3\alpha_4}(\omega_1=-\omega_2-\omega_3+\omega_4;-\omega_2,-\omega_3,\omega_4)$) and there is no absorption at any of the frequencies ω_n. This is referred to as full permutation symmetry and further reduces the number of independent elements to 27.

If we are far from resonance we can permute the indices and the frequencies of $\chi^{(3)}_{\alpha_4\alpha_1\alpha_2\alpha_3}(\omega_4;\omega_1,\omega_2,\omega_3)$ independent of each other (i.e. $\chi^{(3)}_{\alpha_4\alpha_1\alpha_2\alpha_3}(\omega_4;\omega_1,\omega_2,\omega_3)=\chi^{(3)}_{\alpha_1\alpha_2\alpha_3\alpha_4}(\omega_4;\omega_1,\omega_2,\omega_3)$). This is referred to as Klienman symmetry and applies in regions

where the dispersion of χ can be neglected, further reducing the number of independent elements to 18.

In the case of certain crystal geometries, the number of elements can be further reduced due to the symmetry properties of the crystals. There are very few crystal geometries that have sufficient symmetries for a unique determination of all tensor elements. One such geometry is for isotropic materials, for which the relations between the tensor elements are

$$\begin{gathered}\chi^{(3)}_{yyzz} = \chi^{(3)}_{zzyy} = \chi^{(3)}_{zzxx} = \chi^{(3)}_{xxzz} = \chi^{(3)}_{xxyy} = \chi^{(3)}_{yyxx} \\ \chi^{(3)}_{yzyz} = \chi^{(3)}_{zyzy} = \chi^{(3)}_{zxzx} = \chi^{(3)}_{xzxz} = \chi^{(3)}_{xyxy} = \chi^{(3)}_{yxyx} \\ \chi^{(3)}_{yzzy} = \chi^{(3)}_{zyyz} = \chi^{(3)}_{zxxz} = \chi^{(3)}_{xzzx} = \chi^{(3)}_{xyyx} = \chi^{(3)}_{yxxy} \\ \chi^{(3)}_{xxxx} = \chi^{(3)}_{yyyy} = \chi^{(3)}_{zzzz}.\end{gathered} \tag{1.31}$$

Applying the condition that the total polarization must be invariant with rotation of the axes, we can establish that

$$\chi^{(3)}_{xxxx} = \chi^{(3)}_{xxyy} + \chi^{(3)}_{xyxy} + \chi^{(3)}_{xyyx}. \tag{1.32}$$

In the case of Kleinman symmetry $\chi^{(3)}_{xxyy} = \chi^{(3)}_{xyxy} = \chi^{(3)}_{xyyx}$ so the ratio $\chi^{(3)}_{xxxx}/\chi^{(3)}_{xxyy}$ = 3. Determining the dispersion of these tensor elements will be an important part of this work.

1.1.1.6. Classical Model of Electronic Response

In understanding the origins of these phenomena, it is instructive to examine various models for the nonlinear response. We will begin by examining a simple classical model that considers the nonlinear response of a mass on spring that follows Hooke's law, which corresponds to a quadratic potential [1]

$$F(x) = -k\,x, \tag{1.33}$$

$$U(x) = \frac{1}{2} m\,\omega^2 x^2, \tag{1.34}$$

where F is the force on the mass, x is the displacement from the equilibrium position, k is the spring constant, U is the potential energy and $\omega = \sqrt{k/m}$. The equation of motion for the electron under this potential is

$$m\,\ddot{x}(t) + m\,\Gamma\,\dot{x}(t) + m\,\omega_0^2 x(t) = -e\,E(t). \tag{1.35}$$

Assuming an oscillatory driving electric field $E(t) = E_0 e^{-i\omega t}$ and the relations in Eq. **(1.7)** we can solve for $\chi^{(1)}$

$$\chi^{(1)}(\omega) = \frac{N\,e^2}{\epsilon_0 m\,D(\omega)}, \tag{1.36}$$

$$D(\omega) = \omega_0^2 - \omega^2 - 2\,i\,\omega\,\gamma, \tag{1.37}$$

where ω_0 is the resonance frequency, $D(\omega)$ is the denominator term and γ is the damping. In the case of higher order optical nonlinearities, we include higher order terms into the potential.

For a second order nonlinearity, we have a third order non-centrosymmetric potential

$$U(x) = \frac{1}{2} m\,\omega^2 x^2 - \frac{1}{3} m\,a x^3, \tag{1.38}$$

where a is the second order nonlinear absorption coefficient. Performing a similar analysis and using the results from the linear case yields the following expression for $\chi^{(2)}$

$$\chi^{(2)}(\omega_1 + \omega_2; \omega_1, \omega_2) = \frac{N\,e^3 a}{\epsilon_0 m^2 D(\omega_1 + \omega_2) D(\omega_1) D(\omega_2)}, \tag{1.39}$$

where now we have responses not only at ω_1 and ω_2, but for the sum of the frequencies $\omega_1 + \omega_2$.

In the case of a third order nonlinearity we have a fourth order centrosymmetric potential we have

$$U(x) = \frac{1}{2} m\,\omega^2\,x^2 - \frac{1}{4} m\,b\,x^4, \tag{1.40}$$

where b is the third order nonlinear coefficient. Performing a similar analysis as before yields the following expression for $\chi^{(3)}$

$$\chi^{(3)}(\omega_1 + \omega_2 + \omega_3; \omega_1, \omega_2, \omega_3) = \frac{N\, b\, e^4}{\epsilon_0\, m^3\, D(\omega_1 + \omega_2 + \omega_3)\, D(\omega_1)\, D(\omega_2)\, D(\omega_3)}. \quad (1.41)$$

This model works well for estimating the first order effects. However, in order to get a better estimate of higher order effects, we will need to employ a more advanced model based on quantum mechanics.

1.1.1.7. Three Level Sum Over States Model

In the case of substances in which transitions are from discrete energy levels, we model the third order susceptibility using the three level Sum Over States (SOS) model proposed by Orr [27] and Ward [28]. While this model works well for organics, it should not be applied to semiconductors or other solid state materials in which we are dealing with absorption bands. For these substances other approaches are used, such as the two parabolic band model implemented by Sheik-Bahae et al [29]. By applying first order quantum mechanical perturbation theory two times $\chi^{(3)}_{ijkl}$ can be determined as

$$\chi^{(3)}_{ijkl}(\omega_p + \omega_q + \omega_r; \omega_p, \omega_q, \omega_r) = \quad (1.42)$$

$$\frac{N f^{(3)}}{\epsilon_0 \hbar^3}\left(\sum_{v,n,m}\left(\frac{\mu_{gv}^{i}(\mu_{vn}^{l}-\mu_{gg}^{l})(\mu_{nm}^{k}-\mu_{gg}^{k})\mu_{mg}^{l}}{(\bar{\omega}_{vg}-\omega_p-\omega_q-\omega_r)(\bar{\omega}_{ng}-\omega_q-\omega_p)(\bar{\omega}_{mg}-\omega_p)}\right.\right.$$

$$+\frac{\mu_{gv}^{j}(\mu_{vn}^{k}-\mu_{gg}^{k})(\mu_{nm}^{i}-\mu_{gg}^{i})\mu_{mg}^{l}}{(\bar{\omega}_{vg}^{*}+\omega_p)(\bar{\omega}_{ng}^{*}+\omega_q+\omega_p)(\bar{\omega}_{mg}-\omega_r)}$$

$$+\frac{\mu_{gv}^{l}(\mu_{vn}^{i}-\mu_{gg}^{i})(\mu_{nm}^{k}-\mu_{gg}^{k})\mu_{mg}^{j}}{(\bar{\omega}_{vg}^{*}+\omega_r)(\bar{\omega}_{ng}-\omega_q-\omega_p)(\bar{\omega}_{mg}-\omega_p)}$$

$$\left.+\frac{\mu_{gv}^{j}(\mu_{vk}^{k}-\mu_{gg}^{k})(\mu_{nm}^{l}-\mu_{gg}^{l})\mu_{mg}^{i}}{(\bar{\omega}_{vg}^{*}+\omega_p)(\bar{\omega}_{ng}^{*}+\omega_q+\omega_p)(\bar{\omega}_{mg}^{*}+\omega_p+\omega_q+\omega_r)}\right)$$

$$+\sum_{v,n}\left(\frac{\mu_{gn}^{i}\mu_{ng}^{l}\mu_{gm}^{k}\mu_{mg}^{j}}{(\bar{\omega}_{ng}-\omega_p-\omega_q-\omega_r)(\bar{\omega}_{ng}-\omega_r)(\bar{\omega}_{mg}-\omega_p)}\right.$$

$$+\frac{\mu_{gn}^{i}\mu_{ng}^{l}\mu_{gm}^{k}\mu_{mg}^{j}}{(\bar{\omega}_{mg}^{*}+\omega_q)(\bar{\omega}_{ng}-\omega_r)(\bar{\omega}_{mg}-\omega_p)}$$

$$+\frac{\mu_{gn}^{l}\mu_{ng}^{i}\mu_{gm}^{j}\mu_{mg}^{k}}{(\bar{\omega}_{ng}^{*}+\omega_r)(\bar{\omega}_{mg}^{*}+\omega_p)(\bar{\omega}_{mg}-\omega_q)}$$

$$\left.\left.+\frac{\mu_{gn}^{l}\mu_{ng}^{i}\mu_{gm}^{j}\mu_{mk}^{k}}{(\bar{\omega}_{ng}^{*}+\omega_r)(\bar{\omega}_{mg}^{*}+\omega_p)(\bar{\omega}_{ng}^{*}+\omega_p+\omega_q+\omega_r)}\right)\right).$$

Where *v*, *n*, and *m* are the states over which the summation is performed, μ_{vn}^{i} is the transition dipole moment from state *v* to state *n* along direction *i*, $\bar{\mu}^{x}{}_{vm} = \mu_{vm}^{x} - \delta_{vm}\,\mu_{gg}^{x}$, where μ_{gg}^{i} is the ground state permanent dipole, and $\bar{\omega}_{vm} = \omega_{vm} - i\,\Gamma_{vm}$ where ω_{vm} is the angular frequency between state *v* and *m*, Γ_{vm} is the damping factor between *v* and *m* and $f^{(3)}$ is the local field correction

$$f^{(3)}= \qquad (1.43)$$

$$\left(\frac{\epsilon_r^i(\omega_p+\omega_q+\omega_r)+2}{3}\right)\left(\frac{\epsilon_r^j(\omega_p)+2}{3}\right)\left(\frac{\epsilon_r^k(\omega_q)+2}{3}\right)\left(\frac{\epsilon_r^l(\omega_r)+2}{3}\right),$$

where $\epsilon_r^i(\omega) = n^i(\omega)^2$ is the relative permittivity of free space along the direction of beam i.

In the case where the dipole moments are not aligned with each other the effective dipole moment

$$\mu_{ee'}^{eff} = \mu_{ee'}\sqrt{\frac{2\,cos(\theta)^2-1}{3}} \tag{1.44}$$

should be used where θ is the angle between μ_{ge} and $\mu_{ee'}$ [30].

For the co-polarized nondegenerate case, there are six perturbations that add to the total susceptibility

$$\begin{aligned}\hat{\chi}_{xxxx}^{(3)}(\omega_p;\omega_e) = \chi_{xxxx}^{(3)}(\omega_p;\omega_p,\omega_e,-\omega_e) + \chi_{xxxx}^{(3)}(\omega_p;\omega_p,-\omega_e,\omega_e) + \\ \chi_{xxxx}^{(3)}(\omega_p;-\omega_e,\omega_p,\omega_e) + \chi_{xxxx}^{(3)}(\omega_p;\omega_e,\omega_p,-\omega_e) + \\ \chi_{xxxx}^{(3)}(\omega_p;\omega_e,-\omega_e,\omega_p) + \chi_{xxxx}^{(3)}(\omega_p;-\omega_e,\omega_e,\omega_p).\end{aligned} \tag{1.45}$$

For the case of a symmetric molecule, quantum mechanical selection rules require that the permanent dipole moment is zero, 1PA transitions must change parity, while 2PA transitions must conserve parity. Thus, for a three level system with ground state g, first excited state e, and second excited state e', $\mu_{gg}^i = \mu_{ee}^i = \mu_{e'e'}^i = \mu_{ge'}^i = 0$. Performing the summations and dropping the nonresonant terms we can simplify to

$$\chi_{xxxx}^{(3)}(\omega_p;\omega_e) = \tag{1.46}$$

$$
-\frac{f^{(3)}N{\mu_{ge}^{x}}^{4}}{\hbar^{3}\epsilon_{0}}\left(\frac{2}{\left(-\omega_{e}+\bar{\omega}_{eg}\right)\left(-\omega_{p}+\bar{\omega}_{eg}\right)^{2}}\right.
$$

$$
\left.+\frac{2}{\left(-\omega_{e}+\bar{\omega}_{eg}\right)\left(-\omega_{p}+\bar{\omega}_{eg}\right)\left(-\omega_{e}+\bar{\omega}_{eg}^{*}\right)}\right)
$$

$$
+\frac{f^{(3)}N{\mu_{ee'}^{x}}^{2}{\mu_{ge}^{x}}^{2}}{\hbar^{3}\epsilon_{0}}\left(\frac{1}{\left(-\omega_{p}+\bar{\omega}_{eg}\right)^{2}\left(-\omega_{e}-\omega_{p}+\bar{\omega}_{ge'}\right)}\right.
$$

$$
+\frac{1}{\left(-\omega_{e}+\bar{\omega}_{eg}\right)\left(-\omega_{p}+\bar{\omega}_{eg}\right)\left(-\omega_{e}-\omega_{p}+\bar{\omega}_{ge'}\right)}
$$

$$
+\frac{1}{\left(-\omega_{e}+\bar{\omega}_{ge}\right)\left(-\omega_{e}-\omega_{p}+\bar{\omega}_{ge'}\right)\left(-\omega_{e}+\bar{\omega}_{ge}^{*}\right)}
$$

$$
\left.+\frac{1}{\left(-\omega_{p}+\bar{\omega}_{ge}\right)\left(-\omega_{e}-\omega_{p}+\bar{\omega}_{ge'}\right)\left(-\omega_{e}+\bar{\omega}_{ge}^{*}\right)}\right).
$$

In this expression we can identify two types of terms: two-photon terms shown in green (T-terms), and negative terms shown in blue (N-terms). T-terms correspond to 2PA from the ground state g to state e' and the N-terms correspond to the relaxation from state e and e' to state g and is due to the quadratic AC Stark effect [29], also known 'virtual saturation' since for near resonance this term would represent saturation.

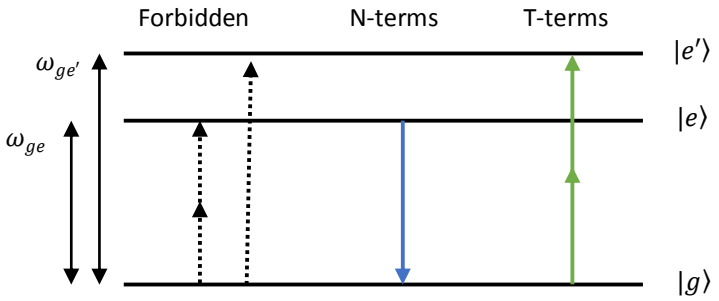

Figure 2: Energy level diagram for three level SOS model for symmetric molecules.

For simplicity of illustration, we consider the case of degenerate beams $\omega_p = \omega_e = \omega$. In this case the total susceptibility reduces to

$$\hat{\chi}^{(3)}_{xxxx}(\omega;\omega) = -\frac{Nf^{(3)}{\mu^x_{ge}}^4}{\hbar^3\epsilon_0}\left(\frac{1}{\left(\bar{\omega}_{eg}-\omega\right)^3}+\frac{1}{\left(\bar{\omega}_{eg}-\omega\right)^2\left(\bar{\omega}^*_{eg}-\omega\right)}\right) + \frac{Nf^{(3)}{\mu^x_{ee'}}^2{\mu^x_{ge}}^2}{\hbar^3\epsilon_0}\left(\frac{1}{\left(\bar{\omega}_{eg}-\omega\right)^2\left(\bar{\omega}_{e'g}-2\omega\right)} + \frac{1}{\left(\bar{\omega}_{eg}-\omega\right)\left(\bar{\omega}_{e'g}-2\omega\right)\left(\bar{\omega}^*_{eg}-\omega\right)}\right). \quad (1.47)$$

where the T and N-terms are colored as before. The value of $\hat{\chi}^{(3)}_{xxxx}(\omega;\omega)$ is the sum of the T and N terms. In Figure 3 we show the real and imaginary parts of the N, T and the sum of both terms as a function of frequency.

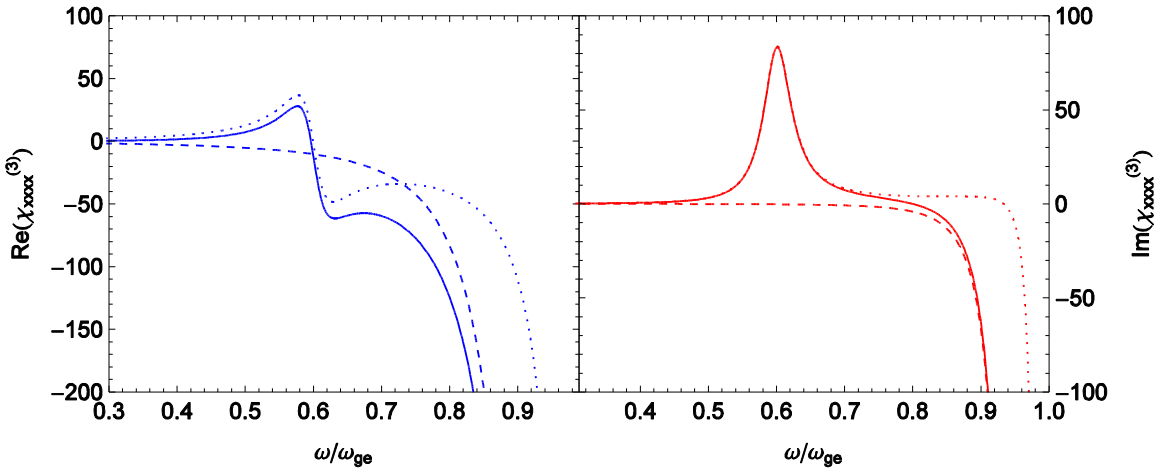

Figure 3: Real (left) and imaginary (right) parts of N terms (dashed) and D terms (dotted) and total (solid) vs. frequency with $\omega_{e'g} = 1.2\omega_{eg}$, $\Gamma_{eg} = \omega_{eg}/200$, $\Gamma_{e'g} = \Gamma_{eg}$ and $\mu^x_{ge} = \mu^x_{ee'}$ and ω_{eg} = 1.

There is a peak in the imaginary part of the T terms at approximately half of $\omega_{ge\prime}$ which is due to 2PA, with a corresponding change in the real part consistent with the Kramers-Kronig relations [31]. Further approaching the 1PA edge both the real and imaginary parts become increasingly negative. The N terms remain flat until we approach the absorption edge, at which point, like the T terms, they too become increasingly negative. There is some debate regarding the physical interpretation of $Im(\chi^{(3)})$, which can be regarded as a reduction of the 1PA near resonance [32, 33] (ground state bleaching effect) or whether it is only an artifact of the TL-SOS model.

The effect of the damping is to reduce the peak and broaden the 2PA features, while also reducing the modulation of the NLR features near the 1PA edge as seen in Figure 4.

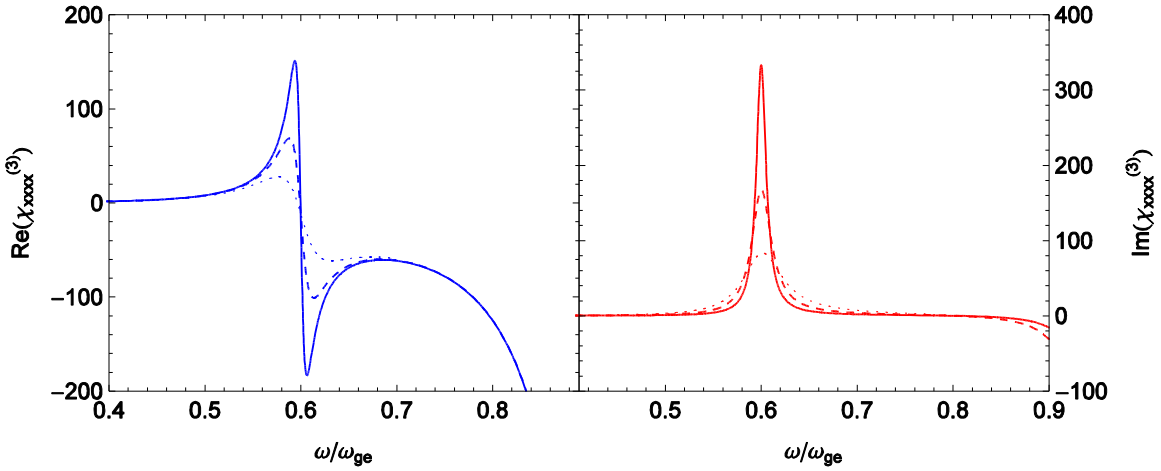

Figure 4: (left) Real and (right) imaginary parts of $\chi^{(3)}_{xxxx}$ for damping values Γ_{eg} = 1/200 (dotted), 1/400 (dashed) and 1/800 (solid), $\Gamma_{e\prime g} = 10\Gamma_{eg}$, $\omega_{e\prime g}$ = $1.2\omega_{eg}$, and $|\mu_{eg}|$ = $|\mu_{e\prime g}|$. Increasing the damping parameter Γ reduces the peak and broadens the features of $\chi^{(3)}_{xxxx}$.

The effect of adjusting the ratio of the first and second excited states $\omega_{e'g}/\omega_{eg}$ is to adjust both the magnitude and peak location of the 2PA and NLR features as seen in Figure 5. The magnitude of the peak is increased, while its location is pushed to longer wavelengths.

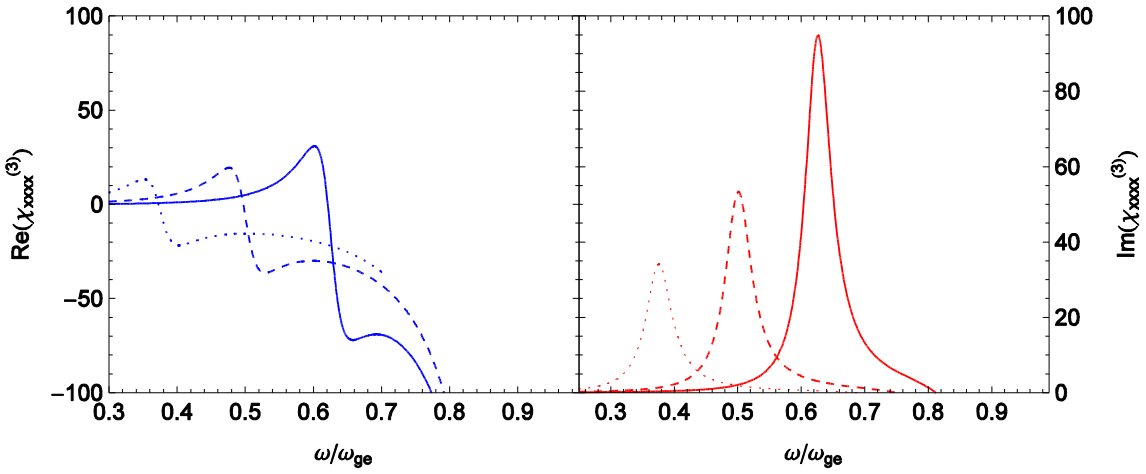

Figure 5: (left) Real and (right) imaginary parts of $\chi^{(3)}_{xxxx}$ for $\omega_{e'g}/\omega_{eg}$ = 0.75 (dotted), 1 (dashed) and 1.25 (solid), Γ_{eg} = 1/200ω_{eg}, $\Gamma_{e'g} = 10\Gamma_{eg}$, and $|\mu_{eg}| = |\mu_{e'g}|$. Increasing $\omega_{e'g}/\omega_{eg}$ increases the magnitude of the peak of $\chi^{(3)}_{xxxx}$ as well as shifting it to longer wavelengths.

In AOSP applications we typically desire large NLR with small NLA in order to reduce nonlinear optical losses. Hence we define the figure of merit $FOM = Re\left(\chi^{(3)}_{xxxx}(\omega;\omega)\right)/Im\left(\chi^{(3)}_{xxxx}(\omega;\omega)\right)$ [19]. The FOM becomes large at the point where $Im\left(\chi^{(3)}_{xxxx}(\omega;\omega)\right)$ approaches zero. The location and width of this feature can be altered by adjusting either the damping parameters Γ_{eg} and $\Gamma_{e'g}$ or the ratio of the second and first excited state energy levels $\omega_{e'g}/\omega_{eg}$. The width of the FOM peak can be increased by increasing the damping parameter Γ, while the

location of the peak can be biased toward higher frequencies by increasing the ratio of $\omega_{eg}/\omega_{e'g}$, as shown in Figure 6.

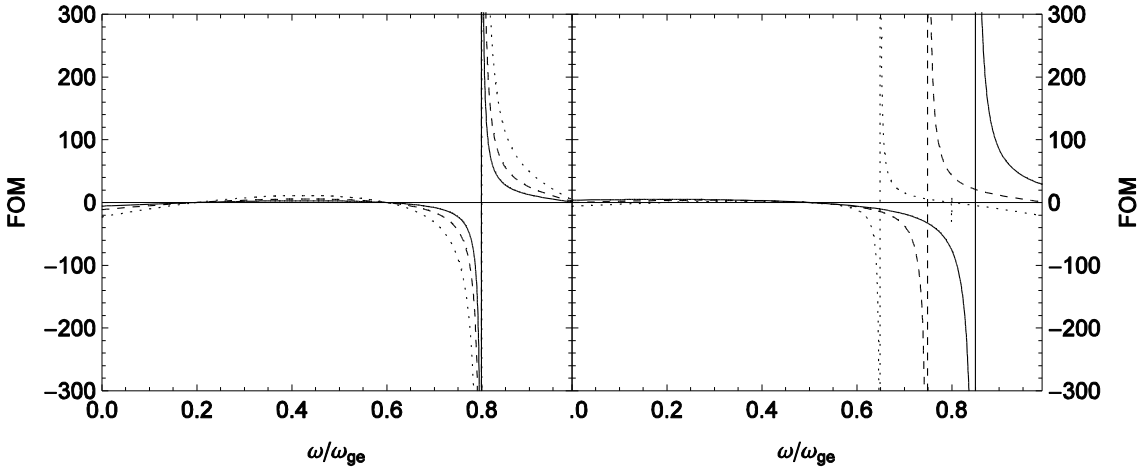

Figure 6: (left) FOM for damping values Γ_{eg} = 1/200 (solid), 1/400 (dashed) and 1/800 (dotted) and $\Gamma_{e'g} = 10\Gamma_{eg}$; (right) FOM for ratio of transition dipole moments $\omega_{eg}/\omega_{e'g}$ = 0.8 (dotted), 1.0 (dashed) and 1.2 (solid). All other parameters are the same as those used in Figure 3.

Much work in the development of AOSP technologies centers on the understanding of the structure-property relationships that connect the molecular structure properties of organic molecules to these TL-SOS parameters [26, 33, 34], which enables chemists to synthesize molecules with the desired properties.

1.1.2. Reorientational Response

The reorientational response is due to the rotation of the molecules to align with the electric field of the excitation, which occurs in linear molecules in the liquid phase. Consider one such

molecule, Carbon Disulfide (CS_2), shown in Figure 7. CS_2 is a cylindrical molecule with differing polarizability $\alpha_{\parallel}$ and $\alpha_{\perp}$ along the longitudinal and transverse axes respectively.

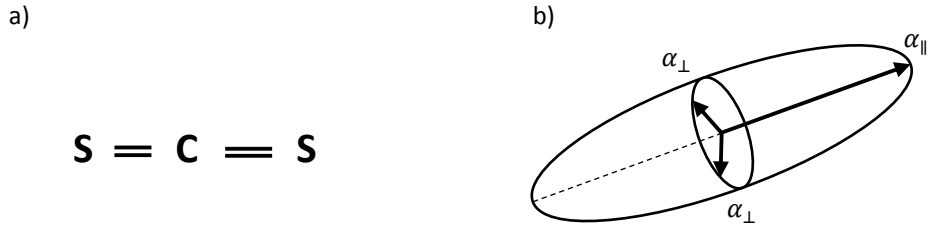

Figure 7: a) diagram of CS_2; b) diagram of transverse and longitudinal polarizability. For a linear molecule of this type the longitudinal polarizability is much higher than the transverse polarizability due to the increased length.

Because the molecule is symmetric, there will be no permanent dipole moment. However, in the presence of a strong electric field, the electronic orbitals will be distorted, creating an induced dipole moment [15]. This distorted electronic orbital creates an asymmetry in the molecule that allows the electric field to generate a torque that rotates the molecule, altering α. This is a $\chi^{(1)}:\chi^{(1)}$ cascaded process, but since the change in α is proportional to I, it appears as a $\chi^{(3)}$ process.

For the case where the excitation and probe beams are co-polarized, we expect that Δn should be positive, since the longitudinal axis which has the larger α is being aligned to the probe axis. For the cross polarized case, Δn should be negative, given that now the longitudinal axis is being turned away from the probe. Heuristically, we expect that the magnitude of Δn for the cross polarized case to be half that of the co-polarized case. In the co-polarized case all of the molecules are being aligned to the probe axis, while in the cross polarized case only the molecules in the

plane of the excitation and probe are being aligned away from the probe, while those orthogonal to this are do not contribute to the polarization change.

Mathematically, for the electric field E_z aligned with the $\hat{z}$ axis, the induced polarization due to the reorientational effect along the laboratory axes are [15]

$$\begin{gathered} P_x = N(\bar{\alpha}_\perp\langle -sin(\theta)\,sin(\psi)\,sin(\phi)\,cos(\psi) - \\ sin(\theta)\,cos(\theta)\,cos(\phi)\,sin(\psi)^2 - sin(\theta)\,sin(\phi)\,sin(\psi) - \\ sin(\theta)\,cos(\theta)\,cos(\phi)\,cos(\psi)^2\rangle + \bar{\alpha}_\parallel\langle sin(\theta)\,cos(\theta)\,cos(\phi)\rangle)E_z f^{(1)^2} = \\ N\langle \bar{g}_x(\theta,\phi,\psi)\rangle E_z f^{(1)^2}, \end{gathered} \tag{1.48}$$

$$\begin{gathered} P_y = N(\bar{\alpha}_\perp\langle sin(\theta)\,cos(\psi)\,cos(\phi)\,sin(\psi) - \\ sin(\theta)\,cos(\theta)\,sin(\phi)\,sin(\psi)^2 - sin(\theta)\,cos(\phi)\,sin(\psi)\,cos(\psi) - \\ sin(\theta)\,cos(\theta)\,sin(\phi)\,cos(\psi)^2\rangle + \bar{\alpha}_\parallel\langle sin(\theta)\,cos(\theta)\,sin(\phi)\rangle)E_z f^{(1)^2} = \\ N\langle \bar{g}_y(\theta,\phi,\psi)\rangle E_z f^{(1)^2}, \end{gathered} \tag{1.49}$$

$$\begin{gathered} P_z = N(\bar{\alpha}_\perp\langle sin(\theta)^2\,sin(\psi)^2 - sin(\theta)^2\,cos(\psi)^2\rangle + \bar{\alpha}_\parallel\langle cos(\theta)^2\rangle)E_z f^{(1)^2} = \\ N\langle \bar{g}_z(\theta,\phi,\psi)\rangle E_z f^{(1)^2}, \end{gathered} \tag{1.50}$$

where $\bar{\alpha}_\parallel$ and $\bar{\alpha}_\perp$ are the polarizabilities of the molecule along the longitudinal and transverse axes, and $\bar{g}(\theta,\phi,\psi)$ is the function of angular dependencies in the above expressions. The bar above the symbol indicates that the quantity is measured in the molecular frame as opposed to the laboratory frame.

In order to perform the orientational averaging of the terms given within the brackets, we must consider both the potential well $\bar{V}_{int}$ generated by the electric field that tends to align the

molecules, and the thermal agitation which tend to randomize the molecular orientation. The potential well is given by

$$\bar{V}_{int} = -1/4\,(\bar{\alpha}_{\parallel}\cos(\theta)^2 + \bar{\alpha}_{\perp}\sin(\theta)^2). \tag{1.51}$$

The orientational averaging can be explicitly written as an integral over all angles

$$P_{x,y,z} = \frac{\iint_0^{2\pi}\int_0^{\pi}\bar{g}_{x,y,z}(\theta,\phi,\psi)\exp\left(-\frac{V_{int}}{k_B T}\right)d\theta d\phi d\psi}{\iint_0^{2\pi}\int_0^{\pi}\exp\left(-\frac{V_{int}}{k_B T}\right)d\theta d\phi d\psi}, \tag{1.52}$$

where k_B is Boltzmann's constant and T is the temperature in units of Kelvin (K). The factor $exp(-V_{int}/k_b T)$ accounts for the randomization of the molecular orientations due to thermal agitation. In the limit that the field is very weak ($\bar{V}_{int} \approx 0$), $P_z = 1/3\,(\bar{\alpha}_{\parallel} + 2\bar{\alpha}_{\perp})$, which is consistent with our intuition for randomly oriented molecules, as the polarizability along the transverse axes should have twice the effect of the longitudinal axis, since on average, there are twice as many molecules with one of their transverse axis aligned with the field.

Evaluating this integral for the general case ($\bar{V}_{int} < 0$) we find that

$$\begin{aligned} P_z &= P_z^L + P_z^{NL}, \\ P_z^L &= 1/3\,(\bar{\alpha}_{\parallel} + 2\bar{\alpha}_{\perp}), \\ P_z^{NL} &= NE_z f^{(1)^4}\frac{(\bar{\alpha}_{\parallel} - \bar{\alpha}_{\perp})^2}{45k_B T}E_z^2. \end{aligned} \tag{1.53}$$

Converting Eq. (1.53) from terms of electric field to irradiance we can write the nonlinear index of refraction for the co-polarized case $n_{2,\parallel}(\omega,\omega)$ as

$$n_{2,\parallel}(\omega,\omega) = \frac{N}{n^2\epsilon_0^2 c}\frac{(\bar{\alpha}_\parallel - \bar{\alpha}_\perp)^2}{45k_BT} f^{(1)^4}. \tag{1.54}$$

Performing this procedure for the cross polarized case we can determine that

$$n_{2,\perp}(\omega,\omega) = -\frac{N}{n^2\epsilon_0^2 c}\frac{(\bar{\alpha}_\parallel - \bar{\alpha}_\perp)^2}{90k_BT} f^{(1)^4} = -\frac{1}{2}n_{2,\parallel}(\omega,\omega). \tag{1.55}$$

This result affirms the heuristic argument explained previously. This relation between the cross and co-polarized cases will prove useful when we study the polarization dependence of the nonlinear response of liquids.

1.1.3. Excited State Absorption

Excited State Absorption (ESA) is the absorption of a photon by an electron that has been promoted to the excited state by a previous interaction [2]. As such ESA is not an electronic nonlinear response as we have defined it, rather it is a $\chi^{(2n-1)}{:}\chi^{(1)}$ cascaded process that can be confused with $\chi^{(2n+1)}$ effects. For the simplest $\chi^{(1)}{:}\chi^{(1)}$ case, the rate equations governing the population dynamics are

$$\begin{aligned}
\frac{dI(z)}{dz} &= -\sigma_{01}N_0(t)I(z) - \sigma_{12}N_1(t)I(z), \\
\frac{dN_0(t)}{dt} &= -\frac{\sigma_{01}N_0(t)I(z)}{\hbar\omega} + \frac{N_1(t)}{\tau_{10}}, \\
\frac{dN_1(t)}{dt} &= \frac{\sigma_{01}N_0(t)I}{\hbar\omega} - \frac{N_1(t)}{\tau_{10}} + \frac{N_2(t)}{\tau_{21}} - \frac{\sigma_{12}N_1(t)I(z)}{\hbar\omega},
\end{aligned} \tag{1.56}$$

$$\frac{dN_2(t)}{dt} = \frac{\sigma_{12}N_1(t)I(z)}{\hbar\omega} - \frac{N_2(t)}{\tau_{21}},$$

$$N = N_0 + N_1 + N_2,$$

where σ_{ij} is the absorption cross section from state i to state j, N_i is the population of state i, τ_{ij} is the decay constant from state i to state j, $\hbar = h/(2\pi)$ is the reduced Planck's constant and ω is the angular frequency of the incoming beam. For typical conditions $\tau_{20} \gg \tau_{21}$, $\tau_{20} \gg \tau_{10}$, $N_1 \gg N_2$ and for pulse durations much shorter than τ_{10}, these equations can be solved analytically to determine

$$\frac{\partial F(z)}{\partial z} = -\alpha F(z) - \frac{N_g\sigma_g\sigma_{ex}}{2\eta\omega} F(z)^2, \tag{1.57}$$

where $F(z)$ is the fluence, N_g is the number of electrons in the ground state, σ_g is the ground state to first excited state cross section, and σ_g is the first to second excited state cross section. The second term of the expression has the same fluence dependence as 2PA, so that care needs to be taken in discriminating ESA from 2PA.

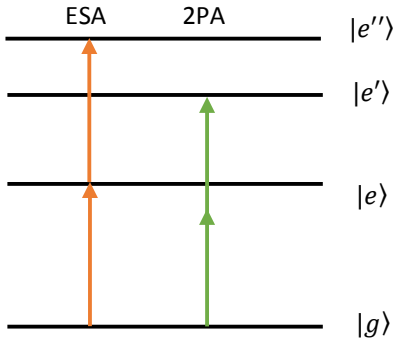

Figure 8: Energy level diagram of ESA.

In this case the ESA is induced by 1PA, so that it is an effective $\chi^{(3)}$ ($\chi^{(1)}$:$\chi^{(1)}$) cascaded process. However, as ESA can be induced by any order of multi-photon absorption, so it may also appear as an odd order effective $\chi^{(2n+1)}$, $\left(\chi^{(2n-1)}:\chi^{(1)}\right)$ cascaded process. Of particular concern is 2PA induced ESA an effective $\chi^{(5)}$, $\left(\chi^{(3)}:\chi^{(1)}\right)$ cascaded process that can often distort measurements of $\chi^{(3)}$ processes. In the next section we will discuss how these contributions can be separated.

CHAPTER 2: MEASUREMENT TECHNIQUES

In this chapter we will examine the various linear and nonlinear characterization techniques for measuring several important parameters connected to the real and imaginary parts of $\chi^{(3)}$.

2.1. Linear Characterization Techniques

Typically, the first step in characterizing a molecule is to determine its linear optical properties. This data is used to identify wavelength regions of low 1PA, which are of interest for nonlinear spectroscopy.

The 1PA spectrum is measured using a spectrophotometer. This device uses a broad band radiation source and a grating to select a very narrow bandwidth of light. The light is then passed through the sample and the transmission T of the material at that particular wavelength is measured. The transmission is used to calculate the absorption of the sample per molecule, the molecular absorptance ϵ

$$T = e^{-OD}, \tag{2.1}$$

$$OD = \epsilon CL, \tag{2.2}$$

where OD is the optical density, ϵ is the molecular absorptance, C is the molar concentration, and L is the path length of the material.

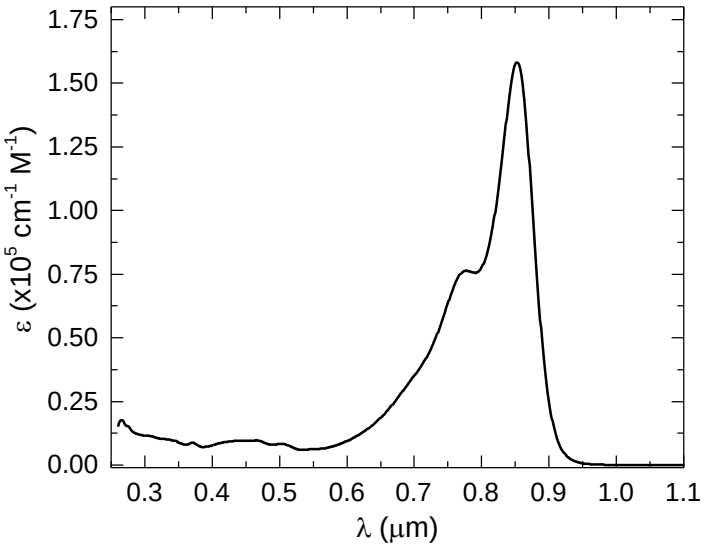

Figure 9: 1PA spectrum of AJBC 3702 Dimethylformamine (DMF). The peak molar absorbance is 1.58×10^5 cm^{-1} M^{-1} at a wavelength of λ = 853 nm.

Typically, a reference sample is used to isolate the effects due to the sample of interest from the solvent. A background scan is performed prior to the sample scan using only the empty sample mounting equipment. This background scan is then subtracted from the sample scan in order to reduce the effects of stray light inside the measurement chamber.

In addition to identifying regions where it possible to perform nonlinear spectroscopy, the 1PA spectrum can be used to determine ground state transition dipole moment.

2.2. Nonlinear Characterization Techniques

The primary nonlinear properties of interest in this investigation are 2PA and NLR. Typically, 2PA is the easier of the two to determine, as it can be measured from an induced change in T. The NLR is typically more complicated to determine, as the induced phase change is typically

not directly measured, instead being converted to some phenomena that can be easily measured such as a change in intensity or polarization. In the case of polarization, the conversion is based on the phenomena of induced birefringence, while in the case of irradiance, the underlying mechanism is interference. These changes in the observables are then related to the refractive index change, Δn.

2.2.1. Excitation Source

In order to generate the high irradiances required to observe nonlinear optical phenomena, two high power femtosecond pulse lasers were used as the excitation source, a Clark MXR CPA Series Model 2110 and a Coherent Elite Duo.

The Clark MXR is a Chirped Pulse Amplification (CPA) [35] laser producing 780 nm pulses at 140 fs (FWHM) temporal pulse duration at a pulse energy of 1 mJ at a repetition rate of 1 kHz. For the generation stage, a 980 nm diode laser oscillator operating at 27 MHz is used to pump an erbium doped fiber with an output wavelength of 1550 nm. The oscillator output is then doubled using periodically poled lithium niobate (PPLN) and then stretched using a diffraction grating to reduce the irradiance of the pulse before amplification. The pulse is then output from the generation stage to be amplified by a titanium doped sapphire (Ti:Al_2O_3Ti:sapph) amplifier.

For the amplification stage a Ti:sapph gain medium is pumped by a frequency doubled, Q-switched, neodymium-doped yttrium aluminum garnet (Nd:$Y_3Al_5O_{12}$, Nd:YAG) laser, with an output wavelength of 532 nm at a 1 kHz repetition rate. A Pockels cell allows a single pulse from the generation stage into the amplifier cavity where it resonates for ten passes before reaching the

1 mJ level. Once this pulse is amplified it is switched out of the cavity. The pulse is then compressed using a diffraction grating to achieve a pulse duration of 140 fs (FWHM) before emission from the laser.

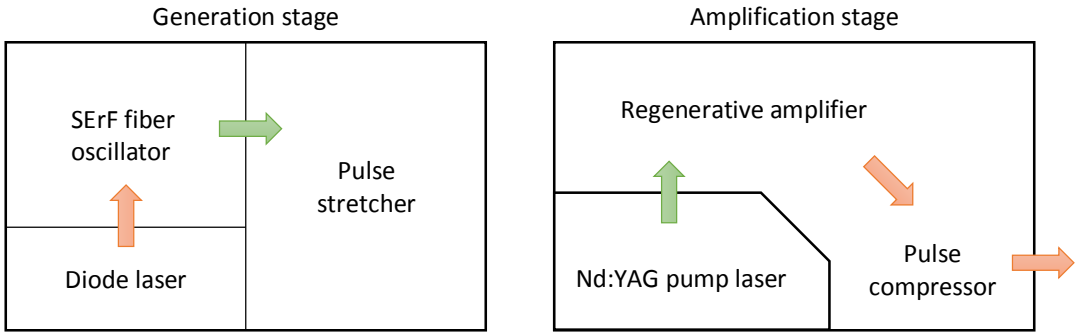

Figure 10: Diagram of Clark-MXR CPA 2110, (left) generation stage (right) amplification stage.

The Coherent Elite Duo is a CPA laser producing pulses at a repetition rate of 1 kHz with a temporal pulse duration of ~35 fs (FWHM) at a pulse energy of 12 mJ. The seed pulse is provided by a Coherent Vitara Ti:sapph laser oscillator with an output of 532 nm at 80 Mhz. The amplifier is pumped by a Coherent Evolution HE and Evolution 45 diode-pumped, frequency doubled, Q-switched neodymium-doped yttrium lithium fluoride ($Nd:LiYF_4$, Nd:YLF) lasers producing 45W of power of 527 nm at 1kHz repetition rate. The seed pulse from the Vitara oscillator enters the oscillator cavity where it is amplified by a Ti:sapph regenerative amplifier pumped by the two Evolution diode lasers. The pulse passes through the amplifier 14 times before reaching the 12 mJ level, at which point it is switched out of the cavity via the Pockels cells and compressed before output.

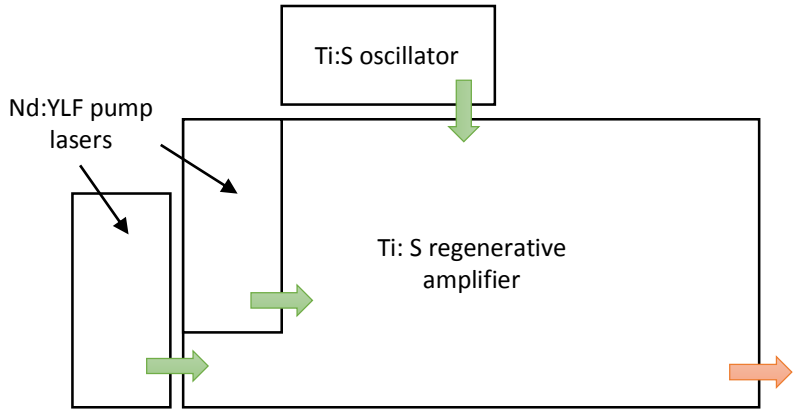

Figure 11: Diagram of Coherent Elite Duo.

2.2.2. Tunable Frequency Source

In order to determine the degenerate nonlinearity a two types of tunable frequency sources were used. The first type of source was an Optical Parametric Amplifier (OPA). In our experiments, three different OPAs were used - Light Conversion Traveling wave Optical Parametric Amplification System (TOPAS) Model C, Model 800, and Model HE. All three devices work on the principle of generating spectrally filtered White Light Continuum (WLC), passing this through nonlinear crystal to generate the signal and idler and then amplifying the signal and idler.

To illustrate, we will describe the operation of the TOPAS-C, which is nominally tunable from 1140-2600 nm, and can be extended from 189 nm to 20 μm when using mixer crystals to generate the sum and difference frequencies of the signal and idler. The TOPAS-C splits the 780 nm input beam into three beams, two low energy and one high energy beam. First one of the low energy beams is used to generate supercontinuum in a beta-barium borate (Beta-BaB_2O_4, BBO) crystal. This WLC is then dispersed using a diffraction grating, and the seed frequency is picked

off the dispersed beam by use of a slit. The seed frequency is the passed through the BBO crystal again where it is mixed with the second low energy beam of the pump, which creates the signal and idler frequencies. Phase matching is achieved by careful rotation of the BBO to create the signal and idler. Finally the signal and the idler are amplified by passing through the BBO crystal where the high energy beam of the pump amplifies both frequencies, which are then output to the mixer crystal for sum frequency generation, if required.

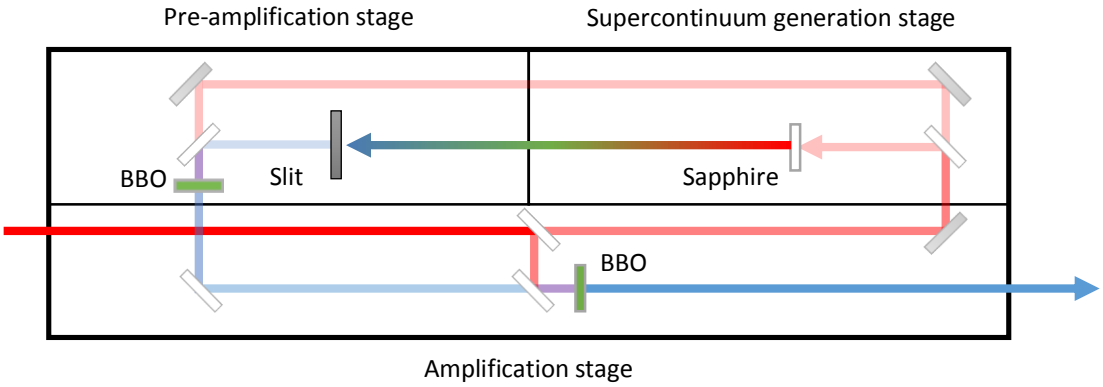

Figure 12: Diagram of Light Conversion TOPAS-C. Path length equalization optics have been omitted for clarity.

The TOPAS Model HE utilizes the same hardware as the TOPAS-C, except for the addition of an additional amplification stage to achieve much higher power output. The TOPAS Model 800 takes a different approach, with the WLC generated using superfluorescence and the seed wavelength generated by temporally dispersing the WLC using and using a time delay to select the wavelength.

The second type of tunable frequency source used was spectrally filtered supercontinuum generated in either water or sapphire, depending on the output wavelength desired. When femtosecond pulses are focused in transparent materials without multi-photon absorption, a

spectrally broad output is produced. The primary source of supercontinuum generation Self-Phase Modulation (SPM) [36]. This is the temporal analogue of self-focusing, in which new temporal, instead of spatial frequencies are generated due to SPM. In our experiments, the output of the Coherent Elite Duo was focused into either a 1 cm water cell or a 1 mm sapphire plate, producing a supercontinuum with a useful spectral range for our experiments of 400-900 nm for water and 400-1100 nm for sapphire. Typically, water is preferred for generating visible wavelengths, as it is easier to produce a stable supercontinuum. Above 900 nm, sapphire is preferred due to the 1PA in water. This output is then spectrally filtered using dielectric filters with a bandwidth of 10 nm.

While the spatial profile of the spectrally filtered supercontinuum follows the input pulse, the temporal profile is significantly broadened from the input pulse. This is due in part to the narrow bandwidth of the spectral filters used to select the output frequency and the dispersion of water cell. The 10 nm bandwidth of the dielectric filters limits a transform limited pulse at 650 nm to no less than 66 fs (FWHM). In addition, there will be some dispersion of both the input pulse and the output supercontinuum as it propagates through the material used to generate it which will also broaden the output pulse duration. Typically, the pulse duration of the spectrally filtered supercontinuum is about 100-150 fs (FWHM) for water and about 200 fs (FWHM) for sapphire.

2.2.3. Excite-Probe

The excite-probe technique, often referred to Transient Absorption Spectroscopy (TAS) is a commonly used technique for resolving the time dynamics of absorption processes, illustrated in Figure 13. In the resonant version of this technique, a strong excitation beam is used to promote

electrons from the ground state to some higher excited state. A weak probe beam is used to determine the absorption [37] or reflection [38] due to the population of electrons promoted into the higher state. A delay line is used to adjust the overlap of the excitation and probe pulses and determine the time dynamics of the interaction. A wave plate is used to adjust the relative polarization of the excitation and probe beam in order to measure the anisotropy of the material. In nonresonant excite-probe the excitation is tuned away from resonance, which in concert with the probe beam which allows for determination of the ND-2PA.

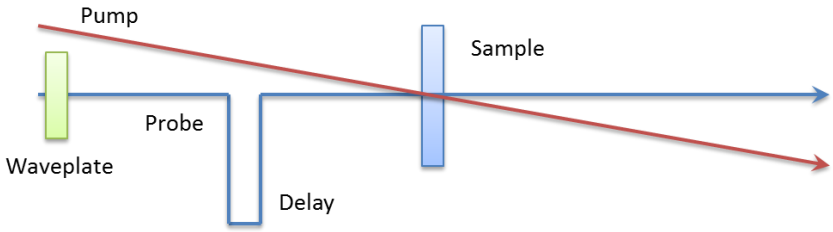

Figure 13: Excite-probe schematic.

The ability to resolve the time dynamics by adjusting the delay between the excitation and probe beams is particularly useful, as it allows for examination of the time dynamics of the nonlinearity and has been applied to numerous materials such as semiconductors [38] and organic compounds [39]. In addition to adjusting the delay between pulses, the polarization between pulses can also be varied, allowing for examination of off diagonal components of $\chi^{(3)}$.

For the general case of excite-probe in a material exhibiting 2PA, the equations are

$$\frac{dI_p(z,t)}{dz} = -2\alpha_2(\omega_e,\omega_p)I_p(z,t)I_e(z,t) - \alpha_2(\omega_p)I_p(z,t)^2 - \alpha(\omega_p)I_p(z,t)$$
$$\frac{dI_e(z,t)}{dz} = -2\alpha_2(\omega_e,\omega_p)I_p(z,t)I_e(z,t) - \alpha_2(\omega_e)I_e(z,t)^2 - \alpha(\omega_e)I_e(z,t), \quad (2.3)$$

where $I_p(z,t)$ is the irradiance of the probe, $I_e(z,t)$ is the irradiance of the excitation, $\alpha_2(\omega_e,\omega_p)$ is the nondegenerate 2PA coefficient, $\alpha_2(\omega)$, is the degenerate 2PA coefficient, $\alpha(\omega)$ is the 1PA coefficient ω_p is the frequency of the probe beam and ω_e is the frequency of the excitation beam.

Considering the simplest case in which we approximate that the probe beam is weak ($I_p(z,t) \ll I_e(z,t)$), the excitation is undepleted ($dI_e(z,t)/dz = 0,\ I_e(z,t) = I_e(t)$) there is negligible linear absorption ($\alpha(\omega_p) \approx 0,\ \alpha(\omega_e) \approx 0$) and we are tuned away from the D-2PA resonance ($\alpha_{2,D}(\omega_p) = 0$) this can be simplified to

$$\frac{dI_p(z,t)}{dz} = -2\alpha_2(\omega_e,\omega_p)I_p(z,t)I_e(t),$$
$$I_p(L,t) = I_p(0,t)\exp\left(-2\alpha_2(\omega_e,\omega_p)I_e(t)L\right), \tag{2.4}$$

where L is the sample length.

For the case where the excitation and probe beams have a Gaussian temporal profile ($I_p(z,t) = I_p(z)\,exp\left(-(t-\tau_d)^2/\tau_p^2\right)$, and $I_e(t) = I_{e,0}\,exp(-t^2/\tau_e^2)$) and the temporal response of the material is much shorter than the pulse duration (as in the case of electronic nonlinearities) the signal as a function of temporal delay of the excitation and probe beams is

$$T(\tau_d) = 1 - \frac{2\sqrt{\pi}\,e^{-\frac{\tau_d^2}{\tau_e^2+\tau_p^2}}q_0}{\sqrt{1/\tau_e^2 + 1/\tau_p^2}}, \tag{2.5}$$

where $q_0 = \alpha_2 I_0 L$ is the NLA parameter.

In this case the signal as a function of delay follows the cross correlation of the pulses, as shown in Figure 14.

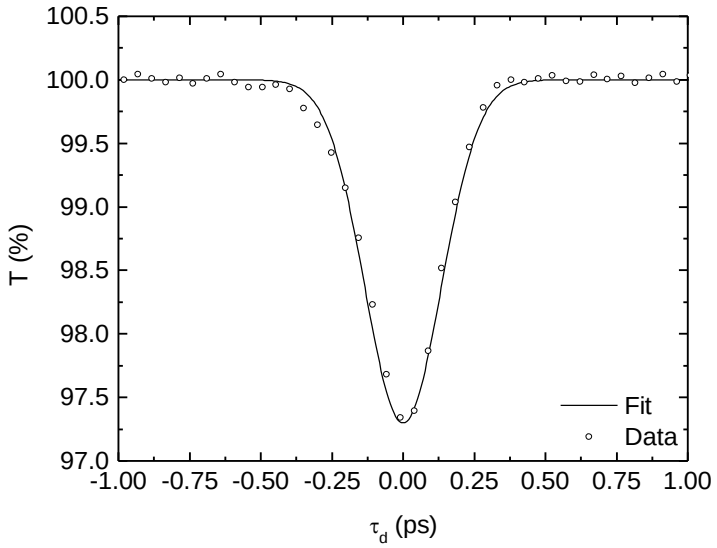

Figure 14: Nondegenerate excite-probe measurement of ZnO with λ_e = 1800 nm, λ_p = 440 nm.

In the case where the response of the nonlinearity is noninstantaneous (such as excited state absorption or nuclear effects) the signal will have a long tail at positive delays. For extremely long lived effects (such as thermal effects), this long tail may blend into the measurement of the next pulse, so that the transmission before zero delay will also be less than unity. This would make normalization of the transmission problematic so that the signal would be erroneous. However, by varying the repetition rate of the laser the presence of thermal effects could be determined out by looking for a repetition rate dependent signal.

The excite-probe technique is quite flexible having been applied to numerous applications such as time dynamics and polarization anisotropy [40]. However, the technique is limited to measurement of NLA, and requires some mechanism to convert the induced index change to a measurable phenomenon in order to measure NLR.

2.2.4. Z-Scan

One of the primary tools used to determine the nonlinear properties of materials is the Z-Scan technique [23]. In the Z-Scan technique the sample is translated along the Z direction through the beam waist of a focused Gaussian laser beam in a tight focusing configuration, as seen in Figure 15. As the sample approaches focus the spot size decreases, increasing the irradiance on the sample and the induced nonlinear effects. Once the sample passes through focus, the irradiance drops along with the nonlinear effects.

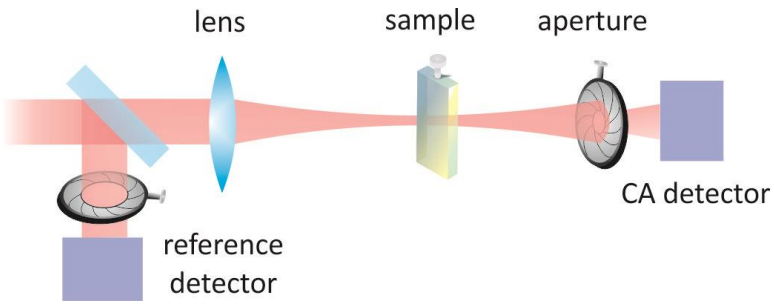

Figure 15: Z-Scan schematic.

Beyond the sample, the beam is split along two paths, the Open Aperture (OA) and the Closed Aperture (CA). As the irradiance increases, the NLA will increase within the sample, reducing the amount of energy collected at the OA detector as seen in Figure 16.

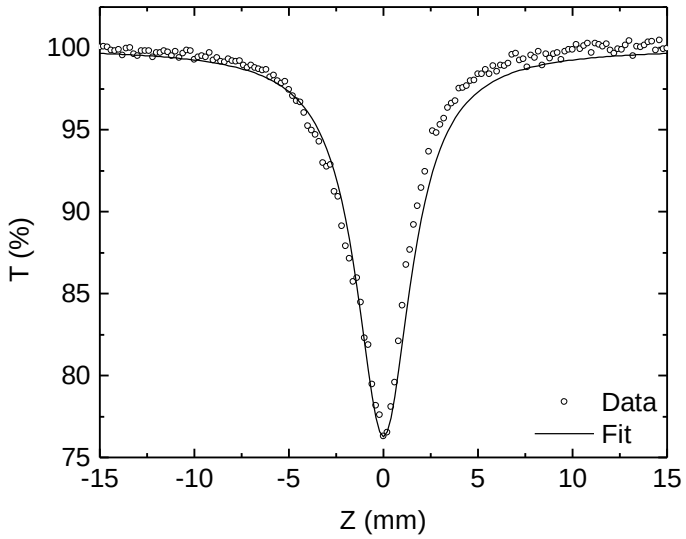

Figure 16: OA signal for GaAs for λ = 1300 nm, E = 1.52 nJ, w_0 = 24.5 μm (HW1/e^{2}M), τ = 120 fs (FWHM), n = 3.4, and L = 0.48 mm. The fit value for α_2 = 2.4×10^{-10} m/W.

The transmission is calculated by dividing the measured energy by the measured energy at a Z-position far from focus, where the irradiance is low and the nonlinear effects are negligible.

Analytically, we can follow the calculation of the OA signal presented by Sheik-Bahae et al [23]. The amplitude and phase are governed by the following equations.

$$\frac{dI(Z)}{dz} = -\alpha(Z)\, I(Z), \tag{2.6}$$

$$I(Z) = \frac{2E}{\pi^{\frac{3}{2}}\, w(Z)^2\, \tau}, \tag{2.7}$$

$$w(Z) = w_0 \sqrt{1 + \frac{Z^2}{z_0^2}}, \tag{2.8}$$

where $I(Z)$ is the irradiance, $\alpha(I)$ is the intensity dependent absorption coefficient, E is the pulse energy, $w(Z)$ is the spot size, τ is the pulse duration, w_0 is the beam waist, Z is the sample position and z_0 is the Rayleigh range. For the OA signal these can be solved analytically to yield

$$T(Z) = \frac{q(Z)}{2\sqrt{2}} \frac{1}{1 + x(Z)^2}, \tag{2.9}$$

$$q(Z) = \alpha_2 \, I(Z) L_{eff}, \tag{2.10}$$

$$L_{eff} = \frac{1 - e^{-\alpha \, L}}{\alpha}, \tag{2.11}$$

where $q(Z)$ is the absorption parameter, $x(Z) = Z/z_0$, L_{eff} is the effective length, L is the sample thickness and α is the linear absorption coefficient.

In the case of NLR, as the sample is moved closer to focus and the irradiance increases, for a positive value of n_2 the beam will experience self-focusing. This self-focusing will further reduce the beam waist at the focus, thereby increasing the divergence angle once the beam leaves the sample. This larger beam will be clipped by the aperture, reducing the normalized transmission. On the other side of focus, the self-focusing also reduces the beam waist, but because the distance to the closed aperture is less, the beam on the closed aperture is smaller. This leads to an increase of the measured normalized transmission which can exceed unity resulting in the CA trace seen in Figure 17. For negative n_2 instead of inducing self-focusing the higher irradiance induces self-defocusing, so that now the peak occurs before the valley.

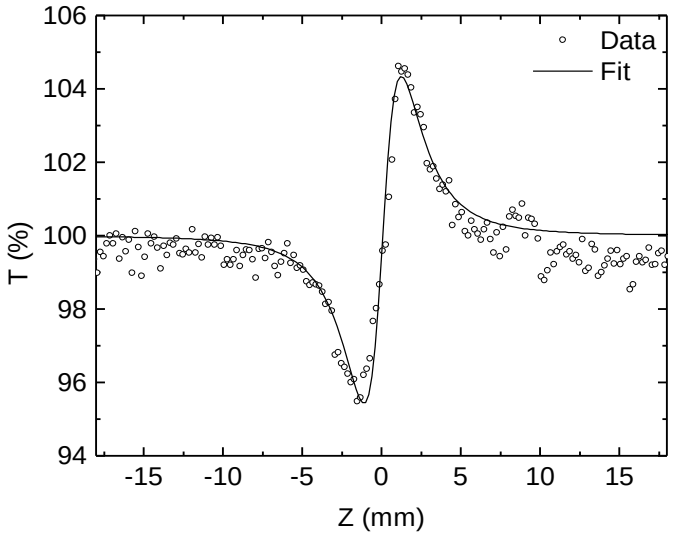

Figure 17: CA signal for CS_2 with λ = 1300 nm, E = 23 nJ, w_0 = 24.5 (HW1/e^{2}M), τ = 120 fs (FWHM), n = 1.6 and L = 1 mm. The fit value for n_2 = 4.0×10^{-19} m^2/W.

Analytically, we follow the derivation given by Sheik-Bahae et al [23]. The governing equation for the phase is

$$\frac{d\Delta\phi(Z)}{dZ} = k_0\,\Delta n(I). \tag{2.12}$$

The initial electric field is given as

$$E_i(Z,r,t) = E_0\,\frac{w_0}{w(Z)}\,e^{\left(-\frac{r^2}{w(Z)^2}+i\frac{\pi\,r^2}{\lambda\,R(Z)}+i\,\phi\right)}, \tag{2.13}$$

$$R(Z) = Z\left(1+\left(\frac{Z_0}{Z}\right)^2\right), \tag{2.14}$$

where w_0 is the beam waist, $w(Z)$ is the beam radius at Z-Scan position Z, r is the radial position from the center of the beam, λ is the free space wavelength of the field, $R(Z)$ is the field radius of curvature, and $z_0 = \pi\,w_0^2/\lambda$ is the Rayleigh range.

The irradiance and phase change at the exit surface are

$$I_e(Z,r,t) = \frac{I(Z,r,t)e^{-\alpha L}}{1+q(Z,r,t)}, \tag{2.15}$$

$$\Delta\phi(Z,r,t) = \frac{k_0 n_2}{\alpha_2}\ln\big(1+q(Z,r,t)\big). \tag{2.16}$$

From these equations we can determine the complex electric field at the exit of the sample

$$E_e(Z,r,t) = E_i(Z,r,t)e^{-\frac{\alpha L}{2}}(1+q(Z,r,t)^{\left(-\frac{i k_0 n_2}{\alpha_2}-\frac{1}{2}\right)}. \tag{2.17}$$

Having calculated the electric field at the exit surface of the sample, this is then propagated to the closed aperture plane using a Huygens-Fresnel integral.

At the closed aperture position the electric field is integrated over the aperture and pulse duration to give the total pulse energy

$$E(Z) = \int_{-\infty}^{\infty}\int_{0}^{r_a}\frac{1}{2}n\, c\, \epsilon|E_a(Z,r,t)^2|\, r\, dr\, dt, \tag{2.18}$$

where r_a is the radius of the closed aperture. The collected pulse energy is then normalized with respect to the pulse energy at a distance away from focus such that the irradiance is low and the nonlinear effects are negligible

$$T(Z) = \frac{E(Z)}{E(Z_\infty)} = \frac{E(Z)}{S\, E_i}, \tag{2.19}$$

$$S = 1 - e^{-2\frac{r_a^2}{w_0^2}}, \tag{2.20}$$

$$E_i = I_0\frac{\pi^2 w_0^2 \tau}{2\sqrt{2}}, \tag{2.21}$$

where Z_∞ is a position far from focus (typically $5z_0$ is sufficient), S is the aperture transmission, E_i is the total pulse energy, I_0 is the peak irradiance.

This expression for the transmission is non-analytic, and needs to be evaluated numerically. However, following the treatment provided by Weaire [41] we can decompose the electric field at the exit face of the sample into a series of Gaussian beams. This has the advantage that the sum can be limited to the number of terms needed to achieve the required accuracy, with a typical number being ten. Decomposing the electric field in this way gives us

$$E_e(Z,r,t) = E_0 \frac{w_0}{w(Z)}\, e^{-\frac{\alpha L}{2}} \sum_{m=0}^{\infty} F_m(Z,t) e^{\frac{2\, m\, r^2}{w(Z)^2}}, \tag{2.22}$$

where the coefficients of the expansion are given by

$$F_m(Z,t) = \frac{(i\, \Delta\phi_0(Z,0,t)^m}{m!} \prod_{j=1}^{m} \left(1 + i\left(j - \frac{1}{2}\right)\frac{\lambda\, \beta}{2\, \pi\, n_2}\right). \tag{2.23}$$

Propagating this to the aperture plane via a Huygens-Fresnel integral as before gives us the electric field at the closed aperture plane.

$$\begin{aligned} &E_a(Z,r,t) \\ &= E_i(Z,0,t) e^{-\frac{\alpha L}{2}} \sum_{m=0}^{\infty} F_m(Z,t) \frac{w_{m0}(Z)}{w_m(Z)}\, e^{\left(-\frac{r^2}{w_m^2(Z)} + \frac{i\, \pi\, r^2}{\lambda\, R_m(Z)} + i\, \theta_m(Z)\right)}, \end{aligned} \tag{2.24}$$

$$w_{m0}(Z) = \frac{w(Z)^2}{2m+1}, \tag{2.25}$$

$$w_m(Z) = w_{m0}^2 \left(g(Z)^2 + \frac{d^2}{d_m^2}\right), \tag{2.26}$$

$$R_m(Z) = d\left(1 - \frac{g(Z)}{g(Z)^2 + \frac{d^2}{d_m^2}}\right)^{-1}, \tag{2.27}$$

$$\theta_m(Z) = tan^{-1}\left(\frac{g(Z)}{d/d_m(Z)}\right), \tag{2.28}$$

$$d_m(Z) = k\frac{w_{m0}^2(Z)}{2}, \tag{2.29}$$

$$g(Z) = 1 + \frac{d}{R(Z)}, \tag{2.30}$$

where $w_{m0}(Z)$ is the beam waist, $w_m(Z)$ is the beam size, $R_m(Z)$ is the radius of curvature, $\theta_m(Z)$ is the divergence angle and $d_m(Z)$ is the Rayleigh range of the m^{th} Gaussian of the decomposition.

Taking the first two terms of the expansion (m = 0 & 1), with no NLA, $T(x)$ can be analytically evaluated to yield the small signal approximation for the normalized transmission

$$T_{app}(x) = \frac{4x}{(x^2+9)(x^2+1)}\Delta\phi_0, \tag{2.31}$$

where $\Delta\phi_0 = k_0 n_2 I_0 L_{eff}$ is the peak on axis phase distortion. This is valid for small phase changes $\Delta\phi_0 < 0.5$, where the higher order terms in the expansion can be ignored with an accuracy to within 2% [42]. Inclusion of higher order terms to account for larger phase distortions requires numerical evaluation. The small signal approximation for $T(x)_{app}$ allows us to determine some interesting features of the CA signal. The Z position distance between the peak and valley of the CA signal ΔZ_{p-v} is determined by taking the derivative of $T(x)_{app}$ and solving for the position at which it is zero

$$\Delta Z_{p-v} \approx \pm 0.85\, z_0. \tag{2.32}$$

The expression for the peak to valley change in the normalized transmission ΔT_{p-v} can be determined by numerical fitting over the closed aperture transmission S [23]

$$\Delta T_{p-v} \approx 0.406(1-S)^{0.25}|\Delta\phi_0|. \quad (2.33)$$

The Z-Scan technique is noted for its relative simplicity, as it uses a single beam that does not require overlapping pulses in time or space. The requirement for a Gaussian beam does tend to reduce the maximum available pulse energy, as spatial filtering typically discards much of the beam energy. However, the Z-Scan is sufficiently sensitive and the pulse energies available are so high that this does not present a problem in practice.

When fitting Z-Scan data, it should be noted that the OA signal contains information regarding the NLA, while the CA signal contains information on both NLR and NLA. For small NLA, it is possible to take the division of the Closed Aperture over Open Aperture signal (CA/OA) to eliminate the NLA, so that a single parameter fit for the NLR can be performed. However, this does not work once the NLA becomes significant, as the NLA will distort the CA/OA signal so that it cannot be fit using the procedure outlined previously.

In addition to the approximations derived previously, additional approximations have been made to cover a wider range of applications, such as non-negligible NLA [43, 44], thick samples [45, 46] and higher order optical nonlinearities [47].

As it is often the case the effect of the NLA cannot be removed by dividing CA/OA, it is possible to determine the following relation for the CA transmission in the presence of non-negligible 2PA [43]

$$T_{app}(x) = 1 + \frac{2(-\rho\, x^2 + 2x - 3\,\rho)}{(x^2+9)(x^2+1)}\Delta\phi_0. \quad (2.34)$$

Where $\rho = \alpha_2/(2k_0n_2)$ is the NLA factor. This expression is valid under the condition

$$\rho < \frac{3}{2}\left(\frac{1}{|\Delta\phi_0|} - 0.2\right), \tag{2.35}$$

which ensures that the NLA is not too large compared to the NLR. Based on this, the relation for ΔT_{p-v} in the presence of non-negligible 2PA is given as

$$\Delta T_{p-v} = (0.406 + 0.268\rho^2)|\Delta\phi_0|. \tag{2.36}$$

As the NLA is increased, the valley-peak structure begins to lose its symmetry, with the ratio of the peak to the valley determined to be

$$\Delta T_p/\Delta T_v = 1 - 3.4\rho + 2.88\rho^2, \tag{2.37}$$

where ΔT_p is the height of the peak above unity, and ΔT_v is the depth of the valley below unity. The CA signal still retains its distinctive valley-peak structure so long as $|\rho| < 1/\sqrt{3}$. In the limit $\alpha_2 \to 0$, Eq. (2.34) and (2.36) revert back to their familiar forms in Eq. (2.31) and (2.33) in the limit $S \to 0$, with a symmetric valley-peak structure $\Delta T_p = \Delta T_v$. These analytic expressions are useful for calculating the initial estimates for α_2 and n_2 when attempting to fit the Z-Scan signals using any of the above described algorithms.

The above analysis is valid under the condition that the irradiance does not change significantly within the sample. This is referred to as the thin sample approximation and is valid under the following conditions [23]

$$L < z_0, \tag{2.38}$$

$$L \ll \frac{z_0}{\Delta\phi_0}. \tag{2.39}$$

Typically, since $\Delta\phi_0$ is small, the condition in Eq. (2.38) is automatically met when Eq. (2.39) is met. This is equivalent to stating that there is no self-focusing, which allows us to take

the irradiance profile as constant throughout the sample. Typical Z-Scan values of z_0 are on the order of 1 mm, which is also the path length of a quartz cuvette used to measure materials in solution. While this limitation is not problematic for materials with large nonlinearities, this can be an issue for materials with small nonlinearities as it prevents us from increasing the signal by making L arbitrarily large. This condition often occurs when dealing with organic solutes in solution whose concentration is limited by low solubility and aggregation.

For a system noise of 0.2% of the normalized transmission, the sensitivity $2\pi/\Delta\phi_0$ is $\lambda/250$ where $\Delta\phi_0 = k_0 n_2 I_0 L$ is the peak on-axis phase change. This is similar to the performance of interferometric techniques [48]. To compare the performance of the Z-Scan technique to other techniques, we define the peak signal per unit peak phase shift which we call the responsivity $R = S_{max}/\Delta\phi_0$, where S_{max} is the peak signal measured in a scan. For the Z-Scan in the limit of small signals the peak signal is simply $S_{max} = \Delta T_{p-v}$ so that

$$R = \frac{\Delta T_{p-v}}{\Delta\phi_0} = 0.406(1-S)^{0.25}. \tag{2.40}$$

For a typical Z-Scan, S = 0.33, so that R = 0.367. The maximum theoretical responsivity in the limit $S \to 0$ is R = 0.406. We will return to this value as we develop experimental techniques and compare their performance to the Z-Scan.

Due to its relative simplicity and sensitivity, the Z-Scan has become one of the standard techniques used for NLO materials characterization, and has been applied to a wide variety of materials and circumstances. The technique has been applied to semiconductors [47, 49, 50], solvents [42, 50] organic molecules in solution [47, 51], and thin films [52, 53].

2.2.4.1. Z-Scan Interpretation

While the Z-Scan technique allows the measurement of the NLR and NLA, some degree of interpretation is required to determine the sources, whether n_2, α_2, $\chi^{(5)}$ effects, Excited State Effects (ESE) or some combination of these.

Since the OA signal contains NLA only, we can use Eq. (2.9) to estimate α_2 using a one parameter fit. The CA signal contains both NLR and NLA, which both need to be taken into account. One option is to fit both α_2 and n_2 using a two parameter fit. Alternatively, for small NLA, dividing the CA scan by the OA scan can recover the NLR in the absence of NLA as seen in Figure 18, so that the estimation of n_2 from the CA signal can be performed as a one parameter fit.

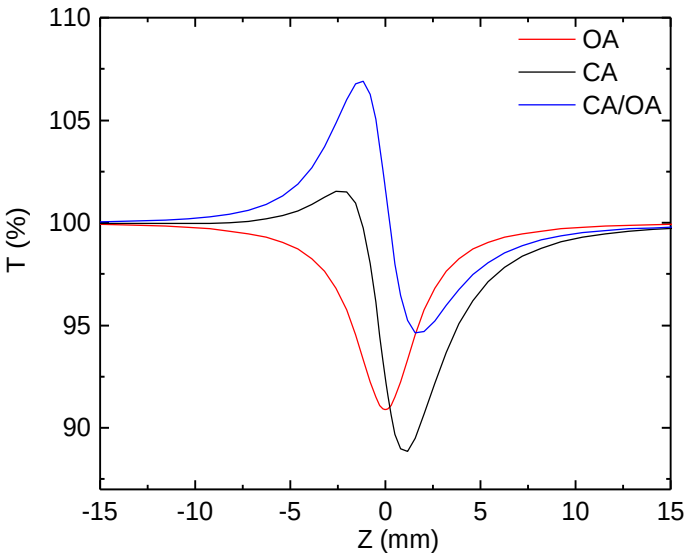

Figure 18: OA, CA and CA/OA Z-Scan signal [54] for $\Delta\phi_0$ = -0.5 and q_0 = 0.3.

This can only be done if the NLA is small, since a large NLA will distort the CA signal so that it is no longer symmetric. In this case, the OA signal must be fit first to determine α_2, which can in turn be used when fitting for n_2.

In addition to the simultaneous presence of NLA and NLR, scans performed at high irradiance may have significant 2PA induced ESE (2PA-ESE). The effect of positive 2PA induced Excited State Refraction (2PA-ESR) is to make negative n_2 appear more negative, while making positive n_2 less positive, while negative ESR will do the opposite. For 2PA induced Excited State Absorption (2PA-ESA), the effect is to make α_2 appear larger than it actually is.

One technique to separate $\chi^{(3)}$ from ESE is to take advantage of the fluence dependence of the ESE [55]. If the only effects present are $\chi^{(3)}$ effects, n_2 and α_2 should be constant with irradiance. However, if it appears that there is some irradiance dependence of n_2 and α_2, this is an possible indicator that there is some kind of ESE occurring. To separately determine the $\chi^{(3)}$ processes, we can plot n_2 or α_2 vs. irradiance and find the $\hat{y}$-intercept of the linear fit line through the points. This yields the value of n_2 or α_2, while the slope of the line gives us the excited state cross section σ_{ESA}.

Aside from 2PA-ESA, an effective $\chi^{(5)}$ (cascaded $\chi^{(3)}$: $\chi^{(1)}$) process, direct $\chi^{(5)}$ processes may also be significant at very high irradiances. Gu et. al [46] examined the effect of $\chi^{(5)}$ processes on the Z-Scan signals and determined that in the small signal limit, the transmission due to $\chi^{(5)}$ processes can be approximated as

$$T_2(x, \Phi_{02}) \approx 1 + \frac{8\,x\,\Phi_{02}}{(x^2+1)^2(x^2+25)^2} + \frac{48\,x\,(x^2-3)\Phi_{02}}{(x^2+1)^4(x^2+25)(x^2+81)}, \qquad (2.41)$$

where $x = Z/z_0$, and Φ_{02} is the phase distortion due to $\chi^{(5)}$ effects. As for $\chi^{(3)}$ effects, for small phase distortion, $\Delta T_{p-v}^{(5)}$, the peak to valley change in transmission due to $\chi^{(5)}$ effects can be approximated [23] as

$$\Delta T_{p-v}^{(5)} \approx 0.21(1-S)^{0.25}\left|\Delta\phi_0^{(5)}\right|, \tag{2.42}$$

where $\Delta\phi_0^{(5)}$, the phase distortion for a $\chi^{(5)}$ nonlinearity is

$$\Delta\phi_0^{(5)} = kn_3 I^2 L_{eff}^{(5)}, \tag{2.43}$$

$$L_{eff}^{(5)} = \frac{1-e^{-2\alpha L}}{2\alpha}, \tag{2.44}$$

where n_3 is the third order nonlinear index of refraction and $L_{eff}^{(5)}$ is the effective length for $\chi^{(5)}$ effects.

The approximate transmission in Eq. (2.41) can be generalized to any order $\chi^{(2n+1)}$ effects [46] as

$$T_n(x,\Phi_{0n}) \approx \lim_{M\to\infty}\left(\sum_{m=0}^{M}\frac{1}{m!}\left(\frac{\Phi_{0n}}{(1+x^2)^n}\right)^m \frac{i^m(x+i)}{x+i(2mn+1)}\right)^2, \tag{2.45}$$

$$\left|\Phi_{0n}^{M_{opt}}/M_{opt}!\right| = 0.5. \tag{2.46}$$

The minimum number of terms in the summation M required for accurate results is numerically determined by solving Eq. (2.46).

2.2.4.2. Two Color Z-Scan

A further extension of the Z-Scan technique involved using two different beams on the sample. As in the case of excite-probe, this allows us to independently vary the wavelength, timing, and polarization of the two beams to examine the nondegenerate nonlinearity, time dynamics and anisotropy of the nonlinearity [56].

Using this technique the nonlinear properties of Semiconductor Doped Glasses (SDG) were determined at 538 nm, which is within the absorptive region, using a beam at 630 nm, at which the material is transparent. Initially, the excitation and probe beam waists were set to be equal. In subsequent work, Ma et al demonstrated [57] that by adjusting the relative size of the two beam waists, an improvement in $\Delta T_{p-v}$of 2.3 times could be achieved by making the probe beam about 50% smaller than the excitation beam. This effect was observed using samples of borosilicate glass doped with nanocrystals of Cd(S,Se), and is due to the enhanced interference between the center and wings of the probe beam.

2.2.4.3. Z-Scan Error Analysis

As in all experiments, there will be some error in determination of n_2 due to noise in our signals and uncertainty of the experimental parameters. The total error of function F assuming normally distributed error of its inputs x, y is [58]

$$\sigma_F^2 = \left|\frac{\partial F}{\partial x}\right|^2 \sigma_x^2 + \left|\frac{\partial F}{\partial y}\right|^2 \sigma_y^2 + 2\frac{\partial F}{\partial x}\frac{\partial F}{\partial y} Cov(x, y). \tag{2.47}$$

In the case of the Z-Scan $F = \Delta T_{p-v}$. Assuming that the errors in the irradiance parameters τ, E, w_0 and ΔT_{p-v} are normally distributed and uncorrelated ($Cov(x, y) = 0$), in the limit of small signals and negligible NLA we can calculate the fractional error $\eta_{n_2} = \sigma_{n_2}/n_2$

$$\eta_{n_2} = \sqrt{\frac{{\sigma_\tau}^2}{\tau^2} + \frac{{\sigma_E}^2}{E^2} + \frac{4\,{\sigma_{w_0}}^2}{w_0^2} + \frac{{\sigma_{\Delta T_{p-v}}}^2}{\Delta T_{p-v}^2}} = \sqrt{\eta_p^2 + \left(\frac{1}{SNR}\right)^2}, \tag{2.48}$$

$$\eta_p^2 = \frac{{\sigma_\tau}^2}{\tau^2} + \frac{{\sigma_E}^2}{E^2} + \frac{4\,{\sigma_{w_0}}^2}{w_0^2} = \eta_\tau^2 + \eta_E^2 + 4\eta_{w_0}^2, \tag{2.49}$$

where σ_i is the standard deviation of parameter i, $\eta_i = \sigma_i/i$ is the fractional error in the parameter i, η_p is the total fractional error due to parameter uncertainty, and $SNR = \Delta T_{p-v}/\sigma_{\Delta T_{p-v}} = 1/\eta_f$ is the Signal-to-Noise Ratio which is the inverse of the fitting error η_f.

The fractional error in n_2 as a function of SNR for typical Z-Scan parameters and fractional parameter uncertainties $\eta_\tau = \eta_E = \eta_{w_0}$ = 10% is shown in Figure 19.

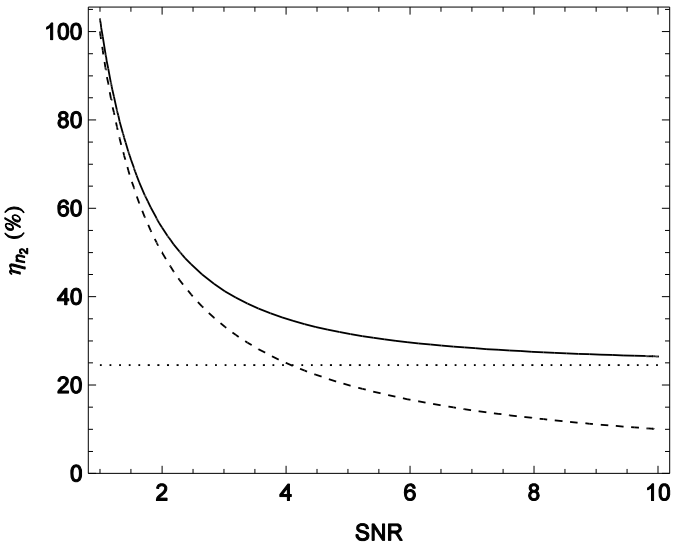

Figure 19: Fractional error in n_2 vs. SNR (solid), fitting error (bashed), parameter uncertainty (dotted)

When the parameter uncertainty is specified fractionally, η_p is a constant value independent of the magnitude of the SNR. Hence, while parameter uncertainty obscures the magnitude of n_2, it does not obscure the sign of n_2. On the other hand, since $\sigma_{\Delta T_{p-v}}$ is an absolute number, η_{n_2} increases as the SNR is reduced. Once the SNR is less than unity the total error exceeds 100%, at which point neither the magnitude nor sign of n_2 can be determined. We will take this as the limit of detection of the signal.

Below a SNR of 4, η_f is the largest component of η_{n_2}, while above this, η_p is the larger component. Hence, to improve accuracy in the case of high SNR, reducing the parameter uncertainty is most effective, while in the case of low SNR, the better approach is to improve the SNR.

In Section 2.2.4.4 we will examine several techniques to improve the SNR. Note that even in the case of high SNR, there will always be some minimum error determined by the parameter uncertainty. For the Z-Scan using typical experimental parameters and uncertainties, this minimum error floor is about 25%.

2.2.4.4. Z-Scan Error Reduction

From the above analysis, for high SNR, the primary component of error in the Z-Scan technique is due to parameter uncertainty. This can be minimized by making independent measurements of E, τ, and w_0. However, when dealing with low SNR signals, the proper strategy is to reduce η_f by reducing $\sigma_{\Delta T_{p-v}}$. Various techniques have been implemented to deal with the various sources of experimental error in the Z-Scan technique that contribute to $\sigma_{\Delta T_{p-v}}$. Sources of

this error include linear background artifacts, pulse energy fluctuations, beam pointing instabilities, and deviations from Gaussian beam profiles. In order to reduce these noise sources, various techniques such as reference arms [56], relative measurement [59] and differential techniques [54] have been employed.

The addition of a second reference arm with an identical aperture [56], can be used to reduce the noise associated with the pulse energy fluctuations and pointing instabilities.

The signal from the sample is divided by the reference signal, eliminating much of the noise,

$$S(Z)_{filt} = \frac{S(Z)_{sample}}{S(Z)_{ref}}. \tag{2.50}$$

This technique is very successful in reducing the noise associated from these two sources. However, as it is difficult to ensure that both apertures are aligned exactly the same and have the same transmission, there is typically still some residual noise due to beam pointing instability that is not fully removed. In addition, in order to account for both CA and OA signals, two reference arms are required, one with and without an aperture, so that the pointing instability noise is not inadvertently injected into the open aperture signal.

Another technique for reducing error is relative measurement. The analysis of Z-Scan data assumes that the beam used has a Gaussian profile (M^2 = 1). Beams with a non-Gaussian profile can be accounted for through relative determination of n_2 by measuring a sample with a known n_2 and then measuring the sample with the unknown n_2, and scaling the result using

$$n_{2,s,c} = \frac{n_{2,r,c}}{n_{2,r,m}}\, n_{2,s,m}, \tag{2.51}$$

where $n_{2,s,c}$ is the corrected value for sample, $n_{2,s,m}$ is the measured value of the sample, $n_{2,m,c}$ is the actual value of the reference material and $n_{2,r,m}$ is the measured value of the reference material.

This technique works well even for beams with profiles that are severely distorted from a Gaussian profile [59]. Hence, checking results against a reference material before and after scanning the sample of interest is a standard calibration technique. If the known and measured values of the calibration samples are off by a consistent factor, the measured value of the sample may be multiplied by this factor to correct for this error. This technique works only if the order of the nonlinearity is the same in the reference and sample materials. Examination of each at several pulse energies can be used to ensure the order of nonlinearities [55].

CHAPTER 3: TECHNIQUE DEVELOPMENT

In this section we will discuss the proposed work that will compose the body of the dissertation. The proposed work will fall under two broad categories, technique development and applications. The techniques that will be developed are designed to overcome two longstanding problems in the field of nonlinear characterization.

The first problem concerns the measurement of small NLR in the presence of large nonlinear backgrounds. This is particularly common in the study of organic dyes in solvents and thin films on substrates, where the signals from the solvents and substrates used can be much larger than the signals due to the materials under study. Having techniques to overcome these limitations, we will apply this to a study of thin films and organic materials which have proved challenging to measure using traditional nonlinear characterization techniques.

The second problem concerns resolution of the time dynamics of ultrafast nonlinearities. The typical techniques used to determining the time dynamics of ultrafast nonlinearities have drawbacks. Two-color Z-Scan is difficult to align and implement, while OKE is limited to measurements of induced birefringence. In this work we will adapt a technique previously applied to the study of very small absorption to the study of ultrafast nonlinearities, and then use this technique to study the time dynamics of electronic, nuclear and reorientational nonlinearities in various materials.

3.1. Dual-Arm Z-Scan

Reference arms, relative measurement and background subtraction work by isolating the unwanted errors so that they may be removed from the Z-Scan signal in post-processing, leaving only the signal due to NLR or NLA. The Dual-arm Z-Scan (DA Z-Scan) technique takes these ideas of correlated noise removal one step further by placing a sample with the identical solvent in a closely matched arm along with the solution of interest. Properly aligned, much of the noise on the solution and solvent arms will be correlated, reducing the fitting error significantly so that the ability to determine n_2 is greatly enhanced. This is particularly important when determining small NLR in the presence of large nonlinear backgrounds, as in the case of solutes in solvents and thin films on substrates.

When studying the optical nonlinearities of a material, it is common to place the material (solute) into a solvent so that it may be placed in the Z-Scan. Hence the selection of the proper solvent is essential to accurately determine the nonlinear properties under study. Ideally, we would like a solvent that will create a stable solution, and with NLR and NLA is small compared to that of the solute.

In the case of NLA this is typically not problematic, as it is possible to find solvents that negligible NLA. However this is not true for NLR as there will always be some amount of NLR. Often times the NLR of the solvent is much higher than that of the solute. This is true even in cases where the per-molecule NLR of the solute is much higher than that of the solvent due to the much higher density of solvent molecules compared to the solute.

Additionally, there is a small contribution to the NLR due to the cells used to contain the samples. Typically, this contribution is small and can be ignored (0.25×10^{-19} m^2/W for quartz cuvettes [60]), although this may not be true if the NLR of the solute is similarly small. In this case, large discrepancies can arise when reporting the nonlinearity of the solute if the NLR of the solvent and cells are not properly accounted for. These factors have complicated the determination of small NLR, so that for many materials there are large spectral ranges over which the NLR cannot be effectively determined.

There are several ways in which the large nonlinear background can be accounted for. The easiest method is to simply subtract the known value of $n_{2,V}$ of the solvent from the measured value of $n_{2,U}$ of the solution, which should yield the $n_{2,U}$ of the solute. However, literature values tend to vary since there are a wide range of values reported using different techniques. For example, Gong et al. [61] reported a value for toluene at 800 nm of 2.2×10^{-15} cm^2/W using the optical Kerr effect, while Couris et al. [62] reported a value of 0.88×10^{-15} cm^2/W using spectral shearing interferometry and 1.3×10^{-15} cm^2/W using single-arm Z-Scan. The proper approach is to measure both the solvent and solution n_2 in situ in order to avoid such large discrepancies.

There are two ways of accounting for the solvent NLR in situ by performing two sequential Z-Scans, one for the solution and one for the solvent. The first method is to fit each Z-Scan curve individually to determine the nonlinear refractive index for the solution, $n_{2,S}$ and the solvent, $n_{2,V}$, separately. These values are then subtracted to yield the nonlinear refractive index of the solute, $n_{2,U} = n_{2,S} - n_{2,V}$. This is referred to as the "fit-subtract" method. Secondly we can subtract the

solution $T_S(Z)$ and solvent $T_V(Z)$ Z-Scan traces from each other and fit the resulting solute trace $T_U(Z) = T_S(Z) - T_U(Z)$. This is known as the "subtract-fit" method.

While these methods may work fine for materials with large NLR signals, these methods do not perform well when measuring very small NLR, when the noise is on the order of the solute signal. This noise injects an error into the signal which makes determination of the solute n_2 very difficult. In subtracting two separate Z-Scans, this noise cannot be eliminated because the noise in the two sequential scans is uncorrelated. However, if the two Z-Scans are taken simultaneously using identical Z-Scan arms, much of the noise is correlated on a laser shot by laser shot basis and will be eliminated upon subtraction, leaving only the uncorrelated noise.

3.1.1. Experimental Apparatus

The experimental apparatus consists of a standard Z-Scan setup with an additional sample arm which has been carefully aligned so that both arms have the same response by matching the irradiance parameters and sample positions. In addition, the equipment in each arm is also matched, using the same model of photodetectors, optics and sample cuvettes matched to within tight tolerances.

Matching the pulse durations is accomplished by ensuring that each beam traverses through identical lengths of dispersive optics. This is typically not a problem for pulse durations greater than 100 fs (FWHM), as the bandwidth of the pulse it typically small enough that the dispersion of the optics can be neglected. However, for shorter pulses (~50 fs FWHM) care must be taken to

ensure any dispersive optical elements in one are compensated for in the other arm via the use of compensator plates.

Matching the beam waists is done by collimating the beam prior to the first beam splitter, using matched optics in each arm, and equalizing the arm path lengths. To ensure that signal fluctuations due to pointing instability of the laser are correlated between the arms, the number of mirror reflections beyond the 50/50 beam splitter shown in Figure 20 is matched so that any asymmetries in the beam profile are clipped in the same manner by the apertures placed after the samples.

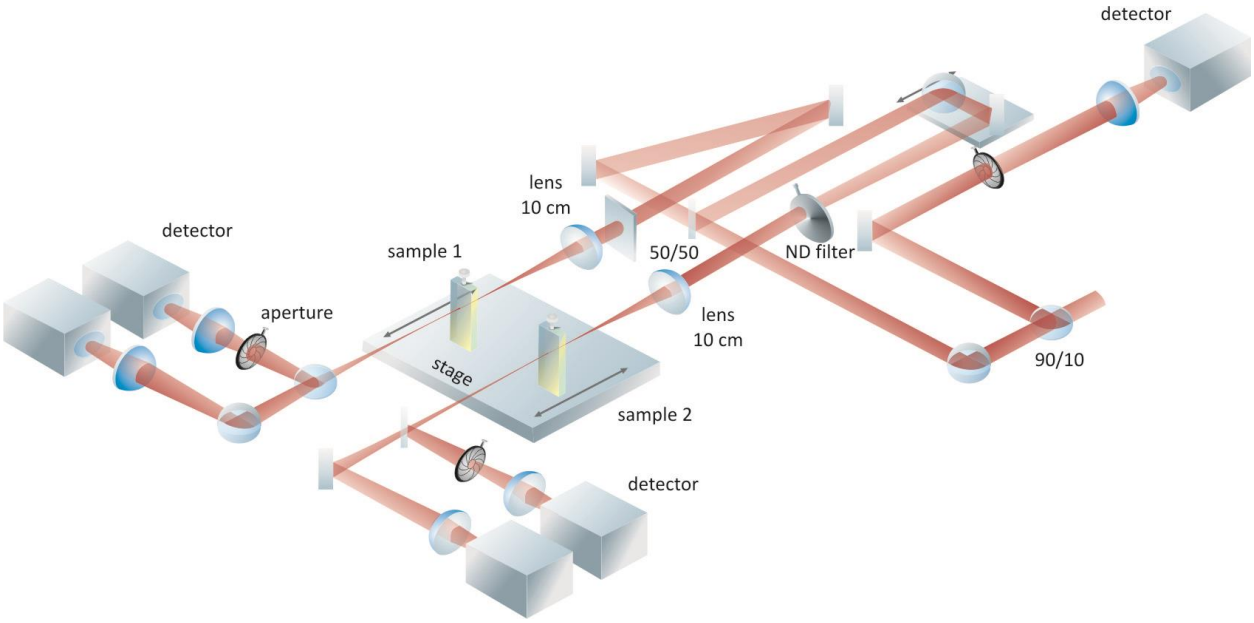

Figure 20: DA Z-Scan experimental apparatus.

Equalizing the pulse energy is accomplished by scanning two cells filled with the same solvent with large NLR such as carbon disulfide (CS_2), and attenuating one of the beams using a continuously variable ND filter until ΔT_{p-v} on each arm is equal. To ensure that the two samples experience the same irradiance and noise simultaneously at all points along the Z-axis, the relative

Z-position of the samples is adjusted until the CA signals from both arms lie directly on top of each other.

Once the difference between CA signals of both arms has been minimized, the cells used for alignment are replaced with cells containing the solution in one arm and the solvent in the other arm and scanned as described in Section 3.1.1 to isolate the solute signal.

3.1.2. Theory and Analysis

Isolation of the solute signal requires removing the solvent signal from the solution signal. In this process it is assumed that the solution signal is merely the sum of the solute and solvent signal $T_S(z) = T_V(Z) + T_U(Z)$. In the small signal approximation this is equivalent to stating the solution optical nonlinearity is the sum of the solute and solvent optical nonlinearities $n_{2,S} = n_{2,U} + n_{2,V}$.

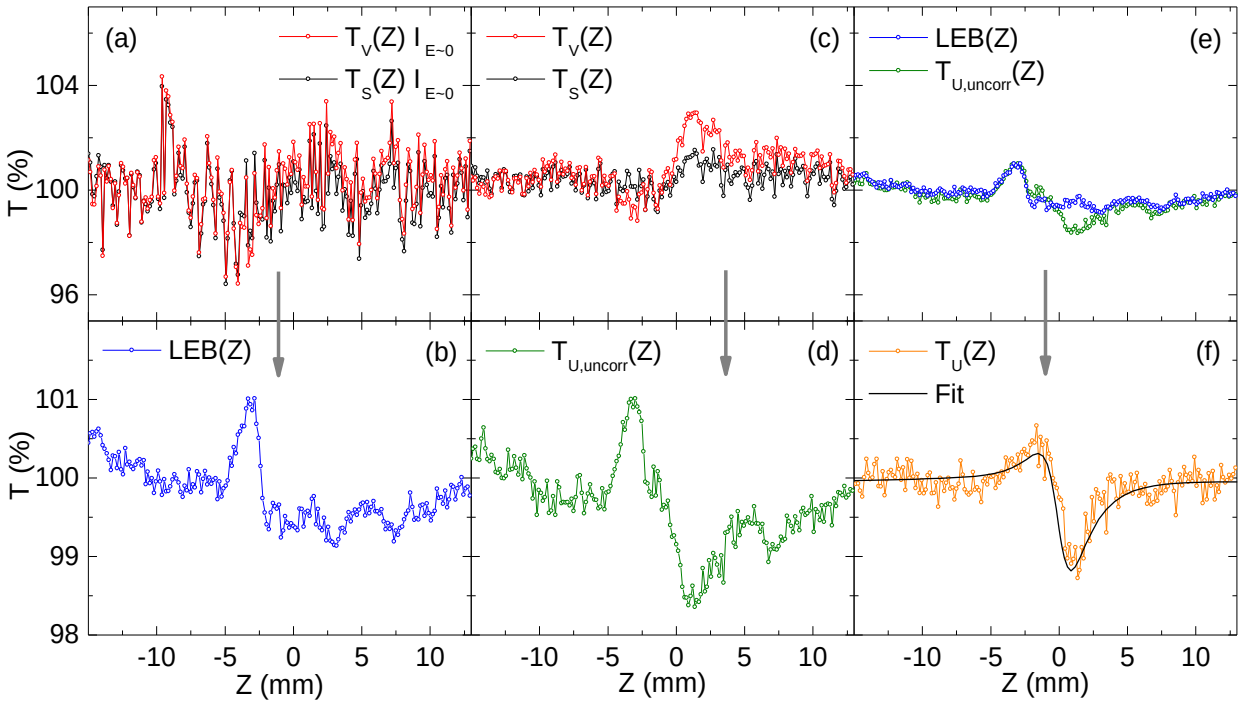

Figure 21: DA Z-Scan data analysis. (a) Low energy scans of solution $T_S(Z)|_{E\approx0}$ and solvent $T_V(Z)|_{E\approx0}$. (b) Subtraction of $T_S(Z)|_{E\approx0}$ and $T_V(Z)|_{E\approx0}$. (c) High energy scans of solution $T_S(Z)$ and solvent $T_V(Z)$. (d) Subtraction of $T_S(Z)$ and $T_V(Z)$. (e) Extracted solute signal $T_U(Z)$ and fit with $\Delta\phi_0$ = -0.06 and q_0 = 0.03.

The solute signal is simply the solvent signal subtracted from the solution signal. However, for the CA signal there is typically a linear background that must also be accounted for. Hence, first we need to isolate this linear background signal which we refer to as the Low Energy Background (LEB). The LEB is the signal due to purely linear differences in the two arms, and is determined by scanning the sample and solvent at a low pulse energy at which the nonlinear effects are negligible as shown in Figure 21 (a-b). This procedure is similar to the linear background subtraction performed by Ma et al [56]

$$LEB(Z) = T_S(Z)|_{E\approx 0} - T_V(Z)|_{E\approx 0}. \quad (3.1)$$

In order to avoid injecting additional noise due to this subtraction, smoothing of the LEB using a Savitzky-Golay algorithm [63] is applied.

The pulse energy is then increased and the samples are scanned to measure the nonlinear properties of the solution and solvent. The solvent CA signal is then subtracted from the solution CA signal to yield the uncorrected transmittance for the solute $T_{U,uncorr}(Z)$ as shown in Figure 21 (c-d)

$$T_{U,uncorr}(Z) = 1 + \big(T_S(Z) - T_V(Z)\big). \quad (3.2)$$

The addition of unity normalizes the signal. Subtracting $LEB(Z)$ from the uncorrected transmittance of the solute yields the corrected solute CA signal as seen in Figure 21 (e-f)

$$T_U(Z) = T_{U,uncorr}(Z) - LEB(Z). \quad (3.3)$$

For small signals this is nearly equivalent to a CA Z-Scan performed on the isolated solute. This data is then fit using the usual Z-Scan analysis described in Section 2.2.4 to determine the nonlinear parameters. In cases where there is both NLR and NLA the OA Z-Scan signal can be processed in a similar way to determine $\alpha_{2,U}$ separately. As before the OA signal can be fit and $\alpha_{2,U}$ used as a parameter for the fit of the CA signal.

To quantify the relative merits of the dual-arm vs. single-arm Z-Scan techniques, we compare the fitting error of each approach. As previously discussed in Section 2.2.4.3, our CA signal will have some amount of noise that obscures the determination of ΔT_{p-v}. Thus the

determination of n_2 is bound by some fitting error Δn_2. For small signals where $n_2 \propto \Delta T_{p-v}$, this can be written as

$$n_2 \pm \Delta n_2 \propto \Delta T_{p-v} \pm \delta \, . \tag{3.4}$$

In the single-arm case the NLR for the solute is the error of the solution and solvent added in quadrature, as the two errors are uncorrelated

$$n_{2,U} \pm \Delta n_{2,U} \propto \left(\Delta T_{p-v,S} - \Delta T_{p-v,V}\right) \pm \sqrt{\delta_S^2 + \delta_V^2}, \tag{3.5}$$

where $\Delta n_{2,U}$ is the fitting error in $n_{2,U}$ and δ_S and δ_V are the errors in $\Delta T_{p-v,S}$ and $\Delta T_{p-v,V}$ which are the peak-to-valley changes in the transmittance of the solution and solvent, respectively. In the dual-arm case we arrive at a similar expression, except that now a portion of the noise is correlated (δ_C) and a portion is uncorrelated (δ_{UnC}). The correlated noise subtracts out, so only the uncorrelated noise remains

$$n_{2,U} \pm \Delta n_{2,U} \propto \left(\Delta T_{p-v,S} - \Delta T_{p-v,V}\right) \pm \sqrt{\delta_{S,UnC}^2 + \delta_{V,UnC}^2}, \tag{3.6}$$

where $\delta_{S,UnC}$ and $\delta_{V,UnC}$ are the uncorrelated components of δ_S and δ_V, respectively. Since in the single-arm case all of the noise is uncorrelated, and in the dual-arm case a large part of the total noise is correlated, $\Delta n_{2,U}$ for the dual-arm case will be reduced. The advantage of the dual-arm Z-Scan technique becomes particularly apparent when $\Delta T_{p-v,S} - \Delta T_{p-v,V}$ is about the same or less than $\sqrt{\delta_S^2 + \delta_V^2}$ where the single-arm Z-Scan technique cannot adequately distinguish the signal.

3.1.2.1. Maximum Tolerable Arm Mismatch

One of the primary challenges in utilizing this technique is matching the arms sufficiently so that the noise on each arm is correlated and can be subtracted out. There are two types of mismatch errors that need to be minimized, parameter mismatch errors and sample position errors. Parameter mismatch errors are errors that contribute to differing irradiances in each arm, such as differing pulse energies, beam waists or pulse durations. Sample position errors are due to the samples being in differing positions relative to the beam waist as they are scanned in the Z direction. This causes the CA traces of each arm to be shifted relative to each other, so they cannot be subtracted from each other without breaking the correlation of the noise.

For small signals, the sensitivity of the system to the irradiance parameter mismatch can be calculated. For two identical samples placed in each arm the difference between normalized transmittances is $T_{err}(Z) = T_A(Z) - T_B(Z)$ where $T_i(Z)$ is the normalized transmission down the arm indicated by the subscript i. Assuming that the maximum difference occurs when the signal is an extrema ($Z = \pm 0.85 z_0$) we can determine that peak equalization error ΔT_{err} is

$$\Delta T_{err} = \Delta T_{p-v,B} - \Delta T_{p-v,A} \approx 0.406 \Delta\Delta\phi_0 \; = 0.406 \; k_0 n_2 \Delta I_0 L, \tag{3.7}$$

where $\Delta T_{p-v,j}$ is the peak to valley transmission change in transmission of the arm indicated by the subscript j and $\Delta\Delta\phi_0$ and ΔI_0 are the differences in the peak nonlinear phase shift and irradiance between arms due to parameter mismatch. From this, the maximum allowable mismatch in the peak irradiance can be calculated as

$$\frac{\Delta I_0}{I_0} = \frac{0.392\ \Delta T_{err}\ \lambda}{n_2 \ell\ I_0} = \frac{\Delta T_{err}}{\Delta T_{p-v}}. \tag{3.8}$$

Consider the needed precision for two 1 mm cells filled with the same solvent using a value of $n_2 = 1.0 \times 10^{-19}$ m^2/W and typical Z-Scan parameters given in Table 3. We will use these typical parameters frequently in our calculations.

Table 3: Typical Z-Scan parameters used in calculations.

Parameter	Value
Wavelength (λ)	700 nm
Pulse duration (τ, FWHM)	120 fs
Pulse energy (E)	15 nJ
Index of refraction (n)	1.5
Beam waist (w_0, HW1/e^{2}M)	20 µm
Sample length (L)	1 mm

For ΔT_{err} equal to the system noise of 0.2% (equivalent to a total nonlinear phase shift of less than λ/1000) and ΔT_{p-v} = 6.8% this evaluates to a maximum allowable irradiance difference of 2.9%.

Since we do not equalize the irradiance directly, we will write this in terms of the irradiance parameters E and w_0

$$\begin{gathered}\Delta T_{err} = 0.406 k_0 n_2 \ell \cdot \big(I(E + \Delta E/2) - I(E - \Delta E/2)\big) \\ \frac{\Delta E}{E} = \frac{2.183 {w_0}^2 \tau\ \Delta T_{err}\ \lambda_0}{E n_2\ \ell} = \frac{\Delta T_{err}}{\Delta T_{p-v}},\end{gathered} \tag{3.9}$$

which translates into a maximum allowable $\Delta E/E$ of 2.9%. Figure 22 shows the signal due to varying amounts of energy mismatch $T_{A-B}(Z) = T_A(Z) - T_B(Z)$.a

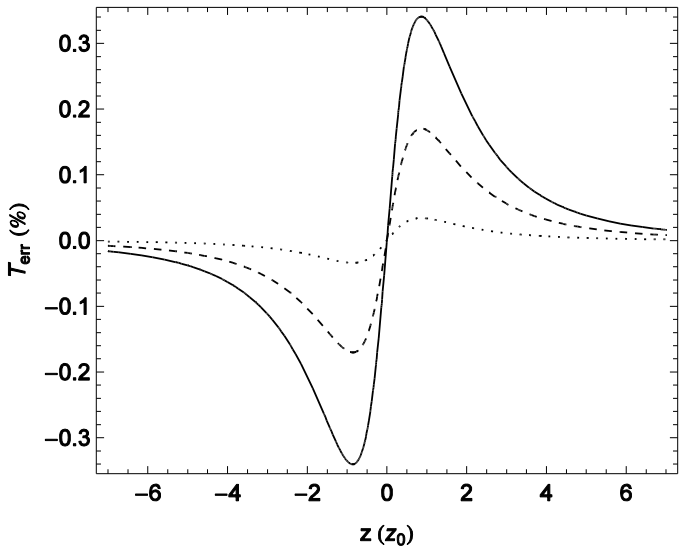

Figure 22: Signal due to 1% (dotted), 5% (dashed) and 10% (solid) energy mismatch for typical Z-Scan parameters in Table 3.

Performing the same analysis for the beam waist we can determine

$$\Delta T_{err} = 0.406 k_0 n_2 \ell \cdot \left(I(w_0 + \Delta w_0/2) - I(w_0 - \Delta w_0/2)\right)$$

$$\frac{\Delta w_0}{w_0} = \frac{1.091\, {w_0}^2 \tau \Delta T_{err} \lambda_0}{E n_2 \ell} = \frac{1}{2}\frac{\Delta T_{err}}{\Delta T_{p-v}}, \tag{3.10}$$

which translates into a maximum allowable $\Delta w_0/w_0$ of 1.5%. Equalizing w_0 is done by equalizing the path lengths of each arm from the beam splitter to the respective focusing lens. For a well collimated beam, this level of path length equalization is typically not difficult to achieve. For a beam collimated by focusing over a long distance (a 2 mm beam focused to a 0.5 mm spot over a

length of 7 m) the maximum allowable path length difference is an easily attainable 6 cm. Figure 23 shows the signal due to varying degrees of beam waist mismatch.

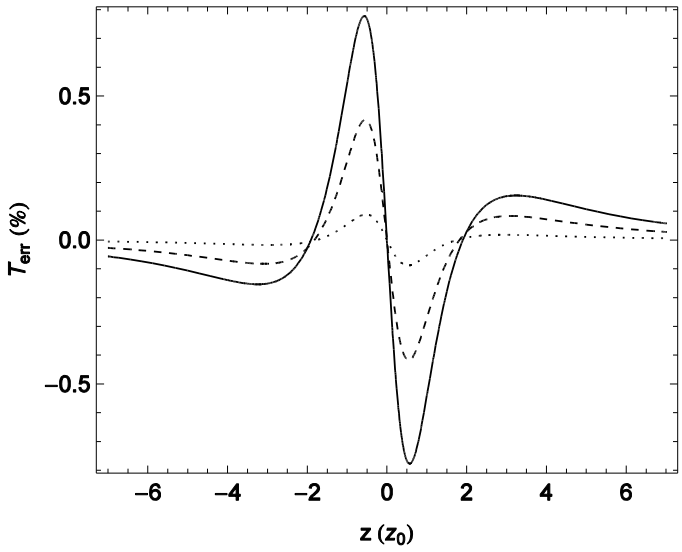

Figure 23: Signal due to 1% (dotted), 5% (dashed) and 10% (solid) beam waist mismatch for typical Z-Scan parameters in Table 3.

The cell Z-positioning mismatch is calculated by taking one copy of $T(Z)$ and shifting it with respect to another copy by some small distance ΔZ and subtracting the two curves. Hence, the mismatch is simply the derivative of $T(Z)$, which is minimum at the peak and valley and maximum at Z = 0. Unlike mismatches in E and w_0, the cell Z-positioning mismatch does not affect ΔT_{p-v}. However, as in the case of E and w_0, mismatches should be minimized by proper cell Z-positioning so as to not introduce unwanted artifacts into the solute CA signal that may complicate fitting. Performing the same analysis as above we determine that

$$\Delta T_{err} = T\left(Z - \frac{\Delta Z}{2}\right) - T\left(Z + \frac{\Delta Z}{2}\right)\Big|_{Z=0} = \Delta Z \cdot \frac{dT(Z)}{dZ}\Big|_{Z=0}, \tag{3.11}$$

$$\frac{\Delta Z}{z_0} = \frac{9\, z_0\, \tau \Delta T_{err} {\lambda_0}^2}{16 E n_2 \sqrt{\pi} \ell} = 0.9 \frac{\Delta T_{err}}{\Delta T_{p-v}}.$$

This translates into a Z-positioning tolerance $\Delta Z / z_0$ of 2.7%, which for typical Z-Scan parameters is about 30 μm. Figure 24 shows the signal due to varying amounts of sample Z-positioning mismatch.

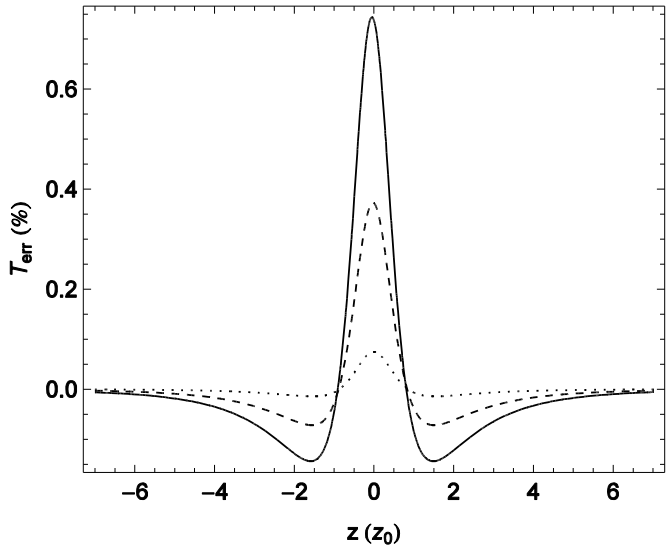

Figure 24: Signal due to 1% (dotted), 5% (dashed) and 10% (solid) of z_0 sample Z-positioning mismatch for typical Z-Scan parameters in Table 3.

Mismatches in the CA linear transmittance and distance from focus must be calculated numerically and are determined to have little effect, with mismatches of up to 25% still resulting in ΔT_{err} below the typical system noise.

Because the maximum allowable parameter mismatch is inversely proportional to ΔT_{p-v}, it is best to perform the equalization at high energy using a calibration solvent with a large n_2. If $T_{err}(Z)$ can be reduced below the noise floor under these conditions, then $T_{err}(Z)$ will remain

under the noise floor when switching to a solvent with n_2 lower than the calibration solvent, as is usually the case.

3.1.3. Application - Organic Solutes in Solvents

The rapid development of applications for photonic switching has driven efforts to find materials with large optical nonlinearities [64, 65]. To this end, many different types of materials have been extensively studied such as semiconductor–polymer hybrids [66], chalcogenide glasses [67], and various photonic microstructures [68, 69]. Organic materials having been identified as being particularly promising due to the ability to tailor the nonlinear properties, ease of processing and large FOM [18, 19].

SD-O 2405 is a squaraine molecule synthesized by the Georgia Institute of Technology as part of the Center for Organic Materials for All optical Switching (COMAS) Multi-University Research Initiative (MURI). The objective of the COMAS MURI is to design, synthesize and characterize organic materials for AOSP applications. The material properties of interest are high NLR and low NLA, along with photochemical stability, low aggregation potential and ease of deposition onto substrates.

Nonlinear characterization of SD-O 2405 requires that it be dissolved in toluene, a solvent with a large nonlinear background [62]. Hence, it is an excellent material to compare the performance of single-arm and dual-arm Z-Scan techniques. The structure and 1PA spectrum of SD-O 2405 is shown in Figure 25.

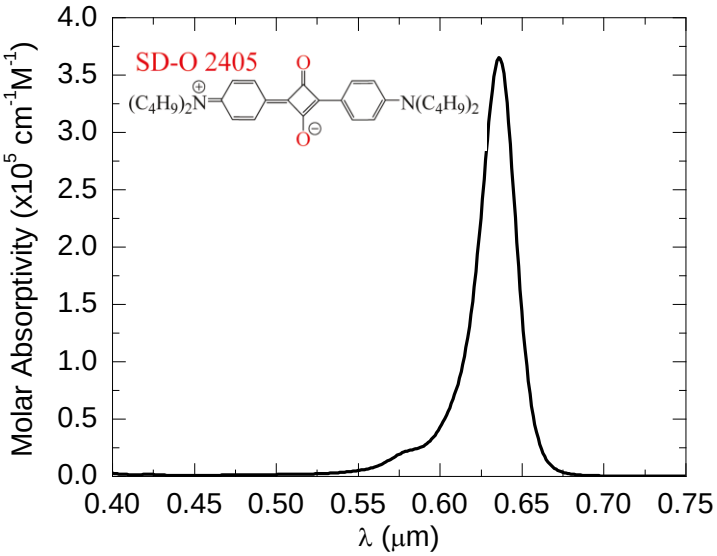

Figure 25: Structure and linear absorption spectra of SD-O 2405.

We perform both single and dual-arm Z-Scans on this solution at wavelengths from 695 nm to 920 nm, using pulses generated from a TOPAS-C pumped by a Clark-MXR CPA 2110 described in Sections 2.2.2 and 2.2.1, respectively.

Figure 26 shows sequential single-arm Z-Scans of the solution at 695nm at a peak irradiance of 51 GW/cm^2.

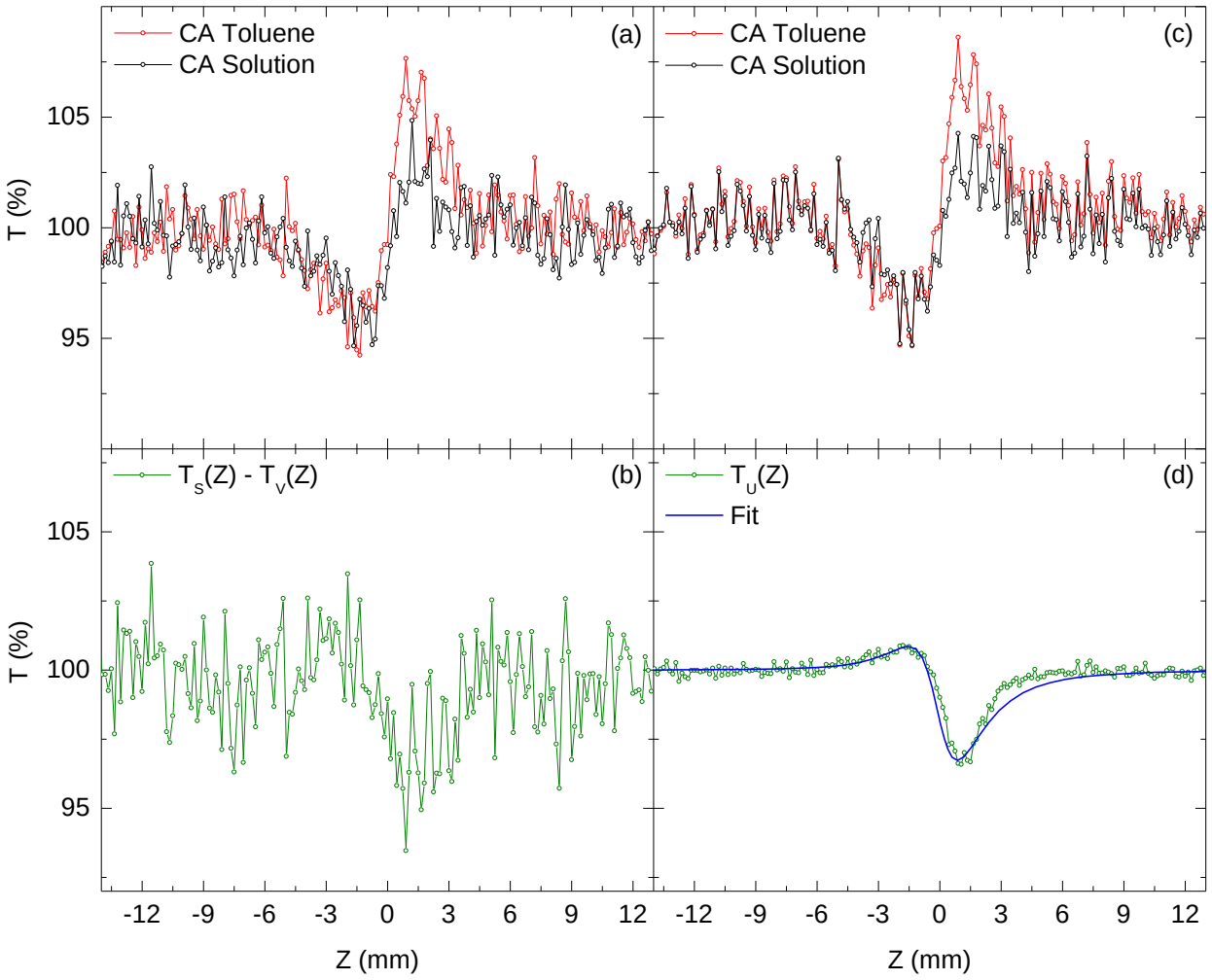

Figure 26: Sequential CA single-arm Z-Scans of toluene (open red triangles) and SD-O 2405 in toluene (closed black squares) at 695 nm with C = 47 μm, E = 31 nJ (I_0 = 51 GW/cm^2) and S = 0.33; (b) the subtraction of $T_V(Z)$ from $T_S(Z)$ from sequential scans (open green squares); (c) Simultaneous CA DA Z-Scans of toluene (open red triangles) and SD-O 2405 in toluene (closed black squares) at 695 nm; (d) the subtraction of $T_V(Z)$ from $T_S(Z)$ from simultaneous scans after LEB subtraction (open green squares) and corresponding fit using $\Delta\phi_0$ = -0.16, q_0 = 0.077 (solid blue).

At this pulse energy (E = 31 nJ) and corresponding irradiance and concentration (C = 47 μM), the differences between the Z-Scan signals of the solvent and solution are just barely

distinguishable, given the noise amplitude and, thus, $\Delta T_{p-v,S} - \Delta T_{p-v,V} \approx \sqrt{\delta_S^2 + \delta_V^2}$. Also, notice the level and uncorrelated nature of the noise between the two scans. Applying the high-pass filter to the individual single-arm Z-Scans in Figure 26 (a) yields δ_S = 1.2% and δ_V = 1.3%. This translates to $\Delta n_{2,S}$ = 0.10 × 10^{-19} m^2/W and $\Delta n_{2,V}$ = 0.11 × 10^{-19} m^2/W, which yields $\Delta n_{2,U}$ = 0.15 × 10^{-19} m^2/W using the irradiance parameters listed in Figure 26 (a). Subtracting $T_V(Z)$ from $T_S(Z)$ yields the signal shown in Figure 26 (b). Taking a high-pass filter of the curve in Figure 26 (b) yields the same result, δ = 1.8% corresponding to $\Delta n_{2,U}$ = 0.16 × 10^{-19} m^2/W. Due to the uncorrelated nature and amplitude of the noise between the two Z-Scans, the total signal of the solute is nearly the same as the noise so that $n_{2,U}$ cannot be accurately determined. With the respective signal and noise values for this case, the single-arm Z-Scan technique cannot accurately determine $n_{2,U}$, regardless of which of the two methods is used.

Next, we perform a dual-arm Z-Scan with the same experimental parameters as in Figure 26 (a). Figure 26 (c) shows $T_V(Z)$ and $T_S(Z)$ measured simultaneously using the dual-arm technique. Figure 26 (d) shows the corrected CA signal of SD-O 2405 after solvent subtraction when using the dual-arm Z-Scan technique. Because most of the noise is correlated between the arms, the correlated noise is cancelled out and the SNR is increased, thus reducing the fitting error. In this case δ = 0.19% which corresponds to a $\Delta n_{2,U}$ = 0.016 × 10^{-19} m^2/W, more than a 9 times reduction in $\Delta n_{2,U}$ compared to the single-arm Z-Scan and hence a 9.3× enhancement in SNR when using the dual-arm technique.

Even in cases where the solute CA signal is readily apparent from the single-arm Z-Scan, the dual-arm Z-Scan technique is still advantageous compared to the single-arm technique. Fig.

5(a) shows sequential single-arm Z-Scans of the solution and solvent at a wavelength of 780 nm, irradiance of 88 GW / cm^2, and concentration of 0.60 mM, where the difference between the solvent and solution signals is large.

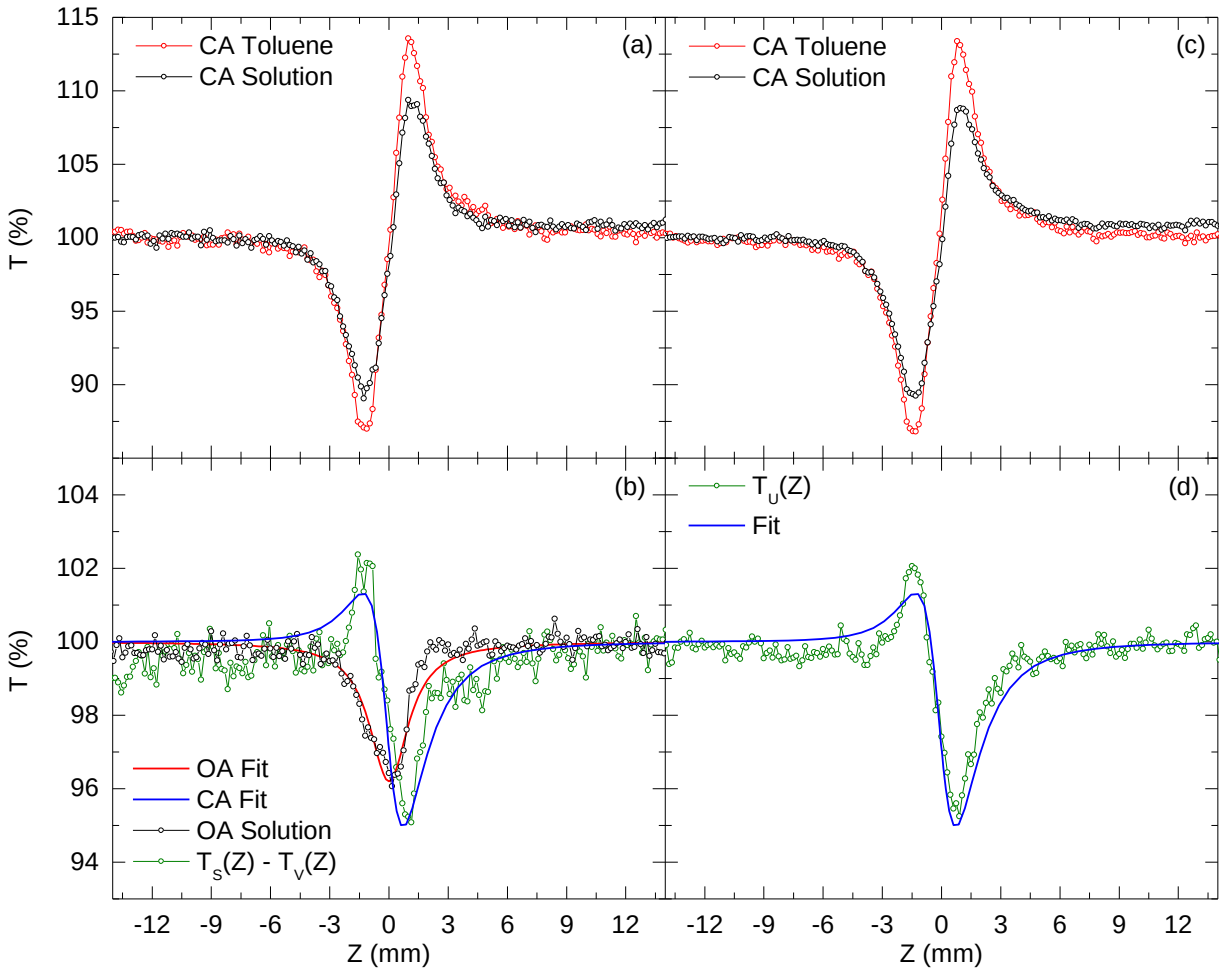

Figure 27: Sequential Z-Scans of the solution SD-O-2405 in toluene (closed black squares) and solvent toluene (open red triangles) at 780 nm, E = 50 nJ (I_0 = 88 GW/cm^2), C = 0.60 mM and (b) subtraction of solution and solvent CA Z-Scan signals (open green squares) along with the OA Z-Scan of the solution (closed black circles) and corresponding 2PA and CA fit (solid red and blue line, respectively) with $\alpha_{2,U-Fit}$ = 0.013 cm/GW and $n_{2,U-Fit}$ = -0.35 ×10^{-19} m^2/W; (c) DA Z-Scans of solution (closed black

squares) and solvent (open red triangles) taken simultaneously; (d) Simultaneous subtraction of solution and solvent yielding solute signal (open green squares) and fit incorporating both 2PA and NLR (solid blue line) with $\Delta\phi_0$ = -0.25, q_0 = 0.11, using S = 0.33.

In this case $\Delta T_{p-v,S} - \Delta T_{p-v,V} \gg \sqrt{\delta_S^2 + \delta_V^2}$, thus $n_{2,U}$ can be easily extracted from the noise. Taking a high-pass filter of $T_S(Z)$ and $T_V(Z)$ independently yields δ_S = 0.31%, and δ_V = 0.32% respectively. This translates into $\Delta n_{2,S}$ = 0.017 × 10^{-19} m^2/W and into $\Delta n_{2,V}$ = 0.018 × 10^{-19} m^2/W, yielding $\Delta n_{2,U}$ = 0.025 × 10^{-19} m^2/W.

Figure 27 (b) shows the subtraction of $T_V(Z)$ from $T_S(Z)$ for the sequential single-arm Z-Scans. Taking a high pass FFT filter of this subtraction yields δ = 0.42% which corresponds to $\Delta n_{2,U}$ = 0.023 × 10^{-19} m^2/W. The fit gives $n_{2,U}$ = -0.35 × 10^{-19} m^2/W. Figure 27 (c) shows dual-arm Z-Scans of the solution and solvent using the same experimental parameters as in Fig. 5(a). Fig. 5(d) shows $T_U(Z)$ after subtraction of the curves in Figure 27 (c) and its associated $LEB(Z)$. From this dual-arm subtraction, we find δ = 0.23% corresponding to $\Delta n_{2,U}$ = 0.013 × 10^{-19} m^2/W. This gives a reduction in $\Delta n_{2,U}$ by a factor of 1.9 compared to fitting the two single-arm Z-Scans individually and then subtracting their n_2 values, and a factor of 1.8 compared to fitting the subtraction of the two sequential scans as shown in Figure 27 (b). These reductions are approximately equal as expected, the only difference coming from the high-pass filtering of the data sets. At this wavelength the solution shows considerable 2PA. The OA Z-Scan is shown in Figure 27 (b) along with the 2PA fit with q_0 = 0.11, or $\alpha_{2,U}$ = 0.013 cm/GW. Dividing this OA signal from the CA signal of the solution in Fig. 5(a) yields $n_{2,S}$ and $n_{2,V}$ of 1.05 × 10^{-19} m^2/W and 1.4 × 10^{-19} m^2/W for the solution and toluene, respectively. The difference in the values agrees

with the $n_{2,U}$ = -0.35 × 10^{-19} m^2/W ($\Delta\phi_0$ = -0.25) of the subtracted curve of Figure 27 (d), thus showing the agreement between measurements with the single-arm and dual-arm techniques when the signal is far enough above the noise. Correspondingly, the enhancement of SNR is 1.9× for the dual-arm technique compared to the single-arm technique. Again, a two parameter fit to the data of Figure 27 (d) gives the same $\alpha_{2,U}$ as the OA Z-Scan. Note that the noise level of the OA Z-Scan is approximately the same as that of the dual-arm as shown in Figure 27 (b) and Figure 27 (d).

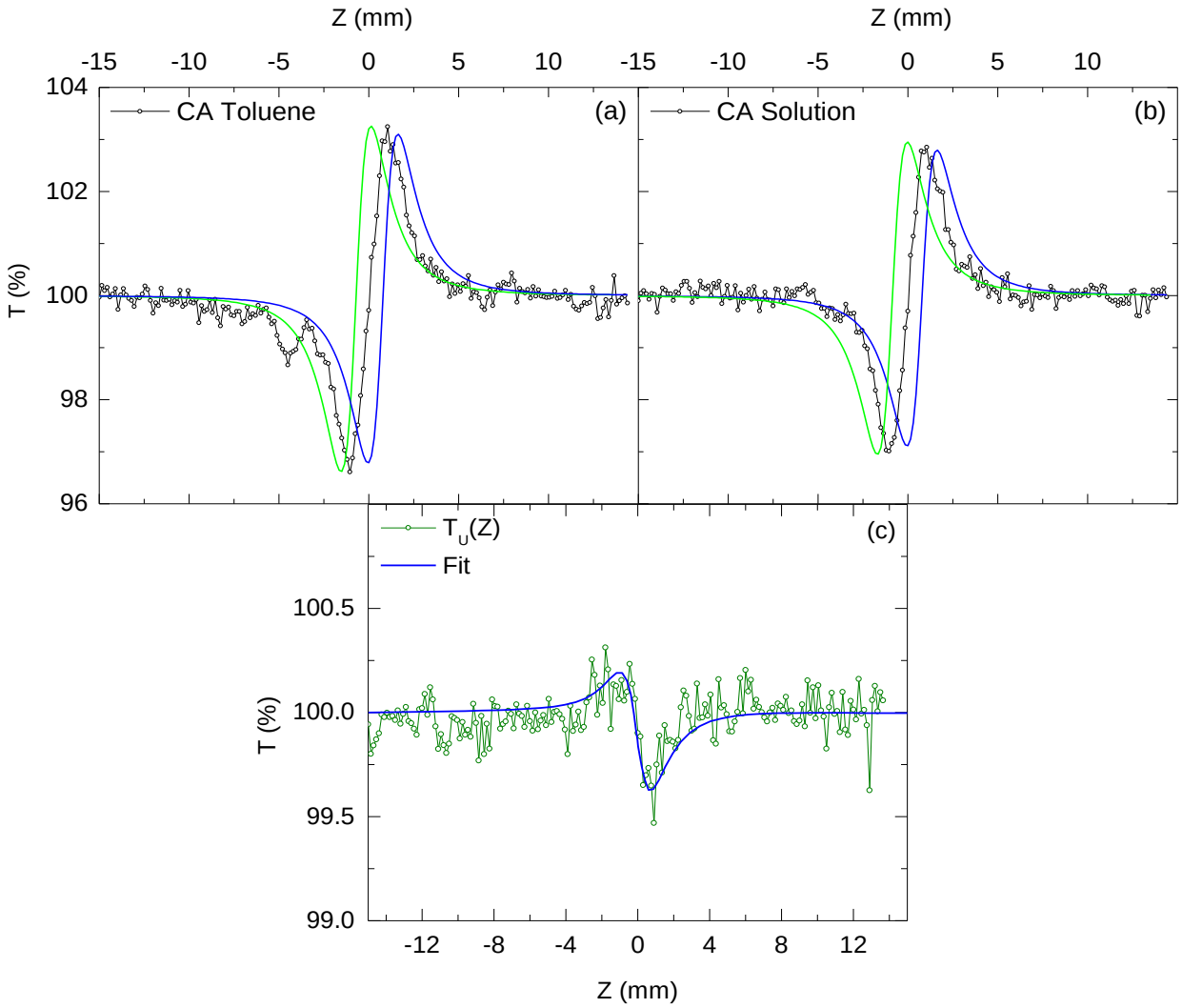

Figure 28: CA DA Z-scans at λ = 880 nm, E = 13 nJ, C = 0.60 mM, , S = 0.33, and I_0 = 22 GW/cm^2 for (a) toluene (open black circles) and (b) solution (open black circles) along with independent fits for $n_2 - \Delta n_2$ (solid blue line) and $n_2 + \Delta n_2$ (solid green line) ; (c) $T_U(Z)$ (open green squares) of SD-O 2405 and fit (solid blue line) with $\Delta\phi_0$ = -0.023, q_0 = 0.0020.

Figs. 6(a) and 6(b) show DA Z-scans for the solvent and solution, respectively, at λ = 880 nm at C = 0.6 mM. At this wavelength and irradiance, ΔT_{p-v} from the solvent and solution are similar. To illustrate how important it is to determine $n_{2,U}$ by the subtract-fit method as opposed

to the fit-subtract method, especially for small signals, we analyze this data as if these were single-arm Z-scans even though they were taken using the dual-arm technique. The best fit for $n_{2,V}$ and $n_{2,S}$ in Fig. 6(a) and 6(b) is 1.63 × 10^{-15} cm^2/W and 1.47 × 10^{-15} cm^2/W, respectively. Applying a high-pass filter to the data in Fig. 6(a) and 6(b) yields δ_V = 0.16% and δ_S = 0.16%, which corresponds to a $\Delta n_{2,V}$ = 0.040 × 10^{-15} cm^2/W and $\Delta n_{2,S}$ = 0.040 × 10^{-15} cm^2/W. Upper and lower bound fits for $n_2 \pm \Delta n_2$ are also shown in Figs. 6(a) and 6(b). Given the noise values, it could be reasonable to report a value of $n_{2,V} \pm \Delta n_{2,V}$ or $n_{2,S} \pm \Delta n_{2,S}$ which would yield a range of values for $n_{2,U}$ from -0.080 to -0.24 × 10^{-15} cm^2/W when subtracting the extrema values, i.e. up to 50% error. For the case of simultaneous subtraction and then fitting the resultant signal (Fig. 6(c)), the best fit for $n_{2,U}$ is -0.15 × 10^{-15} cm^2/W. Taking a high-pass filter yields δ = 0.11% for $T_U(Z)$ which corresponds to $\Delta n_{2,U}$ = 0.026 × 10^{-15} cm^2/W. The uncertainty is 17%, an improvement of nearly three times compared to fitting the Z-scan signals independently. Therefore, it is important to reduce the fitting error by fitting the subtraction rather than the solution and solvent independently specifically in cases where $\Delta T_{p-v,S} - \Delta T_{p-v,V}$ is close to the amplitude of the noise levels. Of note, the $\alpha_{2,U}$ reported in Fig. 6(c) is too small to determine at this irradiance with the OA Z-scan, thus the value is reported from two-photon fluorescence measurements [70] and verified by OA Z-scans performed at higher irradiances.

Figure 29 shows the dispersion of NLR and spectrum of 2PA in terms of cross sections defined as $\delta_{NLR} = \hbar\omega k_0 n_{2,U}/N$ (refractive Göppert-Mayer, RGM) [71] and $\delta_{2PA} = \hbar\omega\alpha_{2,U}/N$ (Göppert-Mayer, GM) where *N* is the concentration in molecules/m^3 of SD-O 2405 using a 0.6

mM concentration measured by dual-arm Z-Scan. The units of GM and RGM are 10^{-50} $cm^4 \cdot s \cdot molecule^{-1} \cdot photon^{-1}$.

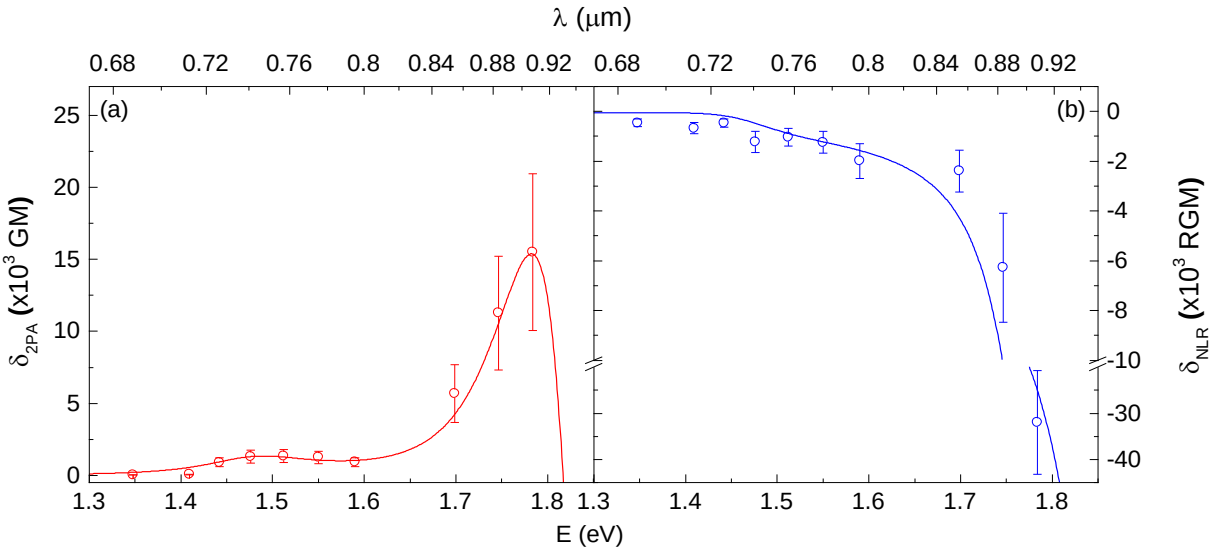

Figure 29: (a) 2PA cross section (open red circles) and three level SOS fit (solid red) vs. wavelength and incident photon energy and (b) NLR cross section (open blue circles) and three level SOS fit (solid blue) vs. wavelength and incident photon energy with the vertical axis expanded for SD-O 2405 measured by the DA Z-Scan technique.

The experimental results agree with the theoretical calculation results based on a three-level sum-over-states model described in Section 1.1.1.7. The $n_{2,U}$ fits of the solute at wavelengths from 800 nm to 920 nm range from -0.1 to -0.25 x 10^{-15} cm^2/W (corresponding to δ_{NLR} from -500 to -1250 RGM).

Comparing the DA Z-Scan measurements against single arm measurements, the DA Z-Scan allows for determination of n_2 farther out into the IR as seen in Figure 30.

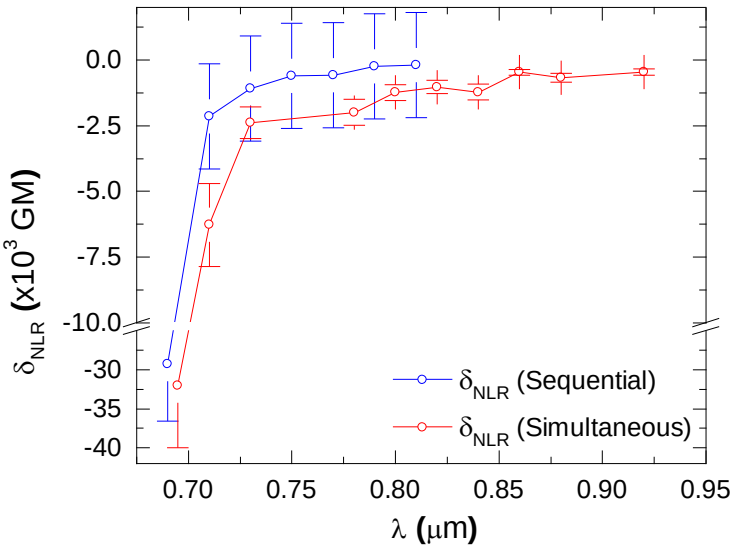

Figure 30: Comparison of nonlinear spectra of single arm and DA Z-Scan techniques. The DA Z-Scan techniques allows for determination of n_2 farther into the IR.

From our dual-arm measurements $n_{2,U}$ remains negative across the wavelengths measured. Given these small magnitudes, in the single-arm Z-Scan technique, any small dispersion of the solvent over the wavelength range could be buried under the noise floor of the Z-Scan signal, which, if not taken into account, could erroneously result in an incorrect or even positive $n_{2,U}$. Hence another advantage of the DA Z-Scan technique is that neither the dispersion of $n_{2,V}$ nor its absolute value need to be known. In the case that this information is required, it can be readily determined through fitting of $T_V(Z)$. The DA Z-Scan technique automatically eliminates any such variations in the solvent nonlinearity, so that any error in determining $n_{2,V}$ is not transferred to determining that of the solute.

3.1.4. Application - Thin Films

Another application in which the DA Z-Scan is beneficial is determining the nonlinear properties of thin films. Thin films are often deposited on a substrate whose signal can be larger than that of the film, due to the very short path length of the film (typically a few microns or less) compared to the substrate (up to 1 mm). In this case, removing the nonlinear background due to the substrate is essential for proper characterization of the film nonlinearity. To examine the performance of the DA Z-Scan for this application, we scan a 3 μm film of ZnO deposited on 1 mm of quartz at 780 nm at an irradiance of I_0 = 260 GW/cm^2 as shown in Figure 31.

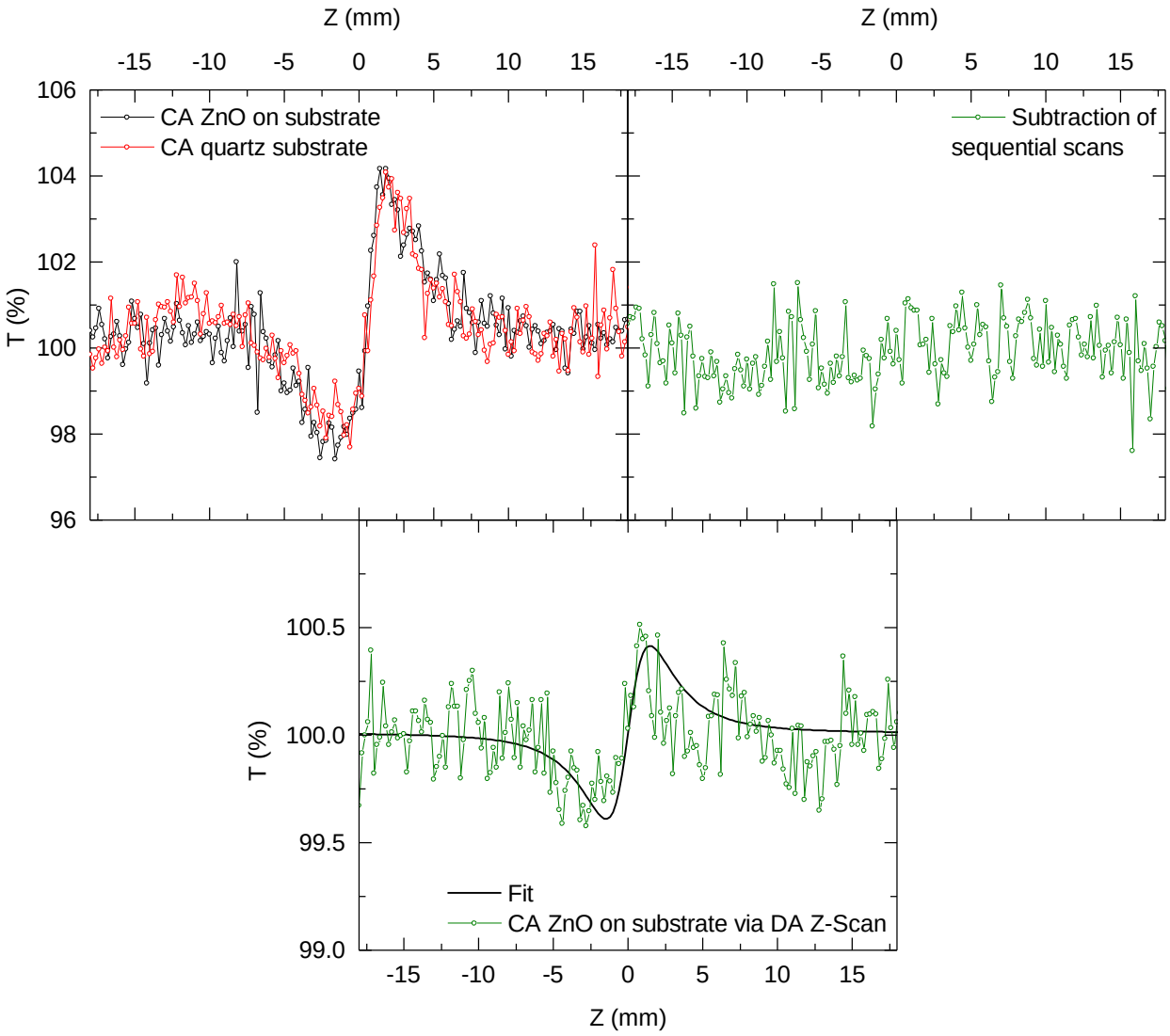

Figure 31: (upper left) Sequential single arm CA Z-Scans of ZnO on quartz substrate (black) and quartz substrate alone (red) and (upper right) subtraction of sequential scans in left figure. Note that the signal is masked by the uncorrelated noise such that n_2 cannot be determined. (lower) CA scan of ZnO via DA Z-Scan (green) and fit (black) with $n_2 = 10 \times 10^{-15}$ cm^2/W.

In this case, subtraction of the sequential scans shows only the noise. As in the case of SD-O 2405 in toluene showed in Figure 26, the signal of the ZnO film is buried in the uncorrelated

noise such that determination of n_2 is not possible. Using the DA Z-Scan allows the signal of the ZnO film to be extracted and determined as n_2 = 10 × 10^{-15} cm^2/W. This matches bulk measurements and the two band parabolic model value of 12 × 10^{-15} cm^2/W [15].

To determine the performance of the DA Z-Scan for thin films, we compare the peak phase change of the substrate and film $\Delta\phi_{0,quartz}/\Delta\phi_{0,ZnO}$ = 8.3, indicating that phase changes nearly an order of magnitude smaller than the substrate can be extracted.

3.2. Beam Deflection

While the degenerate Z-Scan is a simple and sensitive measurement technique for NLR and NLA, a single-beam technique cannot determine the nondegenerate nonlinearities, temporal dependence or the off diagonal elements of $\chi^{(3)}$. Understanding these aspects of the phenomena require the use of a two beam technique.

Other two beam techniques have been used, although these are known to have drawbacks. Two-color Z-scan [57, 72] requires careful beam alignment to ensure collinearity and identical placement of the beam waists. Cross-induced beam deformation [48, 73] and time division/spectral interferometry techniques [74, 75] requires very precise alignment and are more sensitive to environmental perturbations. It is also more flexible than OKE, which measures only the induced birefringence.

Position sensitive bi-cell detectors were previously used in Kerr lens measurements to determine the NLR. The techniques detect the spot size change of the probe beam on the detector,

with the probe and excitation beams aligned concentrically at the sample [76, 77]. However, these techniques were limited to relative measurement in materials without NLA.

What we would like is a way to measure the temporal dynamics of the nondegenerate, polarization dependent real and imaginary parts of $\chi^{(3)}$ in a straightforward, easy to implement experiment. By modifying a previously utilized technique, photothermal beam deflection, for ultrafast nonlinearities we have developed such a technique, the Beam Deflection (BD) technique.

Photothermal beam deflection is a commonly used technique for measuring small absorption from the induced thermal lensing caused by an excitation beam [78-80]. Typically, a strong probe is absorbed in a medium, causing a thermally induced index gradient. This index gradient is sampled with a weak probe beam whose deflection is measured. Various geometries have been used to induce the deflection of the probe beam with Spear et al [81] employing both cross and co-propagating beams, while Sell et al [82] has utilized the "mirage effect" caused by thermal heating of the air directly above the sample.

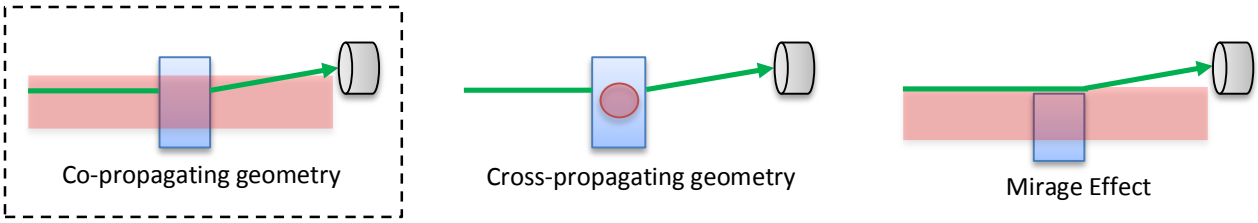

Figure 32: Co-propagating, cross propagating and mirage effect configurations for photothermal beam deflection. We will modify the co-propagating geometry for ultrafast nonlinearities.

In this work we modify the co-propagating geometry for application to measuring ultrafast nonlinearities.

3.2.1. Experimental Apparatus

The experimental apparatus involves a very simple modification to a standard excite-probe setup as described in Section 2.2.3.

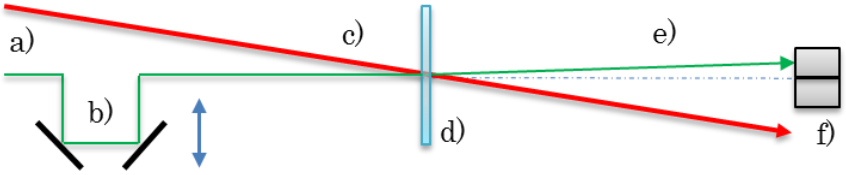

Figure 33: BD schematic. (a) probe beam (b) delay stage (c) excitation beam (d) sample (e) deflected beam (f) segmented bi-cell detector.

The excitation and probe beams are first attenuated and spatially filtered to ensure a Gaussian spatial profile. In the case of short pulse durations (τ < 50 fs FWHM) reflective neutral density filters and telescopes are used to avoid chirping the beams by propagating through dispersive material. As an example a typical polarizer has approximately 8 mm of Schott BK7 glass which stretches the 35 fs (FWHM) output of the Coherent Elite Duo from 35 to 50 fs (FWHM).

After the spatial filters set of wave plates is used to control the polarization of each beam, allowing for studies of the anisotropy of the nonlinear effects. A delay line is used to temporally delay the excitation beam. Both the sample and detector are mounted on 3-D stages to allow for precise translation.

The deflection of the beam is measured by an OSI Optoelectronics QD50-0-SD quad-segmented diode connected to two lock-in amplifiers, one to measure the difference and the other

to measure the total signal. The outputs are digitized by a National Instruments NI-6361 data acquisition card installed in a Personal Computer (PC).

The QD50-0-SD consists of a zero-bias silicon diode operated in photoconductive mode segmented into four sections, as seen in Figure 34.

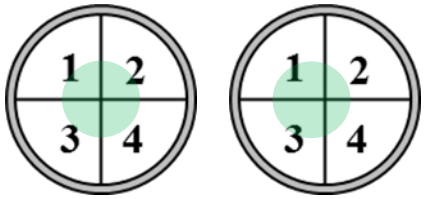

Figure 34: (left) Quad cell detector schematic with probe beam centered on quad cell so that $\Delta E/E = 0$, (right) probe shifted on quad cell so that $S = \Delta E/E > 0$.

The segmentation of the diode allows it to measure very small beam displacements, which will prove critical to our experiments. Each section has an independent output channel which is then converted from current to voltage using four gain matched transimpedence amplifiers. The voltage signals are then processed to give three outputs, left minus right $\Delta V_{L-R} = (V_1 + V_3) - (V_2 + V_4)$, top minus bottom $\Delta V_{T-B} = (V_1 + V_2) - (V_3 + V_4)$, and total $V_T = V_1 + V_3 + V_2 + V_4$. These voltages are then amplified by a factor of 10^4 using gain matched low noise amplifiers.

In order to detect small deflections a lock-in amplifier is used. The lock-in amplifier works on the principle of phase sensitive detection. This takes advantage of the tendency of the noise to be distributed over a wide frequency range. By modulating the signal by use of a mechanical chopper and band pass filtering in a narrow window about the modulation frequency, much of the noise can be eliminated, allowing for extraction of signals as low as one part in 10^5. In our experiment we will make use of two lock-in amplifiers, one for detection of the signal and and one to monitor the low frequency drift in the energy output of the laser.

The experimental procedure is as follows. First, the sample is placed at the beam waist of the probe. This is done by performing an open-aperture Z-Scan using a material with a large NLA such as ZnSe. The beam waist location is determined by finding the Z position of minimum transmission. Next, a knife edge scan is performed on both the excitation and probe beams at the sample plane to determine the spot sizes. By adjusting the collimation optics, $w_e(z)$ can be set to three to five times that of $w_{0,p}$, which provides a good balance of responsivity and linearity of the index gradient. Once the spot sizes are set the beams are overlapped spatially and temporally with the aid of a long lifetime nonlinear absorber such as Silicon Napthocyanine (SiNC). Once zero delay is found the SiNC is replaced with the sample under study and the detector is centered on the probe beam by adjusting its position until $\Delta V_{L-R} = \Delta V_{T-B} = 0$. The excitation beam is then adjusted in the $\hat{x}$ direction until the maximum deflection signal is achieved, which corresponds to placing the probe at the position of maximum index gradient ($x = w_e/2$) as shown in Figure 36. Once the proper spatial and temporal overlap of the excitation and probe is achieved, data is recorded while the delay stage is moved to adjust the temporal delay of the two pulses.

After initial set-up and alignment, the experiment is calibrated using a quartz sample. The nonlinear response of quartz is composed primarily of the ultrafast electronic response, so that the deflection signal follows the cross correlation of the pulses. If the pulse duration of the excitation is known, the pulse duration of the probe can be determined using the relation $\tau_c^2 = \tau_p^2 + \tau_e^2$, where τ_c is the measured cross correlation of the pulses. In addition, since n_2 of quartz is well established and independent of pulse duration, the calibration of the system can be verified.

3.2.2. Theory and Analysis

In order to develop the theory of the BD technique, we will start with a simple approximation of a thin prism without NLA. We will then consider NLA separately, after which we will develop a theory that can account for Group Velocity Mismatch (GVM). In this analysis we will often perform calculations to illustrate the performance of the BD technique. When referring to typical BD parameters, we will use these parameters given in Table 4 unless otherwise specified.

Table 4: Typical BD parameters used for calculations.

	Excitation beam (e)	Probe beam (p)
Pulse energy (E)	100 nJ	0.1 nJ
Wavelength (λ)	780 nm	650 nm
Spot size (w, HW1/e^{2}M)	130 μm	40 μm
Pulse duration (τ, FWHM)	170 fs	120 fs
Linear index (n)	1.5	1.5
Path length (L)	1 mm	
Sample to detector distance (d)	10 cm	
NLA coefficient (α_2)	0.5×10^{-11} m/W ($q_0 = 0.1$)	
NLR coefficient (n_2)	1.0×10^{-19} m^2/W ($\Delta\phi_0 = 0.02$)	

3.2.2.1. Thin Prism

For the simplest case, consider a spatially and temporally Gaussian excitation and probe beam given in Eq. (3.12). The excitation beam induces an index gradient in a material, and a probe beam that traverses through the gradient.

$$I_e(x,y,t) = I_{0,e}\, exp\left(-\frac{2(x^2+y^2)}{w_e^2} - \frac{t^2}{\tau_e^2}\right)$$
$$I_p(x,y,z,t,\tau_d) = I_{0,p}(z)\, exp\left(-\frac{2(x^2+y^2)}{w_p(z)^2} - \frac{(t-\tau_d)^2}{\tau_e^2}\right) \quad (3.12)$$

Where $I_0(z) = 2E/(\pi^{3/2} w(z)^2 \tau)$ is the peak irradiance, t is the time, τ_d is the delay between the excitation and probe, τ is the HW1/eM irradiance temporal pulse duration, $w(z)$ is the HW1/e^2M spot size and the subscripts e and p refer to the excitation and probe beams, respectively.

As in the case of the thin sample approximation of the Z-Scan, assuming that there is negligible NLA, the sample is much thinner than the Rayleigh ranges of the beams, and that the excitation beam is undepleted and the probe beam is weak, we can approximate that the irradiance profile of the beams remains unchanged throughout the sample. Furthermore if we assume no GVM so that the beams do not walk through each other in time, we can approximate this case as a simple prism that deflects the beam an angle θ. The deflection angle due to the index gradient within a material once the beam has propagated through the material is

$$\theta = \int_0^L \nabla n_p(x,y,t) ds \approx \nabla n_p(x,y,t) L, \quad (3.13)$$

as derived in Appendix A. Here θ is the deflection angle as seen from outside the material and $n_p(x, y, t)$ is the spatially and temporally varying index of the material experienced by the probe. The integral is taken over the beam path, which for a the case of a thin sample and small deflection can be approximated as the sample thickness L.

Assuming that the probe spot size is small compared to that of the excitation beam at the plane of the sample ($w_{p,0} \ll w_e$), we can approximate that the index gradient experienced by the probe is linear, and hence the probe experiences only a deflection without significant alteration of the irradiance profile. To determine the minimum ratio $R = w_e/w_{p,0}$ required, we calculate the $\hat{x}$ direction slope of the excitation beam weighted over the probe irradiance profile.

$$\langle I'_e(x_0 = w_e/2)\rangle = \frac{\int_{-\infty}^{\infty}\int_{-\infty}^{\infty} \frac{\partial I_e(x,y,0)}{\partial x} I_p(x - w_e/2, y, 0)dx\,dy}{\int_{-\infty}^{\infty}\int_{-\infty}^{\infty} I_p(x - w_e/2, y, 0)dx\,dy} \tag{3.14}$$

The probe has been shifted to the point where the slope of the index gradient is maximum, yielding the maximum deflection. For a Gaussian excitation this occurs when the probe is offset from the excitation beam a distance $x_0 = w_e/2$.

We would like to find R such that our approximation of a linear slope is arbitrarily close to the weighted average slope, $\Delta I'_e = 1 - \langle I'_e(w_e/2)\rangle / I'_e(w_e/2,0,0)$. Doing so yields

$$\Delta I'_e = 1 - \frac{e^{-\frac{1}{2+2R^2}}(1 + R^2)^{3/2}}{R^3}. \tag{3.15}$$

As we expect, this expression depends only on the ratio of the spot sizes at the sample plane. Numerically solving for a 10% error gives us a minimum spot size ratio R_{min} = 3.2.

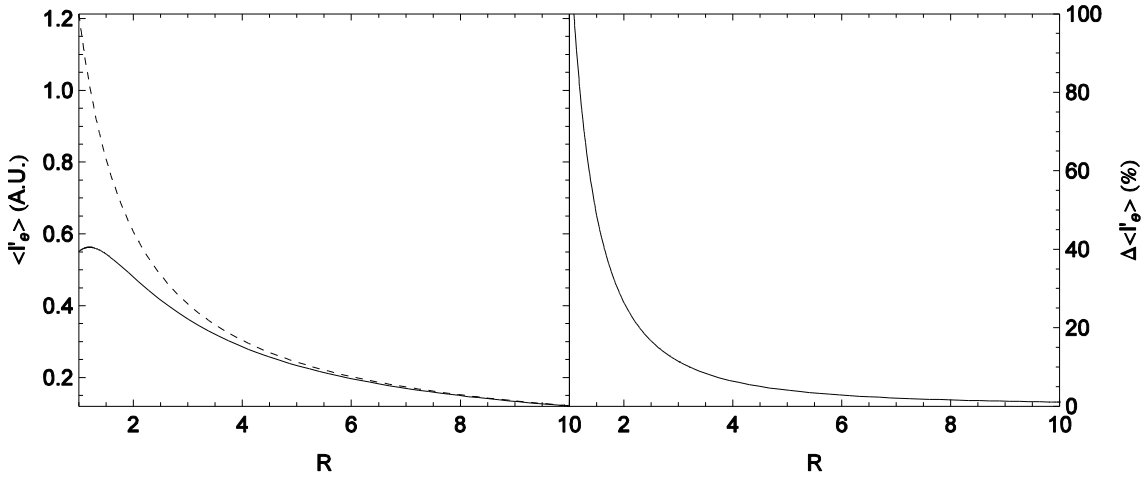

Figure 35: (left) Weighted excitation slope weighted over probe profile (solid) and linear approximation of slope (dashed) of excitation beam at the point of maximum slope vs. R. (right) Error in linear approximation of slope vs. weighted slope vs. R.

We have set the ratio for our typical experimental parameters to be 3.25. Experimentally, it is usually quite tedious to target a specific value of R, so $R_{min} < R < 5$ is considered acceptable, so long as the excitation pulse energy is high enough to generate the needed irradiance at the sample plane.

Another condition imposed by the thin prism approximation is that the angle between the excitation and probe is sufficiently small so that the probe does not move off of the excitation as it propagates through the sample. To determine the limits of this angle we calculate the weighted slope over the probe on the front and back of the sample.

$$\langle I'_e(w_e/2)\rangle = 2\frac{2e^{-\frac{w_e^2}{2(w_e^2+w_p^2)}}w_e^2}{(w_e^2+w_p^2)^{3/2}} \tag{3.16}$$

$$\langle I'_e(w_e/2 + L\theta)\rangle = 2\frac{e^{-\frac{(w_e+2L\theta)^2}{2(w_e^2+w_p{}^2)}} w_e(w_e + 2L\theta)}{(w_e{}^2 + w_p^2)^{3/2}} \tag{3.17}$$

where $\langle I'_e(w_e/2)\rangle$ is the weighted slope over the probe on the front of the sample and $\langle I'_e(w_e/2 + L\theta)\rangle$ is the weighted slope on the back of the sample. The ratio of the two is

$$\Delta I'_e(\theta)_{F-B} = \frac{\langle I'_e(w_e/2)\rangle}{\langle I'_e(w_e/2 + L\theta)\rangle} = 1 - \frac{e^{\frac{2L\theta(w_e+L\theta)}{w_e^2+w_p^2}} w_e}{w_e + 2L\theta} \tag{3.18}$$

For typical experimental parameters, in order that $\Delta I'_e(\theta)_{F-B}$ < 10%, θ should be no more than 1.7˚, which is not difficult to achieve.

These two additional conditions regarding the ratio of the spot sizes and angle between the beams in addition to the conditions contained in the thin sample approximation comprise the "thin prism approximation" that we will be using throughout this analysis.

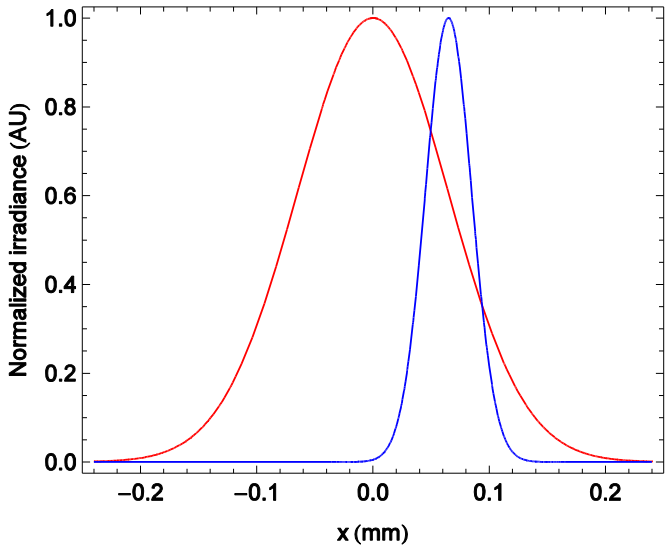

Figure 36: Overlap of excitation (red) and probe (blue) beam for maximum deflection for typical BD parameters given in Table 4.

Generally speaking, the index change is the convolution of the response function with the excitation irradiance [83]

$$\Delta n_p(x,y,t) = R(t) \otimes I_e(x,y,t) = \int_{-\infty}^{\infty} I_e\,(x,y,t-t')R(t')dt', \tag{3.19}$$

where $\Delta n_p(x,y,t)$ is the index change induced by the excitation irradiance. The deflection angle at the peak slope of the index gradient is

$$\theta(t) = \theta(w_e/2\,,0,t) = \frac{2L}{w_e\sqrt{e}}\Delta n_p(t), \tag{3.20}$$

where $\Delta n_p(t) = \Delta n_p(w_e/2\,,0,t)$ is the induced index change at location of the peak slope of the index gradient.

Propagating the deflected probe beam, the irradiance at the detector is

$$I_p(x,y,d,t,\tau_d) = I_{0,p}(d)\ exp\left(-\frac{2\left(\left(x+\Delta S(t)\right)^2+y^2\right)}{w_p(d)^2} - \frac{(t-\tau_d)^2}{\tau_e^2}\right), \tag{3.21}$$

where d is the distance from the sample to the detector and $\Delta S(t) = d\,\theta(t)$ is the lateral translation of the probe on the detector. The power incident on the left side of the detector is

$$\begin{aligned} P_{left}(t,\tau_d) &= \int_{-\infty}^{\infty}\int_{-\infty}^{0} I_p(x,y,d,t,\tau_d)dxdy \\ &= \frac{E_p\left(1-erf\left(\frac{\sqrt{2}\,\pi\,w_p\,\Delta S(t)}{d\,\lambda_p}\right)\right)exp\left(-\frac{(t-\tau_d)^2}{\tau_p}\right)}{2\sqrt{\pi}\,\tau_p}. \end{aligned} \tag{3.22}$$

The power incident on the right side of the detector is

$$P_{right}(t,\tau_d) = \int_{-\infty}^{\infty}\int_{0}^{\infty} I_p(x,y,d,t,\tau_d)dxdy$$
$$= \frac{E_p\left(1+erf\left(\frac{\sqrt{2}\,\pi\, w_p\, \Delta S(t)}{d\,\lambda_p}\right)\right)exp\left(-\frac{(t-\tau_d)^2}{\tau_p}\right)}{2\sqrt{\pi}\,\tau_p}. \tag{3.23}$$

Subtracting the two gives the difference in the power received on the two sides of the detector.

$$\Delta P_p(t,\tau_d) = P_{left}(t,\tau_d) - P_{right}(t,\tau_d)$$
$$= \frac{E_p\, erf\left(\frac{\sqrt{2}\,\pi\, w_p\, \Delta S(t)}{d\,\lambda_p}\right)exp\left(-\frac{(t-\tau_d)^2}{\tau_p}\right)}{\sqrt{\pi}\,\tau_p} \tag{3.24}$$

For small deflections the error function can be approximated by a first order expansion $Erf(x) \approx 2x/\sqrt{\pi}$. From numerical analysis it can be determined the error due to this approximation is actually quite small, with a 20% deflection signal resulting in only a 1% error in the approximation. Hence, the excitation pulse energy is limited to ensure that the peak signal is no more than 20% in order to ensure the validity of the approximation.

Writing in terms of the probe power $P_p(t,\tau_d)$ and the induced index change we have

$$\Delta P_p(t,\tau_d) \cong \frac{2\sqrt{2}\, w_p\, \Delta S(t)\, E_p\, exp\left(-\frac{(t-\tau_d)^2}{\tau_p}\right)}{d\,\lambda_p\tau_p} =$$
$$P_{p,0}exp\left(-\frac{(t-\tau_d)^2}{\tau_p}\right)\frac{2\sqrt{2}\, w_p L}{\lambda_p w_e\sqrt{e}}\,\Delta n(t) = \frac{2\sqrt{2}\, w_p L}{\lambda_p w_e\sqrt{e}}\,P_p(t,\tau_d)\Delta n_p(t). \tag{3.25}$$

Integrating over time and dividing by the probe pulse energy gives us the total signal

$$\Delta E_p/E_p(\tau_d) = \frac{\int_{-\infty}^{\infty} \Delta P_p(t,\tau_d)dt}{\int_{-\infty}^{\infty} P_p(t,\tau_d)dt} = \frac{2\sqrt{2}\, w_p L}{\lambda_p w_e \sqrt{e}} \frac{\int_{-\infty}^{\infty} P_p(t,\tau_d)\Delta n_p(t)dt}{\int_{-\infty}^{\infty} P_p(t,\tau_d)dt} = \frac{2\sqrt{2}\, w_p L}{\lambda_p w_e \sqrt{e}} \langle \Delta n_p(t) \rangle. \tag{3.26}$$

where $\langle \Delta n_p(t) \rangle$ is the index change averaged over the irradiance of the probe. Note that this expression is completely general regardless of the time dynamics of the induced index change and the shape of the probe temporal profile.

The BD signal $\Delta E_p/E_p(\tau_d)$ is proportional to the convolution of the response function $R(t)$ and the excitation power $P_e(t)$ which is the induced index change $\Delta n_p(t)$, which is then cross-correlated with the probe power $P_p(t,\tau_d)$,

$$\Delta E_p/E_p(\tau_d) \propto P_p(t,\tau_d) \otimes \Delta n_p(t) = P_p(t,\tau_d) \star \big(P_e(t) \otimes R(t)\big). \tag{3.27}$$

In order to resolve the material response, we want the pulse durations to be as short as possible. The longer the pulse duration, the more the time dynamics of the material response are lost by the averaging effect of the convolution and cross-correlation operations. The width of the temporal cross correlation of the excitation and probe is the temporal resolution of the experiment, as any features of the material response function shorter than this cannot be resolved. For temporally Gaussian excitation and probe pulses in the absence of GVM, the temporal resolution is $\tau_r^2 = \tau_p^2 + \tau_e^2$.

For electronic nonlinearities the response is much faster than the excitation duration allowing us to consider the response as instantaneous ($R(t) = n_2\delta(t)$). For electronic

nonlinearities the induced index change follows the spatial and temporal profile of the excitation irradiance

$$\Delta n_p(x,y,t) = n_2 I_{e,0}\, exp\left(-\frac{2(x^2+y^2)}{w_e^2} - \frac{t^2}{\tau_e^2}\right). \tag{3.28}$$

From this we can determine the deflection angle as a function of time

$$\theta(t) = 2\, exp\left(-\frac{1}{2} - \frac{t^2}{\tau_e^2}\right)\frac{L\, n_2 I_{e,0}}{w_p}. \tag{3.29}$$

This angle is quite small, usually between 20-100 μrad for typical experimental parameters. For instantaneous nonlinearities the deflection signal can be analytically evaluated as

$$\Delta E_p/E_p(\tau_d) = \frac{\sqrt{2}}{\sqrt{\pi e}}\frac{w_{p,0} exp\left(-\tau_d^2/\left(\tau_p^2+\tau_e^2\right)\right)\Delta\phi_0}{w_e\sqrt{1+\tau_p^2/\tau_e^2}} \tag{3.30}$$

where $\Delta\phi_0 = k_0 \Delta n L$ is the induced peak phase change and $\Delta n = 2n_2(\omega_a, \omega_b) I_{0,e}$ since there are two eigenmodes, one for each beam. Note that even in the case of an instantaneous nonlinearity, the measured value of the index change will always be averaged over the temporal pulse duration of the cross correlation of the excitation and probe.

Figure 37 shows the signal as a function of delay for several values of n_2 using typical BD parameters. As expected for electronic nonlinearities, the signal follows the cross correlation of the pulses.

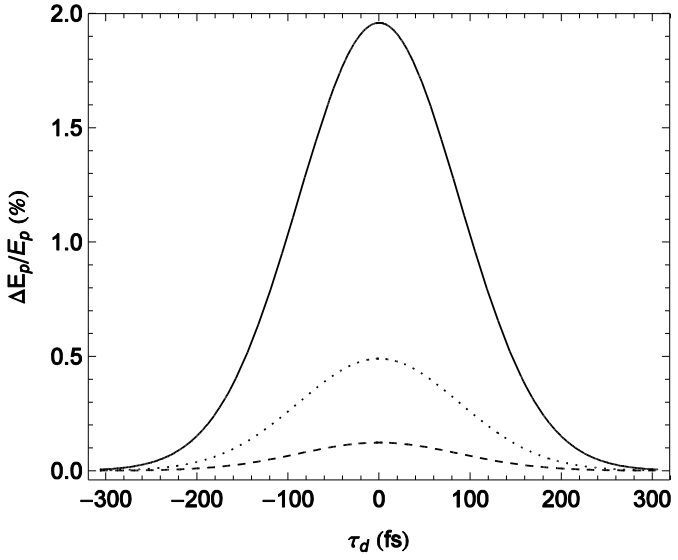

Figure 37: Signal vs. delay using simple prism approximation for typical BD parameters given in Table 4 and n_2 = 0.25 × 10^{-19} m^2/W (dashed), n_2 = 1.0 × 10^{-19} m^2/W (dotted), and n_2 = 4.0 × 10^{-19} m^2/W (solid).

Figure 38 shows the minimum phase change that can be detected as a function of the minimum distinguishable signal for typical BD parameters. With the aid of a lock-in amplifier, minimum signals on the order of 10^{-5} can be detected, giving a maximum theoretical sensitivity of λ/30,000, which corresponds to a minimum index change of 0.5 × 10^{-8} or angular deviation of 0.03 μrad. This sensitivity compares well with other measurement techniques such as the EZ-Scan, which has achieved a sensitivity of λ/20,000 [84].

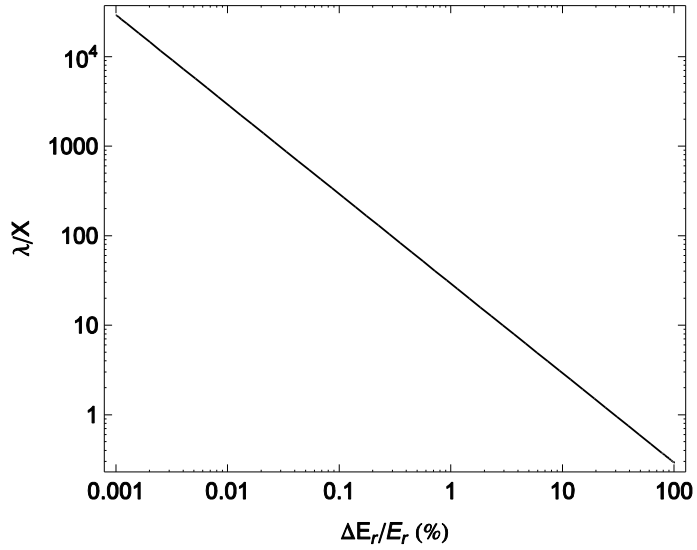

Figure 38: Maximum sensitivity vs. minimum detectable signal for typical BD parameters given in Table 4.

3.2.2.2. Thin Prism with Absorption

In the case where the sample has some NLA, the excitation beam applies not only a phase gradient but a magnitude gradient across the probe beam. This magnitude gradient attenuates one side of the probe beam more than the other, making it appear as if the probe has been translated laterally, as shown in Figure 39.

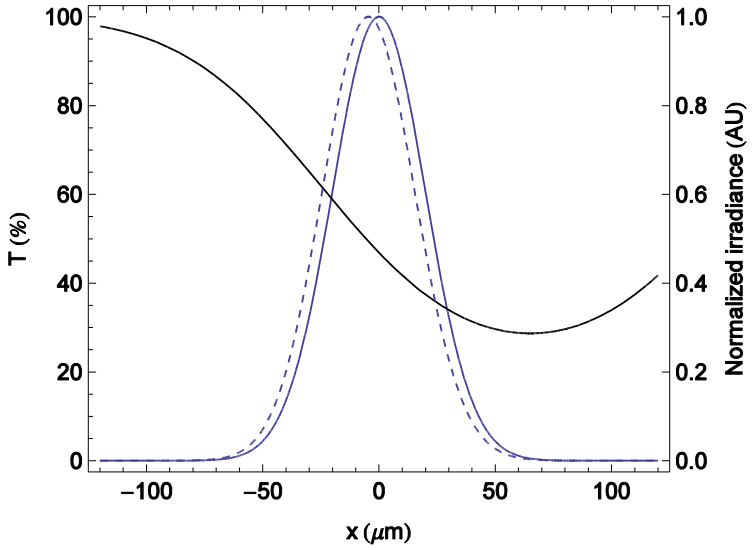

Figure 39: Effect of transmission gradient (solid black) on probe beam (solid blue). The transmission gradient makes it appear as if the probe has been laterally translated (dashed blue). Both the probe and translated probe beam have been normalized to their peak irradiance to facilitate comparison of their profiles.

Note that even for very strong absorption ($\Delta T \approx 70\%$), the probe still retains a Gaussian-like profile, appearing as if it were uniformly attenuated and laterally translated. This is true so long as the transmission gradient does not drop to zero across the probe beam, at which point the probe beam will start to become distorted and lose its Gaussian-like shape. Since we intend to work in the small signals limit ($\Delta T < 10\%$), distortion of the probe beam profile is not an issue.

This is an advantage over the beam deformation techniques in which the excitation and probe line are overlapped concentrically [73], causing the Gaussian profile of the probe beam to be deformed in the presence of NLA. This limits the application of these techniques to materials with negligible NLA, otherwise the value of n_2 determined will be inaccurate. In the case of BD,

the effect of NLA is to only shift the probe laterally without changing its profile so that the thin prism approximation analysis remains valid, once this lateral shift is accounted for.

Mathematically, the magnitude gradient due to NLA is given by

$$T(x,y,z,t) = e^{-I_e(x,y,z,t)\alpha_2 L} = e^{-I_{0,e}\alpha_2 L\, e^{-2\frac{(x-x_0)^2+y^2)}{w_e^2\left(\frac{z}{z_0}\right)^2}-\left(\frac{t^2}{\tau_p^2}\right)}}. \tag{3.31}$$

The irradiance of the probe at the detector is

$$I_{p,T}(x,y,d,t,\tau_d) = T(x,y,d,t)I_p(x,y,d,t,\tau_d). \tag{3.32}$$

This expression cannot be evaluated analytically, hence we are unable to follow the previous procedure where we integrated the irradiance on the detector to determine the deflection signal. However, approximating the transmission appropriately, we can arrive at an integrable expression which allows us to derive an analytic expression accounting for the NLA.

Assuming that the excitation beam is much larger than the probe beam, we can approximate the $\hat{x}$ direction gradient as a straight line and the $\hat{y}$ direction gradient is a flat line. This is a reasonable approximation, as shown in Figure 40.

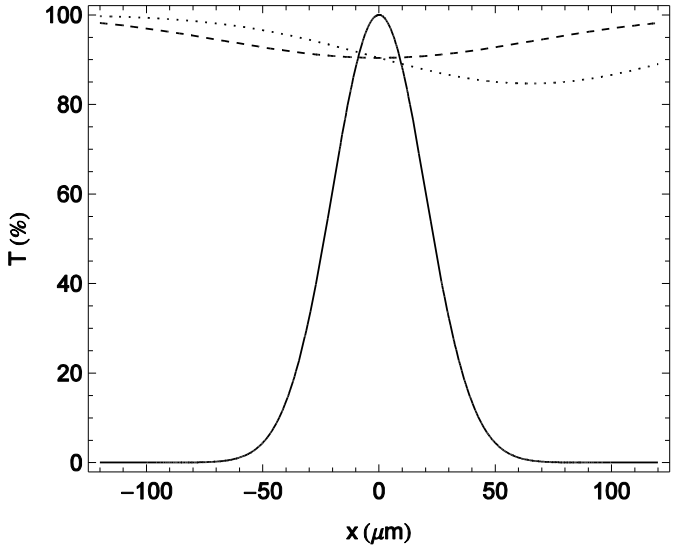

Figure 40: Probe beam (solid) and transmission profiles in $\hat{x}$ (dashed) and $\hat{y}$ (dotted) directions. The $\hat{x}$ direction gradient is approximately uniform, while the $\hat{y}$ direction gradient is approximately linear across the probe beam.

Performing this expansion yields the following expression

$$T(x,y,z,t) \cong e^{-I_{0,e}L\,\alpha_2 e^{-\frac{2\pi^2 w_{0,p}^4 x_0^2}{z^2 w_e^2 \lambda_p^2} - \frac{t^2}{\tau_p^2}}} \times \left(1 - \frac{4 I_{0,e} L\,\alpha_2 e^{-\frac{2\pi^2 w_{0,p}^4 x_0^2}{z^2 w_e^2 \lambda_p^2} - \frac{t^2}{\tau_p^2}} \pi^2 w_{0,p}^4 x\, x_0 \alpha_2}{z^2 w_e^2 \lambda_p^2} \right). \tag{3.33}$$

In order to expand $T(x,y,z,t)$ over time requires that we approximate the exponential as a power series.

$$T(x,y,z,t) \cong \left(1 - \frac{4I_{0,e}L\,\alpha_2 e^{-\frac{2\pi^2 w_{0,p}^4 x_0^2}{z^2 w_e^2 \lambda_p^2} - \frac{t^2}{\tau_p^2}} \pi^2 w_{0,p}^4 x\, x_0 \alpha_2}{z^2 w_e^2 \lambda_p^2}\right) \times \sum_0^N \frac{\left(-I_{0,e}L\,\alpha_2 e^{-\frac{2\pi^2 w_{0,p}^4 x_0^2}{z^2 w_e^2 \lambda_p^2} - \frac{t^2}{\tau_p^2}}\right)^n}{n!} \tag{3.34}$$

The irradiance of the probe on the detector is now

$$I_p(x,y,t,\tau_d) = T(x,y,d,t) I_p(x,y,d,t,\tau_d) =$$

$$e^{-\frac{2\pi^2 w_p^2\left((x-\Delta S(t))^2 + y^2\right)}{d^2\lambda_p^2} - \frac{t^2}{\tau_r^2}} \left(1 - \frac{4I_{0,e}L\,\alpha_2 e^{-\frac{2\pi^2 w_{0,p}^4 x_0^2}{d^2 w_e^2 \lambda_p^2} - \frac{t^2}{\tau_p^2}} \pi^2 w_{0,p}^4 x\, x_0 \alpha_2}{d^2 w_e^2 \lambda_p^2}\right) \times \sum_0^N \frac{\left(-I_{0,e}L\,\alpha_2 e^{-\frac{2\pi^2 w_{0,p}^4 x_0^2}{d^2 w_e^2 \lambda_p^2} - \frac{t^2}{\tau_p^2}}\right)^n}{n!}. \tag{3.35}$$

As before we integrate over space to find the power on the left and right sides of the detector, subtract to find the power difference and expand about small deflections to arrive at the following expression.

$$\Delta P(t,\tau_d) = \frac{d\, e^{-\frac{1}{2}-\frac{\pi^2 w_{0,p}^4 x_0^2}{2d^2\lambda_p^2}-\frac{t^2}{\tau_p^2}-\frac{(t-\tau_d)^2}{\tau_r^2}} I_{0,p}(d)L}{\sqrt{2\pi} w_{0,p} w_e}$$

$$\times\left(\sqrt{e}\, I_{0,e}\alpha_2 w_{0,p}^2 - 4de^{\frac{\pi^2 w_{0,p}^2}{2d^2\lambda_p^2}}\Delta n\right)\lambda_p \sum_0^N \frac{\left(-I_{0,e}L\,\alpha_2 e^{-\frac{2\pi^2 w_{0,p}^4 x_0^2}{d^2 w_e^2\lambda_p^2}-\frac{t^2}{\tau_p^2}}\right)^n}{n!} \tag{3.36}$$

Taking the integral into the sum gives us

$$\Delta E_p(\tau_d) = \frac{d\, I_{0,p}(d)L}{\sqrt{2\pi} w_{0,p} w_e}\left(\sqrt{e}\, I_{0,e}\alpha_2 w_{0,p}^2 - 4de^{\frac{\pi^2 w_{0,p}^2}{2d^2\lambda_p^2}}\Delta n\right)$$

$$\times\sum_0^N \int_{-\infty}^{\infty} e^{-\frac{1}{2}-\frac{\pi^2 w_{0,p}^4 x_0^2}{2d^2\lambda_p^2}-\frac{t^2}{\tau_r^2}-\frac{(t-\tau_d)^2}{\tau_p^2}} \frac{\left(-I_{0,e}L\,\alpha_2 e^{-\frac{2\pi^2 w_{0,p}^4 x_0^2}{d^2 w_e^2\lambda_p^2}-\frac{t^2}{\tau_p^2}}\right)^n}{n!} dt. \tag{3.37}$$

Evaluating the integral gives us the difference in energy between the two sides

$$\Delta E_p(\tau_d) = \frac{d\, I_{0,p}(d)L}{\sqrt{2\pi} w_{0,p} w_e}\left(\sqrt{e}\, I_{0,e}\alpha_2 w_{0,p}^2 - 4de^{\frac{\pi^2 w_{0,p}^2}{2d^2\lambda_p^2}}\Delta n\right)$$

$$\times\sum_0^N \frac{e^{-\frac{1}{2}-\frac{(1+n)\pi^2 w_{0,p}^4}{2d^2\lambda_r^2}-\frac{(1+n)\tau_d^2}{\tau_p^2+(1+n)\tau_r^2}}\sqrt{\pi}\left(-I_{0,e}L\,\alpha_2\right)^n \tau_p\tau_r}{\sqrt{\tau_p^2+(1+n)\tau_r^2}\,\Gamma(1+n)}. \tag{3.38}$$

While this sum does not have a closed form expression, it does converge numerically, indicating that we can just carry the summation into the final expression. Performing the same procedure as above for the total transmitted energy yields

$$E_p(\tau_d) = \frac{d^2 I_{0,p} \lambda_r^2}{2\pi w r 0^2} \sum_0^N \frac{e^{-\frac{n\pi^2 w_{0,p}{}^4}{2d^2\lambda_r^2} - \frac{n\tau_d^2}{\tau_p^2 + n\tau_r^2}} \sqrt{\pi} (-I_{0,p} L \alpha_2)^n \tau_p \tau_r}{\sqrt{\tau_p^2 + n\tau_r^2}\, n!}. \tag{3.39}$$

The transmission is defined as $T(\tau_d) = E_p(\tau_d)/E_0$, where E_0 is the energy of the probe measured in the absence of the excitation beam.

The deflection signal due to both NLR and NLA is thus

$$\Delta E_p / E_p\,(\tau_d) = \frac{\Delta E(\tau_d)}{E(\tau_d)} = \frac{L\sqrt{2\pi}\, w_{0,p}}{d\, w_e \lambda_r} \left(\sqrt{e}\, I_{0,e} \alpha_2 w_{0,p}^2 - 4de^{\frac{\pi^2 w_{0,p}^2}{2d^2\lambda_p^2}} \Delta n \right)$$

$$\times \frac{\left(\sum_0^N \frac{e^{-\frac{1}{2} - \frac{(1+n)\pi^2 w_{0,p}^4}{2d^2\lambda_r^2} - \frac{(1+n)\tau_d^2}{\tau_p^2 + (1+n)\tau_r^2}} \sqrt{\pi} \left(-I_{0,e} L\, \alpha_2\right)^n \tau_p \tau_r}{\sqrt{\tau_p^2 + (1+n)\tau_r^2}\, \Gamma(1+n)} \right)}{\left(\sum_0^N \frac{e^{-\frac{n\pi^2 w_{0,p}{}^4}{2d^2\lambda_r^2} - \frac{n\tau_d^2}{\tau_p^2 + n\tau_r^2}} \sqrt{\pi} (-I_{0,p} L \alpha_2)^n \tau_p \tau_r}{\sqrt{\tau_p^2 + n\tau_r^2}\, n!} \right)} \tag{3.40}$$

Examining the sensitivity of $T(\tau_d)$ to the number of terms in the summation N, in Figure 41 we plot $T(\tau_d)$ for 1, 2, and 11 terms using typical BD parameters.

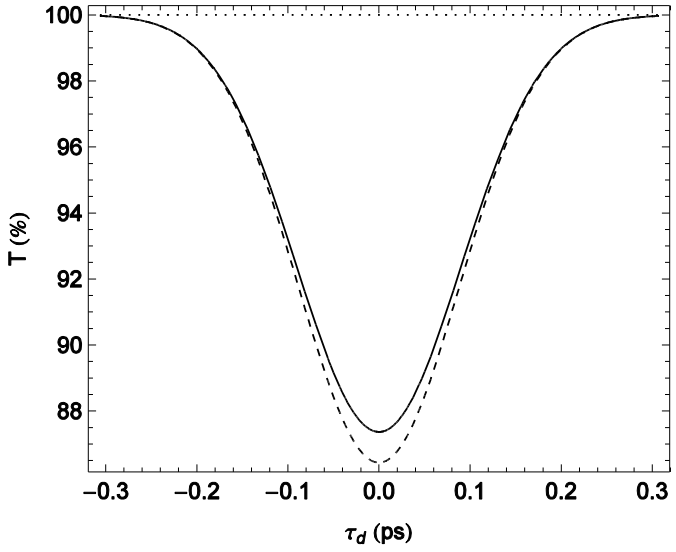

Figure 41: Transmission signal vs. delay with 1 (dotted), 2 (dashed) and 11 (solid) terms in summation using typical BD parameters given in Table 4.

The zero order expansion approximates ($N = 0$), $T(\tau_d)$ = 1, and as such is not physically reasonable. However, even using only two terms in the expansion (N = 1), the error is less than two percent. Hence, a good approximation to use when fitting $T(\tau_d)$ in order to determine α_2 is the first order expansion of $T(\tau_d) = E(\tau_d)/E_p$, where E_p is the initial pulse energy.

$$T(\tau_d) \cong 1 - \frac{4e^{-\frac{\pi^2 w_p^4}{2d^2\lambda_p^2}-\frac{\tau_d^2}{{\tau_e}^2+\tau_p^2}} E_e L\alpha_2}{\pi^{3/2} w_e^2 \sqrt{\tau_e^2+\tau_p^2}} = 1 - \frac{2e^{-\frac{z_0^2}{2d^2}-\frac{\tau_d^2}{\tau_e^2+\tau_p^2}} \tau_e q_0}{\sqrt{\tau_e^2+\tau_p^2}} \tag{3.41}$$

Examining the accuracy of the deflection signal on the number of terms in the summation, in Figure 42 we plot $\Delta E_p/E_p(\tau_d)$ due to NLR, NLA and the total for 1, 2, and 11 terms using typical BD parameters.

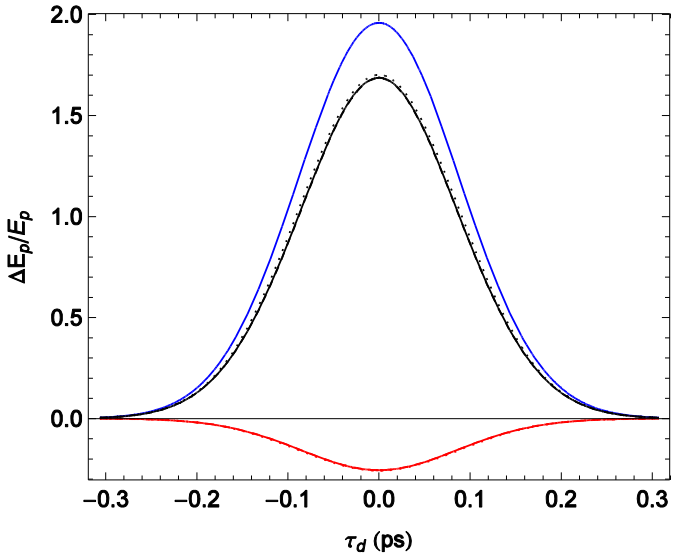

Figure 42: Deflection signal due to NLR (blue), NLA (red) and the total (black) vs. delay with 1 (dotted), 2 (dashed) and 11 (solid) terms in summation using typical BD parameters given in Table 4. Even with only one term in the summation used the accuracy of the approximation is very good, with an error < 1%.

In the case of the total deflection signal, using one term of the summation yields an error or about one percent. Hence, the zero order approximation ($N = 1$) is a reasonable approximation for the small peak transmission changes used in this example.

$$\Delta E_p/E_p\,(\tau_d) = \frac{8\sqrt{2}e^{-\frac{1}{2}-\frac{\tau_d^2}{\tau_p^2+\tau_r^2}}E_e n_2 w_{0,p} L}{\pi {w_e}^3 \lambda_r \sqrt{\tau_p^2+\tau_r^2}} - \frac{2\sqrt{2}e^{-\frac{\pi^2 w_{0,p}^4}{2d^2\lambda_r^2}-\frac{\tau_d^2}{\tau_p^2+\tau_r^2}}E_e w_{0,p}^3 \alpha_2 L}{d\,\pi\,{w_e}^3 \lambda_r \sqrt{\tau_p^2+\tau_r^2}} \tag{3.42}$$

$$= \sqrt{\frac{2}{\pi}}\frac{w_{0,p}}{w_e}\frac{\tau_p}{\sqrt{\tau_p^2+{\tau_r}^2}}\left(\Delta\phi_0 e^{-\frac{1}{2}} - q_0\frac{z_0}{d}e^{-\frac{z_0^2}{2d^2}}\right)e^{-\frac{\tau_d^2}{\tau_p^2+\tau_r^2}}$$

To examine the accuracy of Eq. (3.42) for higher transmission changes, in Figure 43 we plot the error incurred as a function of the NLA parameter.

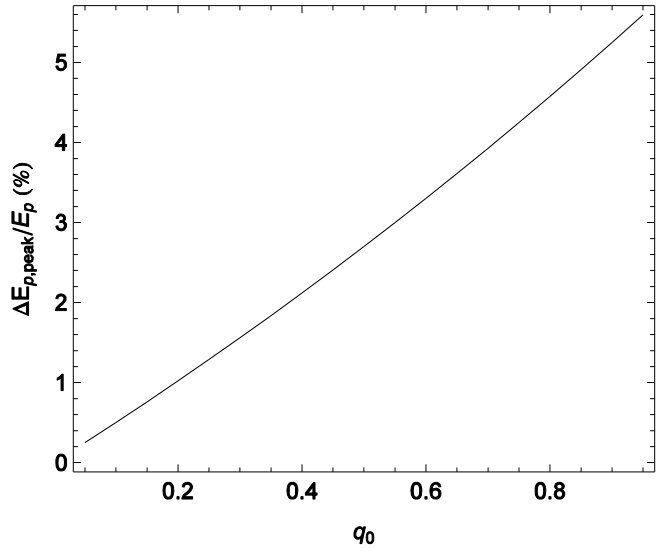

Figure 43: Error in peak deflection signal vs. q_0 using typical BD parameters given in Table 4.

Even for large peak transmission changes of 80%, the error incurred using the zero order approximation is only 5%, which less than the accuracy with which most experimental parameters are known. However, we would like to know how many terms are required for cases in which both high accuracy and large transmission changes are required, as in the case of highly nondegenerate beams where the sum of the photon energies are near the band gap. Figure 44 shows the number of terms required for an error of less than one percent as a function of the peak transmission change.

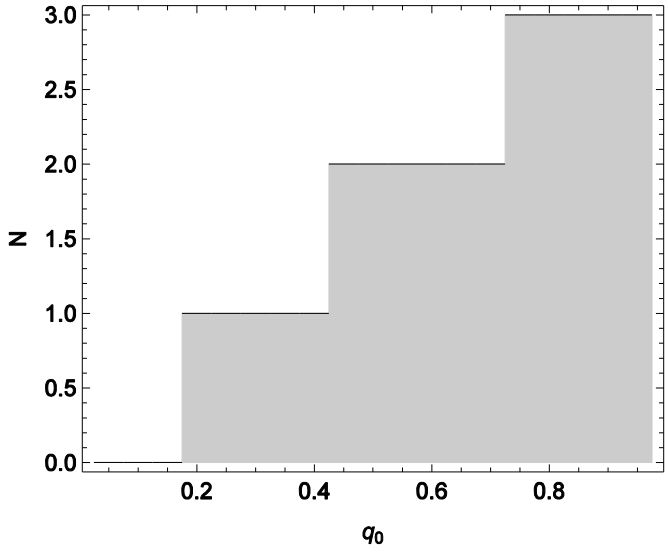

Figure 44: Summation order required for an error of less than 1% as a function of absorption parameter.

Even in the case of very high peak transmission changes (90%), the number of terms required is only four. Using Eq. (3.40) with one term (N = 0) can handle values of q_0 ~0.2, which covers most experimental situations of interest.

The approximation in Eq. (3.42) matches the results from the thin prism approximation in the case of zero absorption. In the zero order approximation, $\Delta E_p/E_p(\tau_d)$ can be separated into a phase change term ($\Delta\phi_0$) and absorption term (q_0). This can be understood as the deflection signal due to the phase change and absorption deriving from different mechanisms. The phase change term is associated with a deflection of the probe by an angle θ due to the prismatic effect, while the absorption term is associated with an apparent translation of the probe at the back of the sample due to the magnitude gradient.

Physically, we expect that as the distance from the sample to the detector increases the deflection signal due to absorption should decrease as illustrated in Figure 46. This is due to the

expansion of the beam once it leaves the sample, so that increasing the distance d from the sample to the detector will yield a larger beam on the quad cell detector. The larger the beam on the quad cell, the less sensitive the quad cell will be to a translation of the beam, as illustrated in Figure 45.

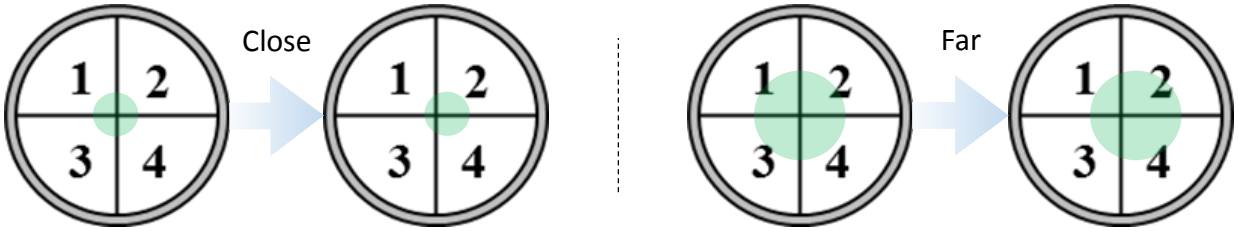

Figure 45: Effect of translation of probe beam on deflection signal. (left) Effect of translation for a small probe spot size on the detector. Most of the probe beam has been shifted to the right side of the detector. (right) Effect of the same translation for a large spot size on the detector. A smaller portion of the probe beam has been shifted to the right side of the detector. As the distance between the sample and the detector is increases, the probe spot size on the detector increases and the effect of the translation on $\Delta E_p/E_p$ is reduced.

This does not affect the NLR deflection signal, as the effect of the expansion of the beam is exactly offset by the greater translation due to the increased propagation distance.

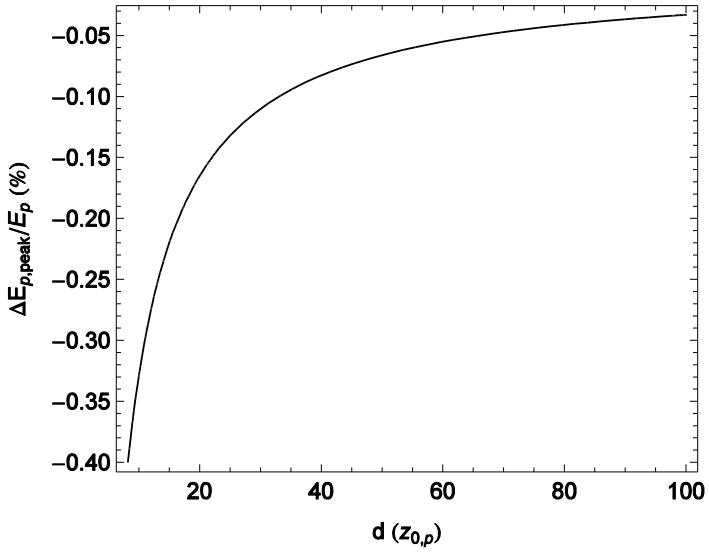

Figure 46: Deflection signal due to absorption as a function of distance from sample to detector.

This is also consistent with our understanding of physical optics, as in the far field the Fraunhofer approximation states that a shift of the beam on the source plane translates to a phase shift on the observation plane, which is not detectable by observing only the irradiance. Hence, as we approach the Fraunhofer condition, the beam shift should be increasingly less detectable.

Care must be taken when measuring samples with large NLA. If the NLA is too high, it is possible that the part of the probe beam may be fully extinguished on one side of the detector, yielding pathological results as the probe beam is no longer Gaussian. Plotting $\Delta E_p/E_{p,peak}(q_0)$, the peak deflection signal as a function of the NLA parameter we see a linear increase in the signal at first, while eventually the curve bends and eventually turns over.

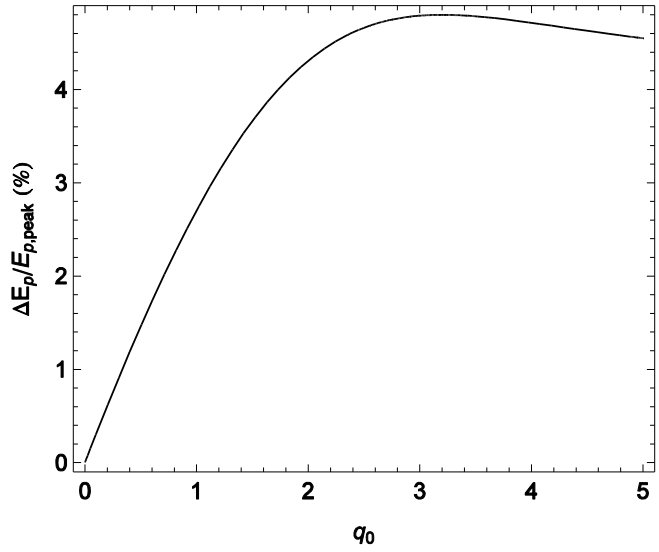

Figure 47: Peak deflection signal due to NLA vs. q_0. At high NLA the peak absorption signal is pathological due to distortion of the probe beam.

This turning over is indicative of a portion of the probe closest to the peak of the excitation irradiance profile being fully extinguished inside the sample, distorting the probe beam thus giving an incorrect value for ΔE_p. The NLA at which distortion becomes significant can be numerically determined as q_0 = 1.6. Practically, since we limit the irradiance in order to remain in small signal limit in both ΔT and $\Delta E_p/E_p$, q_0 in practice would be less than 0.3 which is well within the linear regime of $\Delta E_p/E_{p,peak}(q_0)$.

3.2.2.3. Non-Instantaneous Responses

So far we have focused on the electronic response which for our purposed can be regarded as instantaneous. However, many materials, such as liquids, have non-instantaneous responses. Here we model the response of the material as a bi-exponential decay using a pair of exponential

functions with a finite rise and decay time. The reorientation response of simple solvents (such as CS_2) can be modeled by a bi-exponential decay as the rise and decay times are governed by different processes – the rise time by the electromagnetic field strength and molecular inertia, and the decay governed by thermal randomization.

$$R(t) = \Theta(t) n_{2,eff} \left(1 - e^{-\frac{t}{t_R}}\right) e^{-\frac{t}{t_F}}. \tag{3.43}$$

where $n_{2,eff}$ is the effective nonlinear index of refraction defined as $\Delta n_p = n_{2,eff} I_e$, t_R is the rise time, t_F is the decay time and $\Theta(t)$ is the unit step function $\Theta(t) = 0$ for $t < 0$ and 1 for $t \geq 0$. This non-instantaneous response function is shown in Figure 48.

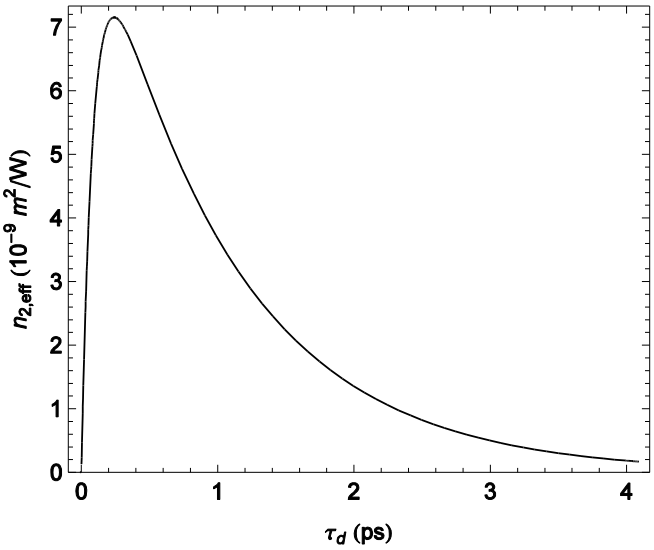

Figure 48: Non-instantaneous response function using typical experimental parameters with rise time of 100 fs (FWHM) and decay time of 1 ps.

As before, $\Delta n_p(t)$ is determined by convolving the response function with the excitation irradiance.

$$\Delta n_p(t) = \frac{1}{2} I_{0,e} n_{2,eff} \sqrt{\pi} \tau_e e^{-t\left(\frac{1}{t_F}+\frac{1}{t_R}\right)-\frac{2(x^2+y^2)}{w_e^2}+\frac{\tau_e^2}{4t_F^2}}$$
$$\left(e^{t/t_R}\left(1 + Erf\left(\frac{t}{\tau_e} - \frac{\tau_e}{2t_F}\right)\right)\right. \tag{3.44}$$
$$\left. + e^{\frac{(t_F+2t_R)\tau_e^2}{4t_F t_R^2}}\left(-2 + Erfc\left(\frac{t}{\tau_e} - \frac{(t_F+t_R)\tau_e}{2t_F t_R}\right)\right)\right)$$

For this induced index change the signal cannot be evaluated analytically. Evaluating Eq. (3.26) numerically gives us the signal as a function of delay as seen in Figure 49.

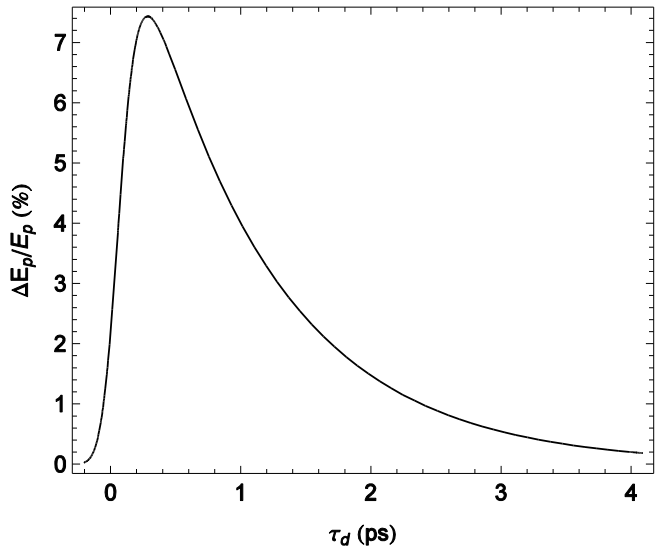

Figure 49: Deflection signal for non-instantaneous material response using parameters used in Figure 48.

This kind of signal is typical of liquids where the reorientational response is significant. However, most materials with non-instantaneous responses tend to have several response mechanisms operating. For example the total response of a linear molecule (such as CS_2) would be the sum of the electronic, nuclear and reorientational mechanisms. For all but the shortest pulse

durations, the electronic response can be considered instantaneous and modeled with a delta function. For the reorientational and nuclear responses, we use the bi-exponential decay described in Eq. (3.43). The total response is

$$R(t) = n_{2,el}\delta(t) + \Theta(t)n_{2,nuc}\left(1 - e^{-\frac{t}{t_{R,nuc}}}\right)e^{-\frac{t}{t_{F,nuc}}} + \Theta(t)n_{2,re}\left(1 - e^{-\frac{t}{t_{R,re}}}\right)e^{-\frac{t}{t_{F,re}}}, \tag{3.45}$$

where the subscripts el, nuc, and re refer to the electronic, nuclear and reorientational responses. Fitting to determine the parameters of each of the responses is difficult without separating the differing mechanisms, given the large number of parameters to determine. In the following sections we will investigate how we can separate these various mechanisms by taking advantage of temporal and polarization dependencies of their responses.

3.2.2.4. Beam Deflection Error Analysis

Since the NLA can be determined from the transmission, this additional deflection signal due to the NLA is a nuisance that can inject error into the determination of the NLR. This contamination of the NLR signal by NLA is a common to many nonlinear characterization techniques.

In the case of the Z-Scan the NLA reduces the irradiance of the beam in both the OA and CA, distorting the CA signal. This additional signal must be accounted for by either dividing by the OA signal, which works for small NLA, or adding an additional parameter α_2 to the fit of n_2.

If there is some uncertainty in the knowledge of α_2, this will inject some additional uncertainty into out knowledge of n_2.

In the case of BD, we apply Eq. (2.47) to Eq. (3.41) to arrive at the error in peak phase change $\Delta\phi_0$ from the various noise sources, including errors in q_0.

$$\begin{aligned}
&\sigma_{\Delta\phi_0}^2 \\
&= \left(\frac{\partial\Delta\phi_0}{\partial\Delta E_p/E_p(0)}\right)^2 \sigma_{\Delta E_p/E_p(0)}^2 + \left(\frac{\partial\Delta\phi_0}{\partial q_0}\right)^2 \sigma_{q_0}^2 + \left(\frac{\partial\Delta\phi_0}{\partial w_{0,p}}\right)^2 \sigma_{w_{0,p}}^2 \\
&+ \left(\frac{\partial\Delta\phi_0}{\partial w_e}\right)^2 \sigma_{w_e}^2 + \left(\frac{\partial\Delta\phi_0}{\partial z_{0,p}}\right)^2 \sigma_{z_{0,p}}^2 + \left(\frac{\partial\Delta\phi_0}{\partial \tau_p}\right)^2 \sigma_{\tau_p}^2 + \left(\frac{\partial\Delta\phi_0}{\partial \tau_e}\right)^2 \sigma_{\tau_e}^2 \\
&+ \left(\frac{\partial\Delta\phi_0}{\partial d}\right)^2 \sigma_d^2
\end{aligned} \tag{3.46}$$

Performing the derivatives and simplifying, we can write the total fractional error $\eta_{\Delta\phi_0} = \sigma_{\Delta\phi_0}/\Delta\phi_0$ as

$$\eta_{\Delta\phi_0} = \sqrt{\frac{1}{SNR^2} + \eta_{NLR}^2 - A\eta_{NLR}^2\rho + \frac{1}{4}A^2(\eta_{NLA}^2 + \eta_{NLR}^2)\rho^2}, \tag{3.47}$$

$$SNR = \frac{\sigma_{\Delta E_p/E_{p,peak}}}{\Delta E_p/E_{p,peak}}, \tag{3.48}$$

$$A = \frac{2e^{\frac{1}{2}\left(1-\frac{z_{0,p}{}^2}{d^2}\right)} z_{0,p}}{d}, \tag{3.49}$$

$$\rho = \frac{Im(\chi^{(3)})}{Re(\chi^{(3)})} = \frac{q_0}{2\Delta\phi_0} = \frac{1}{FOM}, \tag{3.50}$$

$$\eta_{NLR}^2 = \eta_{w_{0,p}}^2 + \eta_{w_e}^2 + \eta_{\tau_p}^2 + \eta_{\tau_e}^2, \tag{3.51}$$

$$\eta_{NLA}^2 = \eta_{q_0}^2 + \eta_{z_{0,p}}^2 + \eta_d^2, \tag{3.52}$$

where A is the distance attenuation factor which accounts for the reduction of the deflection signal due to NLA with distance from the sample to the detector, ρ is the ratio of the imaginary and real parts of the $\chi^{(3)}$, η_{NLR} is the total fractional error in the parameters associated with NLR signal and η_{NLA} is the total fractional error in the parameters associated with the NLA signal. Note that in the absence of NLA, the total fractional error is $\eta_{\Delta\phi_0} = (1/SNR^2 + \eta_{NLR}^2)^{1/2}$, which corresponds to the results from the Z-Scan error analysis presented in Section 2.2.4.3.

In Figure 50 we plot $\eta_{\Delta\phi_0}$as a function of η_{q_0} the case of a 10% error in each of the parameters an, SNR of 10 and $z_{0,p}$ = 2 mm, d = 18.5 cm and ρ = 50. This translates into a 25% error in q_0 and a 20% error in $z_{0,p}$.

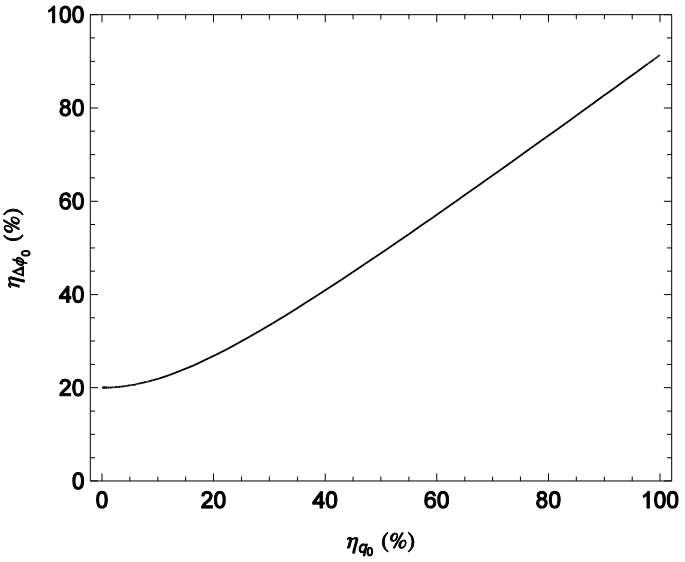

Figure 50: Error in $\Delta\phi_0$ vs. error in q_0 for SNR = 10 and 10% error in parameter knowledge (25% error in q_0 and 20% error in z_0).

Note the case where η_{q_0} = 0 there is still some error in $\Delta\phi_0$ due to the parameter errors in η_{NLR}. As we increase η_{q_0} the relationship with $\eta_{\Delta\phi_0}$ becomes linear. Hence we can define the contamination parameter C_{err} such that

$$\eta_{\Delta\phi_0} = C_{err}\,\eta_{q_0} \tag{3.53}$$

$$C_{err} = \frac{2e^{\frac{1}{2}\left(1-\frac{z_{0,p}{}^2}{d^2}\right)}z_{0,p}\rho}{d} = A\rho \tag{3.54}$$

Given that the contamination factor drops off very quickly with the ratio $z_{0,p}/d$ it is useful to consider if there is any point at which the transmission and deflection signals are effectively independent of each other, i.e. if η_{q_0} = 1 is there a value ρ such that $\eta_{\Delta\phi_0}$ is below some arbitrary tolerance. If we take this tolerance to be η_{NLR}, which is the minimum error achievable in the absence of NLA, ρ = 3.62 or FOM = 27%. Hence, for most materials of interest for AOSP applications where the objective is to maximize the FOM, T and $\Delta E_p/E_p$ are effectively independent of each other.

In Figure 51 we plot $\eta_{\Delta\phi_0}$ as a function of ρ for the same parameters as Figure 50.

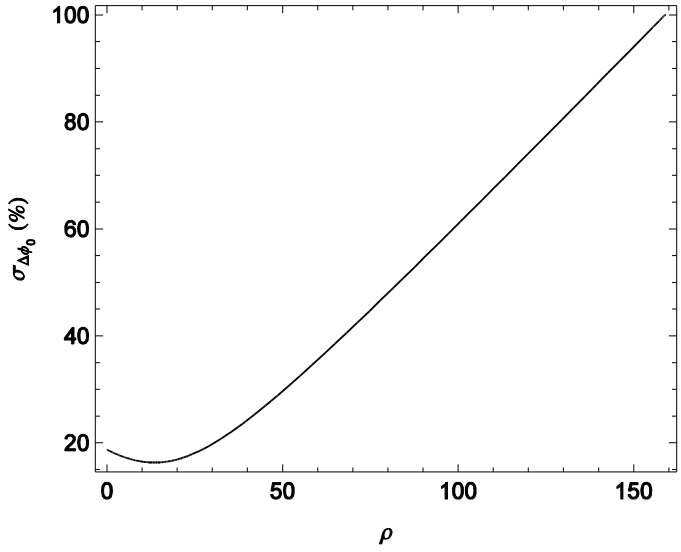

Figure 51: Error in $\Delta\phi_0$ vs. ρ for SNR = 10 and 10% error in parameter knowledge (25% error in q_0 and 20% error in z_0).

Note that there is a range of ρ such that $\eta_{\Delta\phi_0}$ is less than η_{NLR}. Over this range errors in q_0 partly offset the error in η_{NLR}, represented by the second term of (3.47). However, as ρ is further increased, the last term of (3.47) begins to dominate so that the fractional error once again increases.

As we increase ρ there comes a point at which $\eta_{\Delta\phi_0}$ = 1, meaning that the deflection signal is the same size as the standard deviation of the noise. At this point it is no longer possible to determine if $\Delta\phi_0$ is positive or negative outside of the margin of error. We will consider this to be the lower bound on the determination of $\Delta\phi_0$, which occurs at ρ_{max} = 159 or FOM_{min} = 0.6%. This is the minimum FOM that can be measured using the BD technnique.

Calculating the contamination of the Z-Scan is more difficult, since the peak CA signal due to NLR and NLA do not occur in the same Z position. Hence, unlike in BD, the NLA and NLR

signals do not add, rather the NLA signal distorts the CA signal, so that it no longer retains its valley-peak antisymmetric structure. Hence when fitting for α_2 and n_2 the shape of the CA signal must be considered, along with ΔT_{p-v}.

In the absence of NLA, the CA/OA signal has the familiar valley-peak structure seen in Figure 17 for positive nonlinearity. As the NLA is increased, the CA/OA signal begins to change from a valley-peak structure to a valley-peak-valley structure shown in Figure 52, where we plot the CA/OA signal for a fixed value of $\Delta\phi_0$ and increasing values of ρ.

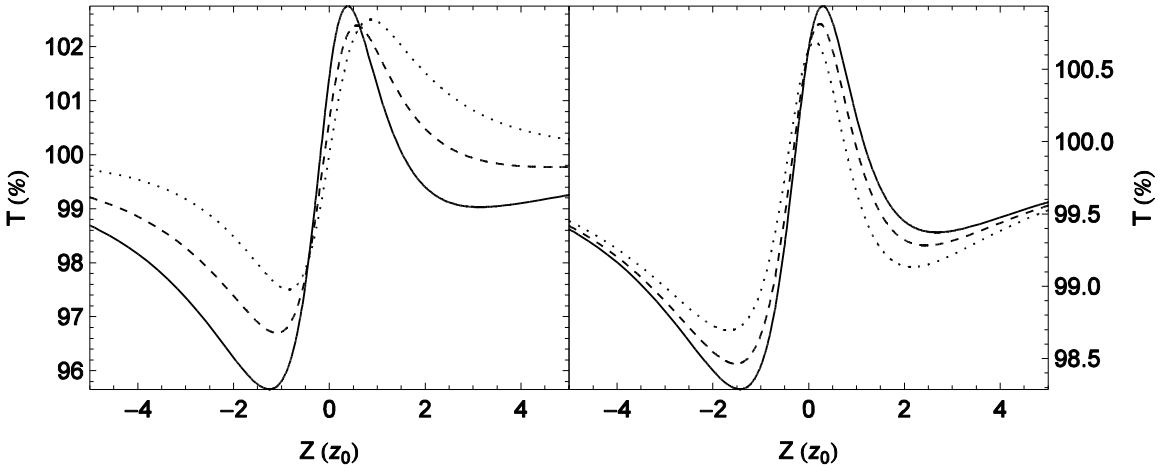

Figure 52: (left) Z-Scan CA/OA signal for $\Delta\phi_0$ = 0.12 and q_0 = 0 (dotted), q_0 = 0.28 (dashed) and q_0 = 0.56 (solid). Increasing the NLA changes the signal from a valley-peak structure to a valley-peak-valley structure; (right) Z-Scan CA/OA signal for q_0 = 0.28 and $\Delta\phi_0$ = 0.041 (solid) corresponding to ρ = 3, 0.031 (dashed) corresponding to ρ = 4 and 0.016 (dotted) corresponding to ρ = 5. As the NLA is increased the positive and negative valleys become closer together.

In the case where $\Delta\phi_0 > 0$, the negative Z valley is lower than the positive Z valley, and vice versa for $\Delta\phi < 0$. As seen in Figure 52, as ρ is increased the difference between the valley

depths $\Delta T_{V_- - V_+}$ decreases and the CA/OA trace becomes more symmetric. In the limit $\rho \rightarrow \infty$, $\Delta T_{V_- - V_+} \rightarrow 0$, so that it would no longer be possible to determine the sign of $\Delta\phi$. Numerically, we can determine at what value of ρ is $\Delta T_{V_- - V_+}$ less than the system noise (0.2%). This is equivalent to the condition that $\eta_{\Delta\phi_0}$ = 1, and is the lower bound on the detection of $\Delta\phi_0$. This can be numerically determined to occur at ρ_{max} = 19, which translates to a FOM of 5%, which is the minimum FOM that can be determined by the Z-Scan. Figure 53 shows the OA, CA and OA/CA signals at the minimum FOM limit.

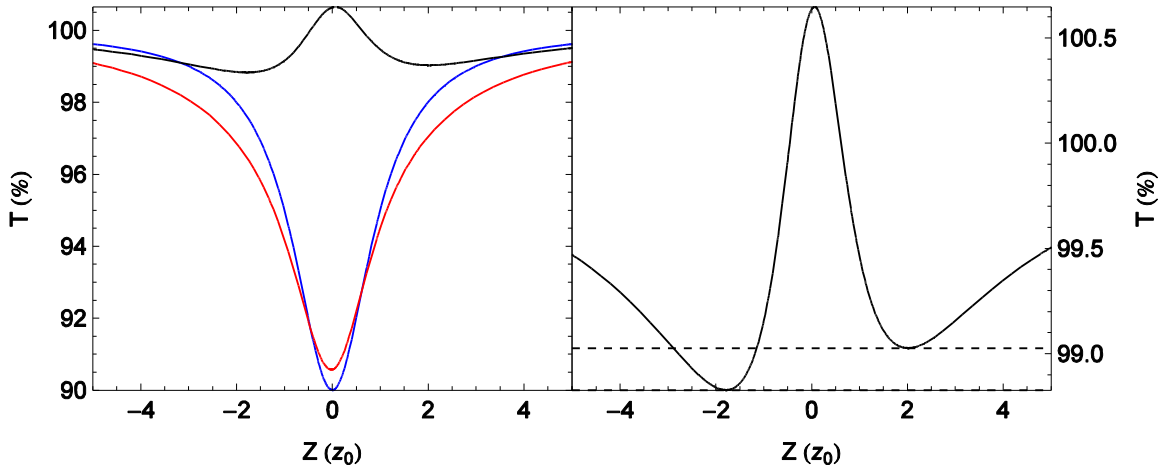

Figure 53: (left) CA (red), OA (blue) and CA/OA (black) signals for q_0 = 0.28 and ρ = 19 ($\Delta\phi_0$ = 0.007). ΔT_{p-v} = 1.82%. The CA and CA/OA signals are nearly symmetric within the system noise, making it very difficult to determine the value of n_2 accurately; (right) zoom of CA/OA in left figure.

At the maximum value ρ_{max}, both the CA and the CA/OA signal are nearly symmetric within the system noise, making it very difficult to determine a value for n_2 with any certainty. Practically, this limit is optimistic, as this analysis does not account for other factors that may distort the CA

signal such as linear backgrounds, non-Gaussian beams and misalignments of the experimental apparatus.

As an example, consider the Z-Scan of AJBC-3702 in DMF shown in Figure 54.

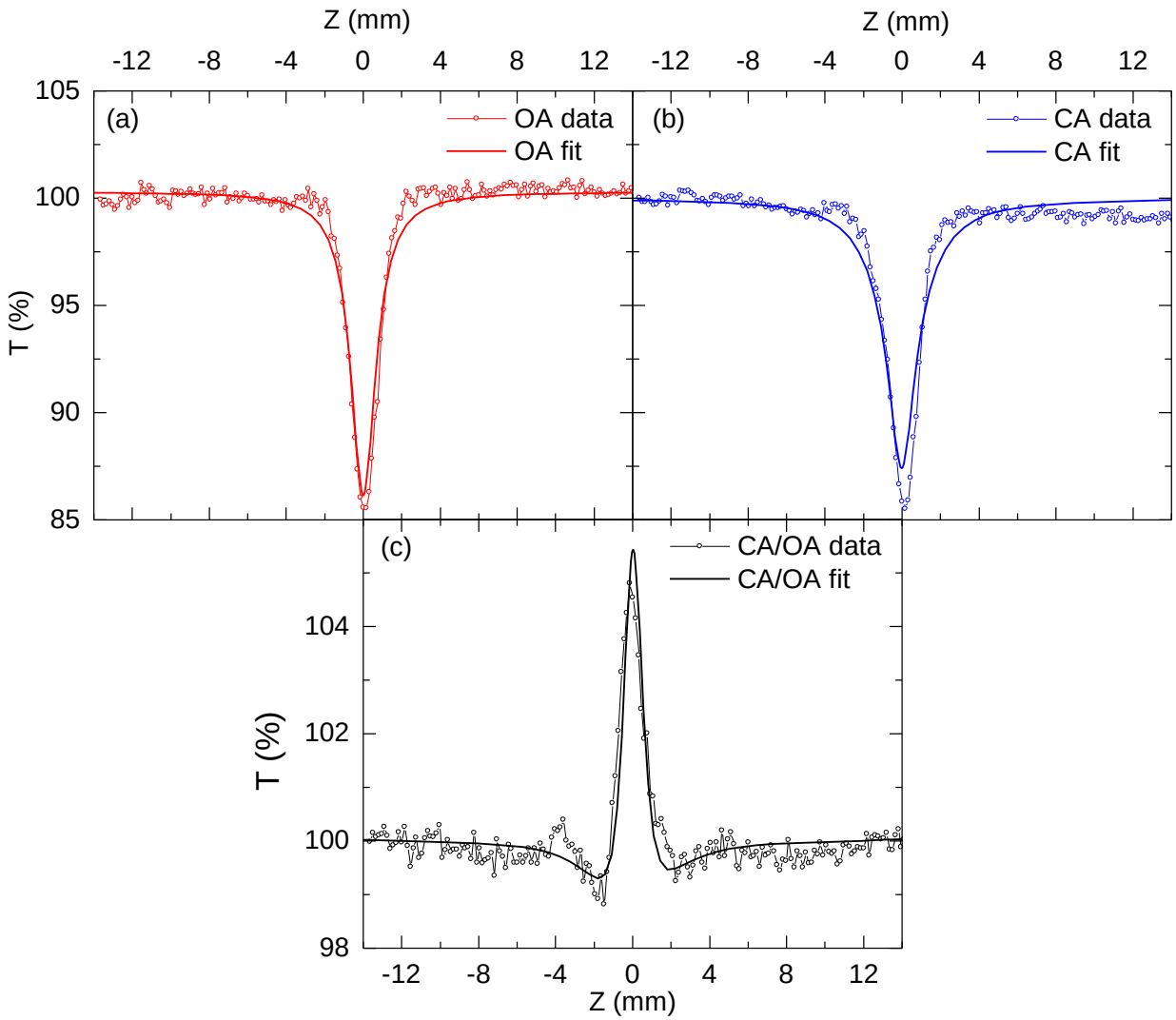

Figure 54: Z-Scan of AJBC-3702 at 1400 nm, (a) OA data (red circles) and fit (solid red), (b) CA data (blue circles) and fit (solid blue), (c) CA/OA data (black circles) and fit (solid black) with α_2 = 0.12 × 10^{-11} m/W and n_2 = 0.1 × 10^{-15} m^2/W (ρ = 13.4). At this ρ it is difficult to determine an accurate value of n_2 since the signal is dominated by the NLA.

AJBC-3702 is a organic dye of interest for use in AOSP applications synthesized by the University of Washington. Near 1300 nm and longer wavelengths n_2 becomes very small, making measurement challenging. Examining Figure 54 it can be seen that determination of n_2 is quite difficult, with the CA dominated by the NLA and nearly symmetric with none of typical structures that would allow us to fit a value for n_2. We can say, based on the CA/OA signal that there is some positive nonlinearity, since the negative valley appears to be lower than the positive valley. In this case we can only bound n_2 to be between $0.0 - 0.1 \times 10^{-19}$ m^2/W, so that with $\alpha_2 = 0.12 \times 10^{-11}$ m/W, $\rho > 13.4$ ($FOM < 7.5\%$). This is consistent with our analysis, where ρ_{max} is 19, and the Z-Scan of Figure 54 is close to the limit of detection of NLR. Since ρ_{max} for BD technique is a factor of eight higher, we expect that BD should be more adept at determining small n_2 in the presence of large α_2.

3.2.2.5. Beam Deflection Performance Analysis

Comparing the performance of the BD technique to the Z-Scan, the responsivity is

$$R = \frac{\Delta E_p / E_{p,max}}{\Delta \phi_0} = \frac{2\sqrt{2}\, W(1 - A\rho/2)}{\sqrt{e\,\pi\,(1+T^2)}} \approx \frac{2\sqrt{2}\, W}{\sqrt{e\,\pi\,(1+T^2)}}, \tag{3.55}$$

where $W = w_p/w_e$ is the beam waist ratio and $T = \tau_p/\tau_e$ is the pulse duration ratio. Note that the effect of NLA is to reduce the responsivity of the technique. However, this effect can be mitigated by increasing d, thus decreasing A. For a typical experimental configuration with $d/z_{0,p} > 100$, $A < 1\%$ so that the absorption term $A\rho/2$ can be disregarded.

In order to improve R it is best to make the spot sizes of the beams as close as possible. This is due to two factors, namely that that a smaller w_e will increase $I_{e,0}$, and thus Δn_p. Secondly, a larger $w_{p,0}$ will result in a smaller spot size on the detector, making it more sensitive for a given lateral translation. This must be balanced against the need to have a linear index gradient across the probe beam, which requires that $w_{p,0} \ll w_e$. Figure 55 shows R as a function of W for typical BD parameters.

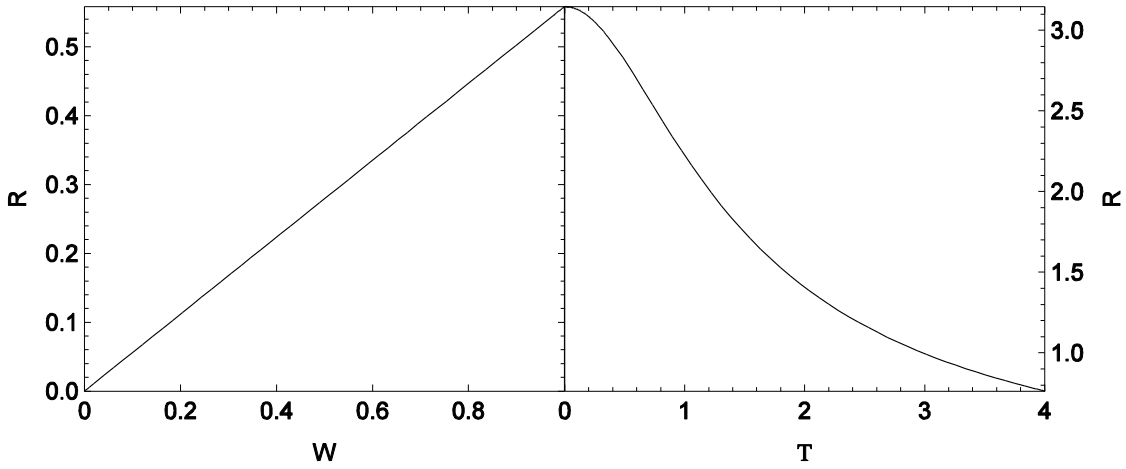

Figure 55: (left) Responsivity vs. beam waist ratio W and (right) responsivity vs. pulse duration ratio T for typical BD parameters given in Table 4.

It is typical in our experiments to target a value of W between 0.2 and 0.33, which provides good responsivity while maintaining a near linear index gradient.

Additionally, R can be increased by minimizing T. This can be understood by examining the extreme cases. When T << 1, the probe beam is much shorter than the excitation, so that over the duration of the probe, Δn_p induced by the excitation is nearly uniform, so that all the energy of the probe is deflected uniformly. However, when τ_p is much longer than τ_e ($T \gg 1$), the index

gradient induced by the excitation exists only for part of the probe duration so that only a fraction of the probe energy is deflected. This reduces the signal $\Delta E_p/E_p$ since ΔE_p will be reduced, but E_p will not.

Note that this is applies when dealing with instantaneous responses where $\Delta n_p(t)$ follows the excitation temporal profile. If one considers a noninstantaneous response where $\Delta n_p(t)$ persists substantially beyond τ_e (such as reorientational responses where the decay time is much longer than the excitation duration), $\Delta E_p/E_p$ will not be reduced as the same way. Hence in the case where we have both instantaneous and noninstantaneous responses, adjusting T will have the effect of changing the prevalence of each component in the total signal. Increasing T will reduce $\Delta E_p/E_p$ from the instantaneous response more than from the long lived noninstantaneous response and vice versa.

Reducing T can be accomplished by using a prism compressor to reduce the probe pulse duration. For the most optimistic case where the probe is generated using an OPA and the excitation is provided by the laser, for the case of SHG in the low conversion limit a bandwidth limited pulse from the laser can be compressed by the OPA by a factor of $\sqrt{2}$ so that T can be as low as 0.707. Given the relative insensitivity of R vs. T as seen in Figure 55 near that range it is generally considered not worth the extra complexity introduced into the experimental apparatus to compress the probe temporal pulse duration. However in the case where the source of the probe is WLC generated in water or sapphire, τ_p may be two to three times longer than τ_e. In this case the use of a pulse compressor for the probe may be warranted, although implementation may be

complicated by the low probe power produced via WLC and the high losses typical of a dispersive beam compressor.

For the case of no NLA ($\rho = 0$) and typical BD parameters of W = 0.31, and T = 0.71, the BD responsivity is 0.24 which is on the same order as the Z-Scan responsivity of 0.367 discussed in Section 2.2.4.

While the analytic approach presented gives us much insight into the BD technique, there is a significant limitation. We assumed that the excitation and probe pulses travel with each other along the length of the sample so that $\Delta\phi_0 \propto L$. This assumes that GVM and GVD are not significant, and hence the analytic approach is limited to nearly degenerate cases or materials with low dispersion. Outside of these cases we must resort to numerical techniques presented in Section 3.2.2.7

3.2.2.6. Beam Deflection Optimization

In order to achieve the best estimates for the nonlinear parameters and the temporal dynamics, it is important to optimize the BD experiment to achieve both high SNR and short pulse durations.

In order to examine the temporal dynamics of a given mechanism, the cross correlation of the excitation and probe pulses must be shorter than the time scale of the mechanism. Utilizing pulse durations of 35 fs (FWHM) (such as those generated by the Coherent laser system) involve particular challenges and solutions not required when using 100 fs (FWHM) pulses (like those produced by the Clark-MXR system) due to the increased bandwidth of the shorter duration pulses (27 nm for the Coherent system vs. 10 nm for the Clark-MXR system).

For pulse durations less than 100 fs (FWHM), lenses should not be used due to the temporal distortion of the beam. This distortion is due to four effects, GVM, SPM, Propagation Time Difference (PTD) and chromatic aberration.

The equations governing the pulse broadening due to GVM are

$$D_\nu = \frac{\lambda_0^3}{c^2}\frac{d^2 n}{d\lambda^2}\bigg|_{\lambda=\lambda_0}, \tag{3.56}$$

$$\xi = \frac{\pi\tau^2}{-D_\nu}, \tag{3.57}$$

$$\tau_{out} = \tau\left(1+\left(\frac{L}{\xi}\right)^2\right)^{1/2}, \tag{3.58}$$

where D_ν is the GVD parameter, ξ is the characteristic dispersion length over which the pulse duration is broadened by a factor of $\sqrt{2}$ and τ_{out} is the output pulse duration. Due to GVM a 35 fs (FWHM), 650 nm pulse traversing through BK7 glass is temporally stretched to by approximately 10% per mm of material. While the effect of each individual optic is small, the accumulated effect can be quite substantial, with a total of 17 mm of BK7 glass required to double the pulse duration.

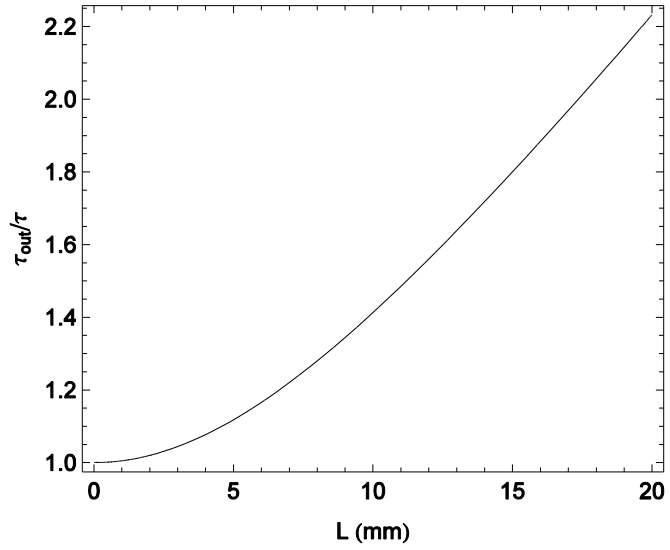

Figure 56: Broadening factor τ_{out}/τ vs. length of BK7 glass traversed at λ = 650 nm.

The high irradiance of ultrashort pulses can also lead to SPM, which broadens the bandwidth of the pulse making it more susceptible to the effects of GVM. To examine this, consider a λ = 650 nm, 35 fs pulse with an irradiance of I_0 = 2.0 × 10^{15} W/m^2 traversing through 5 mm of quartz glass, typical of a beam expansion telescope used to top hat the beam. The electric field at the exit of the material including the effect of SPM is

$$E(t) = E_0\, Exp(i(\omega t + \Delta\phi),$$

$$\Delta\phi = k_0 n_2 L \cdot I_0 Exp\left(-\left(\frac{t}{\tau}\right)^2\right), \tag{3.59}$$

where we have neglected the static phase terms that are not consequential. The spectrum at the exit of the lens can be calculated using numerical Fourier transform.

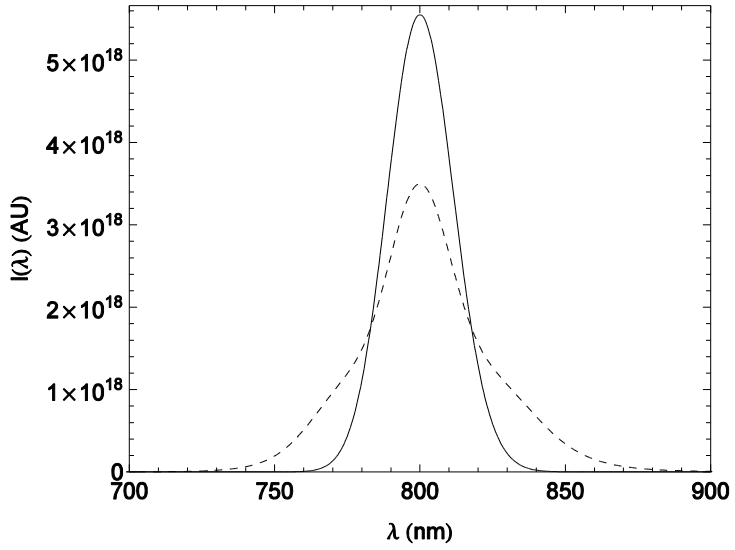

Figure 57: Input pulse (solid) and output pulse (dashed) broadened by SPM in a L = 5 mm thick quartz lens with I_0 = 2.0 × 10^{15} W/m^2, λ = 650 nm and τ = 35 fs (FWHM). The input spectrum is 27 nm (FWHM) while the output spectrum is 34 nm.

Comparing the spectrum of the pulse at the front and back of the lens, we determine that the bandwidth of the pulse is broadened from 27 to 34 nm (FWHM).

While the prior two effects relate to all dispersive optics, two effects pertain specifically to lenses such as those used to focus the excitation and probe beams on the sample. PTD is due to the difference between the phase and group velocities as the pulse travels through the lens [85]. This causes the pulse front to lag the phase front. Hence at the beam waist the phase front is no longer flat, so that our previous analytic expressions are no longer valid, since this is assumed in the Gaussian propagation of the beam from the sample to the detector [86]. The distance between the location of the beam waist and the plane of flat phase fronts is [87]

$$L = \frac{f_0}{n_0 - 1}\left(-\lambda \frac{dn}{d\lambda}\Big|_{\lambda=\lambda_0}\right) \tag{3.60}$$

where r is the input height of the ray of interest, r_0 is the height of the marginal ray, f_0 and n_0 are the focal length and index of the lens at the center wavelength of the pulse. For BK7 lens at 650 nm, $L = 0.04f$.

Lastly chromatic aberration causes different spectral components of the pulse to focus at different locations, lengthening the pulse duration as measured by autocorrelation [88]. Neglecting the GVD induced by the lens, the profile of the pulse $U(v,t)$ at the focal plane is

$$U(v,t) \propto \int_0^1 J_0(rv)\, Exp\left(-\frac{t}{\tau} + r^2\frac{T}{\tau}\right) r dr \tag{3.61}$$

$$T = \frac{a^2 k_0}{2f_0(n_0 - 1)}\frac{dn}{d\lambda}\Big|_{\lambda=\lambda_0} \tag{3.62}$$

Where v is the radial coordinate at the focal plane, T is the dispersion parameter of the lens, a is the radius of the lens, and k_0 is the wave number at the center frequency of the pulse. Along the center of the pulse (v = 0) the temporal profile is

$$U(0,t) \propto \frac{\sqrt{\pi}T\left(-Erf\left(\frac{t}{\tau}\right) + Erf\left(\frac{t+T}{\tau}\right)\right)}{4T}. \tag{3.63}$$

For values of T/τ > 3, the ratio of the measured pulse duration to the actual pulse duration $\tau_{measured}/\tau \approx T/\tau$. For a typical focusing geometry using a 1" BK7 lens with a 10 cm focal length a 650 nm 35 fs pulse (FWHM), T/τ = 3.1, so making the pulse appear to be 110 fs (FWHM).

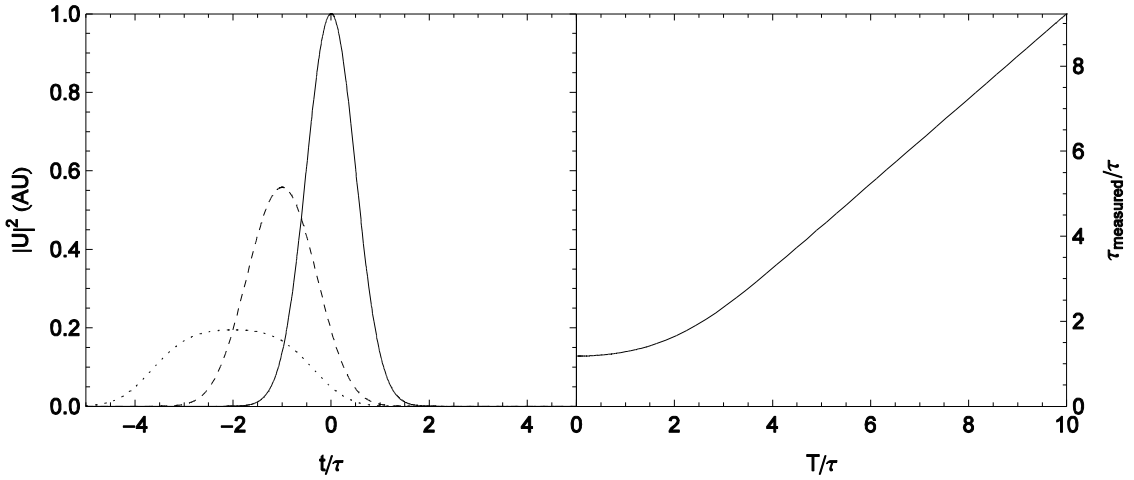

Figure 58: left) Temporal profile $U(0,t)$ of pulse at focus due to distortion by chromatic aberration for various values of T = 0 (solid), T = 2 (dashed) and T = 4 (dotted); right) ratio of apparent pulse duration to actual pulse duration $\tau_{measured}/\tau$ vs. ratio of chromatic aberration parameter to actual pulse duration T/τ.

Note that while we have considered pulse stretching due to chromatic aberration in the context of the BD temporal resolution, this effect will also be present in Z-scan measurements. Additional analysis to understand this effect on Z-Scan measurements and develop mitigation and/or compensation methods will need to be developed before making measurements using ultrashort pulses in spectral regions where there is significant index dispersion. Otherwise, the absolute error introduced in the measurement will be substantial due to fitting using the incorrect pulse duration.

Due to these effects, optimizing BD for short pulse durations requires minimizing dispersive optics wherever possible, especially in the focusing elements in order to ensure that the proper pulse duration is used in the experiment. Experimentally, this can be quite tedious, as many

common operations performed on the excitation and probe beam are most easily done with refractive optics, while the use of reflective optics tends to incur a penalty in terms of astigmatism in the spatial profile, which can complicate absolute calibration.

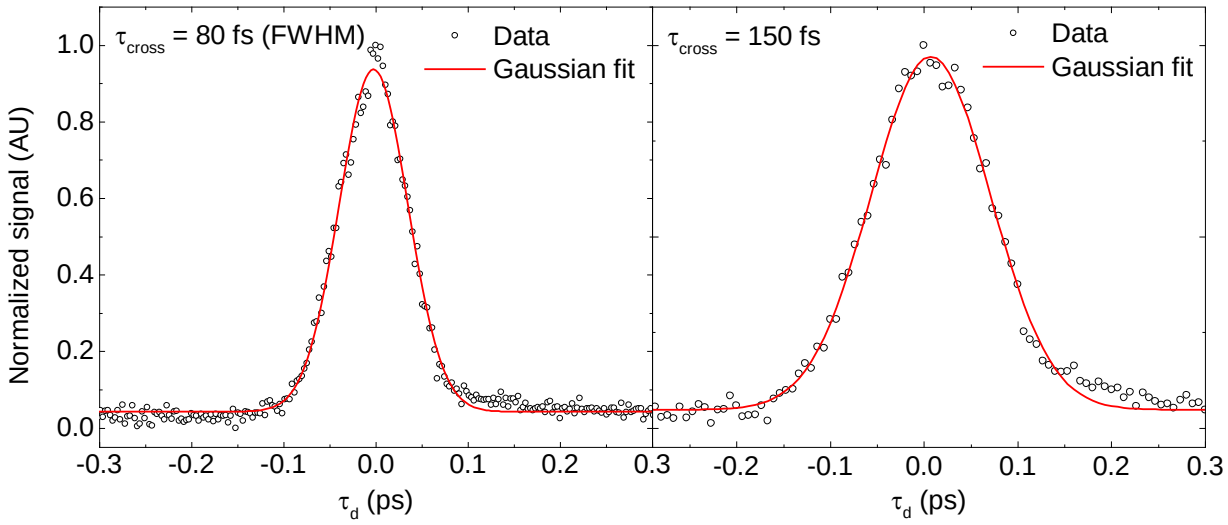

Figure 59: BD of quartz using left) mirrors and right) lenses as the focusing elements before the sample. Using mirrors produces the expected cross correlation signal of 80 fs (FWHM), while using lenses gives an artificially lengthened cross correlation width of 150 fs (FWHM).

3.2.2.7. Numerical Analysis Method

While we have been able to do much with an analytic approach, there are some limitations that preclude the use of our analytic expressions in many common experimental configurations. Most notably, for nondegenerate experiments, the dispersion causes the excitation and probe pulses to travel at different speeds, which is referred to as Group Velocity Mismatch (GVM). To account for GVM we need to solve the equations governing the excite-probe experiment given in Eq. (3.2).

In order to solve this system of equations we follow the derivation of Reichert [89], which is based on the work of Kobyakov [90]. This method accounts for not only GVM, but also for depletion of the excitation due to linear absorption and noninstantaneous responses of arbitrary functional form.

The electric field of the excitation and probe beams are given in Eq. (3.64)

$$E_p(z,t) = \frac{1}{2}\mathcal{E}_p(z,t)e^{i(k_p z-\omega_p t)} + \frac{1}{2}\mathcal{E}_p^*(z,t)e^{-i(k_p z-\omega_p t)}$$
$$E_e(t) = \frac{1}{2}\mathcal{E}_e(t)e^{i(k_e z-\omega_e t)} + \frac{1}{2}\mathcal{E}_e^*(t)e^{-i(k_e z-\omega_e t)} \tag{3.64}$$

Where $\mathcal{E}(z,t)$ is the complex electric field envelope, $k = 2\pi/\lambda$ is the wavenumber, $\omega = 2\pi\nu$ is the angular frequency and the subscripts e and p refer to the excitation and probe beams, respectively. In this analysis we apply the undepleted excitation approximation so that that the electric field of the excitation is unchanged throughout the sample, ($E_p(t,z) = E_p(t)$).

In the case of a bandwidth limited probe in the absence of 1PA or D-2PA of the probe the nonlinear wave equation can be written as

$$i\left(\frac{\partial\mathcal{E}_p(z,t)}{\partial z} + \frac{\alpha_p}{2}\mathcal{E}_p(z,t) + \frac{1}{v_{g,p}}\frac{\partial\mathcal{E}_p(z,t)}{\partial t}\right) - \frac{D}{2}\frac{\partial^2\mathcal{E}_p(z,t)}{\partial t^2} + 2\gamma|\mathcal{E}_e(z,t)|^2\mathcal{E}_p(z,t) = 0, \tag{3.65}$$

$$\frac{1}{v_{g,p}} = \frac{d\omega_p}{dk_p} = \frac{1}{c}\left(n_p - \lambda_p\frac{dn_p}{d\lambda_p}\bigg|_{\lambda_p}\right) = \frac{n_{g,p}}{c}, \tag{3.66}$$

$$D_p = \frac{d^2 k_p}{d\omega_p^2} = \frac{\lambda_p^3}{2\pi c^2} \frac{d^2 n_p}{d\lambda^2}\bigg|_{\lambda=\lambda_p}, \tag{3.67}$$

$$\gamma = \frac{3\pi}{4\lambda_p n_p} \chi^{(3)}(\omega_p; \omega_p, -\omega_e, \omega_e), \tag{3.68}$$

where α_p is the linear absorption coefficient of the probe, and $v_{g,p}$ is the group velocity of the probe, γ is the nonlinear parameter, c is the speed of light in vacuum, n_p is the linear index of refraction for the probe, λ_p is the wavelength of the probe, $n_{g,p}$ is the group index of the probe, D_p is the GVD of the probe and $\chi^{(3)}(\omega_p; \omega_p, -\omega_e, \omega_e)$ is the nondegenerate third order susceptibility of the probe induced by the excitation.

Next using the substitutions $Z = z/L$, $T = t/\tau_e$, $T = T' - z/(v_{g,p}\tau_p)$ and $a_p(Z,T) = \mathcal{E}_p(Z,T)/\mathcal{E}_p$ we transform into normalized coordinates moving with the excitation pulse, where $w_{0,p}$ is the HW1/e^{2}M of irradiance probe beam waist, L is the sample thickness, and τ_e is the HW1/eM irradiance of the excitation temporal pulse duration. Doing so reduces Eq. (3.65) to

$$\begin{aligned} &i\left(\frac{\partial a_p(Z,T)}{\partial Z} + \sigma a_p(Z,T) + \rho \frac{\partial a_p(Z,T)}{\partial T}\right) - \mu \frac{\partial^2 a_p(Z,T)}{\partial T^2} \\ &+ \chi |a_e(T)|^2 a_p(Z,T) = 0, \end{aligned} \tag{3.69}$$

$$\sigma = L\frac{\alpha_p}{2}, \tag{3.70}$$

$$\rho = \frac{L}{\tau_e c}\left(n_p - \lambda_p \frac{dn_p}{d\lambda}\bigg|_{\lambda=\lambda_p} - \left(n_e - \lambda_e \frac{dn_e}{d\lambda}\bigg|_{\lambda=\lambda_e}\right)\right) = \frac{L}{\tau_e c}\Delta n_g, \tag{3.71}$$

$$\mu = \frac{L}{2\tau_p^2} D_p = \frac{\lambda^3 L}{4\pi c^2 \tau_p^2} \frac{d^2 n_p}{d\lambda^2}\bigg|_{\lambda=\lambda_p}, \tag{3.72}$$

$$\chi = \eta + i\Gamma = 4\pi \frac{L}{\lambda_p} \frac{n_p}{n_e} I_{0,e} n_2(\omega_p; \omega_e) + iL \frac{n_p}{n_e} I_{0,e} \alpha_2(\omega_p; \omega_e), \tag{3.73}$$

where σ is the normalized absorption parameter, ρ is the Group Velocity Mismatch (GVM) parameter, Δn_g is the difference in group indices, μ is the Group Velocity Dispersion (GVD) parameter, and χ is the nonlinearity parameter. Assuming no GVD we can rewrite the wave equation as

$$\frac{\partial a_p(Z,T)}{\partial Z} + \rho \frac{\partial a_p(Z,T)}{\partial T} = f(T)\, a_p(Z,T), \tag{3.74}$$

$$f(T) = -\sigma + i\chi |a_e(T)|^2. \tag{3.75}$$

By the defining $a_p(Z,T) = e^{u(Z,T)}$ and changing of variables $Z = \xi + T/\rho$, and $T = \zeta$, this can be rewritten as

$$\frac{\partial e^{u(\xi,\zeta)}}{\partial \xi} + \rho \frac{\partial e^{u(\xi,\zeta)}}{\partial \zeta} = f(\zeta) e^{u(\xi,\zeta)}. \tag{3.76}$$

The solution of which is

$$u(\xi,\zeta) = u_0(\xi) + \left(\frac{1}{\rho}\right) \int f(\zeta) d\zeta. \tag{3.77}$$

Assuming Gaussian temporal profiles for the excitation and probe beam

$$\begin{aligned} a(0,T) &= A \exp\left(-\frac{1}{2} \frac{[T+T_d]^2}{\mathcal{T}_p^2}\right), \\ a_p(T) &= \exp\left(-\frac{T^2}{2}\right), \end{aligned} \tag{3.78}$$

where $\mathcal{T}_p = \tau_p/\tau_e$ is the normalized probe pulse duration, $T_d = \tau_d/\tau_e$ is the normalized delay and $A = \sqrt{I_{0,p}/I_{0,e}}$, the normalized probe irradiance the electric field of the probe at the back of the sample is

$$a(1,T) = A\,exp(-\frac{1}{2}\frac{\left(T_p + T_d - \rho\right)^2}{\mathcal{T}_p^2} - \sigma + i\frac{\chi\sqrt{\pi}}{2\rho}\left|a_p(0)\right|^2(erf(T) - erf(T-\rho))). \tag{3.79}$$

Finally, transforming back into the initial coordinates and dividing by the initial probe electric field gives us the normalized transmission Q,

$$Q(\sigma, \tau_d, W, \rho, \Gamma) = \frac{e^{-2\sigma}}{W\sqrt{\pi}}\int_{-\infty}^{\infty} exp\left(-\left(\frac{\tau + \tau_d - \rho}{W}\right)^2 - \frac{\Gamma\sqrt{\pi}}{\rho}(erf(\tau) - erf(\tau - \rho))\right)d\tau, \tag{3.80}$$

where $W = \tau_p/\tau_e$ is the ratio of the pulse durations and $\Gamma = L\,I_e\,\alpha_2$ is the 2PA parameter.

For the case of no GVM, the pulses travel together along the length of the sample so that the transmission follows the irradiance of the excitation pulse. In the case of increasing GVM, the pulses walk through each other as they travel through the sample. Figure 60 shows the deflection signal for increasing amounts of GVM.

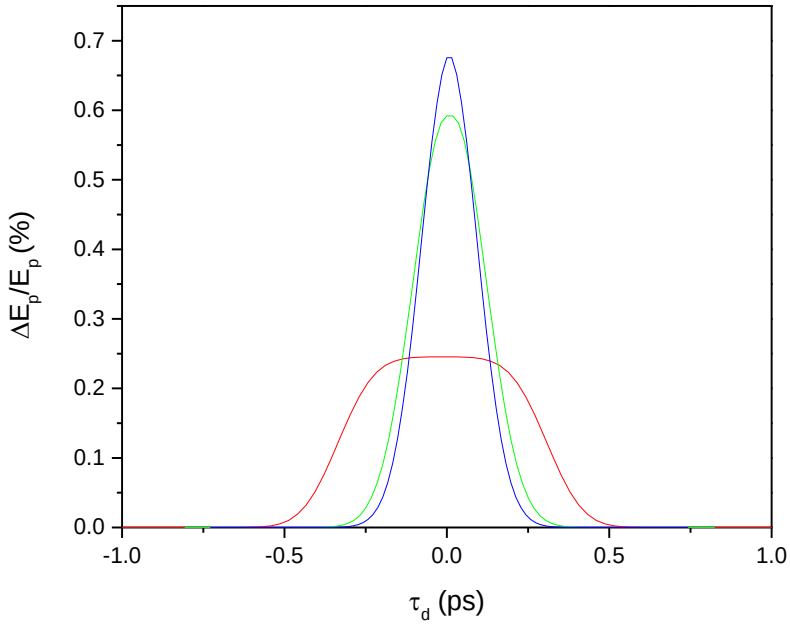

Figure 60: BD signal for typical experimental parameters and increasing amounts of GVM. No GVM (blue), small amount of GVM (green), large amount of GVM (red).

The effect of GVM is to reduce the peak signal as the probe no longer experiences a deflection as it travels through the length of the sample, rather only over the smaller range in which they walk through each other. The temporal duration of the deflection signal will also extend beyond the cross correlation of the pulses as there is a large range of delays over which the probe can walk entirely through the excitation before exiting the sample, yielding a flattened peak. In the case where the probe has a higher index of the excitation, there is a response at longer negative delays, as the excitation can catch up to the probe within the sample. In the opposite case of the probe having the lower index, the response is biased towards longer positive delays.

Since the equation for the electric field at the back of the sample must be true for all transverse positions across the sample, we can write

$$a(X,Y,1,T) = Ae^{-\left(X^2+Y^2\right)}$$
$$Exp\left(-\frac{1}{2}\frac{[T+T_d-\rho]^2}{\mathcal{T}^2} - \sigma + i\frac{\chi\sqrt{\pi}}{2\rho}e^{-2\frac{(X+X_0)^2+Y^2}{W_0^2}}(\mathrm{erf}(T) - \mathrm{erf}(T-\rho))\right). \tag{3.81}$$

Having determined the electric field at the back of the sample, we can then perform a Fresnel transform to arrive at the electric field at the detector

$$a(X_d,Y_d,d,T) = \frac{e^{ik_0 d}}{i\lambda d}\,\mathcal{F}\big(a(X,Y,1,T)\big),$$
$$\mathcal{F}\big(a(X,Y,1,T)\big) = \iint_{-\infty}^{\infty} a(X,Y,1,T)e^{-i\frac{k_0}{d}(X_d X + Y_d Y)}dXdY. \tag{3.82}$$

Once we have the electric field on the detector this can be converted to irradiance and integrated as in Eq. (3.83) in order to determine the deflection signal $\Delta E_p/E_p(\tau_d)$.

$$E_{p,L}(\tau_d) = \iint_{-\infty}^{\infty}\int_{-\infty}^{0} a(X_d,Y_d,d,T)dY_d dT dX_d$$
$$E_{p,R}(\tau_d) = \iint_{-\infty}^{\infty}\int_{0}^{\infty} a(X_d,Y_d,d,T)dY_d dT dX_d \tag{3.83}$$
$$\Delta E_p/E_p(\tau_d) = \frac{E_{p,L}(\tau_d) - E_{p,R}(\tau_d)}{\iiint_{-\infty}^{\infty} a(X_d,Y_d,d,T)dX_d dY_d dT}$$

The effect of GVM is to cause the pulses to walk through each other in time and thus within the sample length, so that the effective interaction length, and hence the deflection signal is reduced. This is most problematic when dealing with large frequency nondegeneracies or materials with very high index dispersion.

3.2.3. Application - Solids Without NLA

To demonstrate this technique, measurements were performed on a quartz sample as seen in Figure 61.

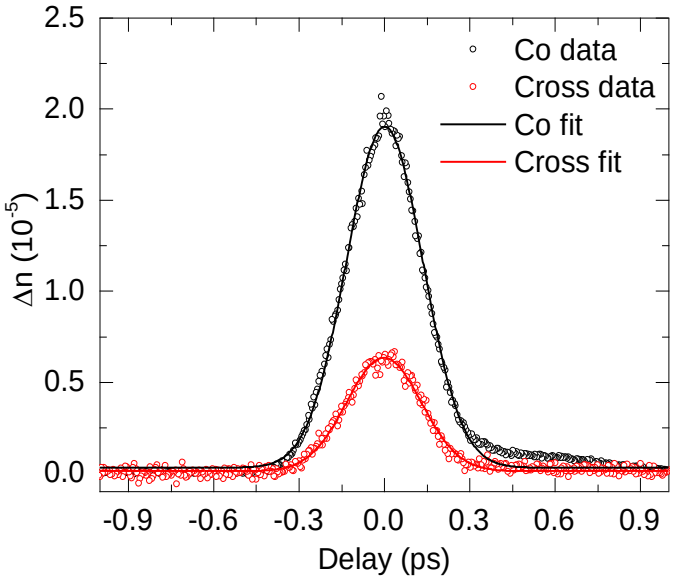

Figure 61: Co-polarized (black) and cross polarized (red) BD scan of quartz with L = 1 mm, λ_p = 650 nm, w_p = 35 µm, τ_p = 170 fs (FWHM), λ_e = 780 nm, w_e = 132 µm, τ_e = 241 fs (FWHM), E_e = 3.6 µJ and $I_{0,e}$ = 5.1 × 10^{14} W/m^2. The asymmetry is due to the nuclear response quartz.

For co-polarized beams we observed a peak index change $\Delta n_{\parallel}$ = 1.96 × 10^{-5} and a peak index changed of $\Delta n_{\perp}$ = 0.63 × 10^{-5} for cross polarized beams. For purely electronic nonlinearity in an isotropic material such as quartz the ratio of the co-polarized and cross polarized index change should be proportional to $\Delta n_{\parallel}/\Delta n_{\perp} = \chi^{(3)}_{1111}/\chi^{(3)}_{1122}$ = 3 [15]. This matches well with our observations, where the ratio is about 3.1. As expected for an ultrafast electronic nonlinearity, the temporal response follows the cross-correlation traces between excitation and probe pulses. Fitting

the deflection signal yields n_2 = 0.24 × 10^{-19} m^2/W which is consistent with the literature value [91].

To further test the sensitivity of this technique, we reduced the excitation irradiance so that the deflection signal is a few times larger than the noise level as seen in Figure 62.

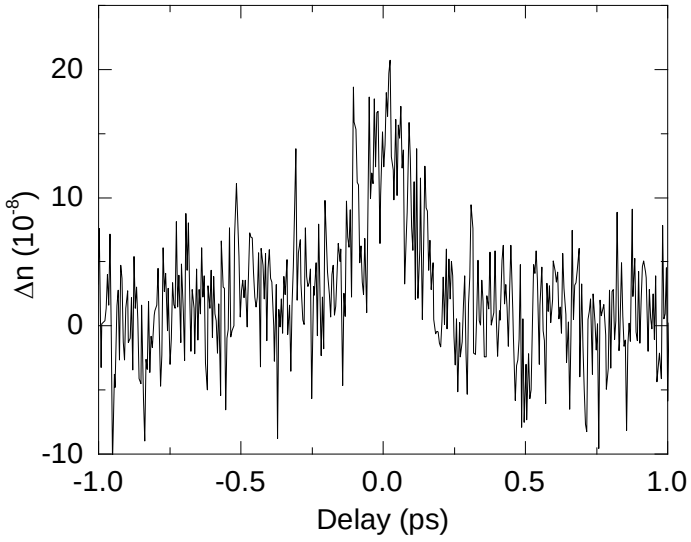

Figure 62: BD scan of quartz with L = 1 mm, λ_p = 650 nm, w_p = 35 µm, τ_p = 170 fs (FWHM), λ_e = 780 nm, w_e = 132 µm, τ_e = 241 fs (FWHM), E_e = 23 nJ and $I_{0,e}$ = 3.5 × 10^{12} W/m^2.

Following the procedure applied in the DA Z-Scan technique, the noise was extracted using a high pass filter and the standard deviation of the noise calculated as seen in Figure 63.

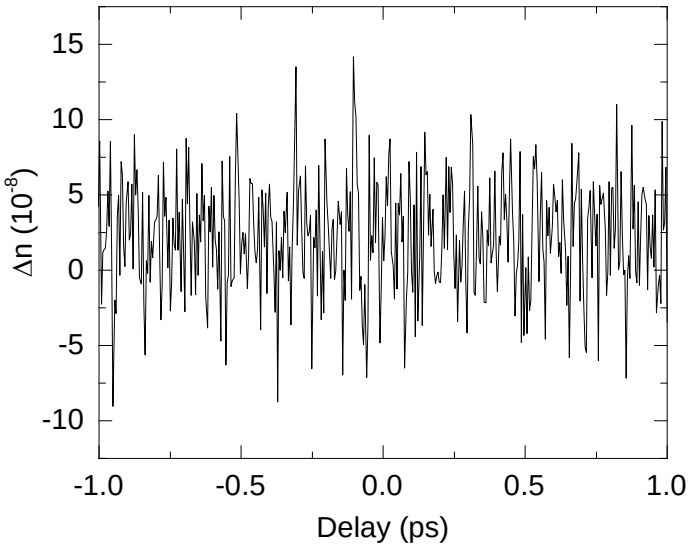

Figure 63: Noise extracted using high pass filter of Figure 62.

Based on the standard deviation of the noise and taking the limit of detection occurs when SNR = 1 [54], we can measure a minimum detectable Δn_{min} = 3.0 × 10^{-8}, corresponding to a minimum detectable phase change of λ/20,000, which compares well to other high sensitivity techniques such as the EZ-Scan [84].

3.2.4. Application - Liquids Without NLA

In order to study the temporal response of the material, of which the non-instantaneous components originate from the nuclear response of the material, we performed the BD technique on carbon disulfide (CS_2) seen in Figure 64. CS_2 is a well-studied molecule with a large nonlinear response [62, 83, 92-94].

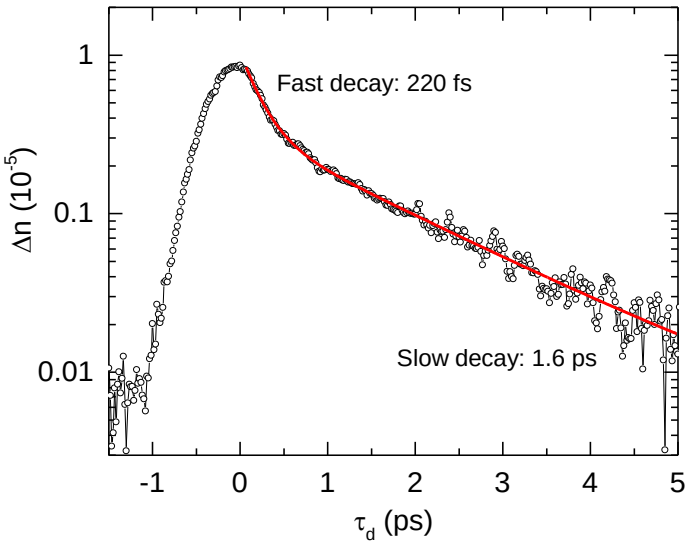

Figure 64: Index change vs. delay for CS_2 with L = 1 mm, λ_p = 650 nm, w_p = 105 µm, τ_p = 110 fs (FWHM), λ_e = 780 nm, w_e = 105 µm, τ_e = 105 fs (FWHM), and $I_{0,e}$ = 7.4 × 10^{13} W/m^2.

Other than the instantaneous electronic response, two decay components are resolved from the temporal response after zero delay, a fast decay with time constant of 220 fs (FWHM), along with a slow decay of 1.6 ps. The slow decay reveals the molecular reorientational relaxation process. The fast decay (220 fs FWHM) is a combination of bound electronic response, molecular libration (< 170 fs FWHM) and inter-molecular interaction-induced response (400-600 fs FWHM) [17, 74]. Note these two mechanisms cannot be separated in our current experiments due to the pulse duration of the excitation and probe pulses.

In addition to examining the time dynamics, we also examined the polarization dependence by measuring at three different angles between excitation and probe beam: co-polarized (0º), cross-polarized (90º), and at the so-called "magic" angle (54.7º), which is used to eliminate the re-orientational response of the material in conventional excite-probe [73] experiments, as seen in Figure 65.

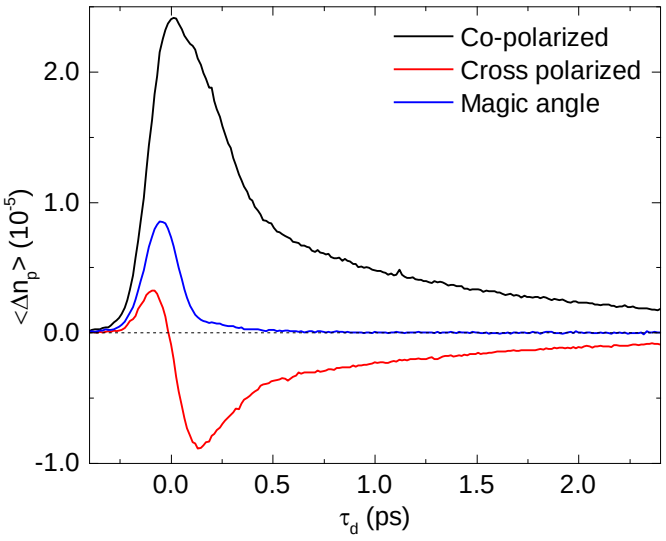

Figure 65: BD scan of CS_2 at co-polarized, cross polarized and magic angle configurations with L = 1 mm, λ_p = 650 nm, w_p = 33 µm, τ_p = 135 fs (FWHM), λ_e = 800 nm, w_e = 175 µm, τ_e = 47 fs (FWHM), and $I_{0,e} = 3.0 \times 10^{14}$ W/m^2.

To better understand the dependence of the response on the polarization of the beams, let us propose that the total nonlinear response of simple liquids like CS_2 is composed of angle-dependent isotropic and reorientational responses [95]

$$\Delta n_{tot}(\theta) = \Delta n_{iso}(\theta) + \Delta n_{re}(\theta). \tag{3.84}$$

In the case of CS_2, the isotropic response is composed primarily of the electronic and nuclear responses, although other mechanisms may also be present [93]. The angular dependence of the isotropic response is [15]

$$\Delta n_{iso}(\theta) = \Delta n_{0,iso}\left(\cos(\theta)^2 + \frac{1}{3}\sin(\theta)^2\right), \tag{3.85}$$

where $\Delta n_{0,iso}$ is the peak index change due to the isotropic response. This can be represented by an ellipse with semi-major and semi-minor axes being one and one third of $\chi^{(3)}_{xxxx}$ respectively, as shown in Figure 66.

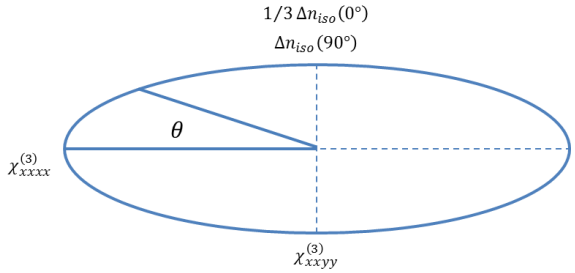

Figure 66: Isotropic response as function of relative polarization angle θ. The cross polarized response is 1/3 the co-polarized response.

The angular dependence of the reorientational response is [15]

$$\Delta n_{re}(\theta) = \Delta n_{0,re}\left(\cos(\theta)^2 - \frac{1}{2}\sin(\theta)^2\right). \tag{3.86}$$

Note here that the reorientational response is zero at the magic angle as discussed in Section 1.1.2. Using these relations it should be possible to decompose the total response and isolate the isotropic and reorientational responses. Since the magic angle response has no reorientational contribution, the isotropic response in the co-polarized case is simply the magic angle response rescaled to θ = 0

$$\Delta n_{iso}(\theta) = \frac{\Delta n_{magic}}{\left(\cos(54.7°)^2 + \frac{1}{3}\sin(54.7°)^2\right)}. \tag{3.87}$$

The reorientational response is now just the isotropic response subtracted from the total response $\Delta n_{re}(\theta) = \Delta n_{\parallel}(\theta) + \Delta n_{iso}(\theta)$, where $\Delta n_{\parallel}(\theta)$ is the co-polarized response. This decomposition for co-polarized beams is shown in Figure 67.

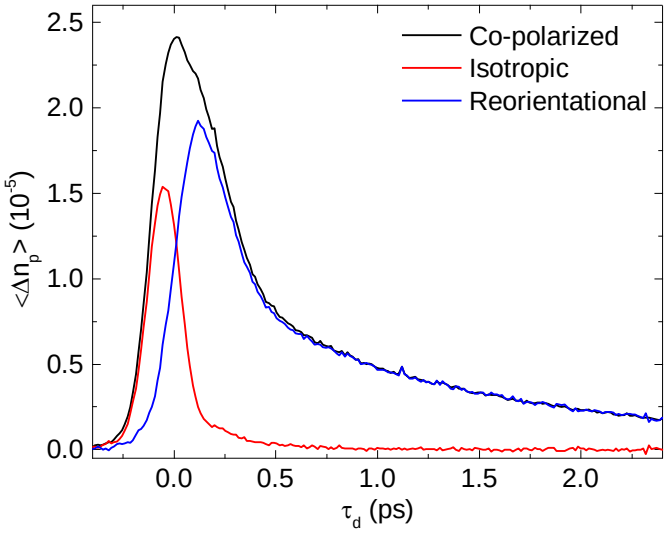

Figure 67: Decomposition of co-polarized signal shown in Figure 65 into isotropic and reorientational responses.

For the reorientational response, the ratio of the co-polarized and cross polarized response should follow the ratio of the tensor elements $\Delta n_{\parallel,rot}/\Delta n_{\perp,rot} = \chi^{(3)}_{1111}/\chi^{(3)}_{1122}$ = -2 [15]. Hence, scaling $\Delta n_{\perp}$ by a factor of -2 should match $\Delta n_{\parallel}$ for delays longer than the decay time of the isotropic response, which in this case is about 500 fs (FWHM). As seen in Figure 68, the match between the curves is excellent, verifying the ratio of the tensor element for the reorientational response.

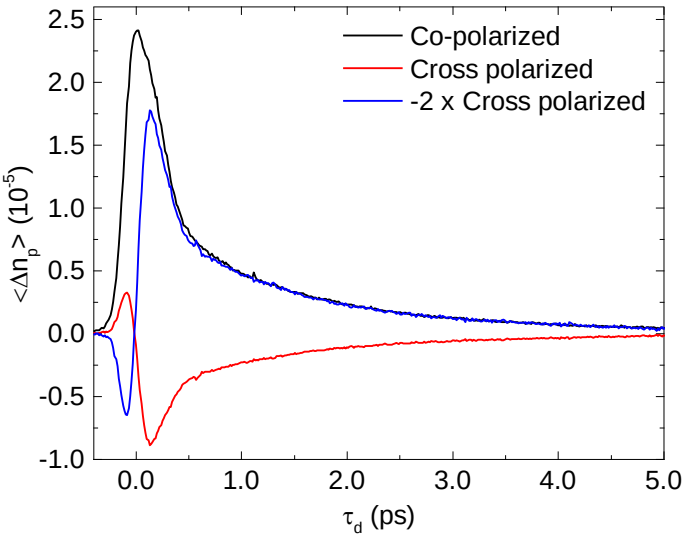

Figure 68: Comparison of co-polarized, cross polarized and reconstructed co-polarized reorientational response.

Now having the isotropic and reorientational responses, the response at any arbitrary angle can be reconstructed using Eq. (3.84). In Figure 69 we reconstruct the cross polarized response from the isotropic and reorientational responses.

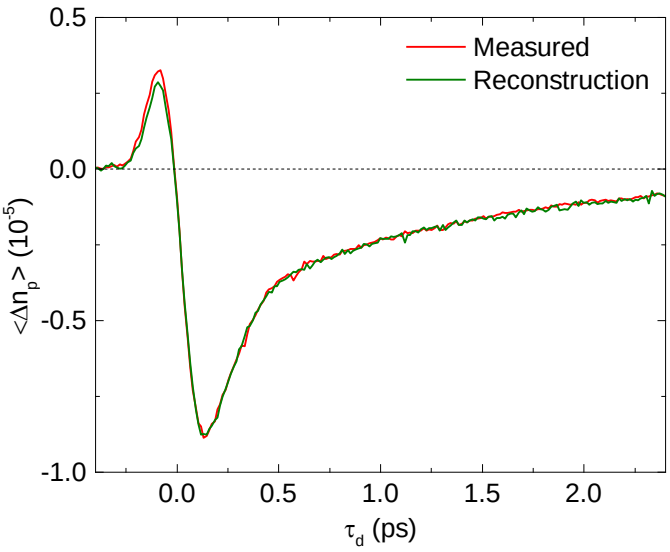

Figure 69: Comparison of measured and reconstructed cross polarized responses from Figure 65.

The match between the data and reconstruction is excellent, with only a small difference between the two, probably due to small errors in setting the polarization angle of the beams, which at the present time is performed manually with an accuracy of about one degree.

3.2.5. Application - Solids with NLA and GVM

Lastly we have applied the BD technique to materials with 2PA and GVM. Zinc Oxide (ZnO) is a semiconductor with large NLR and 2PA, along with significant GVM and GVD. This can be seen by examination of their group indices $n_g = n - \lambda(dn/d\lambda)$. The group indices of ZnO at 400 and 800 nm are 3.51 and 2.05, respectively, which is a significant differential. For the case shown in

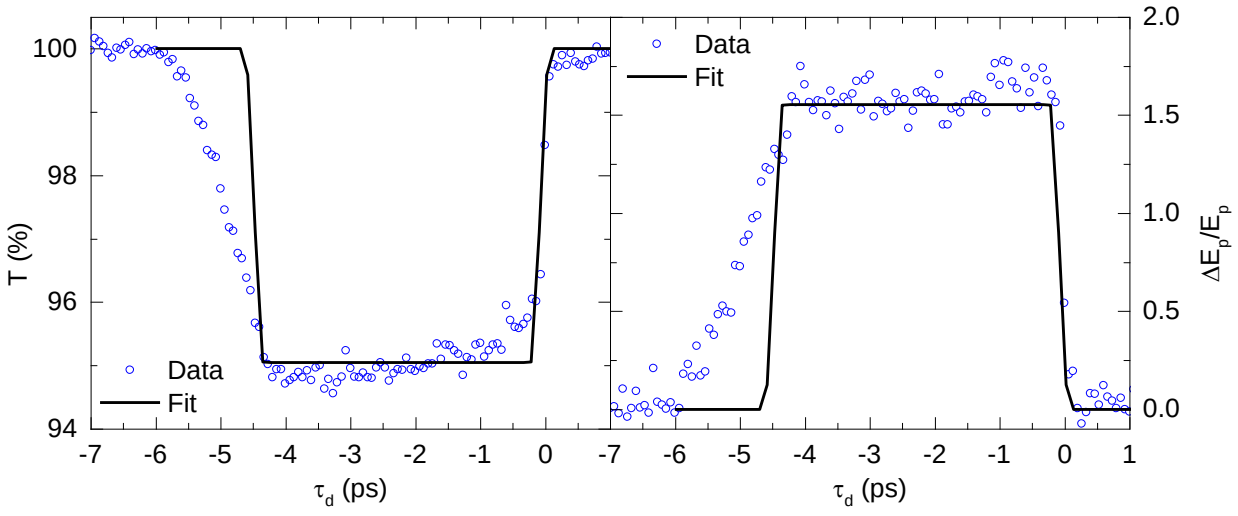

Figure 70, the GVM parameter ρ = 8.5, so that the probe walks through the excitation within about 1/9th of the sample length.

As such, it presents a challenging test case for the BD technique. In

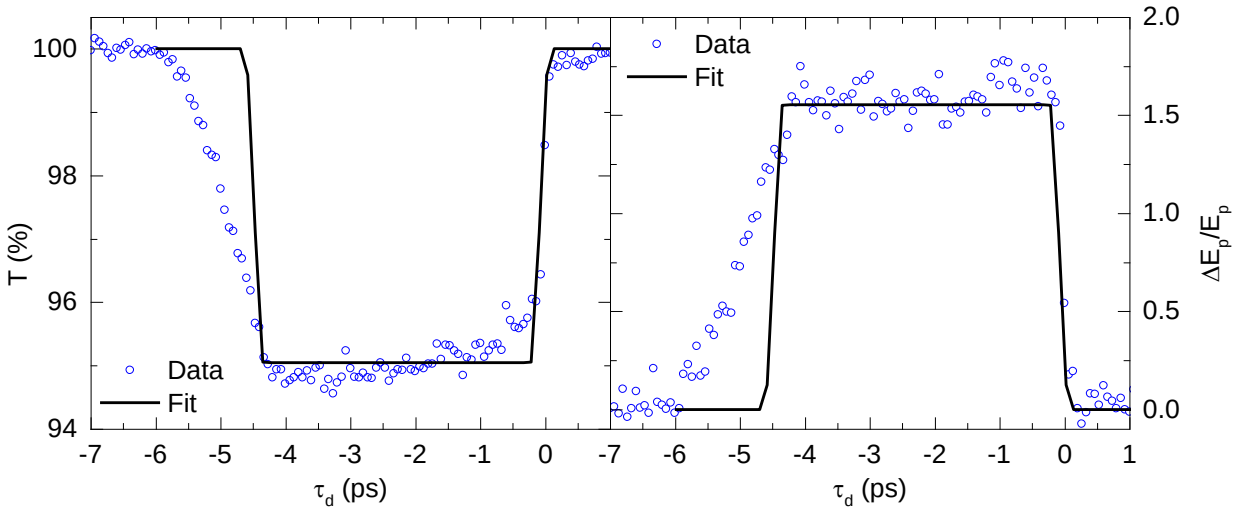

Figure 70 we show the transmission and deflection signal for nondegenerate beams with λ_e = 800 nm and λ_p = 400 nm. Note that zero delay is defined as the point at which the pulses overlap at the front of the sample.

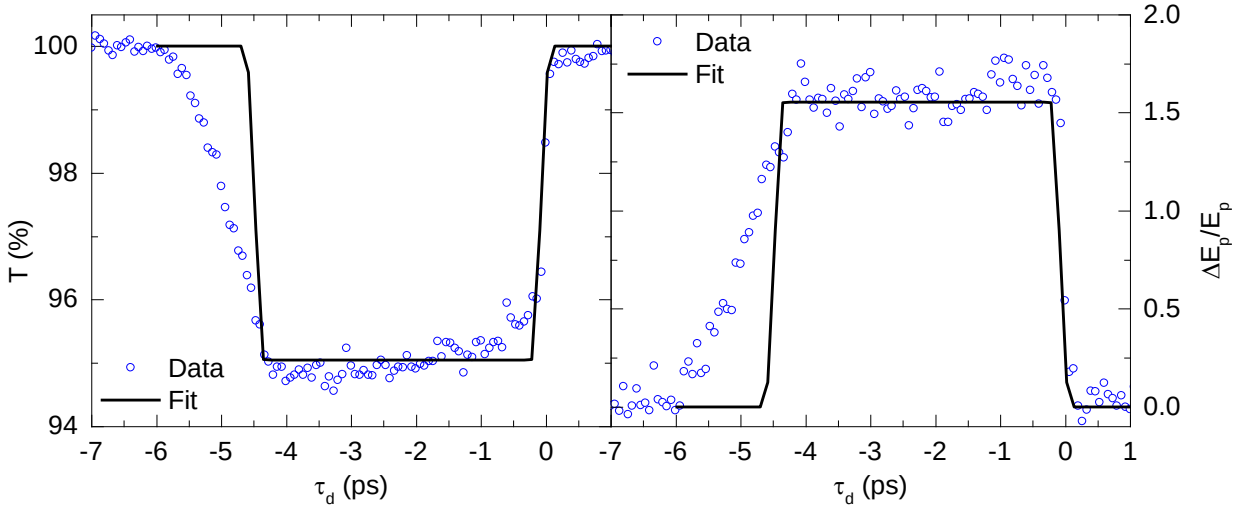

Figure 70: (left) Transmission vs. delay and (right) deflection vs. delay for ZnO with λ_e = 800 nm, λ_p = 400 nm, τ_e = 50 fs (FWHM), τ_p = 100 fs (FWHM), w_e = 178 μm (HW1/e^{2}M), w_p = 45 μm (HW1/e^{2}M),

E_e = 235 nJ, $I_{0,e}$ = 7.94×10^{13} W/m^2, n_e = 1.95, n_p = 2.21, $\partial n_e/\partial\lambda$ = -0.114 μm^{-1}, and $\partial n_p/\partial\lambda$ = -5.56 μm^{-1}. The data (open blue circles) was fit (solid black line) with α_2 = 7.2×10^{-11} m/W and n_2 = -3.9×10^{-18} m^2/W.

As expected, the signal is broadened and flattened due to the presence of GVM. The signal is also asymmetric, with the leading and trailing edges of of T and $\Delta E_p/E_p$ having different slopes. This is due to the effect of GVD, which causes the pulses to broaden as they travel through the sample.

Since the group index of the probe is larger than that of the excitation, at zero delay the pulses meet at the front of the sample and then begin to separate, due to the lag of the probe compared to the excitation. At small negative delay the excitation walks through the probe near the front of the sample, before GVD has lengthened the duration of the pulses. In this case the fall of $\Delta E_p/E_p$ is consistent with the cross correlation of the excitation and probe pulses as seen in Figure 71.

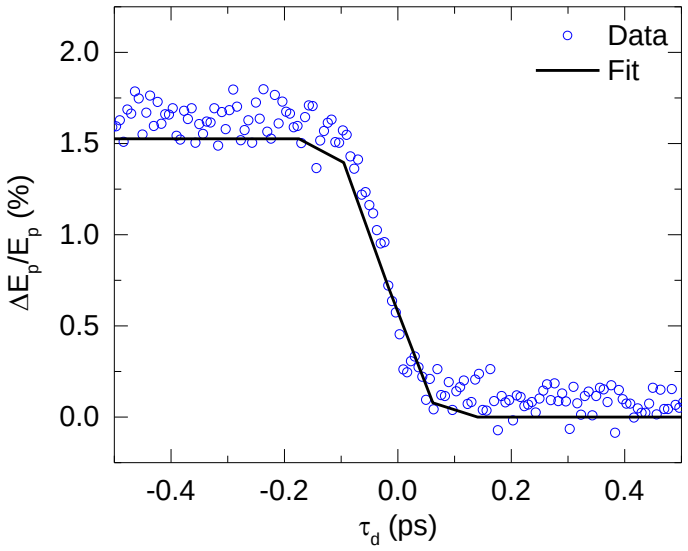

Figure 71: Fine range scan of ZnO for ZnO for λ_e = 800 nm, λ_p = 400 nm, τ_e = 50 fs (FWHM), τ_p = 100 fs (FWHM), w_e = 178 μm (HW1/e^{2}M), w_p = 45 μm (HW1/e^{2}M), E_e = 235 nJ, $I_{0,e}$ = 7.94×10^{13} W/m^2, n_e = 1.95, n_p = 2.21, $\partial n_e/\partial\lambda$ = -0.114 μm^{-1}, and $\partial n_p/\partial\lambda$ = -5.56 μm^{-1}. The data (open blue circles) was fit (solid black line) with α_2 = 7.2×10^{-11} m/W and n_2 = -3.9×10^{-18} m^2/W. Note that the fit line matches the data, indicating that the rise time of the response is the cross-correlation of the pulses.

At larger negative delay, the excitation walks through the probe further back in the sample, at which point GVD has lengthened the pulses considerably. Hence for the negative delay side we see that the rise of $\Delta E_p/E_p$ is much slower than the cross-correlation of the pulses, indicating that the pulses have lengthened considerably. Note that the model presented in Section 3.2.2.7 does not account for GVD, so the fit line does not go through the data points at negative delay where the effect of GVD is significant.

According to the two band model for semiconductors [31] the expected values for the 2PA and NLR are α_2 = 1.165×10^{-11} m/W and n_2 = -4.45×10^{-18} m^2/W. The measured values are α_2 =

7.2×10^{-11} m/W and n_2 = -3.9×10^{-18} m^2/W, which agree with the theoretical values to within a 40% and 15%, respectively, which is considered very good agreement for the two band model.

CHAPTER 4: CONCLUSIONS

In this work we have discussed the origins of the NLA (2PA specifically) and NLR, as well as several commonly used techniques for characterizing them. We have reviewed how 2PA and NLR have their origins in the third-order nonlinear response of materials as well as discussing a simple mass on a spring model as well as a more complicated quantum mechanical three-level sum-over-states model for the nonlinear susceptibility. We then examined several classes of techniques used to determine the nonlinear optical properties of materials. We gave particular attention to the now standard Z-Scan technique, as well as several extensions of that technique to enhance the sensitivity and reduce the noise in order to improve their performance.

We then developed an improvement to the Z-Scan technique that allows for extraction of very small nonlinear signals from large backgrounds, the DA Z-Scan technique. We demonstrated the utility of this technique on organic dyes and thin films. For organic dyes we extended the nonlinear spectrum of SD-O-2405 farther into the IR than was previously possible using the standard Z-Scan technique. For thin films we were able to measure ZnO samples that would otherwise not be measurable using single arm Z-Scan.

Next we developed a straightforward modification of the excite-probe technique that allows us to measure the nondegenerate time resolved NLR and NLA with absolute calibration and high sensitivity, the BD technique. We performed a thorough analysis of the expected performance under a number of different applications, such as materials with and without NLA and with GVM for the cases of instantaneous and non-instantaneous nonlinearities.

We then demonstrated the utility of the BD technique by applying it to a number of different well characterized materials in order to compare its results to other established techniques and experimentally decompose the temporal response into its reorientational and isotropic components.

4.1. Future Work

Our objectives in this dissertation were to improve upon and develop new measurement techniques to solve several longstanding issues in the field of nonlinear characterization. Having done so, the next challenge is in using these techniques to further our understanding of the nonlinear properties of materials. There are two promising applications that may yield useful insights: organic dyes for AOSP applications, and gases.

4.1.1. Nondegenerate Enhancement in Organic Dyes

Previously to development of silicon-organic hybrid devices AOSP devices relied on rare earth–doped optical fiber amplifiers [96] or semiconductor optical amplifiers [97, 98] which are difficult to manufacture and expensive. Silicon-organic hybrid devices which combine silicon integrated circuitry and a highly nonlinear organic material [64] promise to relieve some of these constraints and increase the feasibility of AOSP devices. Organic materials have the advantage of large $\chi^{(3)}$ response, off-resonance nonlinear susceptibilities, ease of molecular design, high damage threshold, and ease of processing.

The most straightforward implementation is a NLR based Mach-Zehnder interferometer, which replaces the electrical delay channel with a nonlinear material that can be illuminated with an intense control beam as seen in Figure 72.

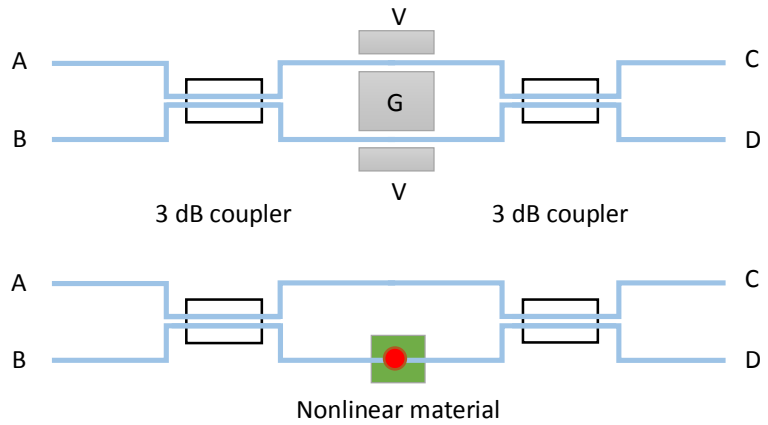

Figure 72: (top) electro-optic based Mach-Zehnder interferometer switch and (bottom) nonlinear based Mach-Zehnder interferometer based switch.

The control beam induces a refractive index change in the material, so that the input on terminal A experiences a π phase shift which switches the output from terminal C to D. Because the switch operates on the Kerr electronic nonlinearity, the switching time can be on the order of femtoseconds, much shorter than electro-optic based switches.

One issue for such NLR based designs are the high control beam irradiances required to delay the information beam. These high irradiances result in high power consumption, complicating the implementation of AOSP technologies into integrated circuits where small size and low power consumption are important parameters. Fortunately, the control beam irradiances required can be reduced by increasing the NLR of material in the delay channel. Unfortunately,

for many materials such as semiconductors, large NLR is accompanied by large NLA, which is undesirable in this application due to attenuation of the information beam [99].

4.1.1.1. Polymethine Dye YZ-V-69

Organic dyes are of particular interest to AOSP applications due to the tunability of their linear and nonlinear responses through engineering of their molecular structure [19]. Increasing the nonlinearity is based on increasing the delocalization of electrons along the length of the molecule. For the pair of atoms shown in Figure 73, the overlap of the wavefunctions of the *s* orbitals can interfere constructively or destructively, leading to a splitting of the energy levels and the formation of two types of bonds, either the σ^+ or σ^- bond, depending on whether the wavefunctions of the individual atoms are added or subtracted. Due to the large overlap of orbitals the σ bond is the strongest type of bond.

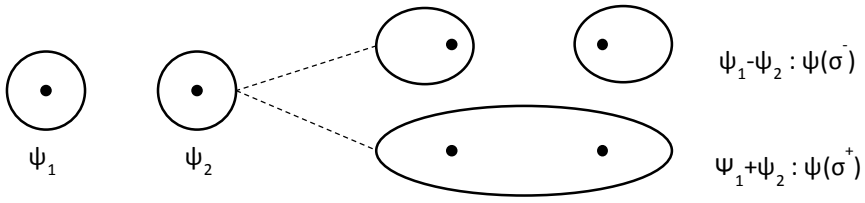

Figure 73: Anti-bonding (top) and bonding (bottom) of σ bond.

For the pair of atoms shown in Figure 74, the overlap of the *p* atomic orbitals leads to a covalent bond extending laterally over both atoms known as a π^+ or π^- bond.

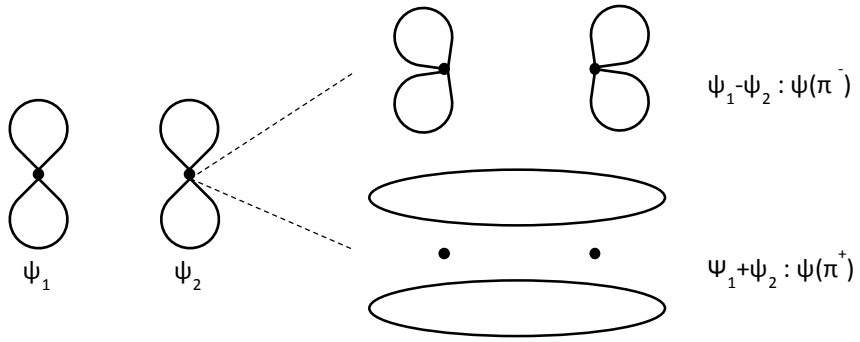

Figure 74: Anti-bonding (top) and bonding (bottom) and of π bond.

Due to the limited overlap of the *p* orbitals, π bonds are weaker than σ bonds. Molecules can employ a mix of both σ and π bonds. The relative weakness of the π bond allows the electrons to delocalize over its extent. We can take advantage of this behavior for enhancement of nonlinear properties by using a linear π conjugated chain to extend the delocalization length of the electrons.

Numerous strategies have been employed to further tailor the properties of the molecules in order to modify the linear absorption to increase the photochemical stability. Techniques include optimization of the end chain groups and inclusion of different center groups to the molecule [34].

Polymethine dyes are a class of cyanine dyes with π conjugated chromophore chain composed of methine groups, comprised of the atoms within the parentheses with two terminal groups on the ends of the chain (R_1 and R_2, respectively), as illustrated in Figure 75 [34].

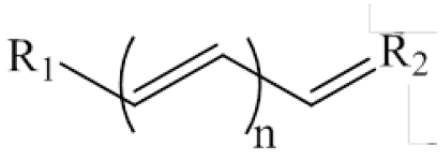

Figure 75: Polymethine dye. n indicates the number of methine groups in the conjugation chain and R_1 and R_2 are the terminal end groups.

The alternating π^+ and π^- bonds along the chromophore chain allow for delocalization of the π electrons, which increases the polarizability of the molecule enhancing $\chi^{(3)}$, as well as increasing the wavelength of the 1PA peak. The longest wavelength for 1PA can be related to the chromophore chain length by

$$\lambda_{max} = \frac{8mc}{n_0} \frac{L}{N+1}, \tag{4.1}$$

where L is the length of the chromophore chain and N is the number of π electrons.

Typically, there is a tradeoff between chromophore length and photochemical stability, with longer chromophore chains tending to distort and lose the bond length symmetry essential to electron delocalization [18], along with being more susceptible to optical damage [100]. Much effort has been dedicated to engineering molecules to increase the optical stability and enable longer chromophore chains by engineering the terminal groups [34]. The terminal groups are of two general types, acceptor groups (A) and donor group (D), depending on whether or not they either remove or contribute charges from the chromophore chain and forming cationic, anionic or neutral structures such as D-π-D, A-π-A, or D-π-A. If the structure is not neutral, a counter-ion may be added to the mixture to maintain electrical neutrality. In addition, these groups may be inserted into the chromophore chain to form neutral structures such as D-π-A-π-D or A-π-D-π-A, which have a reduced tendency towards aggregation at high concentrations.

YZ-V-69 is an organic dye developed by the Georgia Institute of Technology as part of the COMAS MURI. with the terminal groups engineered to enhance the delocalization effect while increasing the optical stability with an additional center group designed to prevent aggregation at high concentrations. The molecule was engineered for AOSP applications, and after much work a

formulation having large NLA with low 2PA, along with a low tendency toward aggregation for use at high concentrations was synthesized.

Full characterization of the nonlinear optical response of YZ-V-69 requires many measurements using different instruments to determine the parameters for the three level model. The linear absorption edge ω_{eg} can be determined through the 1PA spectra, shown in Figure 76.

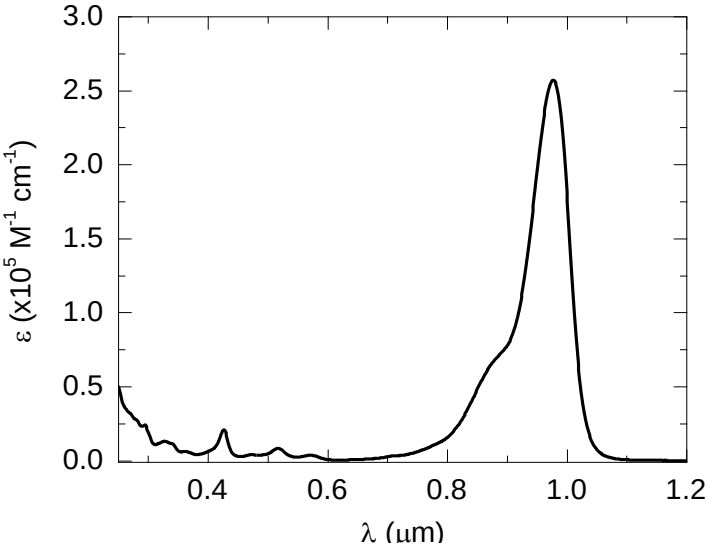

Figure 76: 1PA spectrum of YZ-V-69 in CCl4. The peak molar absorbance is 2.57×10^5 cm^{-1} M^{-1} at 977 nm.

The degenerate NLR and 2PA was measured using the Z-Scan technique as shown in Figure 77 along with the three level model fit as described in Section 1.1.1.7.

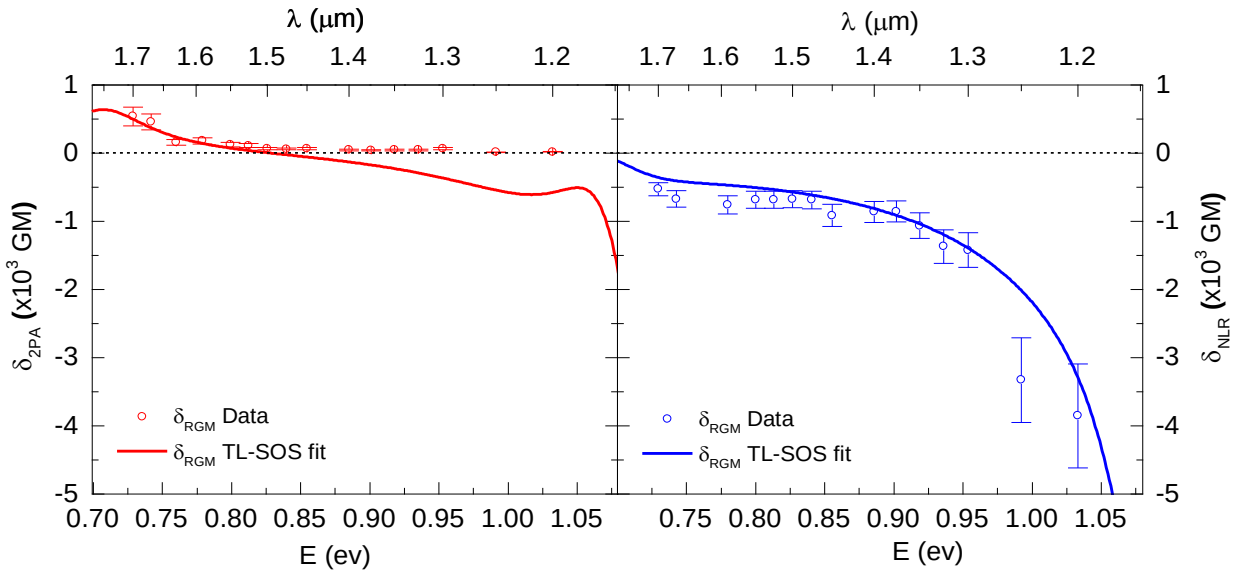

Figure 77: NLR and 2PA of YZ-V-69. Data taken from Hu [33].

The fit was done using two sets of second excited states (ge' (1) and ge' (2)) in order to improve the accuracy of the fit. The parameters used for the fit are given in Table 5.

State	ω_{mn} (eV)	Γ_{mn} (eV)	μ_{mn} (D)
ge	1.27	0.04	12
ge' (1)	1.41	0.08	8
ge' (2)	2.15	0.1	5.5

Table 5: Three level model fit parameters for YZ-V-69.

The three level model fits well for NLR, while slightly underestimating the 2PA. The region where δ_{2PA} is negative does not correspond to two-photon gain, rather it is thought that this is an artifact of the model that does not correspond to a physical phenomenon. This is not reflected in our measurements, hence we typically do not attempt to fit this region, except to ensure that that δ_{2PA} is not larger than the measured value.

Since we know that the nonlinearity should be enhanced due to Intermediate State Resonance Enhancement (ISRE) from the ground state g to the second excited state e' using the intermediate state e we propose that the NLR should be enhanced for nondegenerate beams. To estimate the degree of enhancement, we apply the three level SOS model for nondegenerate beam derived in APPENDIX B:

Assuming that the parameters used to fit the degenerate Z-Scan data are still valid for the nondegenerate case, we show the surface plot GM and RGM as a function of the ratios of the excitation and probe beam to the first excited state energy ($E_e/E_{ge'}$ for the excitation axis and $E_p/E_{ge'}$ for the probe axis) as shown Figure 78.

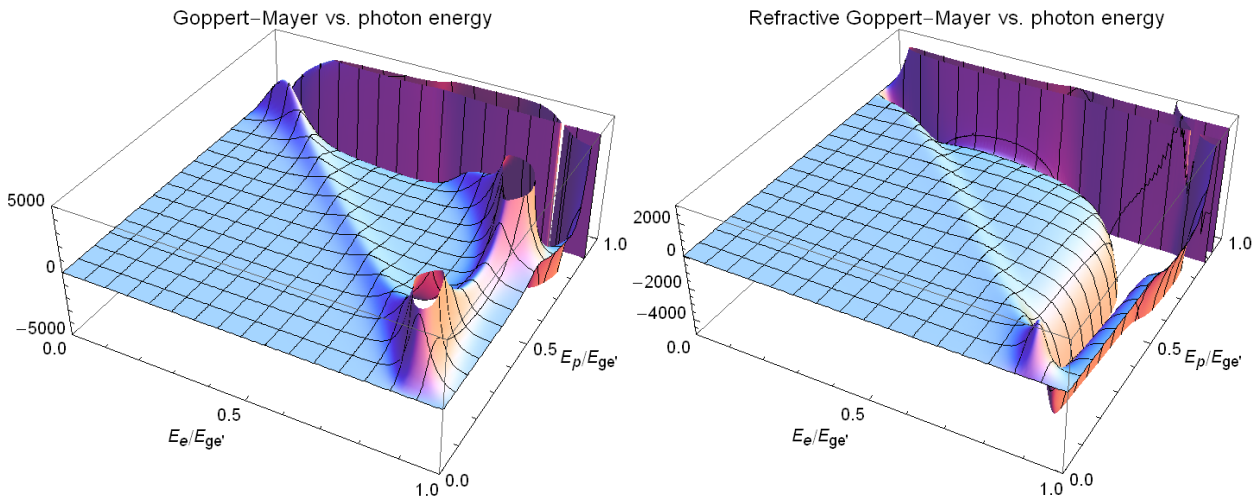

Figure 78: GM and RGM for YZ-V-69 using three level model parameters from Table 5.

There is a clearly defined region of excitation and probe wavelengths where the GM and RGM is very high, due to the ISRE. These wavelength combinations may be of particular use in integrated AOSP devices, especially those wavelengths close to the telecom band around 1.550 μm. Examining one spectral slice more closely, we plot GM and RGM as a function of wavelength

for a 2.03 μm excitation and probing between the linear absorption region at 1.1 μm and the spectral response of the InGaS quad cell detector at 1.8 μm as shown in Figure 79.

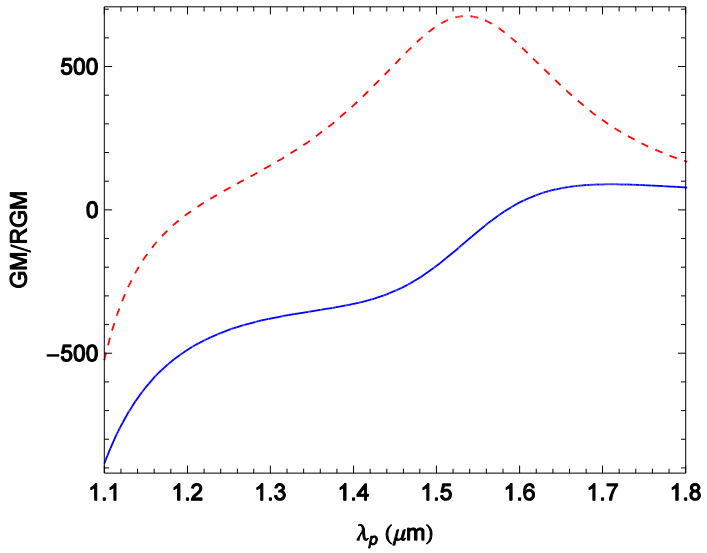

Figure 79: GM (dotted red) and RGM (solid blue) for YZ-V-69 using fit parameters from Table 5 with excitation at 2.03 μm and probe from 1.1 to 1.8 μm.

Comparing the nondegenerate spectrum shown in Figure 79 to the degenerate spectrum shown in Figure 77, we note that there is a significant enhancement of the NLR at 1550 nm, from approximately 50 RGM for the degenerate case to about 300 RGM for the nondegenerate case. Exploration of this nondegenerate enhancement in organic materials such as YZ-V-69 would be an excellent project that would advance the state of AOSP devices.

4.1.2. Nonlinear Measurement of Gases

The second research area of interest is the measurement of gases and vapors. Understanding the response of gases is useful for a wide number of application such as remote

sensing [101, 102] attosecond physics [103], filament formation [104], and pulse compression [105].

Recently there has been much discussion regarding the role that Kerr and ionization effects play in the formation of filaments [106]. The conventional understanding is that ionization induced defocusing counteracts the Kerr induced self-focusing, arresting catastrophic self-focusing and allowing the filament to propagate [107]. Much work has been done to determine the dynamics of filament formation just below the critical self-focusing power P_{cr} with simulations [106, 108-110] and measurements [104, 107, 111] performed to determine the relative importance of the Kerr and ionization effects.

Despite these efforts, the role of Higher Order Kerr Effect (HOKE) terms ($\chi^{(5)}$, $\chi^{(7)}$, etc…) in filament formation is not entirely resolved. Wahlstrand et al measured n_2 of several gaseous species within air via single-shot supercontinuum spectral interferometry [112] in order to provide insight into this discussion [111]. In support of the conventional understanding, they determined that HOKE terms do not play a significant role in the filamentation process [104]. Subsequent measurements [107] have substantiated this view. While this seemed to resolve the debate regarding the effect of HOKE terms near the ionization threshold, subsequent simulations performed by have indicated that while the HOKE terms are masked by ionization effects, some effects in the lower order harmonics of the excitation center frequency should still be observable [106]. Simulation of hydrogen atoms indicate the presence of wavelength windows in which not only are the HOKE significant, but it is possible to produce an ionization-free filament [113]. Alternatively, other simulations have suggested that the onset of HOKE can affect the type of

filamentation with ionization leading to small-scale splitting filaments, and HOKE effects producing thick optical channels [109]. Aside from identifying qualitative features of filament formation, accounting for the HOKE terms can improve quantitative fits of measured data [110].

Thus, the question of the role of HOKE terms play in filamentation formation remains a partially unanswered question that requires additional measurements to resolve. The BD techniques ability to resolve time and polarization dynamics with high sensitivity could contribute greatly to the discussion.

To determine the viability of applying the BD technique to this question, let us consider the nonlinearity of air which has been measured as n_2 = 4.0 × 10^{-23} m^2/W [114]. Currently, we have established that we can measure Δn_p as low as 3.0 × 10^{-8} [86]. In order to observe the nonlinearity of N_2 would require an irradiance $I_{0,min}$ = 7.5 × 10^{14} W/m^2, which is achievable with the Coherent laser system. In order for any measurements to be of use for the discussion of the role of HOKE terms, the required minimum power must be below [15]

$$P_{cr} = \alpha \frac{\lambda^2}{4\pi n_0 n_2}. \tag{4.2}$$

where α is the spatial distribution constant which for Gaussian beams is 1.8962.

Using our typical experimental parameters the power at $I_{0,min}$ is P_{min} = 0.02 GW, which is well below the critical self-focusing power of P_{cr} = 2.3 GW. Hence, it should be possible to measure the n_2 of gas species from below the onset of ionization throughout the formation of the filament. By examining Δn_p as a function of $I_{0,e}$ it may be able to determine the values for the HOKE terms in the same manner that has applied to semiconductors [55]. The dynamic range of

the measurement is P_{crit}/P_{min} = 111, which at only two orders of magnitude mat make it difficult to determine the value of the HOKE terms. However, this limitation might be mitigated if using a sufficiently thin sample such that the excitation beam does not have the distance over which to focus, thus extending the range over which n_2 could be measured. This however, comes at the expense of reduced sample thickness, which reduces the signal and raises P_{min}.

Experimentally, measurement of the nonlinearity of gasses could be performed using a gas jet system [104] in which a tightly focused gas jet is used to create the equivalent of a thin sample that would be compatible with the BD technique. The excitation and probe beam are overlapped and the deflection measured as in previous experiments.

The design and implementation of such an experimental apparatus for use with the BD technique would be a challenging project for the next generation of graduate students in the NLO group.

APPENDIX A: DERIVATION OF ANGULAR DEFLECTION

An index gradient within a material will act as a prism to deflect a beam propagating through the material. Following the treatment of Reichert et al [115], consider a beam propagating through a material with an induced index gradient

$$n_1(\mathbf{r}) = n_1 + \Delta n_1(\mathbf{r}), \tag{A.1}$$

where n_1 is the linear index of refraction of the material and $\Delta n(\mathbf{r})$ is the index gradient induced by the excitation beam.

The path of the beam inside the material is described by the ray equation

$$\frac{\partial}{\partial s}\left(n_1(\mathbf{r})\frac{\partial \mathbf{r}}{\partial s}\right) = \nabla n_1(\mathbf{r}). \tag{A.2}$$

For the case where the index change is small ($\Delta n_1(r) \ll n_1$) and $\nabla n_1 = 0$ this can further be simplified to

$$\frac{\partial}{\partial s}\left(n_1(\mathbf{r})\frac{\partial \mathbf{r}}{\partial s}\right) = \nabla n_1(\mathbf{r}). \tag{A.3}$$

Since the beam is propagating in the z direction and the gradient exists in the x direction this expression can be reduced to

$$\frac{\partial}{\partial z}\left(n_1\frac{\partial x}{\partial z}\right) \approx \frac{\partial \Delta n_1(x)}{\partial x}. \tag{A.4}$$

Since $\theta_1 = \partial x/\partial z$ is the angle of the beam in the medium, we can write this as

$$n_1\frac{\partial \theta_1(z)}{\partial z} \approx \frac{\partial \Delta n_1(x)}{\partial x} \tag{A.5}$$

Integrating from $z = 0$ to L gives us the angular deviation within the material

$$\Delta\theta_1 = \theta_1(z = L) - \theta_1(z = 0) = \frac{1}{n_1}\int_0^L \frac{\partial \Delta n_1(x)}{\partial x}\partial z \tag{A.6}$$

To determine the deflection angle as seen from outside of the medium $\Delta\theta_2$ we apply the paraxial form of Snell's law $n_1\theta_2 = n_2\theta_2$ at the exit interface of the material

$$\Delta\theta_2 = n_1\Delta\theta_1 = \int_0^L \frac{\partial \Delta n_1(x)}{\partial x}\partial z. \tag{A.7}$$

Note that the deflection angle when seen from outside of the material is independent of the index within the material, consistent with previous analyses [116].

APPENDIX B: ESSENTIAL STATE MODEL DERIVATION

Following the treatment performed by Hu [33], the three level SOS model derived by Orr and Ward is

$$
\begin{aligned}
&\chi^{(3)}_{ijkl}(\omega_p+\omega_q+\omega_r;\omega_p,\omega_q,\omega_r)\\
&=\frac{N f^{(3)}}{\epsilon_0\hbar^3}\Bigg(\sum_{v,n,m}\Bigg(\frac{\mu^i_{gv}(\mu^l_{vn}-\mu^l_{gg})(\mu^k_{nm}-\mu^k_{gg})\mu^l_{mg}}{(\omega_{vg}-\omega_p-\omega_q-\omega_r)(\omega_{ng}-\omega_q-\omega_p)(\omega_{mg}-\omega_p)}\\
&+\frac{\mu^j_{gv}(\mu^k_{vn}-\mu^k_{gg})(\mu^i_{nm}-\mu^i_{gg})\mu^l_{mg}}{(\omega^*_{vg}+\omega_p)(\omega^*_{ng}+\omega_q+\omega_p)(\omega_{mg}-\omega_r)}\\
&+\frac{\mu^l_{gv}(\mu^i_{vn}-\mu^i_{gg})(\mu^k_{nm}-\mu^k_{gg})\mu^j_{mg}}{(\omega^*_{vg}+\omega_r)(\omega_{ng}-\omega_q-\omega_p)(\omega_{mg}-\omega_p)}\\
&+\frac{\mu^j_{gv}(\mu^k_{vk}-\mu^k_{gg})(\mu^l_{nm}-\mu^l_{gg})\mu^i_{mg}}{(\omega^*_{vg}+\omega_p)(\omega^*_{ng}+\omega_q+\omega_p)(\omega^*_{mg}+\omega_p+\omega_q+\omega_r)}\Bigg)\\
&+\sum_{v,n}\Bigg(\frac{\mu^i_{gn}\mu^l_{ng}\mu^k_{gm}\mu^j_{mg}}{(\omega_{ng}-\omega_p-\omega_q-\omega_r)(\omega_{ng}-\omega_r)(\omega_{mg}-\omega_p)}\\
&+\frac{\mu^i_{gn}\mu^l_{ng}\mu^k_{gm}\mu^j_{mg}}{(\omega^*_{mg}+\omega_q)(\omega_{ng}-\omega_r)(\omega_{mg}-\omega_p)}\\
&+\frac{\mu^l_{gn}\mu^i_{ng}\mu^j_{gm}\mu^k_{mg}}{(\omega^*_{ng}+\omega_r)(\omega^*_{mg}+\omega_p)(\omega_{mg}-\omega_q)}\\
&+\frac{\mu^l_{gn}\mu^i_{ng}\mu^j_{gm}\mu^k_{mk}}{(\omega^*_{ng}+\omega_r)(\omega^*_{mg}+\omega_p)(\omega^*_{ng}+\omega_p+\omega_q+\omega_r)}\Bigg)\Bigg).
\end{aligned}
\tag{B.1}
$$

Where *v*, *n*, and *m* are the states over which the summation is performed, μ^i_{vn} is the transition dipole moment from state *v* to state *n* along direction *i*, $\bar{\mu}^x{}_{vm}=\mu^x_{vm}-\delta_{vm}\,\mu^x_{gg}$, where μ^i_{gg} is the ground state permanent dipole, and $\bar{\omega}_{vm}=\omega_{vm}-i\,\Gamma_{vm}$ where ω_{vm} is the angular frequency between state *v* and *m*, Γ_{vm} is the damping factor between *v* and *m* and $f^{(3)}$ is the local field correction

$$f^{(3)} = \left(\frac{\epsilon_r^i(\omega_p + \omega_q + \omega_r) + 2}{3}\right)\left(\frac{\epsilon_r^j(\omega_p) + 2}{3}\right)\left(\frac{\epsilon_r^k(\omega_q) + 2}{3}\right)\left(\frac{\epsilon_r^l(\omega_r) + 2}{3}\right), \tag{B.2}$$

where $\epsilon_r^i(\omega) = n^i(\omega)^2$ is the relative permittivity of free space along.

The first summation in Eq. (1.42) (shown in green) is the three level term which originates from the second application of perturbation theory. The second summation that appear (shown in blue) is the two level term which originates from the first application of perturbation theory. The first sum in Eq. (1.42) is taken over thee indices v, n, and m where the indices can refer to either the first excited state e or the second excited state e'. Permuting two distinct elements over thee positions gives us the following permutations

$$\begin{gathered} \text{a) } v = e, n = e, m = e, \text{ b) } v = e, n = e, m = e' \\ \text{c) } v = e, n = e', m = e, \text{ d) } v = e, n = e', m = e' \\ \text{e) } v = e', n = e, m = e, \text{ f) } v = e', n = e, m = e' \\ \text{g) } v = e', n = e', m = e, \text{ h) } v = e', n = e', m = e'. \end{gathered} \tag{B.3}$$

Of the permutations listed in Eq. (B.3), only b) through g) are physically meaningful, with a) and h) not corresponding to a physical transition.

For the case of a symmetric molecule, quantum mechanical selection rules require that the permanent dipole moment is zero, 1PA transitions must change parity, while 2PA transitions must conserve parity. Thus for a three level system with ground state g, first excited state e, and second excited state e', $\mu_{gg}^i = \mu_{ee}^i = \mu_{e'e'}^i = \mu_{ge'}^i = 0$. For the three level summation term in Eq. (1.42) only permutation c) is nonzero, yielding

For the co-polarized nondegenerate case, there are six perturbations that add to the total susceptibility

$$\hat{\chi}^{(3)}_{xxxx}(\omega_p;\omega_e) = \chi^{(3)}_{xxxx}(\omega_p;\omega_p,\omega_e,-\omega_e) + \chi^{(3)}_{xxxx}(\omega_p;\omega_p,-\omega_e,\omega_e) + \chi^{(3)}_{xxxx}(\omega_p;-\omega_e,\omega_p,\omega_e) + \chi^{(3)}_{xxxx}(\omega_p;\omega_e,\omega_p,-\omega_e) + \chi^{(3)}_{xxxx}(\omega_p;\omega_e,-\omega_e,\omega_p) + \chi^{(3)}_{xxxx}(\omega_p;-\omega_e,\omega_e,\omega_p). \quad \text{(B.4)}$$

Performing the summations the three level terms we have

$$\chi^{(3)}_{xxxx}(\omega_p;\omega_p,\omega_e,-\omega_e) = \frac{f^{(3)}N{\mu^x_{ee'}}^2{\mu^x_{ge}}^2}{\hbar^3\epsilon_0}\left(\frac{1}{(-\omega_p+\omega_{eg})^2(-\omega_e-\omega_p+\omega_{ge'})} + \frac{1}{(-\omega_p+\omega_{eg})(-\omega_e-\omega_p+\omega_{ge'})(-\omega_e+\omega^*_{eg})} + \frac{1}{(\omega_p+\omega^*_{eg})^2(\omega_e+\omega_p+\omega^*_{ge'})} + \frac{1}{(\omega_e+\omega_{eg})(\omega_p+\omega^*_{eg})(\omega_e+\omega_p+\omega^*_{ge'})}\right) \quad \text{(B.5)}$$

$$\chi^{(3)}_{xxxx}(\omega_p;\omega_p,-\omega_e,\omega_e) = \frac{f^{(3)}N{\mu^x_{ee'}}^2{\mu^x_{ge}}^2}{\hbar^3\epsilon_0}\left(\frac{1}{(-\omega_p+\omega_{eg})^2(\omega_e-\omega_p+\omega_{ge'})} + \frac{1}{(-\omega_p+\omega_{ge})(\omega_e-\omega_p+\omega_{ge'})(\omega_e+\omega^*_{ge})} + \frac{1}{(\omega_p+\omega^*_{ge})^2(-\omega_e+\omega_p+\omega_{ge'})} + \frac{1}{(-\omega_e+\omega_{ge})(\omega_p+\omega^*_{ge})(-\omega_e+\omega_p+\omega^*_{ge'})}\right) \quad \text{(B.6)}$$

$$\chi^{(3)}_{xxxx}(\omega_p;\omega_e,\omega_p,-\omega_e)$$

$$= \frac{f^{(3)}N{\mu^x_{ee'}}^2{\mu^x_{ge}}^2}{\hbar^3\epsilon_0}\left(\frac{1}{(-\omega_e+\omega_{eg})(-\omega_p+\omega_{eg})(-\omega_e-\omega_p+\omega_{ge'})}\right.$$

$$+\frac{1}{(-\omega_e+\omega_{ge})(-\omega_e-\omega_p+\omega_{ge'})(-\omega_e+\omega^*_{ge})} \tag{B.7}$$

$$+\frac{1}{(\omega_e+\omega_{ge})(\omega_e+\omega^*_{ge})(\omega_e+\omega_p+\omega_{ge'})}$$

$$\left.+\frac{1}{(\omega_e+\omega^*_{ge})(\omega_p+\omega_{ge})(\omega_e+\omega_p+\omega_{ge'})}\right)$$

$$\chi^{(3)}_{xxxx}(\omega_p;-\omega_e,\omega_p,\omega_e)$$

$$= \frac{f^{(3)}N{\mu^x_{ee'}}^2{\mu^x_{ge}}^2}{\hbar^3\epsilon_0}\left(\frac{1}{(\omega_e+\omega_{eg})(-\omega_p+\omega_{eg})(\omega_e-\omega_p+\omega_{ge'})}\right.$$

$$+\frac{1}{(\omega_e+\omega_{ge})(\omega_e-\omega_p+\omega_{ge'})(\omega_e+\omega_{ge})} \tag{B.8}$$

$$+\frac{1}{(-\omega_e+\omega_{ge})(-\omega_e+\omega^*_{ge})(-\omega_e+\omega_p+\omega_{ge'})}$$

$$\left.+\frac{1}{(-\omega_e+\omega^*_{ge})(\omega_p+\omega^*_{ge})(-\omega_e+\omega_p+\omega_{ge'})}\right)$$

$$\chi^{(3)}_{xxxx}(\omega_p;\omega_e,-\omega_e,\omega_p)$$

$$= \frac{f^{(3)}N{\mu^x_{ee'}}^2{\mu^x_{ge}}^2}{\hbar^3\epsilon_0}\left(\frac{1}{(-\omega_e+\omega_{eg})(-\omega_p+\omega_{eg})\omega_{ge'}}\right.$$

$$+\frac{1}{(-\omega_e+\omega_{ge})\omega_{ge'}(\omega_p+\omega_{ge'})}+\frac{1}{(-\omega_p+\omega_{ge})(\omega_e+\omega^*_{ge})\omega^*_{ge'}} \tag{B.9}$$

$$\left.+\frac{1}{(\omega_e+\omega^*_{ge})(\omega_p+\omega^*_{ge})\omega^*_{ge'}}\right)$$

$$\chi^{(3)}_{xxxx}(\omega_p;-\omega_e,\omega_e,\omega_p)$$
$$= \frac{f^{(3)}N{\mu^x_{ee'}}^2{\mu^x_{ge}}^2}{\hbar^3\epsilon_0}\left(\frac{1}{(\omega_e+\omega_{ge})(-\omega_p+\omega_{ge})\omega_{ge'}}\right.$$
$$+\frac{1}{(\omega_e+\omega_{ge})\omega_{ge'}(\omega_p+\omega^*_{ge})}+\frac{1}{(-\omega_p+\omega_{ge})(-\omega_e+\omega^*_{ge})\omega_{ge'}} \quad \text{(B.10)}$$
$$\left.+\frac{1}{(-\omega_e+\omega_{ge})(\omega_p+\omega^*_{ge})\omega_{ge'}}\right)$$

The summations for the two level terms are

$$\chi^{(3)}_{xxxx}(\omega_p;\omega_p,\omega_e,-\omega_e)$$
$$= \frac{f^{(3)}N{\mu^x_{ge}}^4}{\hbar^3\epsilon_0}\left(\frac{1}{(\omega_e+\omega_{eg})(-\omega_p+\omega_{eg})^2}\right.$$
$$+\frac{1}{(\omega_e+\omega_{eg})(-\omega_p+\omega_{eg})(\omega_e+\omega^*_{eg})}+\frac{1}{(-\omega_e+\omega^*_{eg})(\omega_p+\omega_{eg})^2} \quad \text{(B.11)}$$
$$\left.+\frac{1}{(-\omega_e+\omega_{eg})(-\omega_e+\omega^*_{eg})(\omega_p+\omega^*_{eg})}\right)$$

$$\chi^{(3)}_{xxxx}(\omega_p;\omega_p,-\omega_e,\omega_e)$$
$$= \frac{f^{(3)}N{\mu^x_{ge}}^4}{\hbar^3\epsilon_0}\left(\frac{1}{(-\omega_e+\omega_{eg})(-\omega_p+\omega_{eg})^2}\right.$$
$$+\frac{1}{(-\omega_e+\omega_{eg})(-\omega_p+\omega_{eg})(-\omega_e+\omega^*_{eg})}+\frac{1}{(\omega_e+\omega^*_{eg})(\omega_p+\omega^*_{eg})^2} \quad \text{(B.12)}$$
$$\left.+\frac{1}{(\omega_e+\omega_{eg})(\omega_e+\omega^*_{eg})(\omega_p+\omega^*_{eg})}\right)$$

$$\chi^{(3)}_{xxxx}(\omega_p;-\omega_e,\omega_p,\omega_e)$$

$$= \frac{f^{(3)}N{\mu^x_{ge}}^4}{\hbar^3\epsilon_0}\left(\frac{1}{(-\omega_e+\omega_{eg})(\omega_e+\omega_{eg})(-\omega_p+\omega_{eg})}\right.$$

$$+\frac{1}{(-\omega_p+\omega_{eg})(-\omega_e+\omega^*_{eg})(\omega_e+\omega^*_{eg})} \tag{B.13}$$

$$+\frac{1}{(-\omega_e+\omega_{eg})(\omega_e+\omega_{eg})(\omega_p+\omega^*_{eg})}$$

$$\left.+\frac{1}{(-\omega_e+\omega^*_{eg})(\omega_e+\omega^*_{eg})(\omega_p+\omega^*_{eg})}\right)$$

$$\chi^{(3)}_{xxxx}(\omega_p;\omega_e,\omega_p,-\omega_e)$$

$$= \frac{f^{(3)}N{\mu^x_{ge}}^4}{\hbar^3\epsilon_0}\left(\frac{1}{(-\omega_e+\omega_{eg})(\omega_e+\omega_{eg})(-\omega_p+\omega_{eg})}\right.$$

$$+\frac{1}{(-\omega_p+\omega_{eg})(-\omega_e+\omega^*_{eg})(\omega_e+\omega^*_{eg})} \tag{B.14}$$

$$+\frac{1}{(-\omega_e+\omega_{eg})(\omega_e+\omega_{eg})(\omega_p+\omega^*_{eg})}$$

$$\left.+\frac{1}{(-\omega_e+\omega^*_{eg})(\omega_e+\omega^*_{eg})(\omega_p+\omega^*_{eg})}\right)$$

$$\chi^{(3)}_{xxxx}(\omega_p;\omega_e,-\omega_e,\omega_p)$$

$$= \frac{f^{(3)}N{\mu^x_{ge}}^4}{\hbar^3\epsilon_0}\left(\frac{1}{(-\omega_e+\omega_{eg})(-\omega_p+\omega_{eg})^2}\right.$$

$$+\frac{1}{(-\omega_e+\omega_{eg})(-\omega_p+\omega_{eg})(-\omega_e+\omega^*_{eg})}+\frac{1}{(\omega_e+\omega^*_{eg})(\omega_p+\omega^*_{eg})^2} \tag{B.15}$$

$$\left.+\frac{1}{(\omega_e+\omega_{eg})(\omega_e+\omega^*_{eg})(\omega_p+\omega^*_{eg})}\right)$$

$$
\begin{aligned}
&\chi^{(3)}_{xxxx}(\omega_p;-\omega_e,\omega_e,\omega_p)\\
&=\frac{f^{(3)}N{\mu^x_{ge}}^4}{\hbar^3\epsilon_0}\left(\frac{1}{(\omega_e+\omega_{eg})(-\omega_p+\omega_{eg})^2}\right.\\
&+\frac{1}{(\omega_e+\omega_{eg})(-\omega_p+\omega_{eg})(\omega_e+\omega^*_{eg})}+\frac{1}{(-\omega_e+\omega^*_{eg})(\omega_p+\omega^*_{eg})^2}\\
&\left.+\frac{1}{(-\omega_e+\omega_{eg})(-\omega_e+\omega^*_{eg})(\omega_p+\omega^*_{eg})}\right)
\end{aligned}
\tag{B.16}
$$

For wavelengths close to the resonance, we can drop the nonresonant terms and simplify the expression for the total susceptibility

$$
\begin{aligned}
&\chi^{(3)}_{xxxx}(\omega_p;\omega_e)\\
&=-\frac{f^{(3)}N{\mu^x_{ge}}^4}{\hbar^3\epsilon_0}\left(\frac{2}{(-\omega_e+\omega_{eg})(-\omega_p+\omega_{eg})^2}\right.\\
&\left.+\frac{2}{(-\omega_e+\omega_{eg})(-\omega_p+\omega_{eg})(-\omega_e+\omega^*_{eg})}\right)\\
&+\frac{f^{(3)}N{\mu^x_{ee'}}^2{\mu^x_{ge}}^2}{\hbar^3\epsilon_0}\left(\frac{1}{(-\omega_p+\omega_{eg})^2(-\omega_e-\omega_p+\omega_{ge'})}\right.\\
&+\frac{1}{(-\omega_e+\omega_{eg})(-\omega_p+\omega_{eg})(-\omega_e-\omega_p+\omega_{ge'})}\\
&+\frac{1}{(-\omega_e+\omega_{ge})(-\omega_e-\omega_p+\omega_{ge'})(-\omega_e+\omega^*_{ge})}\\
&\left.+\frac{1}{(-\omega_p+\omega_{ge})(-\omega_e-\omega_p+\omega_{ge'})(-\omega_e+\omega^*_{ge})}\right).
\end{aligned}
\tag{B.17}
$$

For the case of degenerate beams $\omega_p=\omega_e=\omega$ which simplifies the expression to

$$\hat{\chi}^{(3)}_{xxxx}(\omega;\omega)$$
$$= -\frac{Nf^{(3)}{\mu^x_{ge}}^4}{\hbar^3\epsilon_0}\left(\frac{1}{\left(\omega_{eg}-\omega\right)^3}+\frac{1}{\left(\omega_{eg}-\omega\right)^2\left(\omega^*_{eg}-\omega\right)}\right)$$
$$+\frac{Nf^{(3)}{\mu^x_{ee'}}^2{\mu^x_{ge}}^2}{\hbar^3\epsilon_0}\left(\frac{1}{\left(\omega_{eg}-\omega\right)^2\left(\omega_{e'g}-2\omega\right)}\right. \tag{B.18}$$
$$\left.+\frac{1}{\left(\omega_{eg}-\omega\right)\left(\omega_{e'g}-2\omega\right)\left(\omega^*_{eg}-\omega\right)}\right).$$

APPENDIX C: BEAM DEFLECTION SCHEMATICS

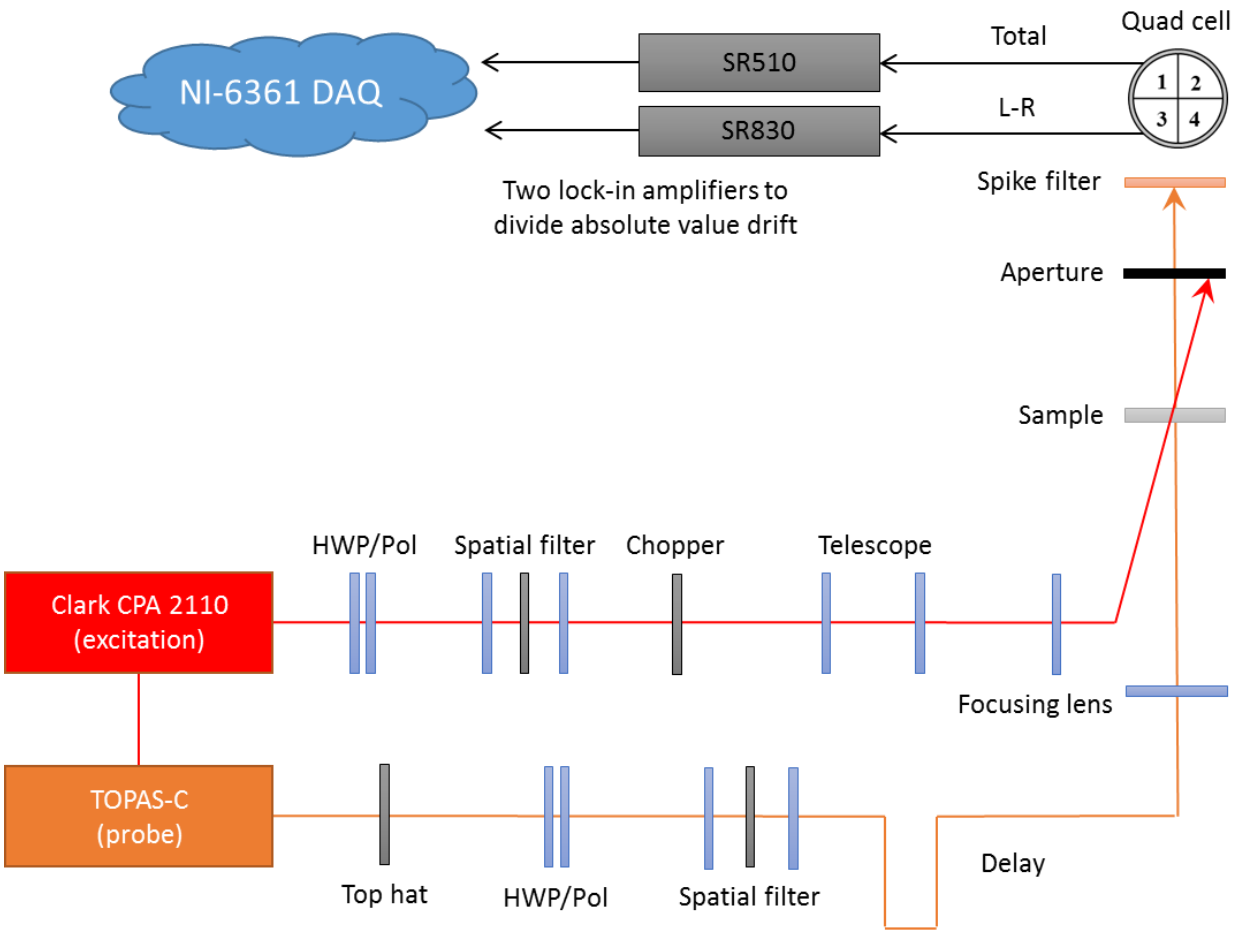

Figure 80: BD schematic using Clark-MXR excitation with TOPAS-C probe (Clark-C).

The initial BD apparatus was constructed in the Clark-MXR laboratory. Because of the relatively narrow bandwidth of the Clark-MXR laser (approximately 10 nm) the spatial filtering telescope and focusing is performed using BK7 lenses, while the attenuation is performed using a wave plate and polarizer pair. Adjustment of the excitation spot size is done using the telescope before the focusing final focusing lens.

A SR830 digital lock in amplifier was used to measure the L-R signal, while a SR510 analog lock in was used to measure the total signal in order to account for drift in the probe energy.

Note that when using two different lock in amplifiers, care must be taken to matching the operating parameters of each so that the second lock in is effective in reducing the noise in the signal.

Note that the attenuation is performed before the spatial filter to ensure that imperfections in the polarizer do not distort the probe profile. Overall, the use of dispersive optics provides the greatest ease of set up and compact footprint, with the penalty of longer pulse durations and reduced temporal resolution.

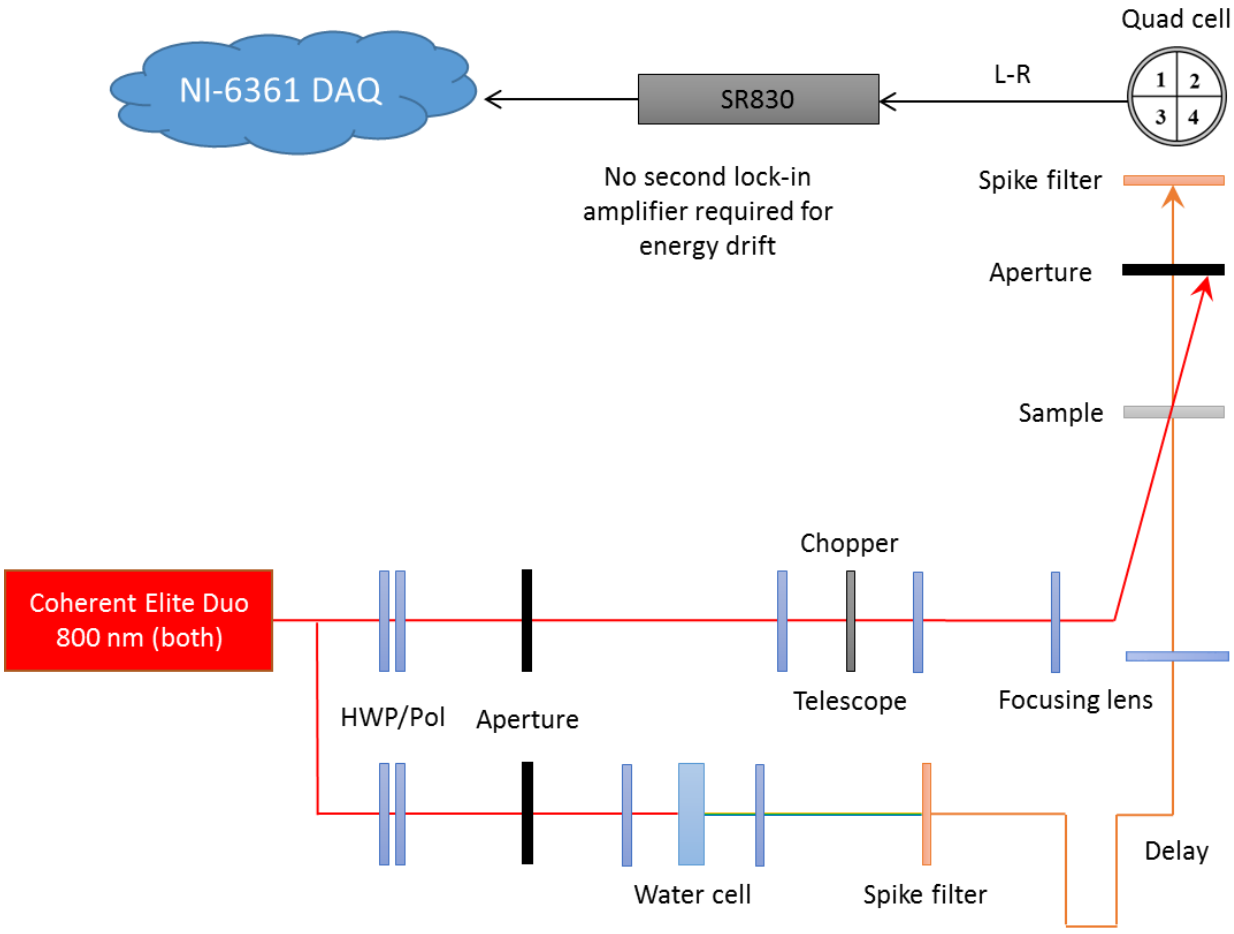

Figure 81: BD schematic using Coherent Elite Duo excitation with WLC probe (Coherent-WL).

The first BD apparatus using the Coherent Elite Duo and was a temporary set up replaced when the TOPAS-800 was upgraded for 35 fs pulses. Typical pulse durations are 50 fs for the excitation and 170 fs for the probe. The broadening of the excitation is due primarily to the wave plate polarizer pair used for attenuation, which uses approximately 8 mm of calcite glass. The broadening of the probe is due in part to chirp induced by the WLC generation in water as well as the narrow band pass filters (10 nm) used to spectrally filter the WLC and generate the probe pulse.

Spatial filtering is performed without the use of a telescope and pinhole, rather the beam is top hatted using an aperture and allowed to propagate a far distance to achieve a Gaussian beam profile. As in the case of a pinhole and telescope, the aperture is placed after the polarizer to maintain the Gaussian beam profile. The chopper was placed at the focus of the excitation spot size adjustment telescope to minimize the noise induced due to partial chopping of pulses by the blades.

It was found that in this configuration, the use of a second lock in did not enhance the SNR significantly. This is due to the excellent energy stability of the Coherent laser output (approximately 0.5%, typically).

Because of the poor temporal resolution, the use of WLC to generate the probe beam is not recommended. It may be possible to improve the temporal resolution by using a prism compressor. However, note that a prism compressor only eliminates the linear chirp associated with GVD. It will not remove higher order nonlinear chirp and hence the minimum attainable pulse duration may be longer than the transform limited pulse duration.

Aside from the long pulse durations, this configuration is limited in the range of wavelengths that can be used for the excitation and probe pulses. In this configuration, the excitation is fixed at 800 nm, while the probe is variable from about 400 – 1100 nm, which is the range of usable wavelengths available from WLC generated in water.

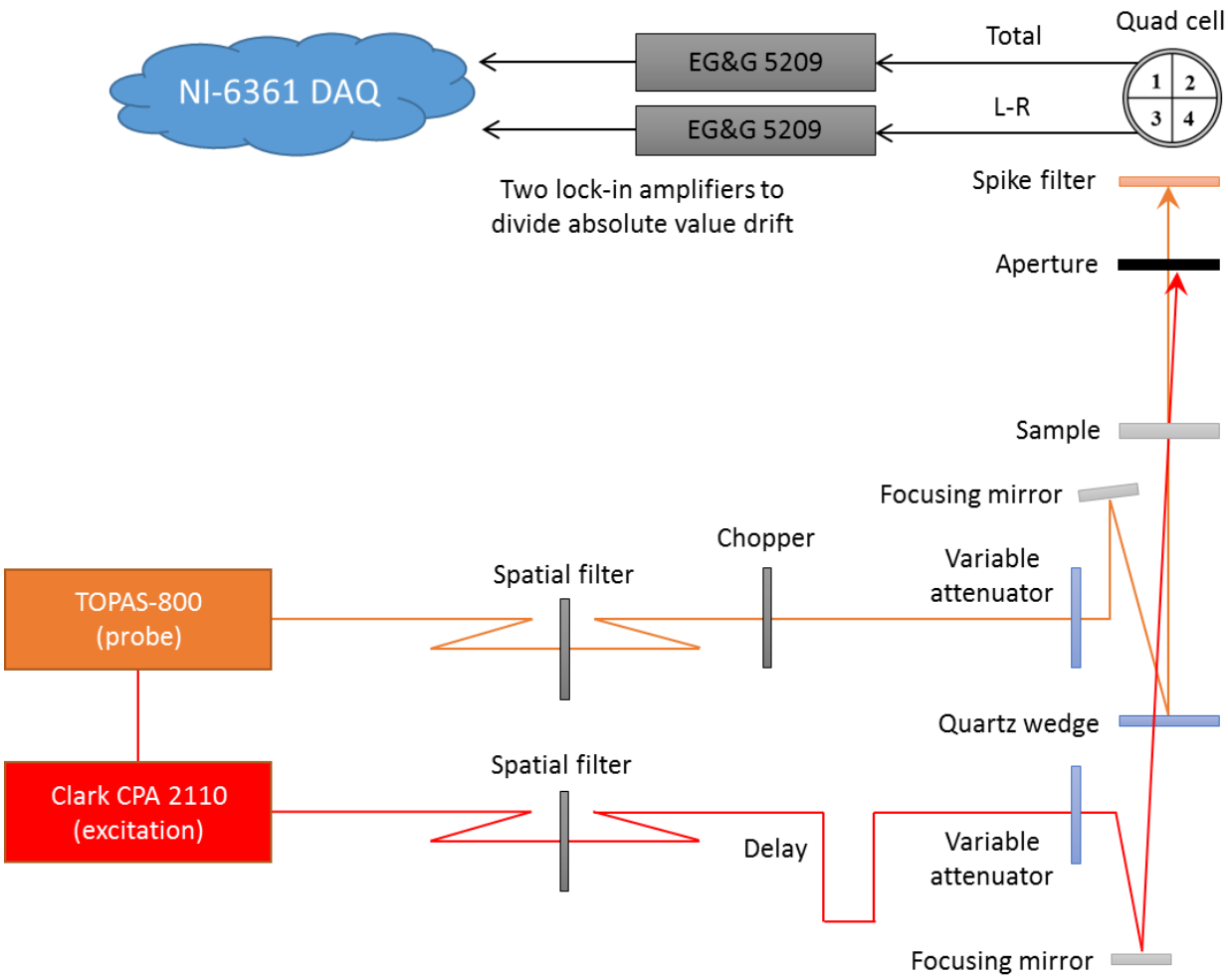

Figure 82: BD schematic using Coherent Elite Duo excitation with TOPAS-800 probe (Coherent-800)

In order to utilize the ultrashort pulse durations available from the Coherent Elite Duo, the spectrally filtered WLC generated in water was replace by the TOPAS-800 upgraded to work with 35 fs pulses. In order to minimize the effects of chirp in dispersive elements as well as chromatic aberration and PTD due to focusing lenses, the spatial filtering and collimation was performed using reflective telescopes, while the focusing onto the sample was performed using mirrors.

Attenuation of the beam was performed using variable neutral density filters similar to those used to those used for equalization of the pulse energy between arms in the DA Z-Scan. When using variable neutral density filters, care should be taken to ensure that the beam passing through the filter is spatially as small as possible, to minimize any distortion of the beam due to variances in the transmission gradient across the beam. For a beam a few millimeters in diameter, this distortion does not appear to be significant.

To ensure a small angle between the excitation and probe beams, a quartz plate was used to spatially overlap the excitation and probe beams. This plate must be wedged as the reflection of the probe from the front and back surfaces of the plate will be parallel and slightly delayed with respect to each other if it is not wedged. This may cause some confusion in finding zero delay between the pulses as well as complicating the calculation of E_p from the lock in signal, as the lock in will register the energy of both pulses, although only one pulse is actually deflected and contributes to ΔE_p.

Additionally, in order to improve the noise reduction from using two lock ins, the SR830 and SR510 were replaced by two EG&G 5209 analog lock in amplifiers. Even though the EG&G 5209 does not have the noise rejection performance of the SR830, it was the only operational matched pair available, and it is thought that the uniformity of the response between ΔE_p and E_p should outweigh the reduced performance.

APPENDIX D: COPYRIGHT PERMISSIONS

Dear Manuel,

We do not provide any such forms. If you wish to provide a form, I can sign it, but we don't prepare anything.

Best wishes,

Hannah

Hannah Bembia, Publishing Administrative Assistant
phone: +1.202.416.1974 | e-mail: hbembia@osa.org

The Optical Society (OSA)
2010 Massachusetts Ave., NW
Washington, DC 20036 USA
www.osa.org

From: Manuel Ferdinandus [mailto:mrf@knights.ucf.edu]
Sent: Monday, October 14, 2013 5:03 PM
To: pubscopyright
Subject: Re: Copyright permission letters

Ms. Bembia,
Is there a form that you can send me that documents these permissions? It is expected in the appendix of my dissertation. I have included two examples of such forms.

On 10/14/2013 4:47 PM, pubscopyright wrote:

Dear Manuel,

Thank you for contacting The Optical Society.

Because you are the author of the source papers from which you wish to reproduce material, OSA considers your requested use of its copyrighted materials to be permissible within the author rights granted in the Copyright Transfer Agreement submitted by the requester on acceptance for publication of his/her manuscript. It is requested that a complete citation of the original material be included in any publication. This permission assumes that the material was not reproduced from another source when published in the original publication.

Please let me know if you have any questions.

Best,

Hannah

Hannah Bembia
October 14, 2013
Authorized Agent, The Optical Society

From: Manuel Ferdinandus [mailto:mrf@knights.ucf.edu]
Sent: Friday, October 11, 2013 11:20 PM
To: pubscopyright
Subject: Copyright permission letters

To whom it may concern,

I am writing my PhD dissertation in optics at CREOL, The College of Optics and Photonics at the University of Central Florida. I am seeking copyright permission letters for the following articles for which I am the first author:

Ferdinandus, M. R., et al. (2012). "Dual-arm Z-scan technique to extract dilute solute nonlinearities from solution measurements." Opt. Mater. Express 2(12): 1776-1790.

Ferdinandus, M. R., et al. (2013). "Beam deflection measurement of time and polarization resolved ultrafast nonlinear refraction." Opt. Lett. 38(18): 3518-3521.

Please let me know what actions are required for me to attain copyright permission letters for these works.

Thanks!

--
Manuel Ferdinandus
Graduate Student
CREOL, The College of Optics and Photonics
University of Central Florida
4000 Central Florida Blvd. Orlando, Florida, 32816
Phone: 781-541-0071
Email: mrf@knights.ucf.edu

--

Manuel Ferdinandus
Graduate Student
CREOL, The College of Optics and Photonics
University of Central Florida

4000 Central Florida Blvd. Orlando, Florida, 32816
Phone: 781-541-0071
Email: mrf@knights.ucf.edu

LIST OF REFERENCES

1. Fox, M., *Optical Properties of Solids*. Oxford Master Series in Condensed Matter Physics, ed. M. Fox, S. Blundell, and J. Stevenson. 2001, New York: Oxford University Press.
2. Boyd, R.W., *Nonlinear Optics*. 3rd ed. 2008, New York: Academic Press.
3. Yariv, A. and W. Louisell, *Theory of the optical parametric oscillator.* Quantum Electronics, IEEE Journal of, 1966. **2**(9): p. 418-424.
4. Pearson, J.E., A. Yariv, and U. Ganiel, *Observations of Parametric Fluorescence and Oscillation in the Infrared.* Appl. Opt., 1973. **12**(6): p. 1165-1171.
5. Venkatram, N., D.N. Rao, and M.A. Akundi, *Nonlinear absorption, scattering and optical limiting studies of CdS nanoparticles.* Opt. Express, 2005. **13**(3): p. 867-872.
6. Heebner, J.E. and R.W. Boyd, *Enhanced all-optical switching by use of a nonlinear fiber ring resonator.* Opt. Lett., 1999. **24**(12): p. 847-849.
7. Birge, R.R. and B.M. Pierce, *Semiclassical time-dependent theory of two-photon spectroscopy. The effect of dephasing in the virtual level on the two-photon excitation spectrum of isotachysterol.* International Journal of Quantum Chemistry, 1986. **29**(4): p. 639-656.
8. Göppert-Mayer and M. Über, *Elementarakte Mit Zwei Quantensprüngen.* Ann. Phys., 1931. **401**: p. 273-294.
9. Kaiser, W. and C.G.B. Garrett, *Two-Photon Excitation in CaF_2: Eu^{2+}*. Physical Review Letters, 1961. **7**(6): p. 229-231.

10. Stryland, E.W.V., et al., *Optical limiting with semiconductors.* J. Opt. Soc. Am. B, 1988. **5**(9): p. 1980-1988.
11. Blair, S., J.E. Heebner, and R.W. Boyd, *Beyond the absorption-limited nonlinear phase shift with microring resonators.* Opt. Lett., 2002. **27**(5): p. 357-359.
12. Le Moal, E., et al., *Two-photon fluorescence isotropic-single-objective microscopy.* Opt. Lett., 2012. **37**(1): p. 85-87.
13. Maruo, S., O. Nakamura, and S. Kawata, *Three-dimensional microfabrication with two-photon-absorbed photopolymerization.* Opt. Lett., 1997. **22**(2): p. 132-134.
14. Negus, D.K., et al. *Sub-100 Femtosecond Pulse Generation by Kerr Lens Mode-locking in Ti:Al2O3*. 1991. Optical Society of America.
15. Stegeman, G.I. and R.E. Stegeman, *Nonlinear Optics: Phenomena, Materials and Devices*. Wiley Series in Pure and Applied Optics, ed. G. Boreman. 2012, Hoboken: Wiley.
16. Owyoung, A. and P.S. Peercy, *Precise characterization of the Raman nonlinearity in benzene using nonlinear interferometry.* Journal of Applied Physics, 1977. **48**(2): p. 674-677.
17. McMorrow, D., W.T. Lotshaw, and G.A. Kenney-Wallace, *Femtosecond optical Kerr studies on the origin of the nonlinear responses in simple liquids.* Quantum Electronics, IEEE Journal of, 1988. **24**(2): p. 443-454.
18. Haque, S.A. and J. Nelson, *Toward Organic All-Optical Switching.* Science, 2010. **327**(5972): p. 1466-1467.
19. Hales, J.M., et al., *Design of Polymethine Dyes with Large Third-Order Optical Nonlinearities and Loss Figures of Merit.* Science, 2010. **327**(5972): p. 1485-1488.

20. Zhong, Q. and J.T. Fourkas, *Optical Kerr Effect Spectroscopy of Simple Liquids†.* The Journal of Physical Chemistry B, 2008. **112**(49): p. 15529-15539.
21. Padilha, L.A., et al., *Excited state absorption and decay kinetics of near IR polymethine dyes.* Chemical Physics, 2008. **352**(1–3): p. 97-105.
22. Abrams, R.L. and R.C. Lind, *Degenerate four-wave mixing in absorbing media.* Opt. Lett., 1978. **2**(4): p. 94-96.
23. M., S.-B., et al., *Sensitive Measurement of Optical Nonlinearities Using a Single Beam.* IEEE Journal of Quantum Electronics, 1990. **26**(4): p. 10.
24. Christodoulides, D.N., et al., *Nonlinear refraction and absorption: mechanisms and magnitudes.* Adv. Opt. Photon., 2010. **2**(1): p. 60-200.
25. Thole, B.T., *Molecular polarizabilities calculated with a modified dipole interaction.* Chemical Physics, 1981. **59**(3): p. 341-350.
26. Fu, J., *Molecular Structure – Nonlinear Optical Property Relationships For A Series Of Polymethine And Squaraine Molecules*, in *College of Optics and Photonics*. 2006, University of Central Florida.
27. Orr, B.J. and J.F. Ward, *Perturbation theory of the non-linear optical polarization of an isolated system.* Molecular Physics, 1971. **20**(3): p. 513-526.
28. Ward, J., *Calculation of Nonlinear Optical Susceptibilities Using Diagrammatic Perturbation Theory.* Reviews of Modern Physics, 1965. **37**(1): p. 1-18.

29. Mansoor Sheik-Bahae, D.C.H., David J. Hagan, and Eric W. Van Stryland, *Dispersion of Bound Electronic Nonlinear Refraction in Solids.* IEEE Journal of Quantum Electronics, 1991. **27**(6): p. 1296-1309.
30. Cronstrand, P., Y. Luo, and H. Ågren, *Generalized few-state models for two-photon absorption of conjugated molecules.* Chemical Physics Letters, 2002. **352**(3): p. 262-269.
31. Hutchings, D.C., et al., *Kramers-Krönig relations in nonlinear optics.* Optical and Quantum Electronics, 1992. **24**(1): p. 1-30.
32. Zojer, E., et al., *Two-Photon Absorption in Quadrupolar π-Conjugated Molecules: Influence of the Nature of the Conjugated Bridge and the Donor–Acceptor Separation.* Chemistry – A European Journal, 2004. **10**(11): p. 2668-2680.
33. Hu, H., *Third Order Nonlinearity of Organic Molecules,* in *College of Optics and Photonics*. 2012, University of Central Florida: Orlando.
34. Hales, J.M., et al., *Design of Organic Chromophores for All-Optical Signal Processing Applications.* Chemistry of Materials, 2013.
35. Maine, P., et al., *Generation of ultrahigh peak power pulses by chirped pulse amplification.* IEEE J. Quantum Electron, 1988. **24**: p. 398–403
36. Shimizu, F., *Frequency Broadening in Liquids by a Short Light Pulse.* Physical Review Letters, 1967. **19**(19): p. 1097-1100.
37. Ruzicka, B.A., et al., *Spatially resolved pump-probe study of single-layer graphene produced by chemical vapor deposition [Invited]*. Opt. Mater. Express, 2012. **2**(6): p. 708-716.

38. Cho, G.C., W. Kütt, and H. Kurz, *Subpicosecond time-resolved coherent-phonon oscillations in GaAs.* Physical Review Letters, 1990. **65**(6): p. 764-766.

39. Lepkowicz, R.S., et al. *Femtosecond to nanosecond characterization of the excited-state properties of polymethine molecules*. 2004. Optical Society of America.

40. Schroeder, W.A., et al., *Intrinsic and induced anisotropy of nonlinear absorption and refraction in zinc blende semiconductors.* J. Opt. Soc. Am. B, 1995. **12**(3): p. 401-415.

41. Weaire, D., et al., *Effect of low-power nonlinear refraction on laser-beam propagation in InSb.* Opt. Lett., 1979. **4**(10): p. 331-333.

42. Sheik-bahae, M., A.A. Said, and E.W.V. Stryland, *High-sensitivity, single-beam n_2 measurements.* Opt. Lett., 1989. **14**(17): p. 3.

43. Liu, X., et al., *Theoretical study on the closed-aperture Z-scan curves in the materials with nonlinear refraction and strong nonlinear absorption.* Optics Communications, 2001. **197**(4–6): p. 431-437.

44. Ming, N.B., et al., *An Accurate Method For Extracting Nonlinear Refraction By Z-Scan Technique In The Presence Of Nonlinear Absorption.* Journal of Nonlinear Optical Physics & Materials, 2003. **12**(03): p. 307-315.

45. Tian, J.-G., et al., *Analysis of beam propagation in thick nonlinear media.* Appl. Opt., 1995. **34**(21): p. 4331-4336.

46. Gu, B., *Theory of Gaussian beam Z scan with simultaneous third- and fifth-order nonlinear refraction based on a Gaussian decomposition method.* J. Opt. Soc. Am. B, 2005. **22**(12): p. 2651-2659.

47. Ding, J.L., et al., *Nonlinear Optical Properties and Ultrafast Dynamics of Undoped and Doped Bulk SiC.* Chinese Physics Letters, 2010. **27**(12).

48. Santran, S., et al., *Precise and absolute measurements of the complex third-order optical susceptibility.* J. Opt. Soc. Am. B, 2004. **21**(12): p. 2180-2190.

49. Balu, M., et al., *Broadband Z-scan characterization using a high-spectral-irradiance, high-quality supercontinuum.* J. Opt. Soc. Am. B, 2008. **25**(2): p. 159-165.

50. Yan, X.-Q., et al., *Polarization characteristics of nonlinear refraction and nonlinear scattering in several solvents.* J. Opt. Soc. Am. B, 2012. **29**(10): p. 2721-2728.

51. Corrêa, D.S., et al. *Excited State Absorption Cross-Section Spectrum of Chlorophyll A.* 2007. Optical Society of America.

52. Chan, Y.-P., et al. *Z-Scan Measurement of ZnO Thin Films Using the Ultraviolet Femtosecond Pulses*. 2008. Optical Society of America.

53. Yang, L., et al., *Excited-state nonlinearity in polythiophene thin films investigated by the Z-scan technique.* Opt. Lett., 1992. **17**(5): p. 323-325.

54. Ferdinandus, M.R., et al., *Dual-arm Z-scan technique to extract dilute solute nonlinearities from solution measurements.* Opt. Mater. Express, 2012. **2**(12): p. 1776-1790.

55. Said, A.A., et al., *Determination of bound-electronic and free-carrier nonlinearities in ZnSe, GaAs, CdTe, and ZnTe.* J. Opt. Soc. Am. B, 1992. **9**(3): p. 405-414.

56. Ma, H., A.S.L. Gomes, and C.B. de Araujo, *Measurements of nondegenerate optical nonlinearity using a two-color single beam method.* Applied Physics Letters, 1991. **59**(21): p. 2666.

57. Ma, H. and C.B. de Araújo, *Two-color Z-scan technique with enhanced sensitivity.* Applied Physics Letters, 1995. **66**(13): p. 1581.

58. Schott, J.R., *Remote Sensing - The Image Chain Approach*. 1997: New York.

59. Bridges, R.E., G.L. Fischer, and R.W. Boyd, *Z-scan measurement technique for non-Gaussian beams and arbitrary sample thicknesses.* Opt. Lett., 1995. **20**(17): p. 1821-1823.

60. Milam, D., *Review and Assessment of Measured Values of the Nonlinear Refractive-Index Coefficient of Fused Silica.* Appl. Opt., 1998. **37**(3): p. 546-550.

61. Gong Qi-huang, L.I.J.-l.Z.T.-q.Y.H., *Ultrafast Third-Order Optical Nonlinearity of Organic Solvents Investigated by Subpicosecond Transient Optical Kerr Effect.* Chinese Physics Letters, 1998. **15**(1): p. 30-31.

62. Couris, S., et al., *An experimental investigation of the nonlinear refractive index (n2) of carbon disulfide and toluene by spectral shearing interferometry and z-scan techniques.* Chemical Physics Letters, 2003. **369**(3–4): p. 318-324.

63. Savitzky, A. and M.J.E. Golay, *Smoothing and Differentiation of Data by Simplified Least Squares Procedures.* Analytical Chemistry, 1964. **36**(8): p. 1627-1639.

64. KoosC, et al., *All-optical high-speed signal processing with silicon-organic hybrid slot waveguides.* Nat Photon, 2009. **3**(4): p. 216-219.

65. Lipson, M., *Guiding, modulating, and emitting light on Silicon-challenges and opportunities.* Lightwave Technology, Journal of, 2005. **23**(12): p. 4222-4238.

66. Zi-Ming, M., Q. Fei, and L. Zhi-Yuan, *Ultrafast all-optical switching in one-dimensional semiconductor–polymer hybrid nonlinear photonic crystals with relaxing Kerr nonlinearity.* Journal of Optics, 2012. **14**(6): p. 065003.

67. Eggleton, B.J., B. Luther-Davies, and K. Richardson, *Chalcogenide photonics.* Nat Photon, 2011. **5**(3): p. 141-148.

68. Aitchison, J.S., A. Villeneuve, and G.I. Stegeman, *All-optical switching in a nonlinear GaAlAs X junction.* Opt. Lett., 1993. **18**(14): p. 1153-1155.

69. Tanabe, T., et al., *All-optical switches on a silicon chip realized using photonic crystal nanocavities.* Applied Physics Letters, 2005. **87**(15): p. 151112-3.

70. Webster, S., et al., *Near-Unity Quantum Yields for Intersystem Crossing and Singlet Oxygen Generation in Polymethine-like Molecules: Design and Experimental Realization.* The Journal of Physical Chemistry Letters, 2010. **1**(15): p. 2354-2360.

71. Gu, B., W. Ji, and X.-Q. Huang, *Analytical expression for femtosecond-pulsed Z scans on instantaneous nonlinearity.* Appl. Opt., 2008. **47**(9): p. 1187-1192.

72. Sheik-Bahae, M., et al., *Measurement of nondegenerate nonlinearities using a two-color Z scan.* Opt. Lett., 1992. **17**(4): p. 3.

73. Terazima, M., *Ultrafast transient Kerr lens in solution detected by the dual-beam thermal-lens method.* Opt. Lett., 1995. **20**(1): p. 25-27.

74. Sato, Y., R. Morita, and M. Yamashita, *Study on Ultrafast Dynamic Behaviors of Different Nonlinear Refractive Index Components in CS2 Using a Femtosecond Interferometer.* Jpn. J. Appl. Phys., 1997. **36**(Pt. 1, No. 4A): p. 2109-2115.

75. Chen, Y.H., et al., *Measurement of transient nonlinear refractive index in gases using xenon supercontinuum single-shot spectral interferometry.* Opt. Express, 2007. **15**(12): p. 7458-7467.

76. Cong, P., Y.J. Chang, and J.D. Simon, *Complete Determination of Intermolecular Spectral Densities of Liquids Using Position-Sensitive Kerr Lens Spectroscopy.* The Journal of Physical Chemistry, 1996. **100**(21): p. 8613-8616.

77. Chang, Y.J., P. Cong, and J.D. Simon, *Isotropic and anisotropic intermolecular dynamics of liquids studied by femtosecond position-sensitive Kerr lens spectroscopy.* The Journal of Chemical Physics, 1997. **106**(21): p. 8639-8649.

78. Jackson, W.B., et al., *Photothermal deflection spectroscopy and detection.* Appl. Opt., 1981. **20**(8): p. 1333-1344.

79. Hömmerich, U., et al., *Optically induced lensing effects in Nd3+-doped laser glass measured by photothermal beam-deflection spectroscopy.* Opt. Lett., 1992. **17**(3): p. 213-214.

80. Boccara, A.C., et al., *Sensitive photothermal deflection technique for measuring absorption in optically thin media: erratum.* Opt. Lett., 1981. **6**(1): p. 51-51.

81. Spear, J.D. and R.E. Russo, *Transverse photothermal beam deflection within a solid.* Journal of Applied Physics, 1991. **70**(2): p. 580-586.

82. Sell, J.A., et al., *Photoacoustic and photothermal beam deflection as a probe of laser ablation of materials.* J. Appl. Phys., 1990. **69**(3): p. 1330-1336.

83. Kamada, K. *Mechanisms of ultrafast refractive index change in organic system*. 2003.

84. Xia, T., et al., *Eclipsing Z-scan measurement of λ/104 wave-front distortion.* Opt. Lett., 1994. **19**(5): p. 317-319.

85. Bor, Z., *Distortion of Femtosecond Laser Pulses in Lenses and Lens Systems.* Journal of Modern Optics, 1988. **35**(12): p. 1907-1918.

86. Ferdinandus, M.R., et al., *Beam deflection measurement of time and polarization resolved ultrafast nonlinear refraction.* Opt. Lett., 2013. **38**(18): p. 3518-3521.

87. Bor, Z., *Distortion of femtosecond laser pulses in lenses.* Optics Letters, 1989. **14**(2): p. 119-121.

88. Kempe, M., et al., *Spatial and temporal transformation of femtosecond laser pulses by lenses and lens systems.* Journal of the Optical Society of America B, 1992. **9**(7): p. 1158-1165.

89. Reichert, M., et al., *Non-Instantaneous Nonlinear Refraction of Carbon Disulfide*.

90. Negres, R.A., et al., *Experiment and analysis of two-photon absorption spectroscopy using a white-light continuum probe.* Quantum Electronics, IEEE Journal of, 2002. **38**(9): p. 1205-1216.

91. Weber, M.J., D. Milam, and W.L. Smith, *Nonlinear Refractive Index Of Glasses And Crystals.* Optical Engineering, 1978. **17**(5): p. 175463-175463.

92. Samoc, A., *Dispersion of refractive properties of solvents: Chloroform, toluene, benzene, and carbon disulfide in ultraviolet, visible, and near-infrared.* Journal of Applied Physics, 2003. **94**(9): p. 6167-6174.

93. Ganeev, R.A., et al., *Nonlinear refraction in CS_2.* Applied Physics B: Lasers and Optics, 2004. **78**(3-4): p. 433-438.

94. Yan, X.-Q., et al., *Third-order nonlinear susceptibility tensor elements of CS2 at femtosecond time scale.* Opt. Express, 2011. **19**(6): p. 5559-5564.

95. DeSalvo, R., et al., *Z-scan measurements of the anisotropy of nonlinear refraction and absorption in crystals.* Opt. Lett., 1993. **18**(3): p. 194-196.

96. Desurvire, E., J.R. Simpson, and P.C. Becker, *High-gain erbium-doped traveling-wave fiber amplifier.* Optics Letters, 1987. **12**(11): p. 888-890.

97. Yiannopoulos, K., et al., *Generation of 40-GHz control signals from flag pulses for switching all-optical gates for use with optical packets.* Optics Letters, 2004. **29**(3): p. 241-243.

98. Stabile, R., A. Albores-Mejia, and K.A. Williams, *Monolithic active-passive 16 × 16 optoelectronic switch.* Optics Letters, 2012. **37**(22): p. 4666-4668.

99. Mizrahi, V., et al., *Two-photon absorption as a limitation to all-optical switching.* Optics Letters, 1989. **14**(20): p. 1140-1142.

100. Lim, J.H., et al., *Polymethine and squarylium molecules with large excited-state absorption.* Chemical Physics, 1999. **245**(1–3): p. 79-97.

101. Kartashov, D., et al., *Third- and fifth-harmonic generationby mid-infrared ultrashort pulses:beyond the fifth-ordernonlinearity.* Optics Letters, 2012. **37**(12): p. 2268-2270.

102. Kasparian, J., et al., *White-Light Filaments for Atmospheric Analysis.* Science, 2003. **301**(5629): p. 61-64.

103. Brabec, T. and F. Krausz, *Intense few-cycle laser fields: Frontiers of nonlinear optics.* Reviews of Modern Physics, 2000. **72**(2): p. 545-591.

104. Wahlstrand, J.K., et al., *Optical nonlinearity in Ar and N2 near the ionization threshold.* Phys Rev Lett, 2011. **107**(10): p. 103901.

105. Nisoli, M., S. De Silvestri, and O. Svelto, *Generation of high energy 10 fs pulses by a new pulse compression technique.* Applied Physics Letters, 1996. **68**(20): p. 2793-2795.

106. Brown, J.M., et al., *On the relative roles of higher-order nonlinearity and ionization in ultrafast light-matter interactions.* Optics Letters, 2012. **37**(10): p. 1604-1606.

107. Ariunbold, G.O., P. Polynkin, and J.V. Moloney, *Third and fifth harmonic generation by tightly focused femtosecond pulses at 2.2 μm wavelength in air.* Optics Express, 2012. **20**(2): p. 1662-1667.

108. Wang, H., et al., *Relative contributions of higher-order Kerr effect and plasma in laser filamentation.* Optics Communications, 2013. **293**(0): p. 113-115.

109. Huang, T.W., et al., *Effects of higher-order Kerr nonlinearity and plasma diffraction on multiple filamentation of ultrashort laser pulses in air.* Physics of Plasmas, 2013. **20**(7): p. 072111-9.

110. Petrarca, M., et al., *Higher-order Kerr improve quantitative modeling of laser filamentation.* Optics Letters, 2012. **37**(20): p. 4347-4349.

111. Wahlstrand, J.K., Y.H. Cheng, and H.M. Milchberg, *Absolute measurement of the transient optical nonlinearity in N_{2}, O_{2}, N_{2}O, and Ar.* Physical Review A, 2012. **85**(4): p. 043820.

112. Chen, Y.H., et al., *Single-shot, space- and time-resolved measurement of rotational wavepacket revivals in H2, D2, N2, O2, and N2O.* Optics Express, 2007. **15**(18): p. 11341-11357.

113. Wang, D. and Y. Leng, *Nonlinear response of hydrogen atom induced by intense few-cycle laser field and its influence on refractive index.* Optics Communications, 2012. **285**(24): p. 5462-5466.

114. Nibbering, E.T.J., et al., *Determination of the inertial contribution to the nonlinear refractive index of air, N2, and O2 by use of unfocused high-intensity femtosecond laser pulses.* Journal of the Optical Society of America B, 1997. **14**(3): p. 650-660.

115. Reichert, M., *Derivation Of Angular Deflection*. 2013.

116. Casperson, L.W., *Gaussian Light Beams in Inhomogeneous Media.* Applied Optics, 1973. **12**(10): p. 2434-2441.